Electronic Structure Studies of Complexes of Technetium and Ruthenium

A thesis submitted for the degree of Doctor of Philosophy of

The Australian National University.

by

Sandra Catherine Nissen

March, 1997.

Do you believe that absolutely everything can be expressed scientifically ?

Yes it would be possible. But it would make no sense. It would be description without meaning - as if you described a Beethoven symphony as a variation of wave pressure.

- Albert Einstein

Declaration

Except where specific reference is made to other sources, the work presented in this thesis is the work of the author. It has not been submitted, in whole or in part, for any other degree.

J. Nissen

Sandra Catherine Nissen

Acknowledgments

There are many people who have provided me with assistance throughout the course of my Ph.D. I would like to take this opportunity to thank them for their time, patience and valuable advice. Just some of these people are listed below, in order of how the work is presented in subsequent chapters.

On the synthetic and instrumental front, and other aspects involved in PART ONE:

- Dr John Baldas and his group at the Australian Radiation Laboratory for providing my initial training in working with technetium.
- Dr Raphael Raptis, Dr Steve Gheller and Dr Klaus Moock for their guidance and assistance with the syntheses and electrochemical analyses of technetium complexes, within the RSC. A special thank-you to Klaus for his efforts in cleaning the top-floor radiation laboratory and enduring its higher room temperatures in summer.
- Dr Keith Murray and Dr Boujemaa Moubaraki from Monash University for running the variable temperature magnetic moments and providing valuable feedback on my descriptions of same.
- Timothy Lovell, Dr John McGrady and Dr Robert Stranger from The Chemistry Faculties, ANU, for a preview of their results and valuable discussions about density-functional calculations of nonahalide dimers.
- Stephen Lee (the group technical officer) for the purification of electrochemical solvents, and all the little things which keep the place going.
- Dénes Bogsányi for running the far-IR and solid state diffuse reflectance spectra.

On the computational front I was fortunate to have two skilled and incredibly patient teachers:

- Dr John McGrady who spent time during his own Ph.D. to teach me the mysteries of the vi editor and how to run the SCF-Xα-SW package.
- Dr Stuart Macgregor who taught me how to use ADF following the loss of the Xα results in the "hard disk crash of '95".

For other contributions to PART TWO, thank-you also to:

- Pam, Nick and Graeme of the RSC Computer unit for not running away every time there was a "minor" disaster.
- Dr Brett Yeomans, Dr Dmitri Menglet and Horst Neuman for allowing me to use their experimental data for computational analyses.

For other more general contributions, I must thank:

- Dr Graham Heath, my supervisor, for his contributions to this study, for allowing me to work in his group, and for giving me the opportunity to establish so many valuable collaborations.
- Prof. Martin Bennett, Dr. Lucjan Dubicki and Dr. Robert Stranger, the members of my advisory panel, for their guidance and advice.
- Stuart, Klaus, Raphael, John, Rob and Graham for proof reading and advising on the construction of the final thesis.

Those responsible for maintenance of my sanity and relaxation:

- The members of the ANU Choral Society (SCUNA) and in particular, fellow sopranı, committee and small group members, and the "RSC Mafia" (fellow choristers drawn from the RSC) Rowena, Karen, Cameron and Kristine.
- The Canberra Community Orchestra (CCO) in particular the viola section who suffered my bad tuning and wit.
- Members of the Canberra City Uniting Church, especially fellow members of the choir and the elders who took time to chat to me.

Finally special mention to three people without whom this thesis may never have got to this final stage:

- Dr Robert Stranger, who supervised my honours research, inspired me to do a Ph.D. in the first place, and who remained a valuable source of computational advice and a supporting and understanding friend throughout.
- Dr Klaus Moock and Dr Stuart Macgregor who upon arrival to the group, during the last half of my Ph.D., rose above and beyond the call of duty to assist with its direction and ultimate completion, and who have considerably increased my knowledge pertaining to the benefits of double glazing in places where it gets <u>really</u> cold, and any minor short-comings of the Aussie cricket team.

Abstract

This thesis is devoted to the study of the electronic structure of binuclear and monomeric, halide complexes of technetium and ruthenium using the techniques of voltammetry, UV-visible spectro-electrochemistry and magnetochemistry, as well as analysis based on density functional calculations. In the first part, the thesis will describe the properties of $[Tc_2Br_9]^{1-}$. A detailed analysis of the nature of the metal-to-metal interaction in $[Tc_2Br_9]^{1-}$ is presented and possible routes to the as yet unknown $[Tc_2Cl_9]^{n-}$ were studied. In parallel with this study, an investigation of related technetium monomer chemistry was performed. The purpose of the second part of the thesis was to investigate the bonding and electronic structure of complexes containing an $\{MX_4\}$ moiety (where M = Tc, Ru and X = Cl, Br) for which both UV-visible spectral and electrochemical data were available. This work commences with a study of the technetium monomers $[TcYX_4]^{n-}$ (where X = Cl, Br and Y = the π donors O, (n = 0, 1) and N (n = 1, 2)) discussed in the first part of the thesis. The study extends to *trans*-$[Ru^{III}Cl_4L_2]^{1-}$ (where L = MeCN, *t*-BuNC, aniline, PMe_2Ph, PEt_3) complexes where L covers a range of π–acceptor abilities.

The introduction highlights the importance of considerations of electronic structure within the context of this thesis. A brief description of the element technetium is provided. This is followed by an outline of the electronic structure of $[MX_6]^{n-}$ monomers which focuses on the information that can be derived using techniques including, density-functional calculations, magnetochemistry, voltammetry and UV-visible spectroscopy, all of which will be employed throughout this thesis . The impact of changes to donor properties of the ligand array from $\{X_6\}$ to $\{OX_4\}$, $\{NX_4\}$ and $\{X_4L_2\}$ is introduced. A brief description of the electronic structure of $[M_2X_8]^{n-}$ and $[M_2X_9]^{n-}$ dimers is also provided.

PART ONE

Chapter 1.1 details the synthesis of the confacial bioctahedral dimer, $[Tc_2Br_9]^{1-}$ and the investigation of its variable temperature magnetic moment, voltammetry and UV-visible spectro-electrochemistry. These analyses, combined with the results of density functional calculations, indicate that the metal-to-metal interaction in d^3d^3 $[Tc_2Br_9]^{1-}$ is at best very weak and is best described as having three 4d electrons localised about each technetium atom. Comparisons with other isoelectronic $[M_2X_9]^{n-}$ (M = transition metal and X = Cl, Br) complexes highlight the similarities of this metal-to-metal interaction to that in $[Cr_2X_9]^{3-}$ and the important differences compared to that in $[Re_2X_9]^{1-}$.

Chapter 1.2 describes the non-bridging, unsupported M-M bonded dimers, $[Tc_2X_8]^{n-}$ (X = Cl, Br and n = 2, 3), and their voltammetry and UV-visible spectro-electrochemistry, emphasising the similarities to $[Re_2X_8]^{n-}$ (X = Cl, Br and n = 2, 3). The chapter concludes with an analysis of unsuccessful routes to $[Tc_2Cl_9]^{n-}$.

Chapter 1.3 describes the voltammetry and UV-visible spectra of $[TcX_6]^{2-}$ (X = Cl, Br) recorded under the same conditions of the dimer study. It also establishes comparisons of the voltammetry of $[MCl_6]^{n-}$ complexes along the second and third row of the periodic table, and between related vertical ($4d^n$, $5d^n$) centres. These comparisons give further insight into the investigation of $[Tc_2Br_9]^{1-}$.

Chapter 1.4 describes the voltammetry and UV-visible spectro-electrochemistry of $[TcOX_4]^{n-}$ (where X = Cl, Br and n = 0, 1), also under the same conditions as the dimer study. The analysis of these measurements was enhanced by the study of $[TcNX_4]^{n-}$ (where X = Cl, Br and n = 1, 2), and the effect of the stronger π donation of the nitrido ligand over the oxo ligand on the observed measurements is investigated.

Chapter 1.5 reports the methods used in preparing the complexes described in the preceding chapters. The equipment used during electrochemical investigations and the criteria employed during analysis of the voltammetric and spectro-electrochemical results are also described.

PART TWO

Chapter 2.1 returns to the $[TcYX_4]^{n-}$ monomers for a more in-depth analysis of their electronic structure. Density functional calculations are used to investigate the effects of modifications to the $\{X_4\}$ moiety, $\{Cl_4\}$ *vs* $\{Br_4\}$, changes to the axial ligand, Y, (O *vs* N) and changes to the oxidation state of the technetium metal centre (Tc^{VI} *vs* Tc^{V}) on the electronic structure. Assignments for the UV-visible spectra observed for these $[TcYX_4]^{n-}$ monomers in chapter 1.4 are proposed.

Chapter 2.2 extends the investigation of complexes containing the $\{MX_4\}$ moiety to another specific series, *trans*-$[RuCl_4L_2]^{1-}$ (where L = MeCN, *t*-BuNC, aniline, PMe_2Ph, PEt_3). The effects of changing axial ligands on the electronic structure are analysed, and assignments for the UV-visible spectra are proposed, on the basis of the density functional calculations performed using model systems for L of = NCH, CNH, NH_3, and PH_3 respectively. The chapter concludes with an analysis of the relationship between the energy of a halide-to-metal charge transfer band (common to all the ruthenium complexes listed), with the corresponding $Ru^{III/II}$ reduction potential.

Chapter 2.3 gives a brief outline of the principles of density functional calculations, and describes the specific parameters used in running calculations with the Amsterdam Density Functional (ADF) package employed here.

Table of Contents

PART TWO

Introduction

Chemistry is the study of the elements and how they combine to form compounds. Understanding of the bonding within such compounds is obtained by focussing attention on the electronic structure of each component (element or group of elements) and studying how these components interact at an atomic level to determine the unique range of properties of the final compound. The depth of understanding of this electronic structure has mirrored the increasing sophistication of the techniques available with which to probe it. These techniques are both observational (for example crystal-structure analysis, magnetic studies, vibrational and electronic spectroscopy, electrochemistry) and computationally based. The computational methods are based on the quantum mechanical model of electronic structure. This model surmises that the electronic charge density of a molecule will be determined by the sum of its atomic parts, and also implies that the electronic properties of atoms are transferable between molecules. (**1**) Hence, the understanding of electronic structure can also be improved by the study of series of compounds with variations selected to probe the desired property (for example, systematic variations in ligands or metals such as will be described in this thesis).

This thesis will focus on the electronic structure of metal halide complexes. It is therefore illustrative to include in the introduction a consideration of the relatively well understood properties of the basic octahedral transition metal complex, $[MX_6]^{n-}$ (X = halide), and to relate these properties to the underlying electronic structure of these species (section I.2). The coordinatively more complex, $[MYX_4]^{n-}$, monomeric species are then introduced (section I.3) where a planar $\{X_4\}$ moiety is maintained but the trans ligands, Y, are varied from π-donors such as O and N, to π-neutral species such as aniline in *trans*-$[MX_4L_2]^{n-}$ and further to π-acceptors such as MeCN, *t*-BuNC and

phosphines in *trans*-$[MX_4L_2]^{n-}$. These systems assist in assessing the impact on the overall electronic structure of these different types of π interacting species within the ligand array.

Another type of interaction (apart from metal-to-ligand) which is also of interest is the direct metal-to-metal interaction. The metal halide dimers of the type $[M_2X_8]^{n-}$ (section I.5) and $[M_2X_9]^{n-}$ (section I. 4) provide ideal models for investigating the impact of two different types of metal-to-metal interaction on electronic structure by comparing these dimers to the $[MX_6]^{n-}$ species. The $[M_2X_9]^{n-}$ dimer can be thought of as two $[MX_6]^{n-}$ species with three bridging halides "supporting" the metal-to-metal interaction. In contrast, $[M_2X_8]^{n-}$ dimers possess a direct metal-to-metal interaction which is "un-supported" by any ligand bridges.

The systems studied within the experimental and computational parts of this thesis are predominantly technetium halide species and in addition one series of ruthenium halide complexes has been investigated in the computational part. These technetium and ruthenium species were chosen on the basis of the experimental data available with which to probe their electronic structure. These data were obtained using the following techniques; magnetochemistry, voltammetry, UV-visible spectro-electrochemistry and density functional calculations. Information available about related complexes based on neighbouring metals has also been used to gain further insight into the systems of interest here.

Technetium halide complexes are of special interest because their chemistry is relatively less-explored in comparison with the amount of information which is available for related complexes of the neighbouring transition metals, for example rhenium.

I.1 Technetium

Technetium means "artifical element" which refers to the fact that technetium was the first new element to be artificially prepared. (**2**) Technetium is radioactive and none

of its isotopes are naturally occurring. It was first identified in 1937 by radiations from a molybdenum plate which had been bombarded with deuterons. (**3**) Its chief source now however, is from uranium fission products, about 6% of which are technetium. (**2**) The first isotopes to be identified were ^{95}Tc and ^{98}Tc, but technetium has since been identified in isotopes ranging from ^{90}Tc to ^{110}Tc which have half-lives from 15.8 seconds (^{100}Tc) to $4.2x10^6$ years (^{98}Tc). (**4**) The isotope on which most of the chemistry of technetium is based (and which was employed in this thesis) is the relatively stable, long-lived isotope ^{99}Tc. (**4**) ^{99}Tc is a β emitter (E_{max} = 0.29 MeV) with a half-life of $2.12x10^5$ years. (**2**)

Recent attention on technetium chemistry has been directed toward its use as a radiopharmecutical. This chemistry has been reviewed focussing on both the medical applications and insights into the general chemistry of technetium complexes. (**5**) Technetium can be used for imaging a variety of internal organs by radioscintigraphic techniques. The isotope of choice is the metastable, γ-emitter, ^{99m}Tc, which can be generated relatively inexpensively in portable molybdenum containing generators. (**5b**) ^{99m}Tc has a half-life of 6 hours so it can be used to deliver a high short-term specific activity without being a long-term hazard. (**5b**) γ-rays are emitted upon decay with sufficient energy (140 KeV) to be detected through layers of tissue. (**5b**) The resultant daughter isotope of this decay, ^{99}Tc emits less hazardous β-radiation. (**5b**) Technetium complexes generally have a total-body biological half-life (that is, the time taken to remove half of the technetium from the body) of 30 hours. (**6**)

Other recent reviews of technetium have focussed on various aspects of its chemistry: including structures (**7**), cluster compounds containing Tc-Tc bonds (**8**), general coordination and reaction chemistry (**4**,**9**,**10**,**11**). It has been stated that (**4**), chemically, technetium resembles rhenium (its third row counterpart) but there are significant differences, in particular associated with the redox chemistry. There are a large number of oxidation states available to both technetium and rhenium. Complexes have been prepared with examples of technetium in every oxidation state from Tc^{VII} (d^0)

$H[TcO_4]$ to Tc^{-I} (d^8) $Na[Tc(CO)_5]$. (**2**) Rhenium has the same range of oxidation states (**12**). In general it has been found that the higher oxidation states of technetium are more easily reduced than those of rhenium, while the lower oxidation states of technetium are more labile toward substitution. (**4**) Further discussion of the differences (and similarities) of technetium and rhenium chemistry will appear throughout this thesis.

The following sections will briefly outline the electronic structure of $[MX_6]^{n-}$ against which the coordinatively more complex systems will be compared. Reference will be made to the different techniques used to probe the structure and the results for each in terms of $[MX_6]^{n-}$ will be described.

I.2 Halide complexes of the general form $[MX_6]^{n-}$

The electronic structure of complexes of the form $[MX_6]^{n-}$ (where X is a halide ligand) has been extensively studied using a variety of techniques. Examples of previous studies employing the methods of interest in this thesis include; density functional calculations (**13**,**14**), magnetic moments (**15**), UV-visible electronic spectroscopy (**16**) and electrochemistry (**17**). A summary of the type of information afforded by each of these techniques is presented in this section.

I.2.1 Density functional calculations

$[MX_6]^{n-}$ has its six halide ligands arranged in octahedral symmetry around the metal centre:

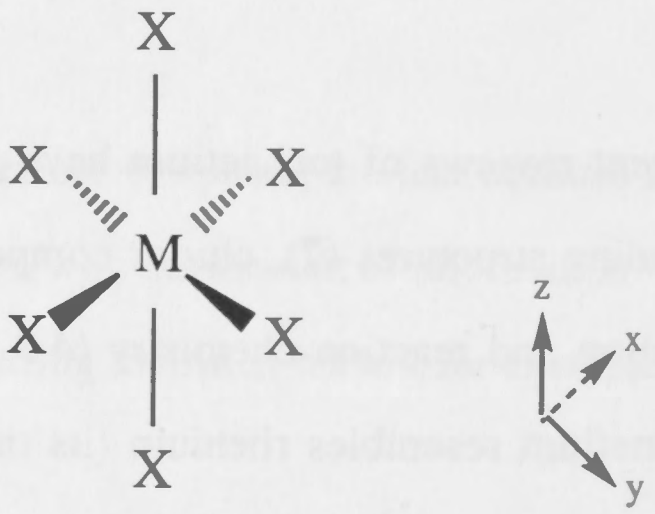

Figure I.1 *The octahedral arrangement of the $[MX_6]^{n-}$ species. The direction of the x, y and z axes is also indicated.*

Under O_h symmetry the nd orbitals of the metal transform as π-type t_{2g} (d_{xy}, d_{xz}, d_{yz}) and σ-type e_g (d_{x2-y2}, d_{z2}). The molecular orbitals arising from the p orbitals of the $\{X_6\}$ manifold (see figure I.2) transform as six σ-type molecular orbitals $a_{1g}+e_g+t_{1u}$ and 12 π-type molecular orbitals $t_{1u}+t_{2u}+t_{1g}+t_{2g}$. (**13b**)

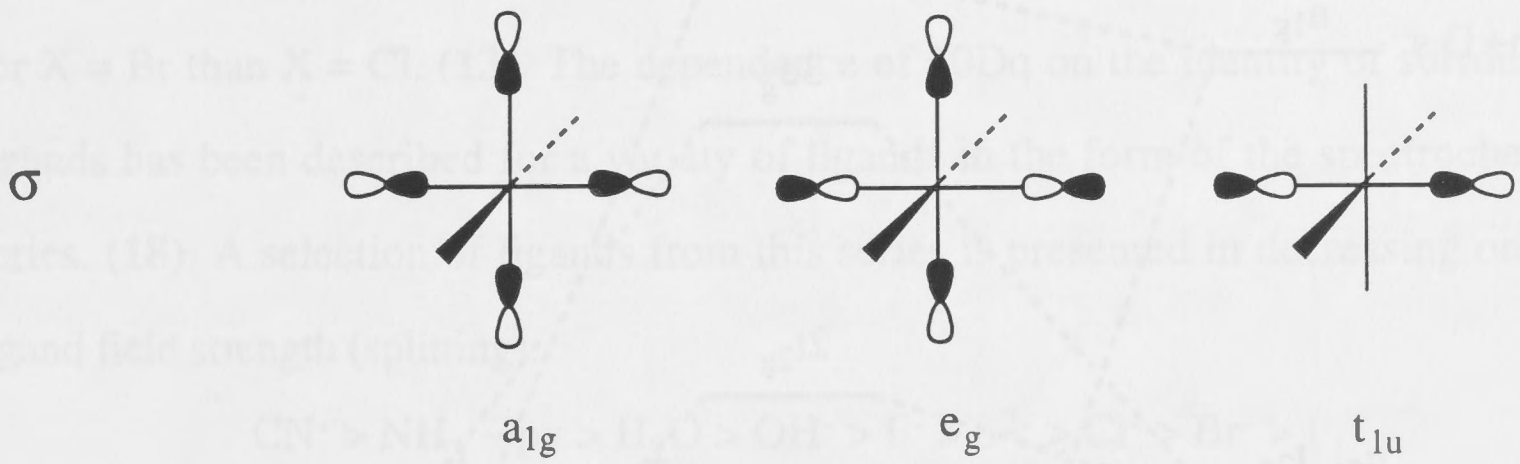

Figure I.2 *The molecular orbitals derived from the $\{X_6\}$ halide ligand array (**13b**). For degenerate orbitals only one orientation is shown in each case.*

It can be seen from figure I.2 that there are molecular orbitals of t_{1u} symmetry within both the σ and π-type sets. These molecular orbitals can mix resulting in levels which are a combination of σ and π character. Calculations using SCF-Xα-SW have shown that in the case of $[MX_6]^{n-}$ the mixing of these levels is such that the levels are not dominated by one character over the other. (**13**) Such levels are marked as π/σ in the following text.

A generalised molecular orbital diagram as derived from a computational study of a series of $[MX_6]^{n-}$ type complexes (M = Ru, Os, Pt, Pd, Rh, Ir; X = Cl, Br) (**13**) is presented in figure I.3. The figure highlights the interaction between the valence, atomic

nd, (n+1)s and (n+1)p orbitals of the metal and the halide based molecular orbitals just described.

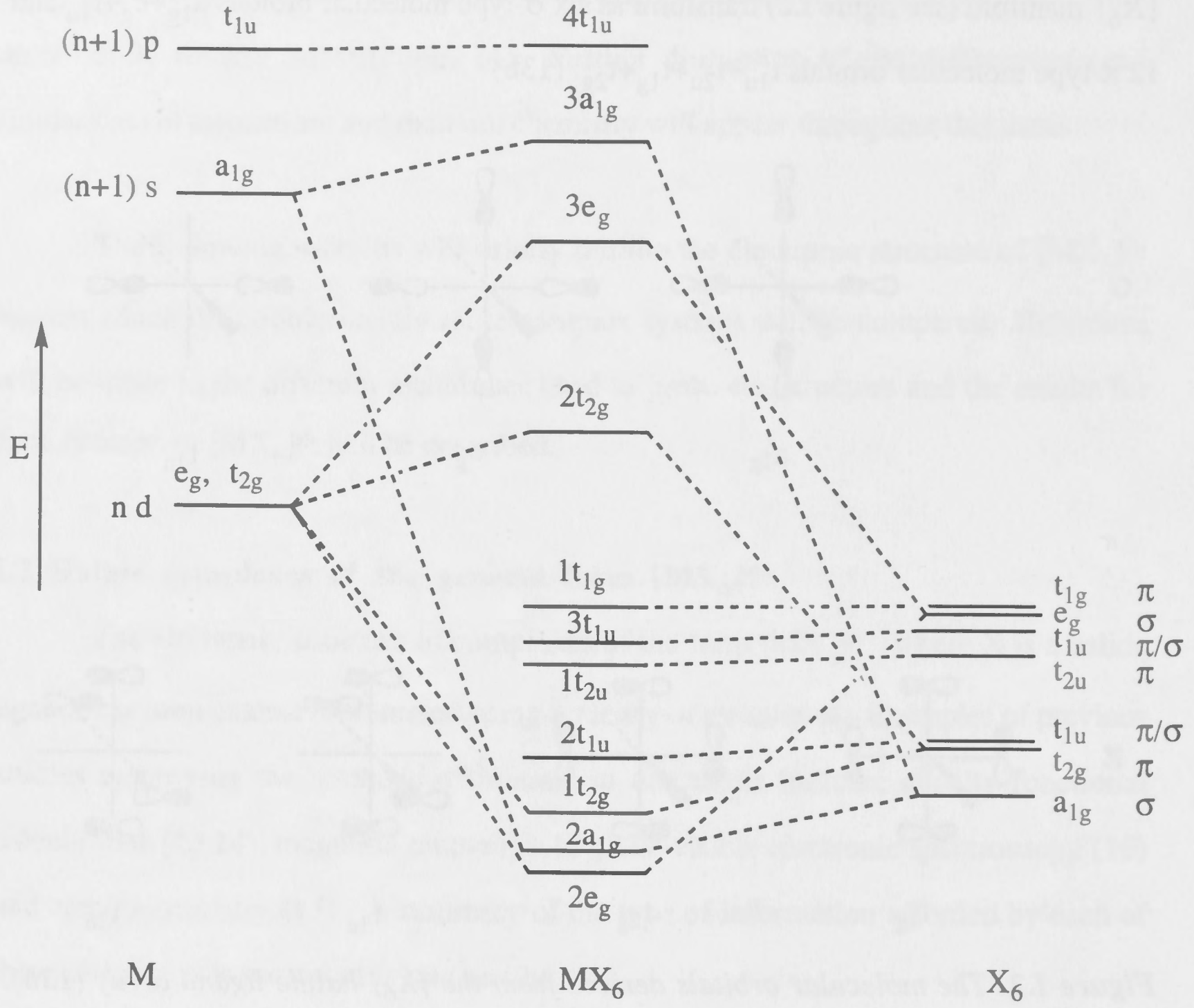

Figure I.3 *A molecular orbital diagram for $[MX_6]^{2-}$, as derived from the metal nd, (n+1)s and (n+1)p atomic orbitals and halide molecular orbitals. (**13**)*

The molecular orbital diagram (figure I.3) highlights the interactions between both $\sigma(e_g)$ and $\pi(t_{2g})$ dominated levels of the metal and the $\{X_6\}$ manifold. A lesser interaction between the a_{1g} levels is also represented. The t_{1u} levels remain non-bonding however (for example, less than 5% metal character was calculated (**13**) for the $3t_{1u}$ and $2t_{1u}$ molecular orbitals in $[RuX_6]^{3-}$) indicating that the (n+1)p levels of the metal play only a small role in the bonding between the central metal and the halide $\{X_6\}$ array. (**13**)

The energy gap between $2t_{2g}$ and $3e_g$, 10Dq, is a function of the σ and π donor strength of the coordinated ligands. (**13**,**18**) In particular, π donor strength will affect t_{2g} energy and σ donor strength will affect the energy of e_g. In the case of X = chloride *vs* X = bromide which is of importance throughout this thesis 10Dq is larger for X = Cl while the energies of the ligand based orbitals (relative to the metal based ones) are higher for X = Br than X = Cl. (**13**) The dependence of 10Dq on the identity of surrounding ligands has been described for a variety of ligands in the form of the spectrochemical series. (**18**) A selection of ligands from this series is presented in decreasing order of ligand field strength (splitting):

$$CN^- > NH_3 \sim py > H_2O > OH^- > F^- > S^{2-} > Cl^- > Br^- > I^-.$$

I.2.2 Magnetochemistry

Much of the chemistry of $[MX_6]^{n-}$ compounds is determined by the extent of occupation of the anti-bonding, metal-dominated $2t_{2g}$ and $3e_g$ molecular orbitals. This is dependent on the identity of the central metal and its oxidation state. Three nd electrons can enter the $2t_{2g}$ level successively, however for a d^4 species the electron can either spin-pair in a low-spin $t_{2g}^4e_g^0$ arrangement or it can enter the e_g levels and produce the high-spin $t_{2g}^3e_g^1$ configuration (similarly for d^5 which can be $t_{2g}^5e_g^0$ or $t_{2g}^3e_g^2$).# Whether a complex takes on a low-spin or high-spin arrangement is determined by the relative energy required in placing an electron in the higher energy level (that is, on the size of 10Dq) *vs* the energy required for spin pairing of electrons in t_{2g} and e_g. (**19**) $[MX_6]^{n-}$ complexes involving first row transition metals tend to show a greater propensity for high-spin arrangements than those involving second and third row transition metals. (**20**) The preferred electron configuration for a given $[MX_6]^{n-}$ species can be investigated using magnetochemistry which provides an indication of the number of unpaired electrons within the species. The observed magnetic moment of first and second row transition metals can be compared against the idealised, spin-only value (table I.4) to get an indication of the number of unpaired spins.## (**19**) For example, the

---

If octahedral symmetry is maintained, configurations of d^6 and above must involve some form of spin pairing.

Spin-orbit coupling is larger in complexes involving third row transition metals and as such a spin-only treatment is less satisfactory.

d^4 system $K_2[RuCl_6]$ has an observed magnetic moment of 2.70 B.M. (**20**) which is more in keeping with the value expected for two unpaired electrons (a low spin arrangement) than four (high spin). Table I.4 includes indications of the range of values for observed magnetic moments of octahedral complexes with high spin arrangements of the first row transition metals (**21**) and examples of low spin arrangements of second row $[MX_6]^{n-}$ species (**20**, **22**).

Table I.4 Magnetic-moment, spin-only values.

unpaired electrons	$\mu_{s.o.}$ (B.M.)	Complex	3d electron count	observed μ_{eff} (B.M.)
1	1.73	Ti^{3+}	d^1	1.7 - 1.8
		Mo^{5+}	d^1	1.31
		Cu^{2+}	d^9	1.9 - 2.1
2	2.83	V^{3+}	d^2	2.8 - 3.1
		Ru^{4+}	d^4	2.70
		Ni^{2+}	d^8	2.9 - 3.9
3	3.88	Cr^{3+}	d^3	3.7 - 3.9
		Tc^{4+}	d^3	3.34 - 3.80
		Co^{2+}	d^7	4.3 - 5.2
4	4.90	Cr^{2+}, Mn^{3+}	d^4	4.8 - 4.9
		Fe^{2+}, Co^{3+}	d^6	5.0 - 5.6
5	5.92	Mn^{2+}, Fe^{3+}	d^5	5.7 - 6.0

1.2.3 Voltammetry

The use of voltammetry to assess the electronic structure of $[MX_6]^{n-}$ complexes has been demonstrated by an extensive study of the redox properties of a series of hexachlorometalates extending along both the second and third row transition metals (for Zr to Pd and Hf to Pt respectively) (**17a**). The potentials for the M^{IV} to M^{III} reduction and M^{IV} to M^{V} oxidation were recorded for each of these species, $[MX_6]^{n/n-1}$ (n = 1-, 2-) and plotted against atomic number as shown in figure I.5. (**17a**)

These processes correspond to progressively filling the t_{2g} level, commencing from d^0 (for $[ZrCl_6]^{2-}$, $[NbCl_6]^{1-}$ and $[TaCl_6]^{1-}$) to d^6 for ($[RhCl_6]^{3-}$, $[IrCl_6]^{3-}$, $[PdCl_6]^{2-}$and $[PtCl_6]^{2-}$). The deviations from linearity corresponding to processes involving the d3/d4 electron configurations and have been previously accounted for in terms of the greater ~~spin-orbit coupling~~ spin pairing energy contribution associated with this particular couple. (**17a**)

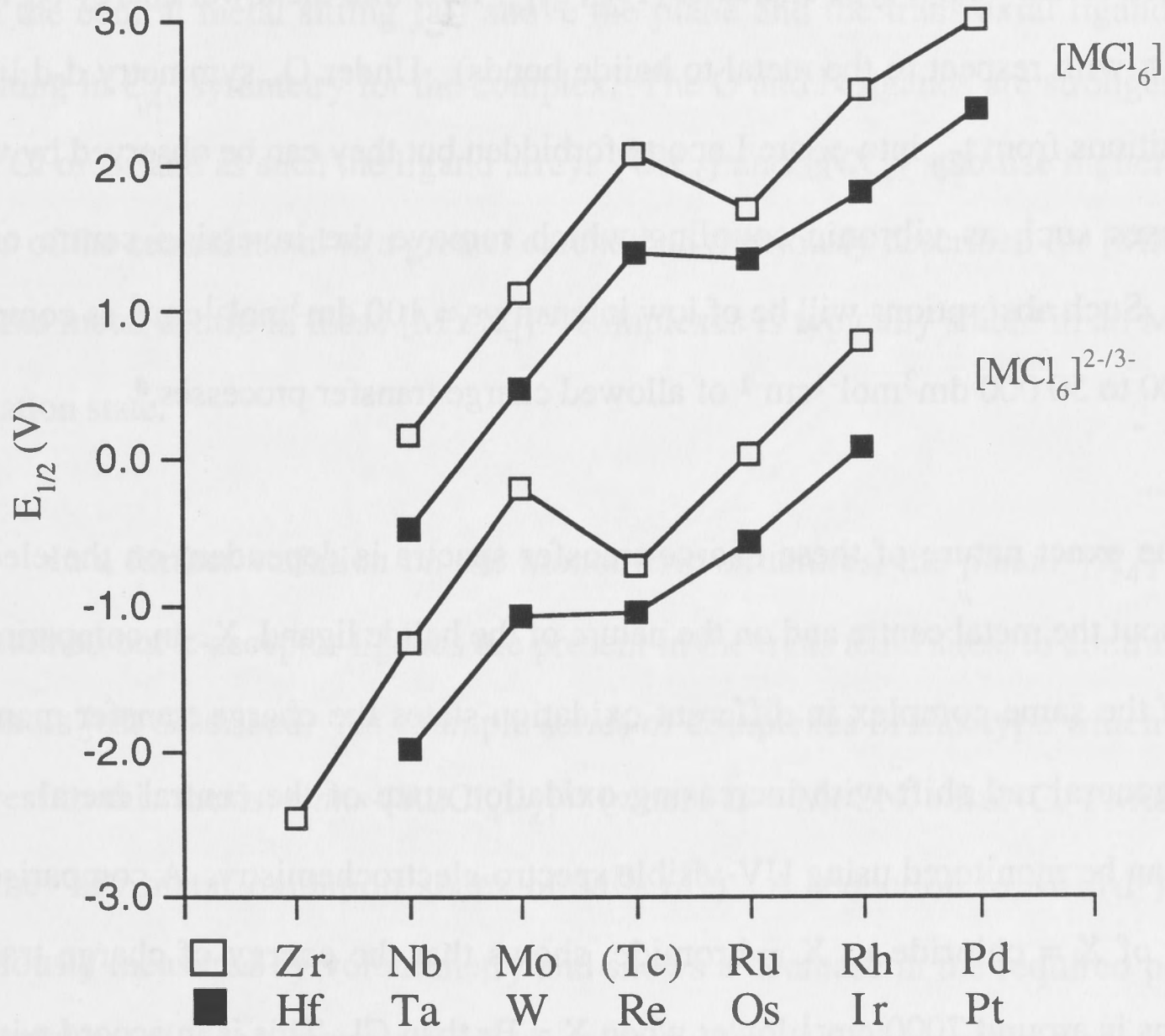

Figure I.5 *A plot of $E_{1/2}$ (V) for the one electron oxidation and reduction of $[M^{IV}X_6]^{n/n-1}$ (n = 1-, 2-) for the second and third row transition elements as reported in reference (**17a**).*#

It should be noted that the authors (**17a**) predicted the values for the oxidation and reduction of $[TcCl_6]^{2-}$ presented in the graph. It will be shown in chapter 1.3 that subsequent observations bear out this prediction.

I.2.4 UV-visible electronic absorption spectroscopy

The tendency for electronic charge to be donated by the $\{X_6\}$ ligand array to the metal in $[MX_6]^{n-}$ complexes is evident in their UV-visible electronic absorption spectra which are dominated by halide to metal charge transfer transitions. In general, the high energy region is dominated by charge transfer from halide based levels with some σ character ($3t_{1u}$) into the e_g acceptor levels of the metal (which are oriented σ with respect to the metal to halide bonds) and the lower energy region is due to charge transfer from halide based levels with π-type character ($1t_{2u}$, $3t_{1u}$, $1t_{1g}$) into the lower energy t_{2g} levels (oriented π with respect to the metal to halide bonds). Under O_h symmetry d-d ligand field transitions from t_{2g} into e_g are Laporte forbidden but they can be observed by virtue of processes such as vibronic coupling which remove the inversion centre of the molecule. Such absorptions will be of low intensity $\varepsilon = 100$ $dm^3mol^{-1}cm^{-1}$ as compared to $\varepsilon = 5000$ to 50 000 $dm^3mol^{-1}cm^{-1}$ of allowed charge transfer processes.#

The exact nature of these charge transfer spectra is dependent on the electron density about the metal centre and on the nature of the halide ligand, X. In comparing the spectra of the same complex in different oxidation states the charge transfer manifold shows a general red shift with increasing oxidation state of the central metal. Such changes can be monitored using UV-visible spectro-electrochemistry. A comparison of the effect of X = chloride *vs* X = bromide, shows that the energy of charge transfer absorptions is around 7000 cm^{-1} lower when X = Br than Cl. This is in accord with the destabilisation of bromide based molecular orbital levels as was described earlier (section I.2.1). (**13**,**18**) The charge transfer spectra where X = bromide also generally show more structure than those due to X = chloride, as a result of the splitting induced by larger spin-orbit coupling for bromide. (**13**,**18**)

I.3 Variations in the nature of the ligand array

Further information about the impact of the nature of the ligand array on electronic structure can be assessed by systematically adjusting the identity of the

---

The electronic dipole allowed transitions under O_h symmetry have transition moment operators which transform as t_{1u}.

coordinated ligands. For example, a study of two series of complexes of molybdenum and tungsten aimed to investigate the effect of varying the σ- and π-donor strength of the ligand array on electronic structure. (**23**) It was found that the relative stability of the higher oxidation states of the metals varied in accordance with increasing σ and π-donor strength of the total ligand array in the order $\{Cl_6\} < \{Cl_5O\} < \{Cl_4N\}$. (**23**) A similar study will be described in this thesis for complexes of $[TcYX_4]^{n-}$ (where X = Cl, Br; Y = O, n = 0, 1 and Y = N, n = 1, 2). These compounds possess a planar $\{X_4\}$ moiety with the central metal sitting just above the plane and the trans axial ligand above it, resulting in C_{4v} symmetry for the complex. The O and N ligands are stronger π donors than Cl or Br and as such the ligand arrays $\{OX_4\}$ and $\{NX_4\}$ stabilise higher oxidation states of the central metal to a greater extent than previously described for $[MX_6]^{n-}$, such that the metal centre in these $[MYX_4]^{n-}$ complexes is typically stable in an M^V or M^{VI} oxidation state.

In a further variation on the monomeric structures, the planar $\{X_4\}$ moiety is maintained but π-acceptor ligands are present in the trans axial sites, to contrast with the π-donors just described. An example series of complexes of this type which will be of interest in this thesis, *trans*-$[RuCl_4L_2]^{1-}$ (where L = MeCN, *t*-BuNC, $PMePh_2$, PEt_3, aniline) has metal oxidation states of M^{III} (d^5). A reduction to M^{II} (d^6) has been previously measured by voltammetry and shows a decrease in the required potential of the metal based, one electron reduction, coinciding with the increasing π-acceptor ability of the trans axial ligands. (**24**) A linear relationship between this reduction potential and the energy of a ligand to metal absorption band was also described. (**24**) Calculations on these complexes were performed during the course of this thesis (chapter 2.2) to determine how successful the computed electronic structure would be at modelling both the π-acceptor ability dependence and the linear relationship between E^0 and hν.

I.4 Dimetallic complexes of the type $[M_2X_9]^{n-}$

The discussion has centred on metal-to-ligand interactions in previous sections. Since direct metal-to-metal interactions were recognised (1930's) their general theoretical

importance and their significance in biological systems (for example, nitrogenases) and catalytic processes (for example, $(\eta^3\text{-}C_3H_5PdCl_2)_2$) have been recognised. (**25**,**26**) It is therefore of interest to assess the impact of this different type of interaction on the electronic structure of metal halide complexes.

Complexes of the type $[M_2X_9]^{n-}$ can be thought of as two $\{MX_6\}$ octahedra sharing one face such that each metal centre is surrounded by three terminal and three bridging halides. The bridging halides are shared between two metal centres and so can be thought of as effectively contributing only 1.5 halides to each, thus resulting in a total, bridging halides plus terminal halides, of $\{MX_{(4.5)}\}$, in a lower symmetry trigonal environment.

The first compound of this kind to be identified was $K_3[W_2Cl_9]$ (in 1935). (**25**) The structure shown in figure I.6 is typical of complexes of this $[M_2X_9]^{n-}$ arrangement.

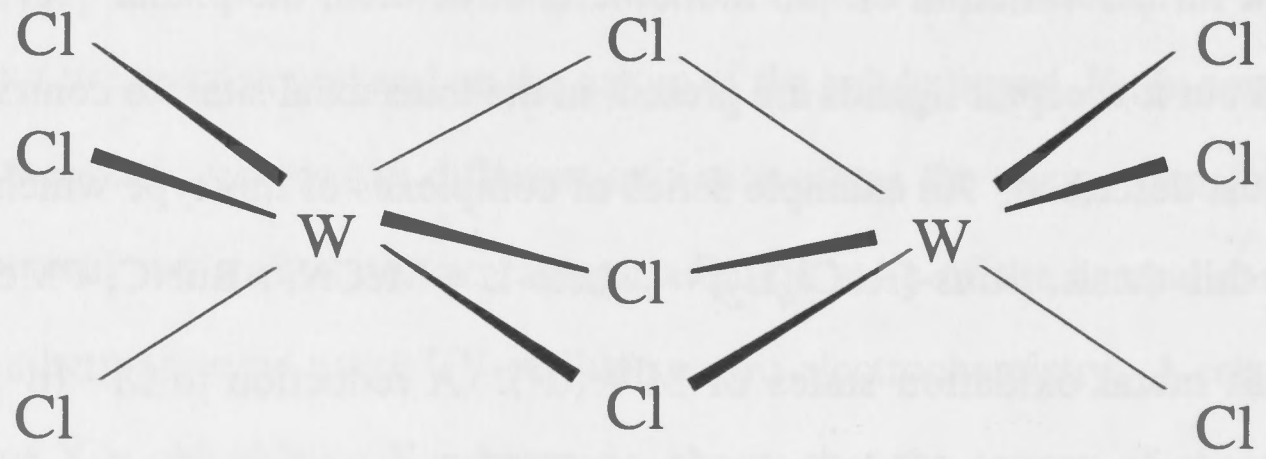

Figure I.6 *Crystal structure of $K_3[W_2Cl_9]$ as originally reported (showing three bridging chloride ligands between the tungsten metal centres). W-W = 2.41 Å (**25**).*

Since its isolation a large series of $[M_2X_9]^{n-}$ complexes has been prepared (**25**) as is indicated by the shaded regions in figure I.7. Figure I.7 is accompanied by table I.8 which lists the identity of the halides for which $[M_2X_9]^{n-}$ coordination is known to be possible for each of the elements, accompanied by example references.

Studies of these complexes using structural analysis (**27**,**28**), magnetochemistry (**29**,**30**), voltammetry (**31**,**32**), UV-visible spectroscopy (**33**,**34**), and density

functional calculations (**13**,**28**,**33**,**35**), have focussed on the varying degrees of metal-to-metal interaction, which can be supported by the bridging ligands. Considerable variation is observed even between isoelectronic analogues such as the d^3d^3 species $[M_2X_9]^{3-}$ (M = Cr, Mo, W) for which the metal-to-metal interaction varies from triple bonding in $[W_2X_9]^{3-}$ to single bonding in $[Mo_2X_9]^{3-}$ and finally to no direct metal-metal bond at all in $[Cr_2X_9]^{3-}$. (**25**)

H																	He
Li	Be											B	C	N	O	F	Ne
Na	Mg											Al	Si	P	S	Cl	Ar
K	Ca	Sc	Ti	V	Cr	Mn	Fe	Co	Ni	Cu	Zn	Ga	Ge	As	Se	Br	Kr
Rb	Sr	Y	Zr	Nb	Mo	Tc	Ru	Rh	Pd	Ag	Cd	In	Sn	Sb	Te	I	Xe
Cs	Ba	La	Hf	Ta	W	Re	Os	Ir	Pt	Au	Hg	Tl	Pb	Bi	Po	At	Rn
Fr	Ra	Ac	Unq	Unp	Unh	Uns		Une									

Ce	Pr	Nd	Pm	Sm	Eu	Gd	Tb	Dy	Ho	Er	Tm	Yb	Lu

Figure I.7 *A periodic table showing the relatively large number of elements for which complexes of the type $[M_2X_9]^{n-}$ are known (as indicated by the shaded areas). The actinides have been omitted from the table because no examples from these groups have been reported to date.*

The bond order of a $[M_2X_9]^{n-}$ system is determined by electron counting into the schematic molecular orbital diagram which is presented as figure I.9. A bond order of zero means that no net bond is possible whereas a bond order of three means that a triple bond is possible, given the appropriate conditions. These formal bond orders are listed with typical examples of each configuration in the table I.10.

Table I.8 Complexes of $[M_2X_9]^{n-}$.

M	F	Cl	Br	I	References
Sc		√		√	**36a,b**
Y				√	**36c**
Ti		√	√		**36d,e**
Zr	√		√		**36f,g**
V	√	√	√		**36e,h**
Nb		√	√	√	**36i**
Ta		√			**36j**
Cr	√	√	√		**36i,29**
Mo	√	√	√	√	**27**
W		√	√		**27**
Mn	√	√			**36l**
Tc			√		**37**
Re		√	√		**27,38**
Fe	√	√	√		**35m**
Ru		√	√		**36n,o**
Os		√	√		**31**
Rh		√	√		**27**
Ir		√	√		**36p**
Pt		√	√		**36q**
Tl		√			**27**
Sb	√	√	√	√	**36r,s**
Bi				√	**27**
Tb			√		**36t**
Dy			√		**36c,t**
Ho			√		**36c,t**
Er			√		**36c,t**
Tm				√	**36u**
Yb		√	√		**36c,t,v**
Lu		√			**36w**

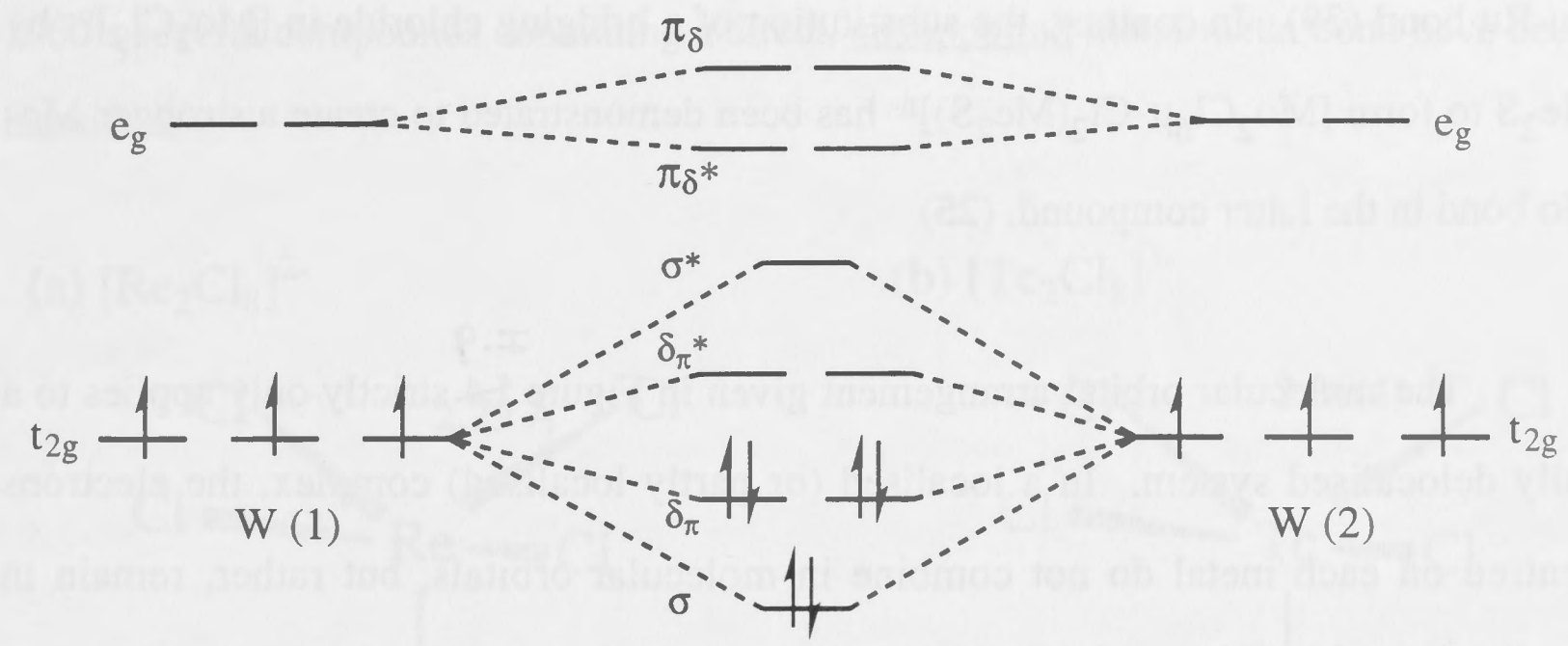

Figure I.9 *The molecular orbitals formed by interaction of the valence d levels of the metal centres in a fully delocalised system. A d^3d^3 occupation is shown indicating the maximum triple bond. (**13**)*

It has been found that the bonding which is ultimately observed in a compound is not only dependent on the bond order but also on the extent to which the electrons from each metal centre are delocalised. This extent of delocalisation is determined by a number of factors including the identity of the metal ions and their oxidation state and the resultant degree of orbital overlap of the metal t_{2g} based levels in particular (**13**).

Table I.10 Bond Orders for example complexes of the type $[M_2X_9]^{n-}$.

Configuration	d^6d^6	d^5d^5	d^4d^4	d^3d^3
Bond Order	0	1	2	3
Examples	$[Rh_2X_9]^{3-}$ $[Ir_2X_9]^{3-}$	$[Ru_2X_9]^{3-}$ $[Os_2X_9]^{3-}$	$[Ru_2X_9]^{1-}$ $[Os_2X_9]^{1-}$	$[Cr_2X_9]^{3-}$ $[Mo_2X_9]^{3-}$ $[W_2X_9]^{3-}$ $[Re_2X_9]^{1-}$ $[Tc_2X_9]^{1-}$

The nature of the bridging and terminal ligands is also important in determining metal to metal bonding. For example, $[Ru_2^{III,III}Cl_9]^{3-}$ has a single bond but with the substitution of terminal phosphine ligands to form $[Ru_2^{III,III}Cl_3(PR_3)_6]^{3+}$ the electrons become completely localised and the complex is best thought of as having no direct

Ru-Ru bond (**39**). In contrast, the substitution of a bridging chloride in $[Mo_2Cl_9]^{n-}$ by Me_2S to form $[Mo_2Cl_6\mu\text{-}Cl_2(Me_2S)]^{n-}$ has been demonstrated to create a stronger Mo-Mo bond in the latter compound. (**25**)

The molecular orbital arrangement given in Figure ~~I.4~~ I.9 strictly only applies to a fully delocalised system. In a localised (or partly localised) complex, the electrons centred on each metal do not combine in molecular orbitals, but rather, remain in localised metal based ones from which antiferromagnetic coupling of these electrons may occur across the anion. The presence of a single, σ bond (or lack thereof) has a larger impact on metal-metal distance and bonding properties than does the occupation of the δ_π and δ_π^* orbitals, that is, the δ_π bond is relatively weak. (**13**)

It is a challenge for computational methods to provide accurate, quantitative descriptions of the bonding in $[M_2X_9]^{n-}$ systems, (**35**) particularly those systems which are not fully delocalised. For example while a standard full symmetry geometry optimisation for $[W_2Cl_9]^{3-}$ will generate a W-W distance of 2.40 Å (**35d**,**e**), in keeping with observation of 2.45 Å (**29**), a similar calculation will fail to accurately represent the bond elongation observed for $[Cr_2Cl_9]^{3-}$ (a localised system) (Cr-Cr distance: observed 3.05 - 3.89 Å (**29**), and full symmetry geometry optimistation 2.3 Å (**35d**,**e**)). Methods involving the use of broken-symmetry techniques (**40**) have been employed to more accurately address electrons which remain localised about the metal centres while also maintaining the ability to also account for delocalisation. (**35d**,**e**) These broken symmetry calculations will be referred to in more detail in the discussion of physicochemical properties of $[M_2X_9]^{n-}$ complexes in chapter 1.1.

I.5 Dimetallic octahalide complexes of the type $[M_2X_8]^{n-}$

Metal-to-metal interactions may be "supported" by bridging ligands as found for the $[M_2X_9]^{n-}$ complexes just described, or they may be "unsupported" in which the metal-metal bond itself is essential for maintaining the dimeric formation. Since the mid-

1960's several compounds containing a direct, unsupported metal-metal bond have been identified.

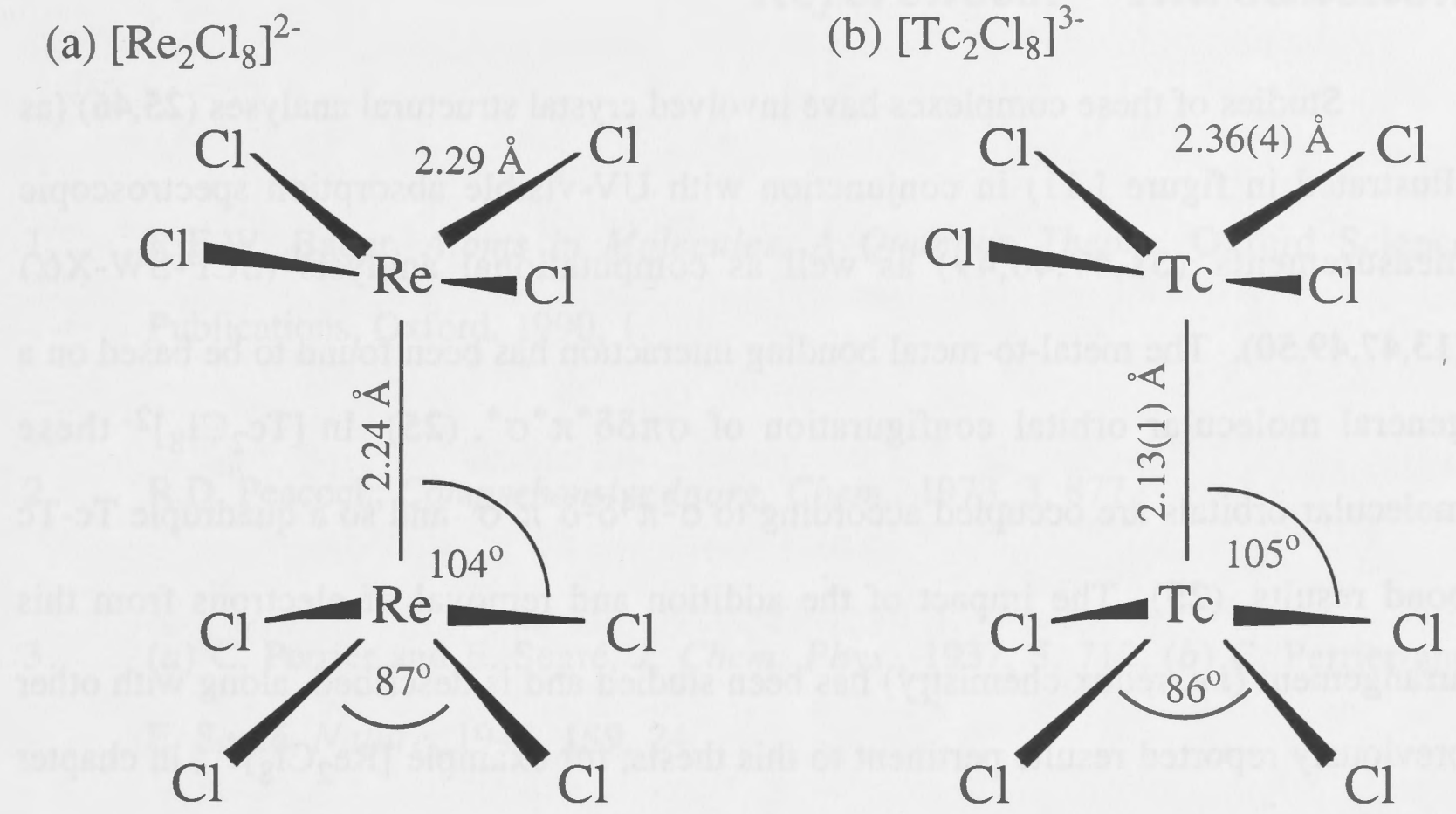

Figure I.11 *Molecular structures of (a) $[Re_2Cl_8]^{2-}$ and (b) $[Tc_2Cl_8]^{3-}$ with dimensions as reported in the early crystal structure determinations of $(TBA)_2[Re_2Cl_8]$ (**41**) and $(NH_4)_3[Tc_2Cl_8]$ (**25**). The similarity in structures was considered strong evidence that the metal-to-metal bonding in the two anions was also similar (**25**).*

The first to be structurally characterised was $(TBA)_2[Re_2Cl_8]$ (**41**). It was found to have a short Re-Re distance of 2.24 Å (figure I.11a). The halides are arranged in an eclipsed fashion, which was thought to be particularly good evidence for the presence of a quadruple Re-Re bond as other forms of bonding would have been expected to favour a staggered arrangement for the eight halide ligands. (**41**) $(NH_4)_3[Tc_2Cl_8]$ was actually prepared (**42**) just prior to the understanding of the nature of the bonding within the rhenium complex. Subsequent crystal structure determinations (**43**) revealed that $[Tc_2Cl_8]^{3-}$ (Tc-Tc 2.13(1) Å) (figure I.11b) is isostructural with $[Re_2Cl_8]^{2-}$ and $[Mo_2Cl_8]^{4-}$ (**44**) and so despite the different charge of the anions, similar bonding was predicted (**43**).

Since the recognition of formal quadruple bonding in $(TBA)_2[Re_2Cl_8]$ and $(NH_4)_3[Tc_2Cl_8]$ sparked much of the initial interest in metal-metal bonded systems,

complexes of this type have been prepared for these and a variety of other metals including, M = Mo, W, Os with various halide (and pseudo halide) ligands (X = F, Cl, Br, NCS) (**25**,**31**,**43**,**45**).

Studies of these complexes have involved crystal structural analyses (**25**,**46**) (as illustrated in figure I.11) in conjunction with UV-visible absorption spectroscopic measurements (**31**,**47**,**48**,**49**) as well as computational analysis (SCF-SW-Xα) (**13**,**47**,**49**,**50**). The metal-to-metal bonding interaction has been found to be based on a general molecular orbital configuration of $\sigma\pi\delta\delta^*\pi^*\sigma^*$. (**25**) In $[Tc_2Cl_8]^{2-}$ these molecular orbitals are occupied according to $\sigma^2\pi^4\delta^2\delta^*\pi^*\sigma^*$ and so a quadruple Tc-Tc bond results. (**25**) The impact of the addition and removal of electrons from this arrangement (*i.e.* redox chemistry) has been studied and is described, along with other previously reported results pertinent to this thesis, for example $[Re_2Cl_8]^{2-}$, in chapter 1.2.

In addition to the studies on the metal-metal bond the possibility of interconversion between the $[M_2X_9]^{n-}$ and $[M_2X_8]^{n-}$ species under various conditions has also been explored. For example, it is reported that $[Re_2X_9]^{1-}$ can be formed from $[Re_2X_8]^{2-}$ in the presence of halide at a potential of +1.55 V for chloride and +1.50 V for bromide. (**32c**,**38**) It was an aim of this thesis to attempt a similar interconversion with the technetium species, firstly between the known $[Tc_2Br_8]^{n-}$ and $[Tc_2Br_9]^{n-}$ and then starting with $[Tc_2Cl_8]^{n-}$ to form the elusive $[Tc_2Cl_9]^{n-}$.

Throughout this thesis the electronic structure of metal halide complexes have been investigated. The important effect of changes to the ligand array and the introduction of direct metal-to-metal interactions have been probed with both experimental and computational techniques. Results for individual complexes are compared with those of related species which contain, for example, a neighbouring metal or variation of the ligand array. Related monomers and dimers are also compared to identify the similarities and differences between their electronic structure and hence mutually increase the understanding of each.

References: Introduction

1. R.F.W. Bader, *Atoms in Molecules, A Quantum Theory*, Oxford Science Publications, Oxford, 1990, 1.

2. R.D. Peacock, *Comprehensive Inorg. Chem.*, 1973, **3**, 877.

3. (*a*) C. Perrier and E. Segré, *J. Chem. Phys.*, 1937, **5**, 712; (*b*) C. Perrier and E. Segré, *Nature*, 1947, **159**, 24.

4. J. Baldas, *Adv. Inorg. Chem.*, 1994, **41**, 1.

5. (*a*) E. Deutsch and K. Libson, *Comments Inorg. Chem.*, 1984, **3**, 83; (*b*) M.J. Clarke and P.H. Fackler, *Structure and Bonding*, 1982, **50**, 57; (*c*) E. Deutsch, K. Libson, S. Jurisson and L.F. Lindoy, *Prog. Inorg. Chem.*, 1983, **30**, 75; (*d*) W.A. Volkert and S. Jurisson, *Topics in Current Chem.*, 1996, **176**, 123, (and other articles in that volume).

6. A. Seidel, *Gmelin Handbook*, Tc Suppl., 1982, **1**, 271.

7. G. Bandoli, U. Mazzi, E. Roncari and E. Deutsch, *Coord. Chem. Rev.*, 1982, **44**, 191.

8. (*a*) V.I. Spitsyn, A.F. Kuzina, A.A. Obolva and S.V. Kryuchkov, *Russ. Chem. Rev.*, 1985, **54**, 373; (*b*) S.V. Kryuchkov, *Topics in Current Chem.*, 1996, **176**, 189.

9. U. Mazzi, *Polyhedron*, 1989, 1683.

10. A. Davison, *Technetium in Chemistry and Nuclear Medicine*, eds., E. Deutsch, M. Nicolini and H.N. Wagner, Cortina International, Verona/Raven Press, New York, 1983, 3.

11. J. Baldas, *Topics in Current Chem.*, 1996, **176**, 37.

12. R.D. Peacock, *Comprehensive Inorg. Chem.*, 1973, **3**, 905.

13. (*a*) G.A. Heath and J.E. McGrady, *J. Chem. Soc., Dalton Trans.*, 1994, 3759; (*b*) J.E. McGrady, *Ph.D. Thesis*, The Australian National University, 1994.

14. (*a*) A. Goursot, H. Chermette and C.Daul, *Inorg. Chem.*, 1984, **23**, 305; (*b*) J.P. Lopez and D.A. Case, *J. Chem. Phys.*, 1984, **81**, 4554.

15. E.N. Sloth and C.S. Garner, *J. Chem. Phys.*, 1954, **22**, 2064.

16. (*a*) C.K. Jørgensen, *Mol. Phys.*, 1959, **2**, 309; (*b*) C.K. Jørgensen, *Acta Chem. Scand.*, 1962, **16**, 1048; (*c*) C.K. Jørgensen, *Prog. Inorg. Chem.*, 1970, **12**, 101.

17. (*a*) G.A. Heath, K.H. Moock, D.W.A. Sharp and L.J. Yellowlees, *J. Chem. Soc., Chem. Commun.*, 1985, 1503; (*b*) S. Brownstein, G.A. Heath, A. Sengupta and D.W.A. Sharp, *J. Chem. Soc., Chem. Commun.*, 1983, 669.

18. A.B.P. Lever, *Inorganic Electronic Spectroscopy*, Elsevier, New York, 1984, **2nd ed.**, 739.

19. A. Earnshaw, *Introduction to Magnetochemistry*, Academic Press, London, 1968, 32.

20. A. Earnshaw, B.N. Figgis, J. Lewis and R.D. Peacock, *J. Chem. Soc.*, 1961, 3132.

21. A.G. Sharpe, *Inorganic Chemistry*, Longman, New York, 1981, 442.

22. (*a*) B.J. Brisdon and R.A. Walton, J. Inorg. Nucl. Chem., 1965, 27, 1101; (*b*) S.V. Kryuchkov, Yu. V. Rakitin, P.E. Kazin, A.I. Zhirov and N. Yu. Konstantinov, *Koord. Khim.*, 1990, **16**, 1230 (eng. trans. 660).

23. K.H. Moock, S.A. Macgregor, G.A. Heath, S. Derrick and R.T. Boeré, *J. Chem. Soc., Dalton Trans.*, 1996, 2067.

24. D. Menglet, *Ph.D. Thesis*, The Australian National University, 1996.

25. (a) F.A. Cotton and R.A. Walton, *Multiple Bonds Between Metal Atoms*, Oxford University Press, 1993, **2nd ed**.,1. (b) C. Brosset, Nature, 1935, 135, 874

26. B. Douglas, D.H. McDaniel and J.J. Alexander, *Concepts and Models of Inorganic Chemistry*, John Wiley and Sons Inc., New York, 1983, **2nd ed**, 647.

27. F.A. Cotton and D.A. Ucko, *Inorg. Chim. Acta*, 1972, **6**, 161.

28. R.H. Summerville and R. Hoffmann, *J. Am. Chem. Soc.*, 1979, **101**, 3821.

29. I.E. Grey and P.W. Smith, *Aust. J. Chem.*, 1971, **24**, 73.

30. J.L. Hayden and R.A.D. Wentworth, *J. Am. Chem. Soc.*, 1968, **90**, 5291.

31. (*a*) G.A. Heath and D.G. Humphrey, *J. Chem. Soc., Chem. Commun.*, 1990, 672; (**b**) D.G. Humphrey, *Ph.D. Thesis*, The Australian National University, 1992.

32. (*a*) V.T. Coombe, G.A. Heath, T.A. Stephenson and D.K. Vattis, *J. Chem. Soc., Dalton Trans.*, 1983, 2307; (*b*) B.J. Kennedy, G.A. Heath and T.J. Khoo, *Inorg. Chim. Acta*, 1991, **190**, 265; (*c*) G.A. Heath and R.G. Raptis, *Inorg. Chem.*, 1991, **30**, 4106.

33. (*a*) R. Stranger, G. Moran, E. Krausz and G. Medley, *Inorg. Chem.*, 1993, **32**, 4555, (and references therein);

34. (*a*) S.F. Gheller, G.A. Heath, D.G. Humphrey, D.C.R. Hockless and J.E. McGrady, *Inorg. Chem.*, 1994, **33**, 3986; (*b*) G.A. Medley and R. Stranger, *Inorg. Chem.*, 1994, **33**, 3976; (*c*) M.D. Hopkins, H.B.Gray and V.M. Miskowski, *Polyhedron*, 1987, **6**, 705;

35. (*a*) B.E. Bursten, F.A. Cotton and A. Fang, *Inorg. Chem.*, 1983, **22**, 2127; (*b*) A. Ginsberg, *J. Am. Chem. Soc.*, 1980, **102**, 111; (*c*) M.B. Hall, *Polyhedron*, 1987, **6**, 679; (*d*) T. Lovell, J.E. McGrady, R. Stranger and S.A. Macgregor, *Inorg. Chem.*, 1996, **35**, 3079; (*e*) R. Stranger, S.A. Macgregor, T. Lovell J.E. McGrady and G.A. Heath, *J. Chem. Soc., Dalton Trans.*, 1996, 4485.

36. (*a*) R.G. Barnes, J.D. Corbett, T.P. McMullen, K.R. Poeppelmeier and D.R. Torgenson, *Inorg. Chem.*, 1980, **19**, 129; (*b*) M.M. Metallinou, L. Nalbandian, G.N. Papatheodoru, W. Voigt and H.H. Emons, *Inorg. Chem.*, 1991, **30**, 4260; (*c*) M. Lenck and A. Weiss, *Z. Naturforsch, A: Phys. Sci.*, 1992, **47**, 54;

(*d*) T.J. Kistenmacher and G.P. Stucky, *Inorg. Chem.*, 1971, **10**, 122; (*e*) A. Stebler, B. Leuenberger and H.U. Güdel, *Inorg. Synth.*, 1989, **26**, 377; (*f*) A.K. Sengupta and U. Bhattacharyya, *J. Flourine Chem.*, 1990, **46**, 229; (*g*) J. Beck, *Chem. Ber.* 1991, **124**, 677; (*h*) N. Bucholz, L. Kiriazis, M. Leimkuhler and R. Mattes, *Inorg. Chem*, 1988, **27**, 2035; (*i*) J.C. Clandy, W.C. Dorman, R.E. McCarley and J.L Templeton, *Inorg. Chem.*, 1978, **17**, 2009; (*j*) E. Babaian-Kibala, F.A. Cotton, L.R. Falvello and M. Shang, *Inorg. Chem.*, 1990, **29**, 2591; (*k*) L. Kiriazis and R. Mattes, *Z. Anorg. Allg. Chem.*, 1991, **593**, 90; (*l*) J. Rong Chang and G.L. McPherson, *Inorg. Chem.*, 1976, **15**, 1018; (*m*) M. Feist, K. Witke and D. Hass, *Z. Anorg. Allg. Chem.*, 1990, **586**, 185; (*n*) J. Darriet, *Rev. Chem. Miner.*, 1981, **18**, 3; (*o*) D.A. Appleby, P.B. Hitchcock, C.L. Hussey, T.A. Ryan, R.J. Sanders. K.R. Seddon, J.E. Turp and J.A. Zora, *J. Chem. Soc., Dalton Trans.*, 1990, 1879; (*p*) W. Preetz and H.J. Steinbach, *Z. Anorg. Allg. Chem.*, 1985, **530**, 155; (*q*) P. Hollmann, W. Preetz, H. Hillebrecht and G. Thiele, *Z. Anorg. Allg. Chem.*, 1992, **611**, 28; (*r*) J. Zaleski, R. Jakubas, L. Sobczyk and J. Mroz, *Ferroelectrics*, 1990, **103**, 83; (*s*) R. Jakubas, Z. Galecuski, L. Sobczyk, J. Matuszewski, *Ferroelectrics*, 1988, **88**, 83; (*t*) A. Dönni, A. Furrer and H.U. Güdel, *J. Solid State Chem.*, 1989, **81**, 278; (*u*) S. Wang, S.M. Luo, H.A. Eick, K. Kraemer and G. Meyer, *J. Less-Common Met.*, 1989, **155**, 45; (*v*) H.U. Güdel, A. Furrer and H. Blank, *Inorg. Chem.*, 1990, **29**, 4081; (*w*) G. Meyer and T. Schleid, *Inorg. Chem.*, 1987, **26**, 217.

37. A. Wendt and W. Preetz, *Z. Anorg. Allg. Chem.*, 1993, **619**, 1669.

38. R.G. Raptis and G.A. Heath, *Unpublished results*, (*RSC Annual Report*, 1991, 64).

39. B.D. Yeomans, *Ph.D. Thesis*, The Australian National University, 1995.

40. L. Noodleman and J.G. Norman Jr, *J. Chem Phys.*, 1979, **70**, 4903.

41. (*a*) F.A. Cotton, N.F. Curtis, C.B. Harris, B.F.G. Johnson, S.J. Lippard, J.T. Mague, W.R. Robinson and J.S. Wood, *Science*, 1964, **145**, 1305; (*b*) F.A. Cotton, *Inorg. Chem.*, 1965, **4**, 334.

42. J.D.Eakins, D.G. Humphreys and C.E. Mellish, *J. Chem. Soc.*, 1963, 6012.

43. W.K. Bratton and F.A. Cotton, *Inorg. Chem.*, 1970, **9**, 789.

44. J.V. Brencic and F.A. Cotton, *Inorg. Chem.*, 1970, **9**, 351.

45. G.A. Heath and R.G. Raptis, *J. Am. Chem. Soc.*, 1993, **115**, 3768.

46. (*a*) F.A. Cotton, L. Daniels, A. Davison and C. Orvig, *Inorg. Chem.*, 1981, **20**, 3051; (*b*) F.A. Cotton and L.W. Shive, *Inorg. Chem.*, 1975, **14**, 2032; (*c*) F.A. Cotton, B.A. Frenz, B.R. Stults and T.R. Webb, *J. Am. Chem. Soc.*, 1976, **98**, 2768; (*d*) F.A. Cotton, B.G. DeBoer and M. Jeremic, *Inorg. Chem.*, 1970, **9**, 2143.

47. P.A. Agaskar, F.A. Cotton, K.R. Dunbar, L.R. Falvello, S.M. Tetrick and R.A. Walton, *J. Am. Chem. Soc.*, 1986, **108**, 4850.

48. B.E. Bursten and F.A. Cotton, P.E. Fanwick and G.G. Stanley, *J. Am. Chem. Soc.*, 1983, **105**, 3082.

49. A.P. Mortola, J.W. Moskowitz, N. Rösch, C.D. Cowman and H.B. Gray, *Chem. Phys. Lett.*, 1975, **32**, 283.

50. (*a*) J.G. Norman Jr. and H.J. Kolari, *J. Chem. Soc., Chem. Commun.*, 1974, 303; (*b*) J.G. Norman Jr. and H.J. Kolari, *J. Am. Chem. Soc.*, 1975, **97**, 33; (c) F.A. Cotton and B.J. Kalbacher, *Inorg. Chem.*, 1977, **16**, 2386; (*d*) R. Arratia-Perez and D.A. Case, *Inorg. Chem.*, 1984, **23**, 3271.

PART ONE

Write a wise saying and your name will live forever.

- Anonymous

Chapter 1.1: Physicochemical studies on ditechnetium nonabromide, (TEA)[Tc_2Br_9]

This chapter will focus on the nature of the "supported" metal-to-metal interaction within $[Tc_2Br_9]^{1-}$. The $[Tc_2Br_9]^{1-}$ anion was first prepared as a $(TEA)^+$ salt by refluxing $(TEA)_2[TcBr_6]$ in the halide-abstracting trifluroacetic acid, (**1**) using a method similar to the preparation of $(TBA)[Os_2Br_9]$ (**2**). It was prepared as both the $(TEA)^+$ and $(TBA)^+$ salts as is fully described in the experimental chapter 1.5. $(TEA)[Tc_2Br_9]$ was isolated as a purple-brown, light sensitive solid. The far infra-red spectrum recorded here is in agreement with the previous report (**1**) (see chapter 1.5). The variable temperature magnetic moment analysis (section 1.1.1) followed by the voltammetry (section 1.1.2) and spectro-electrochemistry (section 1.1.3) are all reported for the first time in this thesis. These results will be compared with those previously reported for neighbouring elements, focussing particularly on the isoelectronic $[Re_2X_9]^{1-}$ and $[Cr_2X_9]^{3-}$.

1.1.1 Magnetic moments of $[M_2X_9]^{n-}$ (where X = Cl, Br; M = Tc, Re, n = 1 and M = Cr, Mo, W, n = 3)

The magnetic susceptibilities of powdered samples of $(TBA)[Re_2Cl_9]$, $(TBA)[Re_2Br_9]$ and $(TBA)[Tc_2Br_9]$ were recorded in a field of 10 000 gauss between 5 and 300 K. The results were corrected for diamagnetic contributions from cations and halide ligands to produce values for χ'_M, the corrected magnetic susceptibility. Figure 1.1 shows plots of χ'_M *vs* temperature for $[Tc_2Br_9]^{1-}$ and $[Re_2Br_9]^{1-}$. From χ'_M, values for the exchange coupling constant, J_{ab},# and the effective magnetic moment, μ_{eff}, were determined for each compound. These parameters provided valuable information about the relative strength of the metal-to-metal interaction. They show a marked difference in the magnetochemistry of the $[Tc_2Br_9]^{1-}$ as compared to $[Re_2Br_9]^{1-}$.

The value for J_{ab} relates to the separation between singlet and first triplet state for the complex, based on the exchange hamilition, $H = -2J_{ab}S_a \bullet S_b$ (**3**).

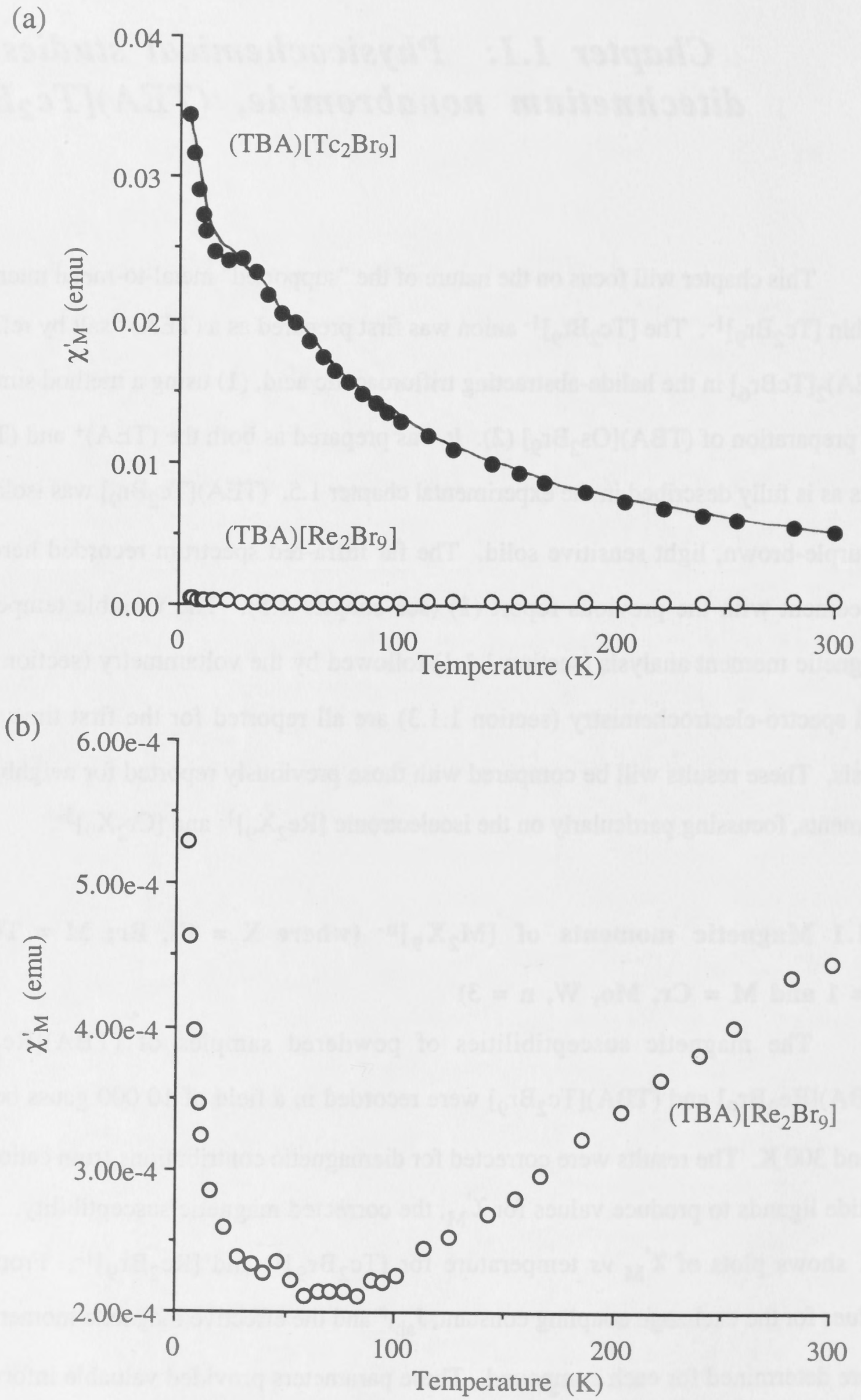

Figure 1.1 *Plots of the diamagnetic corrected molecular susceptibility (χ'_M) vs temperature (in Kelvin) for both (a) (TBA)[Tc_2Br_9] and (TBA)[Re_2Br_9] as measured for this thesis. A line, corresponding to the curve fitting analysis sumarised in table*

1.2, is shown for (TBA)[Tc_2Br_9]. Plot (b) is an amplification of the (TBA)[Re_2Br_9] data. Below about 25 K in both plots the observed data are dominated by paramagnetic impurities.##

There is however, a striking similarity between $[Tc_2Br_9]^{1-}$ and the isoelectronic $[Cr_2Br_9]^{3-}$ (**4**). In analysing the data it is assumed throughout that the observed magnetic behaviour is dominated by intramolecular exchange interactions between the two M^{IV} and M^{III} centres respectively, within each anion (**4**). This kind of assumption is valid in light of the relatively large distance between individual dimeric anions.

The measured data were fitted to the susceptibility equation for binuclear d^3d^3 ions (equation 1) (**3**). The results (at 300 K) are presented in table 1.2 along with data reported previously for $Cs_3[Cr_2Br_9]$ (**4**) and $(TEA)_3[Mo_2Br_9]$ (**4**) for comparison.#

$$\chi_{(\mathrm{perM})} = \frac{g^2 Nb^2}{kT} \bullet \frac{[14 + 5\exp\left(\frac{-6J}{kT}\right) + \exp\left(\frac{-10J}{kT}\right)]}{[7 + 5\exp\left(\frac{-6J}{kT}\right) + 3\exp\left(\frac{-10J}{kT}\right) + \exp\left(\frac{-12J}{kT}\right)]} \qquad \textit{equation (1)}$$

A monomeric impurity with $S = \frac{3}{2}$ of fraction x can be accommodated using

$$\chi_{(\mathrm{obs})} = (1-x)\chi_{(\mathrm{perM})} + x\chi_{(monomer)} + N(\alpha) \qquad \textit{equation (2)}$$

$$\text{where } \chi_{(monomer)} = \frac{g^2 N\beta^2}{3kT} \bullet \frac{15}{4}$$

and $N(\alpha)$ = temperature-independent paramagnetic contribution. (**3**)

Table 1.2 Magnetic data for d^3d^3 complexes of the type $[M_2Br_9]^{n-}$ as determined from the curve fitting analysis.

Complex	g (±5%)	N(α) (cgs) (±10%)	paramagnetic impurity %##	J_{ab} (cm^{-1}) (±10%)
$[Tc_2Br_9]^{1-}$	1.89	6.7×10^{-5}	8	-6.5
$[Re_2Br_9]^{1-}$	~ 1.73	0	0.1	~ -200
$[Cr_2Br_9]^{3-}$	1.97	-	-	-8.8
$[Mo_2Br_9]^{3-}$	2.01	2.3×10^{-5}	-	-450

The results for the chloride species will be described later in this section.

These paramagnetic impurities should not be thought of as contamination of the sample by other compounds (see section 1.5.1.5) rather, they arise largely from lattice site imperfections such as individual sites missing a second metal ion.

1.1.1.1 Interpretation of the magnetic moment of (TEA)[Tc_2Br_9]

The negative value of J_{ab} observed for $[Tc_2Br_9]^{1-}$ is associated with an antiferromagnetic interaction between the technetium centres. The magnitude of J_{ab} ($|6.5|$ cm^{-1}) is indicative of a very weak antiferromagnetic interaction and is similar to that previously reported for $[Cr_2Br_9]^{3-}$ which is recognised as a typical example of weak metal-to-metal interaction (**4**).

Further evidence for the localisation of the $4d^3$ electrons on each technetium centre can be derived from a Curie-Weiss plot of $\chi'_M{}^{-1}$ *vs* temperature see figure 1.3.

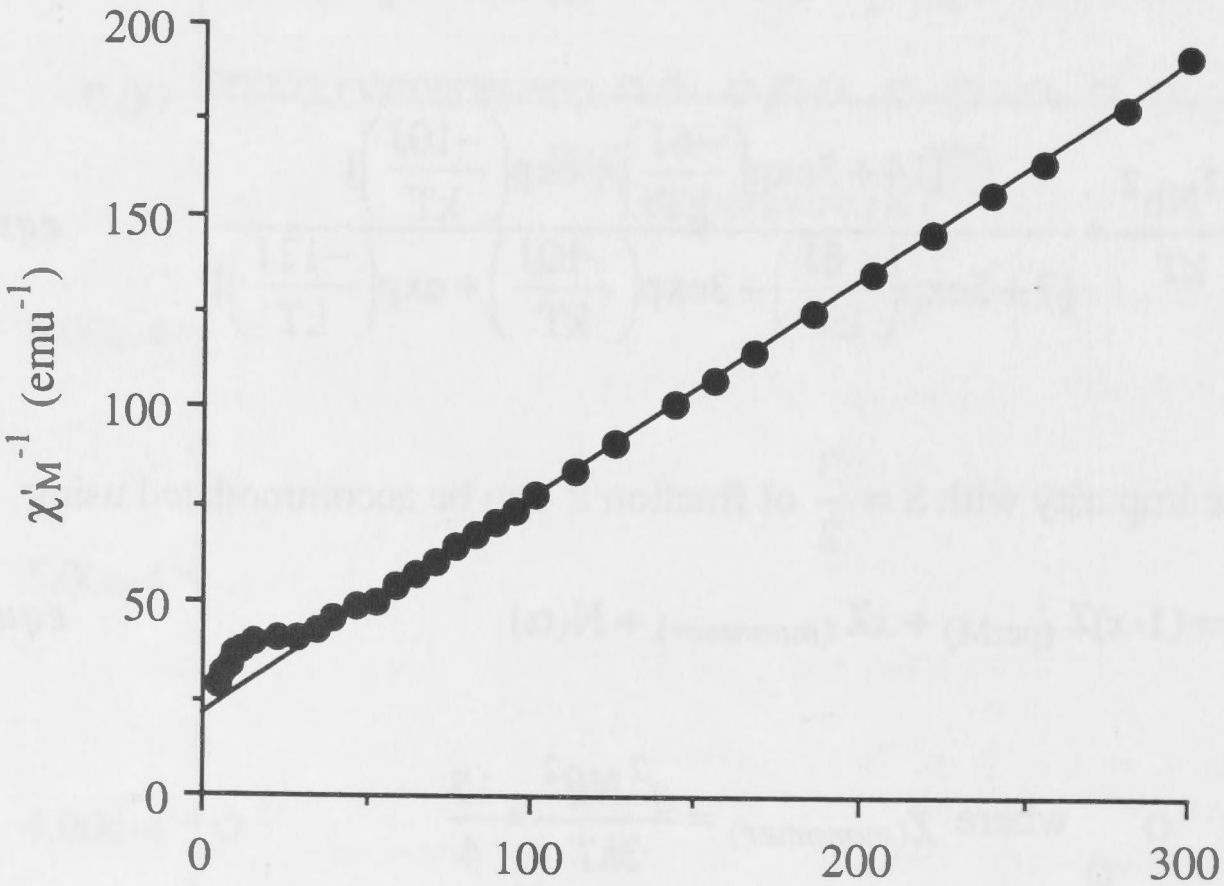

Figure 1.3 *A Curie-Weiss plot of $(\chi'_M)^{-1}$ vs temperature for $[Tc_2Br_9]^{1-}$. A line of best fit (through the data above 75 K) intercepts the x axis at -38 K which corresponds to a Weiss constant (θ) of +38 K for this species.*

The plot is linear over most of the temperature range studied (50 - 300 K). The curvature at the lower temperatures (below 50 K) is typical of compounds possessing weak antiferromagnetic interactions, such as for the isoelectronic (d^3d^3) $[Cr_2Br_9]^{3-}$ species. (**4**) A line of best fit through the "linear data" from above 75 K intersects the

temperature axis at -38 K. This linear relationship and non-zero intercept are in accord with typical Curie-Weiss behaviour where $\chi_M = c/(T+\theta)$. (c = Curie constant for the substance) In this case the Weiss constant θ, is +38 K. This positive value of θ is typical of an intramolecular antiferromagnetic interaction between the two paramagnetic Tc^{IV} (d^3) centres and compares to a similar value of θ = +31 K previously reported for $(Cs)_3[Cr_2Br_9]$ (**4**).

This value of θ can be used in two different ways. Firstly, it can be used to derive an independent estimate of the exchange coupling constant J_{ab}, using equation (4). (**3**)

$$\theta = \frac{2S(S+1)}{3k} \bullet J_{ab} \qquad \textit{equation (4)}$$

$$\text{for } S = \frac{3}{2},\ \theta = \frac{5}{2} \bullet J_{ab}$$

Table 1.4 compares values of J_{ab} determined from θ (using equation 4) and J_{ab} determined from the curve fitting analysis and presented in table 1.2 for both $(TBA)[Tc_2Br_9]$ and $Cs_3[Cr_2Br_9]$ (**4**). This close agreement of J_{ab} determined by both methods supports further the observance of Curie-Weiss behaviour by both anions.

Table 1.4 Magnetic data for $(TBA)[Tc_2Br_9]$ and $(TBA)[Re_2Br_9]$.

complex	θ (K) (± 10%)	J_{ab} from θ (cm^{-1}) (± 10%)	J_{ab} from Curie-Weiss plot (cm^{-1})
$[Tc_2Br_9]^{1-}$	+38	-8	-6.5
$[Cr_2Br_9]^{1-}$	+31	-8.6	-8.8

Secondly, the value of θ can be used in conjunction with the molecular susceptibility to determine the effective magnetic moment of each individual paramagnetic technetium centre in the dimeric anion, using equation 5,

$$\mu_{eff} = \left(\frac{3k}{N}\right)^{\frac{1}{2}} \sqrt{\chi_M (T+\theta)} \qquad \textit{equation (5)}$$

where θ acts as a correction factor which takes account of the effect of antiferromagnetic interactions which may occur between the two technetium centres. This equation strictly applies only at temperatures above θ (**3**) (that is, at above +38 K for $[Tc_2Br_9]^{1-}$). A plot of μ_{eff} (as corrected using equation 5) *vs* temperature for $[Tc_2Br_9]^{1-}$ is presented in figure 1.5.

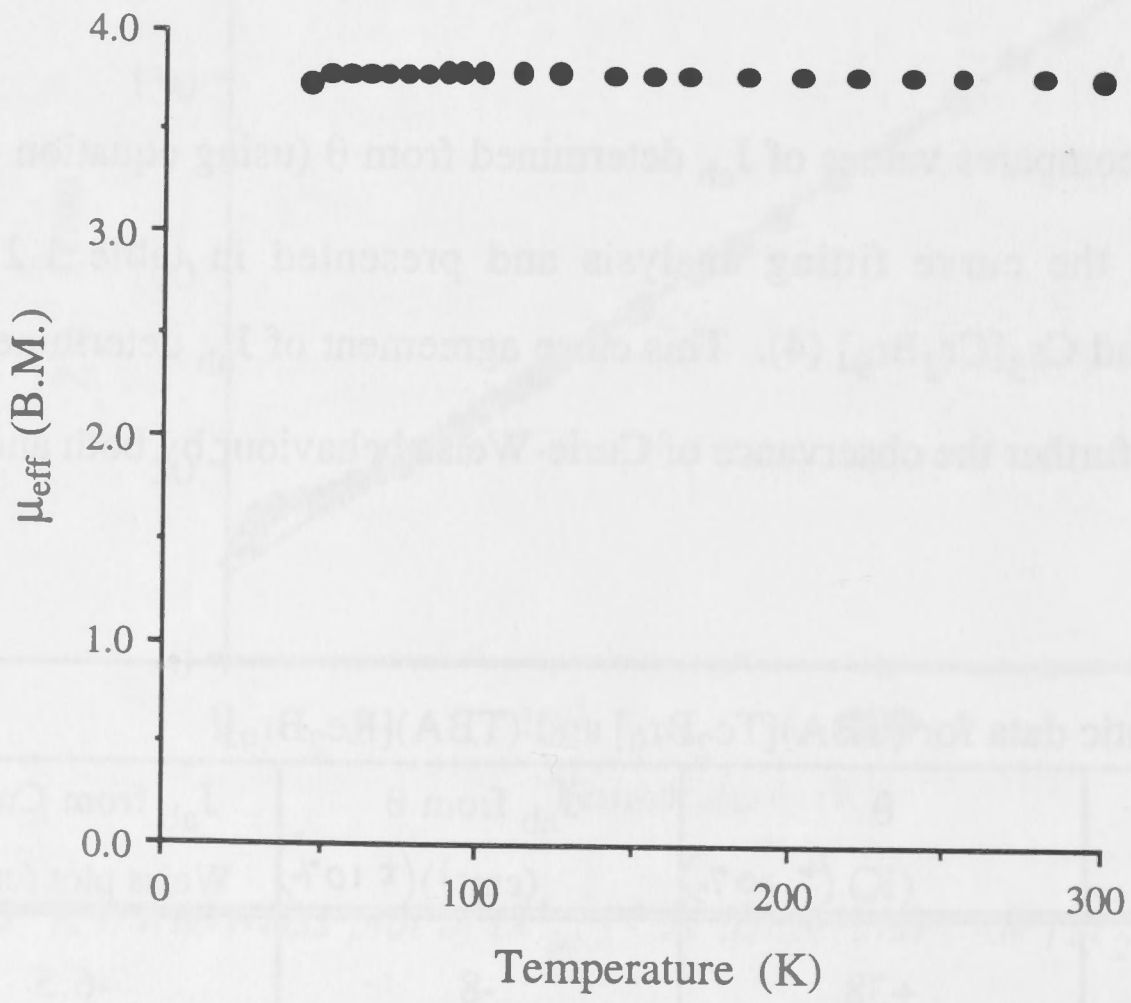

Figure 1.5 *Corrected μ_{eff} plotted against temperature for (TBA)$[Tc_2Br_9]$ to highlight the temperature independence.*#

This plot illustrates the temperature independence of the corrected μ_{eff} (above 50 K) which is consistent with Curie law behaviour. In other words, each technetium

---

The plot only shows points above 50 K, below this temperature equation 3 does not apply, and the line deviates from linearity.

atom is acting as a virtually "independent" paramagnetic centre. The value of μ_{eff} from the analysis above is 3.78 B.M. (in the range 50-300 K). This value can be related to the number of unpaired electrons remaining localised about each technetium metal centre after dimer formation by equation 6.

$$\mu_{eff\,(perTc)} = \sqrt{n(n+2)} = 3.87 \text{ B.M.} \qquad \textit{equation (6)}$$

where n = the number of unpaired electrons per technetium.

This equation is a spin-only formula and assumes that L = 0 in the groundstate. Such an assumption is valid for a d^3, second-row, pseudo-octahedral system as in this case. (**4**) Using this formula one can derive that for a fully localised d^3 system μ_{eff} should approach 3.87 B.M. Hence the observed value of 3.78 B.M. is consistent with a localised d^3 system possessing virtually no direct metal-to-metal bonding between the technetium centres. This value is compared to other corrected μ_{eff} values reported previously for the d^3d^3 dimers, $(TEA)_3[Cr_2Br_9]$ (**4**), $(TEA)_3[Mo_2Br_9]$ (**5**) and $Rb_3[W_2Br_9]$ (**6**) in table 1.6.

Table 1.6 Corrected μ_{eff} at 300 K for $[M_2Br_9]^{n-}$ (n = 3, 1) systems.

Cr 3.89	
Mo 1.09	**Tc** 3.78
W 0.4	**Re** 1.07

The following points are evident from table 1.6:

(i) the magnetic properties of $[Tc_2Br_9]^{1-}$ and $[Re_2Br_9]^{1-}$ are different in magnitude (see also figure 1.1),

(ii) compounds along a given row of transition metals possess different magnetic properties,

(iii) a diagonal relationship appears to exist between $[Mo_2Br_9]^{3-}$ and $[Re_2Br_9]^{1-}$ and also between $[Cr_2Br_9]^{3-}$ and $[Tc_2Br_9]^{1-}$,

(iv) the strength of the metal-metal bonding down the column was shown to increase. This has also been observed for the d^5d^5 complexes of $(TBA)_3[Ru_2Br_9]$ and $(Ph_4P)_3[Os_2Br_9]$ where μ_{eff} was seen to increase from 1.67 to 0.40 B.M. down the column (**2**,**7**).

The discussion to date has focused on the bromide dimers. Since one of the aims of this thesis was to investigate routes to the elusive $[Tc_2Cl_9]^{n-}$, the magnetic behaviour of the related chloride dimers was also of considerable interest. One important question being whether the magnetochemistry of chloride dimers is similar to their bromide analogues.

In comparing bromide and chloride dimers we will consider observed metal-to-metal distance and the magnetic properties of J_{ab} and μ_{eff}, in table 1.7.

Table 1.7 Comparison of observed magnetic data for $[M_2X_9]^{n-}$ where X = Cl and Br.

Anion#	M-M## (Å)	J_{ab} (cm^{-1})	μ_{eff} (B.M.)	Reference
$[Cr_2Cl_9]^{3-}$	3.89	-7	3.91	**4**
$[Cr_2Br_9]^{3-}$	4.00	-8.8	3.89	**4**
$[Mo_2Cl_9]^{3-}$	3.43	-500	0.96	**4**
$[Mo_2Br_9]^{3-}$	3.53	-450	1.09	**4**
$[W_2Cl_9]^{3-}$	2.4	—	0.4	**4**,**6**
$[W_2Br_9]^{3-}$	—	—	0.4	**6**
$[Tc_2Br_9]^{1-}$	—	-6.5	3.78	this work
$[Re_2Cl_9]^{1-}$	2.704	—	—	**8**
$[Re_2Br_9]^{1-}$	2.758	-200	1.07	**9**

Data is as reported for $(TEA)^+$ salts except for $Rb_3[W_2X_9]$.

M-M distance varies according to the cation present. For example, $K_3[Cr_2Cl_9]$ has a Cr-Cr distance of 3.048 Å which is some 0.84 Å shorter than the distance presented in the table for $(TEA)_3[Cr_2Cl_9]$. It should be noted that the magnitude of J_{ab} is not altered by this change in metal-metal distance. (**4**)

It can be seen from the table that the metal-metal bond distances are of the same magnitude for the chloride and bromide species of the same metal (with the bromide slightly longer in each case). It also appears that throughout the chromium triad the magnetochemistry of the chloride dimers is of the same magnitude as that of the related bromide dimer. (**5**)

Calculations have been undertaken using approximate density functional theory on the series of $[M_2X_9]^{n-}$ complexes where M = Cr, Mo, W, Tc, Re and X = Cl and Br. (**10**,**11**) Included in the calculations were geometry optimisations of the metal-to-metal distances, using the broken symmetry formalism (**12**), along with determinations of exchange coupling constants for comparison with observed magnetic data for M = Cr (**4**) and Tc. The calculated geometries are in good agreement with known crystal structures# (selected results are presented in table 1.10, first two columns). The calculated magnetic data also compare well with those observed experimentally (table 1.8).

Table 1.8 Comparison of calculated and observed coupling constants, J_{ab}.

Compound	J_{ab} (cm^{-1})		Reference
	Calculated	Observed	Calc,Obs
$[Cr_2Cl_9]^{3-}$	-3.2	-7	**10**,**4**
$[Cr_2Br_9]^{3-}$	-4.9	-8.8	**10**,**4**
$[Tc_2Cl_9]^{1-}$	-200	-	**11**,-
$[Tc_2Br_9]^{1-}$	-30.3	-6.5	**11**, this work

The calculations on $[Tc_2Cl_9]^{1-}$ (tables 1.8 and 1.10) predict a stronger interaction between the technetium metal centres than for its bromide analogue, $[Tc_2Br_9]^{1-}$. (**11**) This result was surprising because, as was shown in table 1.7, chloride and bromide analogues of other $[M_2X_9]^{n-}$ species tend to have similar bonding properties. In order to

The calculated Mo-Mo separation in $[Mo_2Cl_9]^{3-}$ is not as close to observation as other species, possibly due to cation repulsions in the solid state which are largest when M = Mo (**13**) and are not incorporated into the calculation.

assess the validity of this prediction, it is necessary to analyse how the result was determined from the calculations.

The calculations are most easily interpreted in terms of three distinct states, denoted as $S_{tot} = 0$, 2 and 3, which are defined in table 1.9.

Table 1.9 Three bonding arrangements used in the density functional calculations. (**11**)#

Label	Characteristics	Full Symmetry Electron Configuration
$S_{tot} = 0$	all electrons paired triple bond is present example: $[W_2X_9]^{3-}$	$(a_1')^2(e')^4(e'')^0(a_2'')^0$
$S_{tot} = 2$	two unpaired electrons per metal centre single, σ bond is present examples: $[Mo_2X_9]^{3-}$ and $[Re_2X_9]^{1-}$	$(a_1')^2(e')^2(e'')^2(a_2'')^0$
$S_{tot} = 3$	three unpaired electrons per metal centre no significant bond examples: $[Cr_2X_9]^{3-}$ and $[Tc_2Br_9]^{1-}$	$(a_1')^1(e')^2(e'')^2(a_2'')^1$

The procedure involves initially using full symmetry calculations and enforcing the electron configurations corresponding to the spin-states, $S_{tot} = 0$, $S_{tot} = 2$ and $S_{tot} = 3$ thus determining the metal-metal distance which corresponds to the minimum energy of the anion in each state.## In the broken-symmetry groundstate the metal-based electrons are free to localise on one metal centre or the other, and so weak antiferromagnetic coupling between the electrons which are localised on the metal centres can be distinguished from strong metal-metal bonding which is associated with delocalisation of metal based electrons between the two metal centres. The results from these analyses are presented in table 1.10.

Unpaired electrons are antiferromagnetically coupled across the anion.
The $S_{tot} = 1$ spin state was not assessed computationally because the electron configuration cannot be defined by a single determinant. (**11**)

Table 1.10 Showing calculated (**10**,**11**) and observed bond lengths of $[M_2X_9]^{n-}$. Energy in brackets for calculated distances (eV).

Anion	Observed M-M (Å)	B.S. M-M (Å)	$S_{TOT} = 0$	$S_{TOT} = 2$	$S_{TOT} = 3$	Observed config
$[Cr_2Cl_9]^{3-}$	3.05-3.89 (**4**)	3.22 (0.00)	2.30 (+2.53)	2.78 (+1.07)	3.25 (0.00)	S = 3
$[Mo_2Cl_9]^{3-}$	2.53-3.43 (**4**)	2.29 (0.00)	2.29 (0.00)	2.87 (+0.41)	3.46 (+0.69)	S = 2
$[W_2Cl_9]^{3-}$	2.45 (**4**)	2.40 (0.00)	2.40 (0.00)	2.91 (+0.61)	2.52 (+1.10)	S = 0
$[Tc_2Cl_9]^{1-}$	-	2.87 (0.00)	2.43 (+0.30)	2.79 (+0.08)	3.29 (+0.10)	-
$[Tc_2Br_9]^{1-}$	-	3.44 (0.00)	2.42 (+0.35)	2.84 (+0.15)	3.44 (+0.01)	S = 3
$[Re_2Cl_9]^{1-}$	2.704 (**8**)	2.79 (0.00)	2.49 (+0.04)	2.85 (+0.07)	3.36 (+0.35)	S = 2

Table 1.10 indicates that the optimised metal-to-metal distances determined by calculations using the broken-symmetry method on the $[M_2X_9]^{n-}$ species have electron configurations which are consistent with the observed magnetic data for these species. (**10**,**11**) For example $[Cr_2Cl_9]^{3-}$, has a relatively long metal-metal separation such that the σ and δ_π electrons are localised on the metals centres and so antiferromagnetic coupling results in a singlet groundstate. At this point, the broken-symmetry state is clearly the antiferromagnetic counterpart of the $S_{tot} = 3$ state, in which all electrons are localised and antiferromagnetically coupled and accordingly the two states lie close in energy. (**10**,**11**) Likewise for $[Tc_2Br_9]^{1-}$ the broken-symmetry energy minimum corresponds most closely to that determined for $S_{tot} = 3$, again consistent with a long metal-metal separation and antiferromagnetic coupling of the six electrons (three unpaired electrons per technetium atom). (**11**)

The relatively short metal-metal separation in $[W_2X_9]^{3-}$ is associated with delocalisation of both σ and δ_π type electrons and the broken-symmetry solution is identical to the $S_{tot} = 0$ curve. (**10**,**11**) In $[Re_2Cl_9]^{1-}$ the $S_{tot} = 0$ and $S_{tot} = 2$ states lie very close in energy, with $S_{tot} = 3$ around 0.3 eV higher. Accordingly the equilibrium position in the broken-symmetry curve corresponds to the antiferromagnetic counterpart of the $S_{tot} = 2$ state, with a strong σ bond, but only weak coupling of the δ_π type electrons. (**10**,**11**)

The results for $[Tc_2Cl_9]^{1-}$ indicate that the Tc-Tc distance as optimised using broken-symmetry is considerably shorter than that determined for its bromide analogue. (**11**) The broken symmetry minimum corresponds to the antiferromagnetic counterpart of $S_{tot} = 2$ indicating the presence of a relatively strong Tc-Tc single σ bond and weakly coupled δ_π electrons in the broken-symmetry state. (**11**) This bonding is more akin to that of $[Re_2X_9]^{1-}$ than $[Tc_2Br_9]^{1-}$ and a comparison of calculated exchange coupling constants presented in table 1.8 further highlights the differences between technetium analogues. (**11**) However, this unusual difference between the nature of the bonding in the chloride and bromide analogues which is predicted for $[Tc_2X_9]^{1-}$ should be treated with caution. A further look at table 1.10 reveals that the broken symmetry minimum lies very close to both $S_{tot} = 2$ and $S_{tot} = 3$ states, indicating that the localisation/delocalisation of the σ electrons and consequent large shift in Tc-Tc separation, is a relatively facile process. (**11**) Hence the most stable Tc-Tc bond length in $[Tc_2Cl_9]^{1-}$ may be highly sensitive to small changes, such as environmental influences like the nature of the cation. (**11**) We will return to considerations of factors affecting the possible nature of $[Tc_2Cl_9]^{n-}$ toward the end of chapter 1.2.

The question which shall be explored in the remainder of this chapter on $[Tc_2Br_9]^{1-}$ is whether the differences in the magnetochemistry of $[Tc_2Br_9]^{1-}$ and $[Re_2X_9]^{1-}$ are evident in other properties as well. It was found that this weaker bonding in $[Tc_2Br_9]^{1-}$ as compared to $[Re_2Br_9]^{1-}$ is indeed reflected in the electrochemistry and

UV-visible electronic absorption spectroscopy of the two different species and these observations will be described in the following sections.

1.1.2 Voltammetry of $[Tc_2Br_9]^{1-}$

The voltammetry of (TEA)$[Tc_2Br_9]$ was recorded in 0.5 M $TBABF_4/CH_2Cl_2$ at both -60°C and at room temperature in a vacuum-tight electrochemical cell. Two reversible, and one irreversible, metal-based reduction were observed, and are presented in figure 1.11 and table 1.12.#

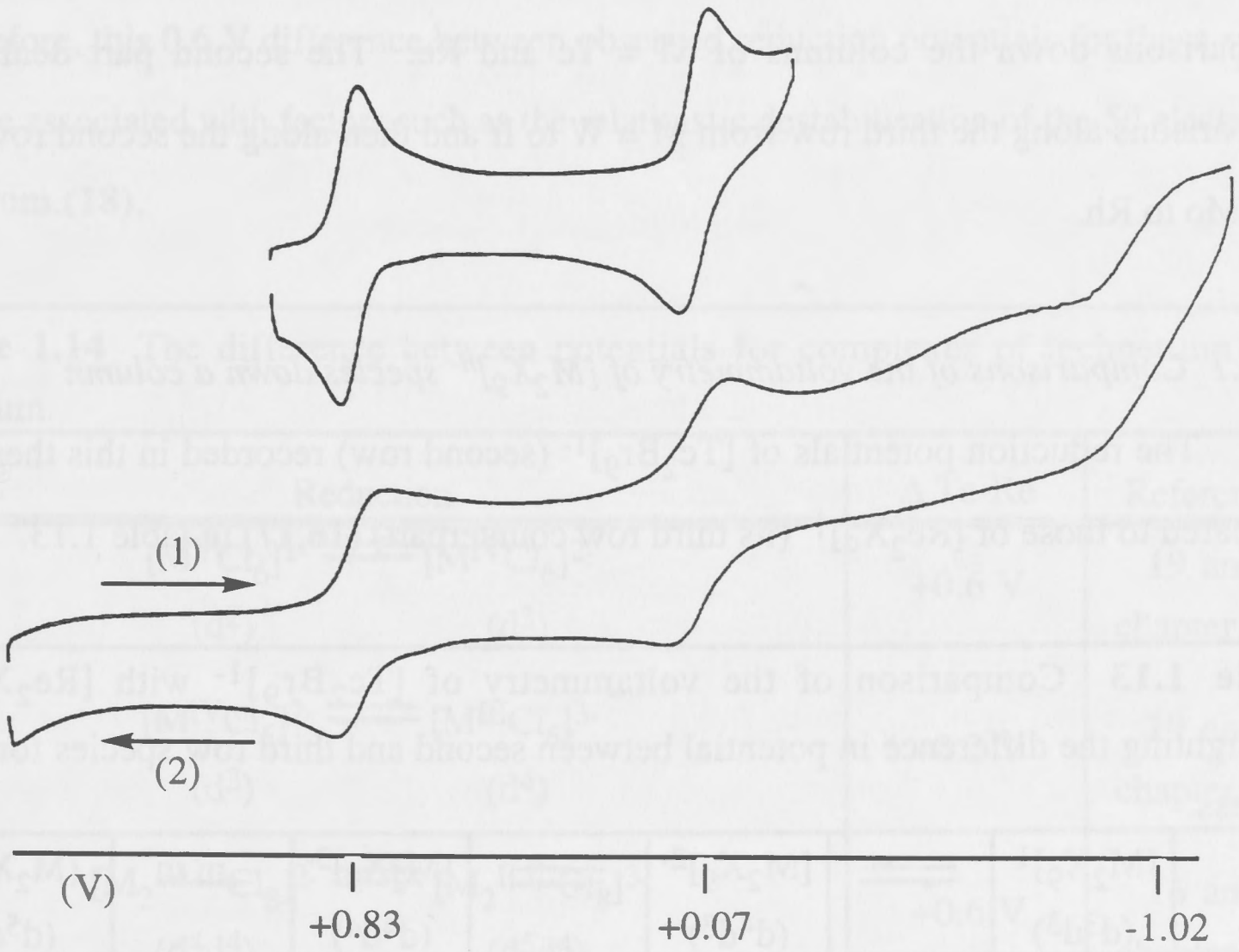

Figure 1.11 *The voltammetry of (TEA)$[Tc_2Br_9]$ recorded in CH_2Cl_2 at -60°C. The arrows indicate the scan direction. The first two reversible reductions are pictured above the full range for clarity.*

Table 1.12 Voltammetry of $[Tc_2Br_9]^{1-}$ recorded in CH_2Cl_2 at -60°C.

$[Tc_2Br_9]^{1-}$ (d^3d^3)	⇌	$[Tc_2Br_9]^{2-}$ (d^4d^3)	⇌	$[Tc_2Br_9]^{3-}$ (d^4d^4)	→	$\{Tc_2Br_9\}^{4-}$ (d^5d^4)
	+0.83 V (rev)		+0.07 V (rev)		-1.02 V (irrev)	

Using CH_3CN as solvent the processes described for electrochemistry in CH_2Cl_2 were observed accompanied by a further irreversible oxidation observed at +2.1 V. The coordinative properties of CH_3CN mean that further work is required before confidently assigning this signal to the $[Tc_2Br_9]^{1-/0}$ oxidation.

The voltammetry has been recorded previously for several of the $[M_2X_9]^{n-}$ complexes including M = Mo, W, Ru, Os and Re which are of interest in this thesis (**2**, **14**, **15**, **16**, **17**). It is common to find two reversible reductions and a further irreversible reduction when starting from the bis tetra-valent oxidation state, as was observed here for $[Tc_2Br_9]^{1-}$.

The following discussion will describe the voltammetry of $[Tc_2Br_9]^{1-}$ in the context of other $[M_2X_9]^{n-}$ species and is divided into two parts. The first part details comparisons down the columns of M = Tc and Re. The second part deals with comparisons along the third row from M = W to Ir and then along the second row from M = Mo to Rh.

1.1.2.1 Comparisons of the voltammetry of $[M_2X_9]^{n-}$ species down a column

The reduction potentials of $[Tc_2Br_9]^{1-}$ (second row) recorded in this thesis, are compared to those of $[Re_2X_9]^{1-}$ (its third row counterpart) (**16**,**17**) in table 1.13.

Table 1.13 Comparison of the voltammetry of $[Tc_2Br_9]^{1-}$ with $[Re_2X_9]^{1-}$ highlighting the difference in potential between second and third row species for each process.

	$[M_2X_9]^{1-}$ (d^3d^3)	⇌	$[M_2X_9]^{2-}$ (d^4d^3)	⇌	$[M_2X_9]^{3-}$ (d^4d^4)	⟶	$\{M_2X_9\}^{4-}$ (d^5d^4)
Tc_2Br_9		+0.83 V (rev)		+0.07 V (rev)		-1.02 V (irrev)	
Re_2Br_9		+0.74 V (rev)		-0.05 V (rev)		-1.65 V (irrev)	
Δ Tc-Re		+0.09		+0.12		+0.63	
Re_2Cl_9[#]		+0.75 V (rev)		-0.17 V (rev)		-1.81 V (irrev)	

[#] A further oxidation to the d^3d^2 neutral species $[Re_2Cl_9]^0$ is also accessible, requiring a potential of +2.53 V (rev).

The table shows that, for the two reversible reductions, the potentials of technetium (second row) and rhenium (third row) are very similar, while the difference for the final irreversible process is considerably larger.

Comparisons of data from other technetium and rhenium halide complexes (table 1.14) indicate that the difference in potential between corresponding reduction processes is most commonly of the order of +0.6 V. The bonding within $[TcCl_6]^{n-}$ is thought to be similar to that in $[ReCl_6]^{n-}$, likewise that bonding in $[Tc_2X_8]^{n-}$ is similar to $[Re_2X_8]^{n-}$. Therefore, this 0.6 V difference between observed reduction potentials for these species can be associated with factors such as the relativistic destabilisation of the 5d electrons in rhenium.(**18**).

Table 1.14 The difference between potentials for complexes of technetium and rhenium.

Reduction	Δ Tc-Re	Reference
$[M^{V}Cl_6]^{1-} \rightleftharpoons [M^{IV}Cl_6]^{2-}$ (d^2) (d^3)	+0.6 V	**19** and chapter 1.3
$[M^{IV}Cl_6]^{2-} \rightleftharpoons [M^{III}Cl_6]^{3-}$ (d^3) (d^4)	+0.2 V	**19** and chapter 1.3
$[M_2^{III,III}Cl_8]^{2-} \rightleftharpoons [M_2^{II,III}Cl_8]^{3-}$ (d^4d^4) (d^5d^4)	+0.6 V	**16** and chapter 1.2
$[M_2^{III,III}Br_8]^{2-} \rightleftharpoons [M_2^{II,III}Br_8]^{3-}$ (d^4d^4) (d^5d^4)	+0.6 V	**17** and chapter 1.2

The difference in potential of +0.2 V for the d^3/d^4 couple between M = Tc and Re in $[MCl_6]^{n-}$ (n = 2, 3) is relatively small, this was rationalised in terms of the difference in spin orbit coupling between second and third row metals. (**19**) The authors report (**19**) that, analysis had shown this effect was likely to exert the largest influence on the d^3/d^4 couple and would have the effect of making the reduction of the third row with this d^3 configuration relatively easy compared to the d^3 species of the second row.

Returning to the consideration of $[Tc_2Br_9]^{n-}$ and $[Re_2X_9]^{n-}$,the differences in potentials for the d^3d^3/d^4d^3 and d^4d^3/d^4d^4 processes of 0.09 and 0.12 V are unusually small. For both $[Tc_2Br_9]^{n-}$ and $[Re_2X_9]^{n-}$ these reduction couples involve the introduction of electrons into orbitals which are localised about individual metal centres containing two electrons which are each antiferromagnetically coupled across the anion. As was shown for other halide complexes of technetium and rhenium, the addition of electrons into similar orbitals may result in a difference in potentials of around +0.6 V except in cases where effects such as spin-orbit coupling dominate over relativistic considerations. It is assumed here that the different nature of the metal-to-metal bonding noted earlier in $[Tc_2Br_9]^{n-}$ as compared to $[Re_2X_9]^{n-}$, is contributing to the apparently coincident potentials for the first two reductions. Comparisons of the potentials for the third reduction process are complicated by its irreversibility and that due to the absence of σ-bonding in $[Tc_2Br_9]^{n-}$ the electron can enter a different level for $[Tc_2Br_9]^{n-}$ as compared to $[Re_2X_9]^{n-}$.

It is interesting to consider a situation where the bonding within a nonahalide pair remains relatively similar. To this end the difference between reduction potentials of $[M_2X_9]^{n-}$ where M = Ru and Os, which in both cases a single metal-metal bond and $[MCl_6]^{n-}$ is presented in table 1.15.

The first thing to note from table 1.15 is that the difference in the potential for the d^3/d^4 couples of $[MCl_6]^{n-}$ (M = Ru, Os and n = 1, 2) is once again relatively small due to the spin orbit coupling associated with that electron configuration in an octahedral system. The differences in potential for $[M_2X_9]^{n-}$ however are consistently larger for M = Ru and Os than for M = Tc and Re as a result of the more similar nature of the bonding in the M = Ru and Os nonahalide pair.

Table 1.15 The difference between potentials for complexes of ruthenium and osmium.

Reduction	Δ Ru-Os	Reference
$[M^{V}Cl_6]^{1-} \rightleftharpoons [M^{IV}Cl_6]^{2-}$ (d^3) (d^4)	+0.33 V	**19**
$[M^{IV}Cl_6]^{2-} \rightleftharpoons [M^{III}Cl_6]^{3-}$ (d^4) (d^5)	+0.59 V	**19**
$[M_2^{IV,IV}Cl_9]^{1-} \rightleftharpoons [M_2^{V,IV}Cl_9]^{2-}$ (d^4d^4) (d^5d^4)	+0.48 V	**2,20**
$[M_2^{IV,IV}Br_9]^{1-} \rightleftharpoons [M_2^{V,IV}Br_9]^{2-}$ (d^4d^4) (d^5d^4)	+0.29 V	**2,20**
$[M_2^{V,IV}Cl_9]^{2-} \rightleftharpoons [M_2^{V,V}Cl_9]^{3-}$ (d^5d^4) (d^5d^5)	+0.72 V	**2,20**
$[M_2^{V,IV}Br_9]^{2-} \rightleftharpoons [M_2^{V,V}Br_9]^{3-}$ (d^5d^4) (d^5d^5)	+0.48 V	**2,20**
$[M_2^{V,V}Cl_9]^{3-} \rightarrow [M_2^{VI,V}Cl_9]^{4-}$ (d^5d^5) (d^6d^5)	+0.89 V	**2,20**
$[M_2^{V,V}Br_9]^{3-} \rightarrow [M_2^{VI,V}Br_9]^{4-}$ (d^5d^5) (d^6d^5)	+0.67 V	**2,20**

1.1.2.2 Comparisons of the voltammetry of $[M_2X_9]^{n-}$ species along a row

The potentials of redox processes for the $[M_2X_9]^{n-}$ species along the third row from W to Ir (**2**,**15**,**16**,**17**) are presented in table 1.16. For corresponding (isovalent) processes, for example $[M_2X_9]^{1-}$ to $[M_2X_9]^{2-}$, reduction potentials become increasingly positive moving from left to right along the row. In other words, reduction becomes easier and the lower oxidation states become more accessible with increasing nuclear charge. Such an observation is also common for other series containing transition metals, for example $[MX_6]^{n-}$ with M = Ta to Pt (**19**).

Table 1.16 Successive reduction potentials for $[M_2X_9]^{1-}$ species of the third row transition metals, highlighting the differences between redox couples.

Complex	d^2d^2/d^3d^2	d^3d^2/d^3d^3	d^3d^3/d^4d^3	d^4d^3/d^4d^4	d^4d^4/d^5d^4	d^5d^4/d^5d^5	d^5d^5/d^5d^6	d^5d^6/d^6d^6
W_2Cl_9	+0.75 (rev)	+0.05 (rev)						
	Δ_0 0.70							
Re_2Cl_9			+0.75 (rev)	-0.17 (rev)	-1.81 (irrev)			
			Δ_2 0.92	Δ_3 1.64				
Re_2Br_9			+0.74 (rev)	-0.05 (rev)	-1.65 (irrev)			
			Δ_2 0.79	Δ_3 1.60				
Os_2Cl_9					+1.10 (rev)	+0.20 (rev)	-1.46 (qr)	
					Δ_4 0.90	Δ_5 1.66		
Os_2Br_9					+1.07 (rev)	+0.35 (rev)	-1.27 (qr)	
					Δ_4 0.72	Δ_5 1.62		
Ir_2Cl_9							+1.77 (rev)	+1.03 (rev)
							Δ_6 0.74	

An analysis of the differences between successive reduction processes presented in table 1.16, labelled as Δ and highlighted by shading, shows that the values are similar (between 0.7 and 0.9 V) except for Δ_3 and Δ_5 which are noticeably larger, around 1.6 V. The equivalent comparison for $[MCl_6]^{n-}$ is presented in detail in chapter 1.3 (see tables 1.37 and 1.38). One noticeably larger difference was also noted in that set of data between the d^2/d^3 and d^3/d^4 reduction couples of $[MCl_6]^{n/n-1}$, (where M = Tc, Re and n = -1, -2). This relatively large difference in potential between these consecutive

couples in $[MX_6]^{n-}$, is assumed to be due to the on set of spin-pairing in the low spin d^4 configuration, (see chapter 1.3). The large Δ_3 value observed for $[M_2X_9]^{n-}$ is analysed here in similar terms. Figure 1.16 illustrates that, Δ_3 corresponds to the first spin-pairing into δ_π* and this may contribute to its relatively large value.

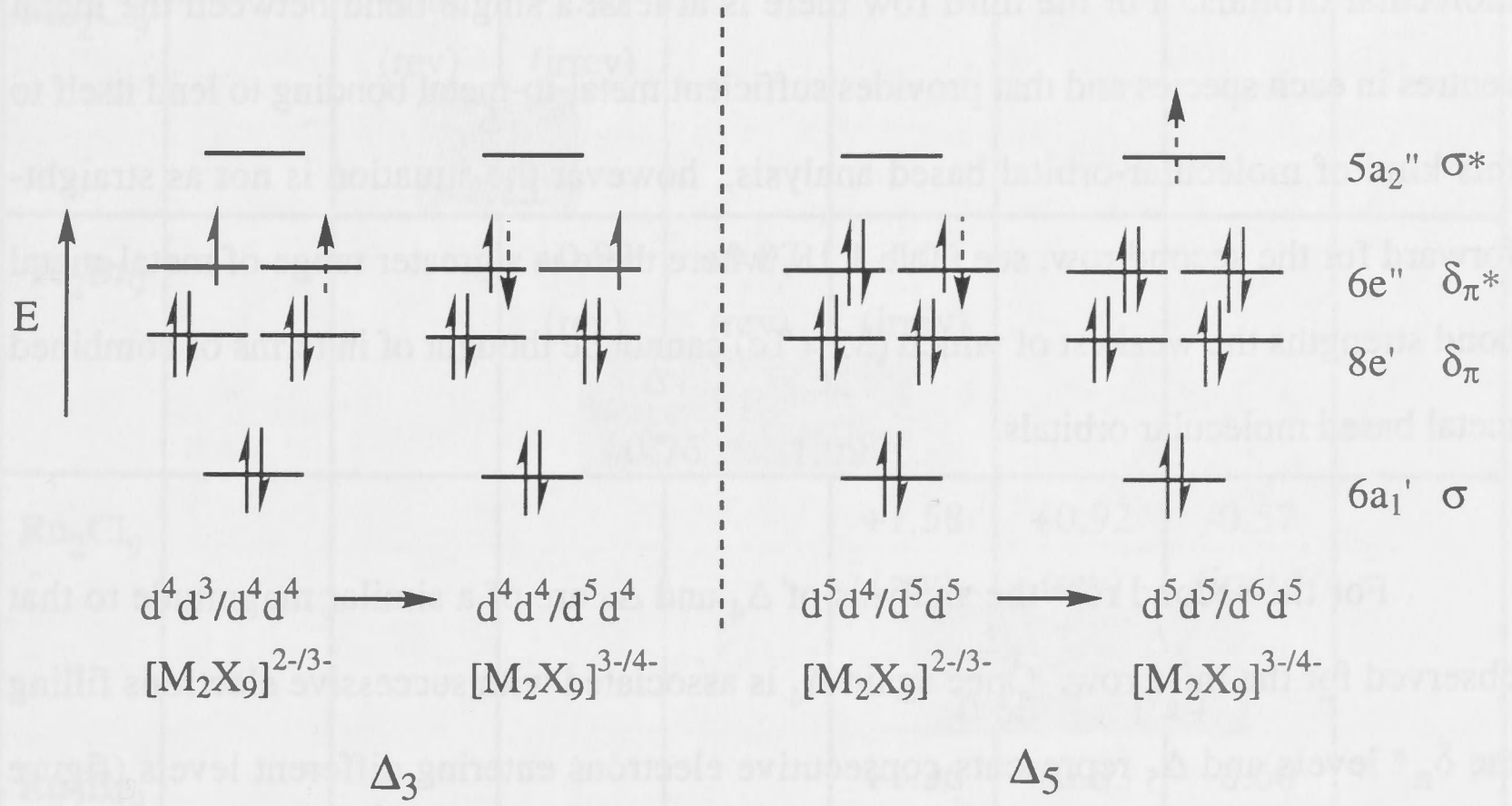

Figure 1.17 *Showing the last added electron as a broken arrow. This highlights that these processes involve the first onset of spin-pairing in δ_π* and the introduction of an electron into σ* respectively.*

The relatively large value for Δ_5 may be attributed to the consecutive electrons entering different types of orbitals, that is δ_π* and the metal-metal bond destabilising σ* level respectively (see figure 1.17), hence the difference in potentials for the two processes is relatively large.

Another possibility for the placement of the electron in the d^4d^4 to d^5d^4 reduction (the second reduction process contributing to Δ_3) is that the electron may enter σ* (instead of pairing into δ_π*) in a type of high spin arrangement. This would probably result in a significant disruption to the metal-metal bonding. It is interesting that under those circumstances the electron would be entering the same level as was necessary for Δ_5, and that Δ_3 and Δ_5 have similar values.

The accuracy of this analysis of the electrochemistry of third row $[M_2X_9]^{n-}$ complexes is dependent upon the validity of the assumptions made about the nature of the metal-to-metal interaction, for each complex, in each oxidation state and the resultant molecular orbital arrangement, combined with the electron configuration within those molecular orbitals. For the third row there is at least a single bond between the metal centres in each species and that provides sufficient metal-to-metal bonding to lend itself to this kind of molecular-orbital based analysis, however the situation is not as straight-forward for the second row, see table 1.18, where there is a greater range of metal-metal bond strengths the weakest of which (M = Tc) cannot be thought of in terms of combined metal based molecular orbitals.

For the second row the analysis of Δ_4 and Δ_5 are of a similar magnitude to that observed for the third row. Once again Δ_4 is associated with successive electrons filling the δ_π^* levels and Δ_5 represents consecutive electrons entering different levels (figure 1.17) and so is comparatively larger. Δ_1 is also of a relatively large magnitude and like Δ_5 corresponds to consecutive electrons entering different levels, δ_π^* and δ_π on this occasion. Δ_2 and Δ_3 for M = Tc (second row) are more similar to each other than the equivalent values for M = Re (third row). If the relative size of Δ can be related to the changes in electron configuration accompanying the successive reductions then this result may be further evidence of a different metal-to-metal bonding within $[Tc_2Br_9]^{n-}$ as compared to $[Re_2X_9]^{n-}$. The evidence from the previous section suggests that the $[Tc_2Br_9]^{n-}$ species should not be thought of in terms of the molecular orbitals presented in figure 1.17. Rather it is more appropriately considered as two independent metal centres, such that Δ_2 and Δ_3 will correspond to electrons adding to each individual metal centre in turn, processes which would be consistent with the similar values observed for Δ_2 and Δ_3.

Table 1.18 Successive reduction potentials for $[M_2X_9]^{1-}$ species of the second row transition metals, highlighting the differences between redox couples.

Complex	d^2d^2/ d^3d^2	d^3d^2/ d^3d^3	d^3d^3/ d^4d^3	d^4d^3/ d^4d^4	d^4d^4/ d^5d^4	d^5d^4/ d^5d^5	d^5d^5/ d^5d^6	d^5d^6/ d^6d^6
Mo_2Cl_9		+0.85 (rev)	-1.40 (irrev)					
		Δ_1 2.25						
Tc_2Br_9			+0.83 (rev)	+0.07 (rev)	-1.02 (irrev)			
			Δ_2 0.76	Δ_3 1.09				
Ru_2Cl_9					+1.58 (rev)	+0.92 (rev)	-0.57 (irrev)	
					Δ_4 0.66	Δ_5 1.49		
Ru_2Br_9					+1.36 (rev)	+0.83 (rev)	-0.60 (rev)	
					Δ_4 0.53	Δ_5 1.43		

Further support for considering $[Tc_2Br_9]^{1-}$ as being made up of independent metal centres was provided by an investigation of its UV-visible spectro-electrochemistry, the details of which will be discussed in the next section.

1.1.3 Spectro-electrochemistry of $[Tc_2Br_9]^{n-}$ (where n = 1, 2, 3)

The voltammetric reversibility of the first two reductions provided ideal conditions for the study of (TEA)$[Tc_2Br_9]$ by spectro-electrochemistry.# Accordingly, the spectra of $[Tc_2Br_9]^{2-}$ and $[Tc_2Br_9]^{3-}$ were reversibly generated and are reported for the first time in this thesis. These measurements were made in 0.5 M (TBA)$[BF_4]/CH_2Cl_2$ at -60°C. The characteristic absorbances of each species are pictured in figure 1.19 and noted in table 1.20.

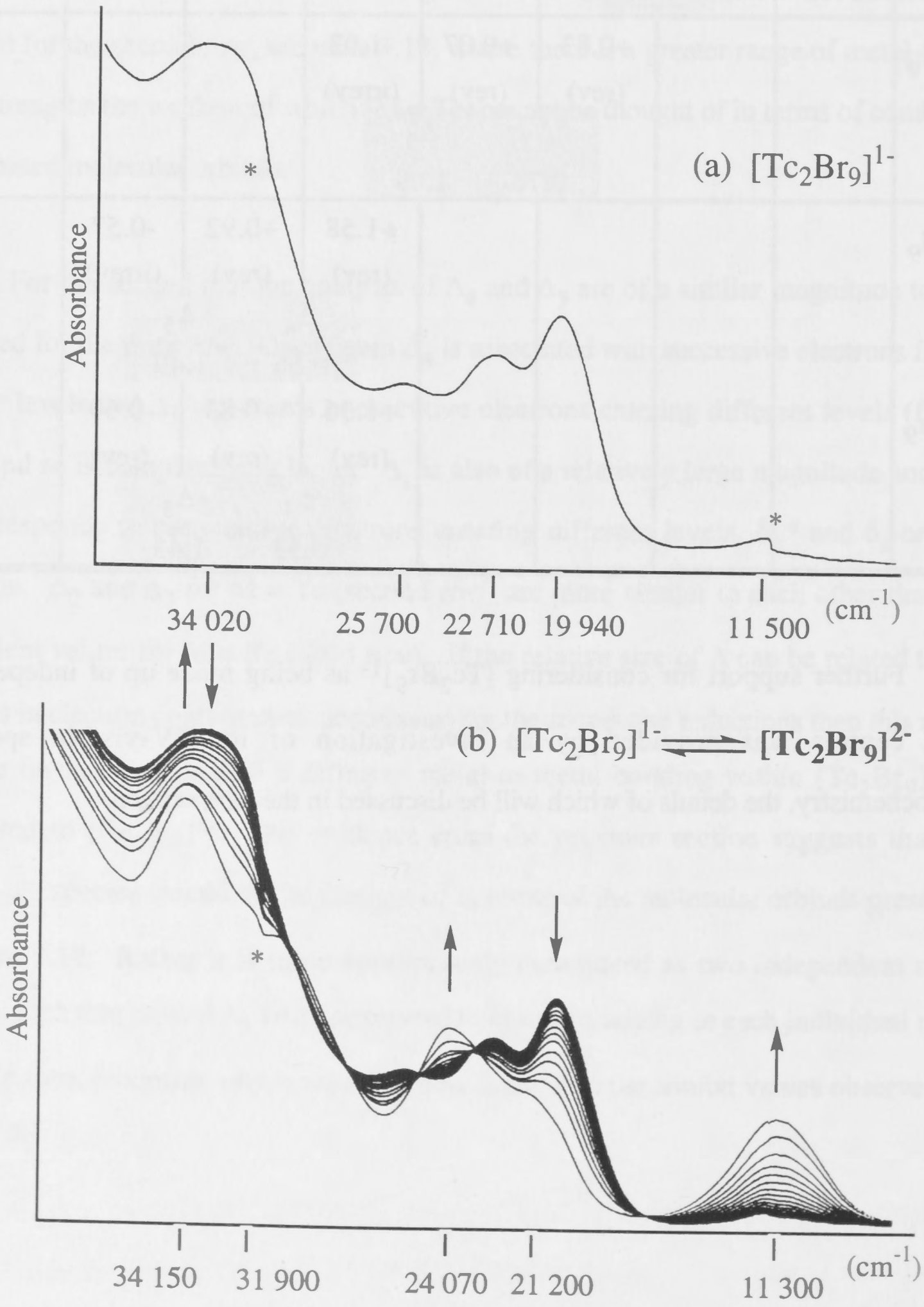

If one can reversibly generate spectra (that is, observe tight isobestic points and recover the starting spectrum 100% intact) one can assume that the new spectrum is related to the species anticipated for the redox process.

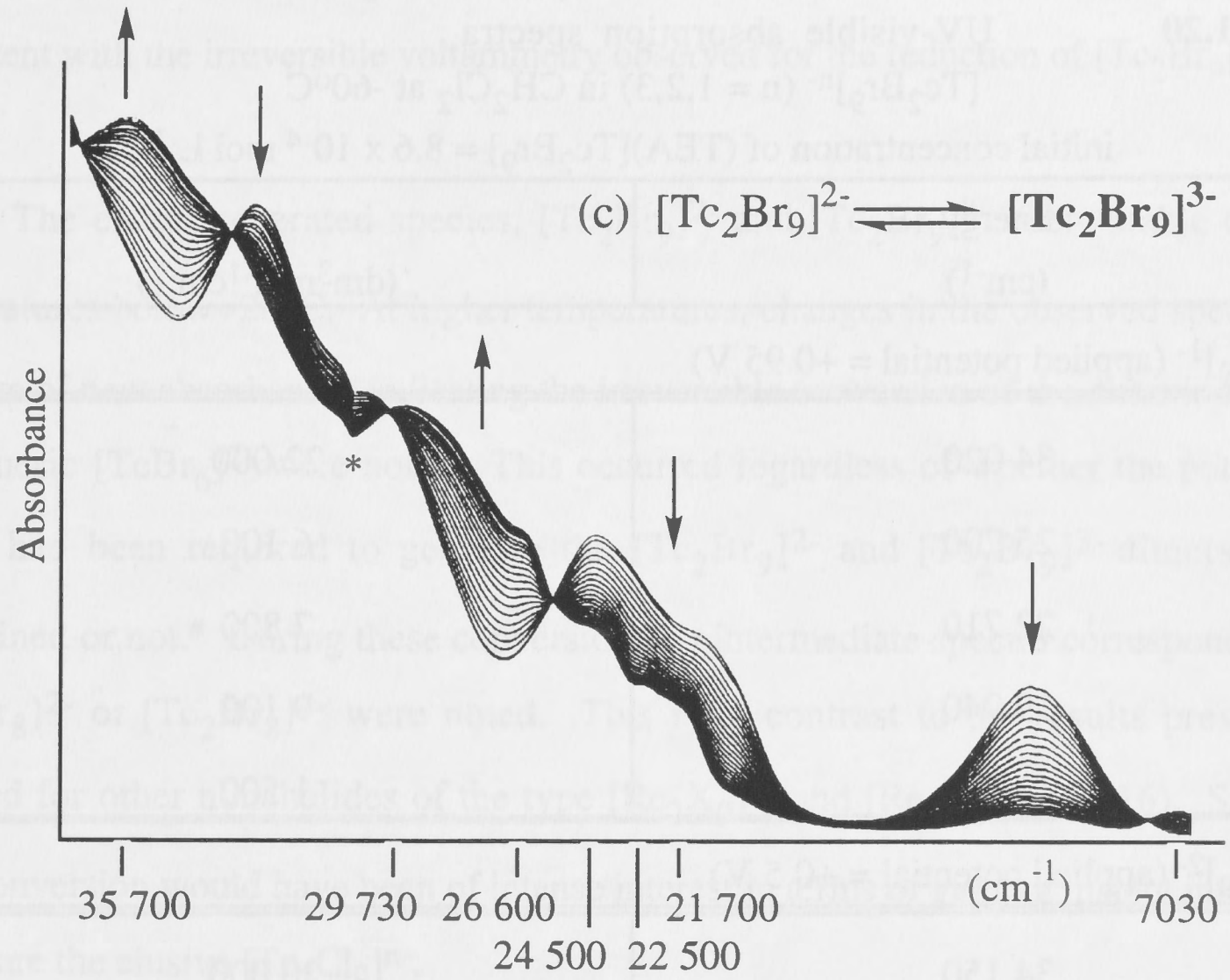

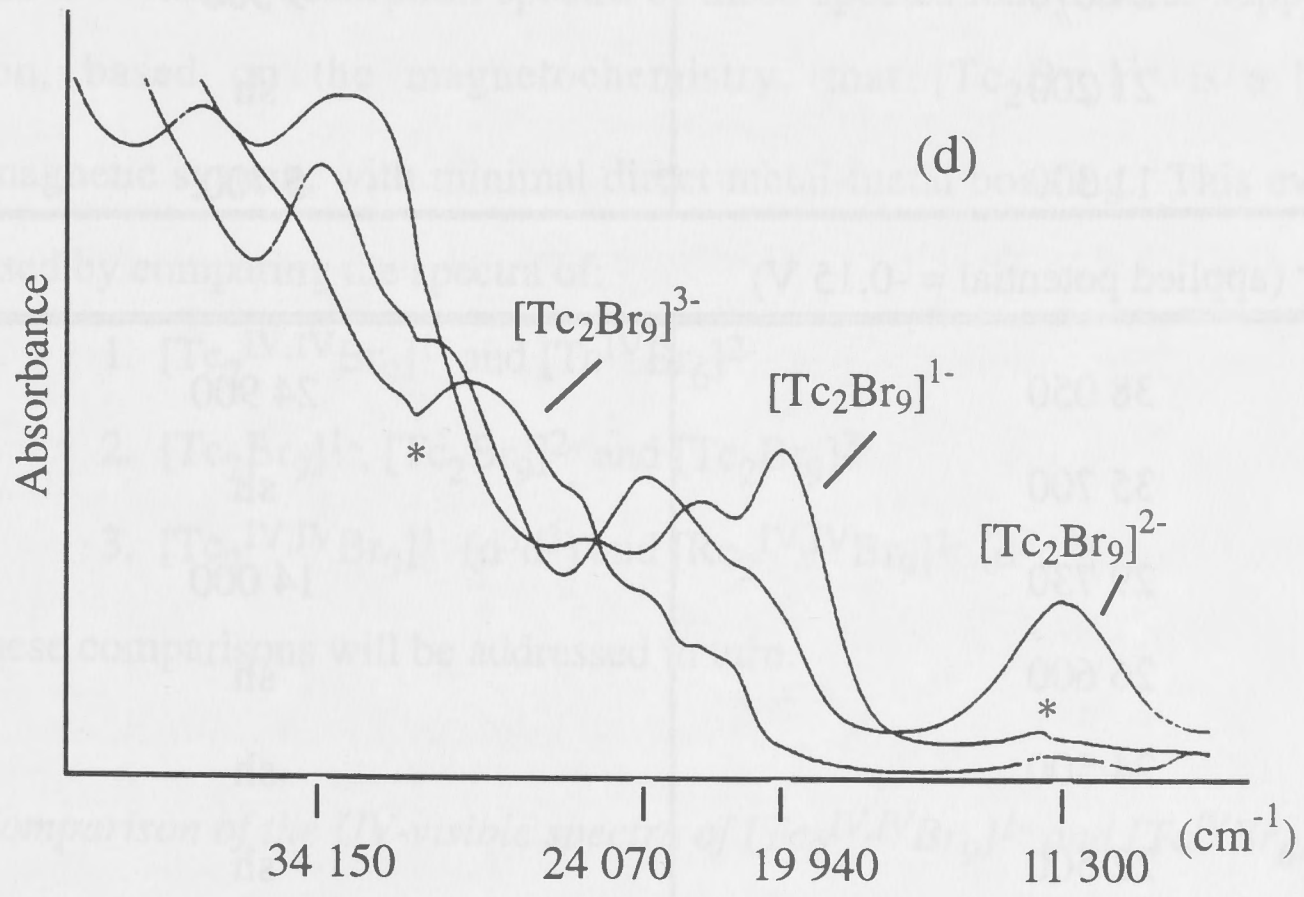

Figure 1.19 *The UV-visible absorption spectra recorded in 0.5 M $TBAPF_6/CH_2Cl_2$ at -60°C of (a) $[Tc_2Br_9]^{1-}$, (b) inter-conversion of $[Tc_2Br_9]^{1-}$ to $[Tc_2Br_9]^{2-}$, (c) inter-conversion of $[Tc_2Br_9]^{2-}$ to $[Tc_2Br_9]^{3-}$ and (d) an overlay of all three oxidation states, $[Tc_2Br_9]^{1-}$, $[Tc_2Br_9]^{2-}$ and $[Tc_2Br_9]^{3-}$. Instrumental glitches resulting from lamp and detector changes are marked by a *.*

Table 1.20 UV-visible absorption spectra
$[Tc_2Br_9]^{n-}$ (n = 1,2,3) in CH_2Cl_2 at -60°C
initial concentration of (TEA)$[Tc_2Br_9]$ = 8.6 x 10^{-4} mol L^{-1}

Energy (cm^{-1})	ε ($dm^3mol^{-1}cm^{-1}$)
$[Tc_2Br_9]^{1-}$ (applied potential = +0.95 V)	
34 020	22 000
25 700	6 100
22 710	7 800
19 940	9 100
11 500	1 500
$[Tc_2Br_9]^{2-}$ (applied potential = +0.5 V)	
34 150	20 000
31 900	sh
24 070	9 500
21 200	sh
11 300	5 700
$[Tc_2Br_9]^{3-}$ (applied potential = -0.15 V)	
38 050	24 900
35 700	sh
29 730	14 000
26 600	sh
24 500	sh
22 500	sh
21 700	sh
7 030	910

It is noteworthy that further reduction to what would have been $[Tc_2Br_9]^{4-}$ at an applied potential of -1.20 V resulted in a general, irreversible collapse of the observed spectra

and did not reveal the emergence of any other new absorbances. This observation is consistent with the irreversible voltammetry observed for the reduction of $[Tc_2Br_9]^{3-}$.

The electrogenerated species, $[Tc_2Br_9]^{2-}$ and $[Tc_2Br_9]^{3-}$, were stable only at temperatures below -20°C. At higher temperatures, changes in the observed spectra, in the form of new absorbances indicating the irreversible conversion of the dimeric form to monomeric $[TcBr_6]^{2-}$ were noted. This occurred regardless of whether the potentials which had been required to generate the $[Tc_2Br_9]^{2-}$ and $[Tc_2Br_9]^{3-}$ dimers were maintained or not.# During these conversions no intermediate spectra corresponding to $[Tc_2Br_8]^{2-}$ or $[Tc_2Br_8]^{3-}$ were noted. This is in contrast to the results previously reported for other nonahalides of the type $[Re_2X_9]^{3-}$ and $[Re_2X_9]^{4-}$ (**17**,**16**). Such an inter-conversion would have been of intense interest in terms of gaining insight into ways to prepare the elusive $[Tc_2Cl_9]^{n-}$.

The UV-visible absorption spectra of these species lend further support to the conclusion, based on the magnetochemistry, that $[Tc_2Br_9]^{1-}$ is a localised, antiferromagnetic system, with minimal direct metal-metal bonding. This evidence is best assessed by comparing the spectra of:

1. $[Tc_2^{IV,IV}Br_9]^{1-}$ and $[Tc^{IV}Br_6]^{2-}$
2. $[Tc_2Br_9]^{1-}$, $[Tc_2Br_9]^{2-}$ and $[Tc_2Br_9]^{3-}$
3. $[Tc_2^{IV,IV}Br_9]^{1-}$ (d^3d^3) and $[Re_2^{IV,IV}Br_9]^{1-}$ (d^3d^3)

Each of these comparisons will be addressed in turn.

1.1.3.1 Comparison of the UV-visible spectra of $[Tc_2^{IV,IV}Br_9]^{1-}$ and $[Tc^{IV}Br_6]^{2-}$

The localised nature of the metal based electrons in $[Tc_2Br_9]^{1-}$ means that the molecular orbitals which would be generated by metal-to-metal interaction are not present as they would normally be for a more delocalised system. Therefore in order to assign the UV-visible spectrum of $[Tc_2Br_9]^{1-}$ the transitions should be thought of in terms of

---

At these applied potentials and when the potential was switched off, monomeric technetium hexabromide would be expected to be in the Tc^{IV} oxidation state, that is as $[TcBr_6]^{2-}$ (see chapter 1.3).

electrons "hopping" between the metal centres or as charge transfer from ligand molecular orbitals into each metal centre. (**21**)

The spectra of $[Tc_2^{IV,IV}Br_9]^{1-}$ (figure 1.18a) and $[Tc^{IV}Br_6]^{2-}$ (figure 1.31b) are both based on bromide to Tc^{IV}, ligand to metal charge transfer. As such, both spectra comprise two absorption regions. The region to high energy (above 30 000 cm^{-1}) exhibits intense absorptions ($\varepsilon > 15\,000$ $dm^3mol^{-1}cm^{-1}$) corresponding to charge transfer from bromide based levels into Tc e_g based levels. The second region (below 30 000 cm^{-1}) contains less intense absorbances which are assigned as either charge transfer from bromide into Tc t_{2g} based levels or metal based transitions.

Both absorbance regions are red-shifted in the spectrum of $[Tc_2Br_9]^{1-}$ as compared to $[TcBr_6]^{2-}$. The energy of charge transfer transitions is determined by the energetic separation of the donor and acceptor orbitals. (**22**) In $[M_2X_9]^{n-}$ the halide ligands contributing to the ligand based molecular orbital array are positioned in two different coordination environments, those being the bridging or terminal halides, and as a result the energy range spanned by the ligand based molecular orbitals is greater than that of $[MX_6]^{n-}$ where all halides are in an equivalent coordination environment (**21**). The relative energies of the observed halide to metal charge transfer transitions of $[Tc_2Br_9]^{1-}$ and $[TcBr_6]^{2-}$ would seem to indicate that as a result of the larger energy range spread of the halide levels, the separation of the metal acceptor and ligand donor levels is smaller in $[Tc_2Br_9]^{1-}$ than $[TcBr_6]^{2-}$.

1.1.3.2 Comparison of the UV-visible spectra of $[Tc_2Br_9]^{1-}$ and $[Tc_2Br_9]^{2-}$

The first obvious difference between these two spectra (figure 1.18 b and d) is the appearance of the broad, low energy band at 11 300 cm^{-1} in the spectrum of the reduced, mixed valence $[Tc_2^{III,IV}Br_9]^{2-}$ oxidation state. This band is assigned as an inter-valence charge transfer band. Such a relatively low energy inter-valence charge transfer band has been identified as being typical of localised systems with two distinct metal centres which have little or no bonding between them and corresponds to an

electron transfer from one metal site to the other. (**21**) The broadness of the band has been attributed to the coupling to vibronic processes which are necessary to accommodate the charge transfer. (**21**) A similar absorbance was observed in the spectra of the localised, weakly bonded $[Ru_2^{III,IV}X_9]^{2-}$ species (**2b**) but a band of this form is not apparent in the spectra of the more strongly interacting $[Re_2Cl_9]^{2-}$ and $[W_2Cl_9]^{2-}$ (**21**).

The remaining absorbances in the spectrum of $[Tc_2Br_9]^{2-}$ have counterparts in the spectrum of $[Tc_2Br_9]^{1-}$ and so are attributed to bromide to technetium charge transfer. A general blue-shift of the absorbances between 32 000 and 20 000 cm^{-1} was observed upon reduction. Such an increase in energy for the halide to metal charge transfer upon reduction is typical of these $[M_2X_9]^{n-}$ systems. (**21**) This corresponds to an expansion of the d orbitals, which results in a destabilisation of the metal based acceptor levels relative to the ligand based donor levels and a resultant increase in ligand to metal charge transfer energies.

1.1.3.3 Comparison of the UV-visible spectra of $[Tc_2Br_9]^{2-}$ and $[Tc_2Br_9]^{3-}$

Further reduction to $[Tc_2Br_9]^{3-}$ where both technetium centres are once again in the same oxidation state $Tc_2^{III,III}$ (d^4d^4) results in the inter-valence charge transfer band no longer appearing in the spectrum. There is a further general blue shift for the remaining absorbances upon reduction (figure 1.18 c and d), which is consistent with the spectra corresponding largely to ligand to metal charge transfer transitions.

1.1.3.4 Comparison of the UV-visible spectra of $[Tc_2Br_9]^{1-}$ and $[Re_2Br_9]^{1-}$

The spectrum of (TBA)$[Re_2Br_9]^{1-}$ has been recorded previously in our laboratory (**15**) and is shown in figure 1.20, for comparison with the spectrum of the isoelectronic $[Tc_2Br_9]^{1-}$ species shown in figure 1.18a.

The spectrum of $[Re_2Br_9]^{1-}$ has been assigned with the aid of SCF-Xα-SW calculations (**21**) in a manner similar to $[Re_2Cl_9]^{1-}$ (**8**). The region above 30 000 cm^{-1} was attributed to halide to metal charge transfer into molecular orbitals derived from the

e_g based levels of the rhenium metal centres. The region below 30 000 cm^{-1} is dominated by an intense multi-component absorption, the most intense feature of which is assigned as the metal based $\sigma \longrightarrow \sigma^*$ transition, a characteristic of $[M_2X_9]^{1-}$ species which possess at least a single σ bond between the metal centres. The other less intense absorptions in the lower energy region are attributed to halide to metal charge transfer into metal based t_{2g} levels. (**21**)

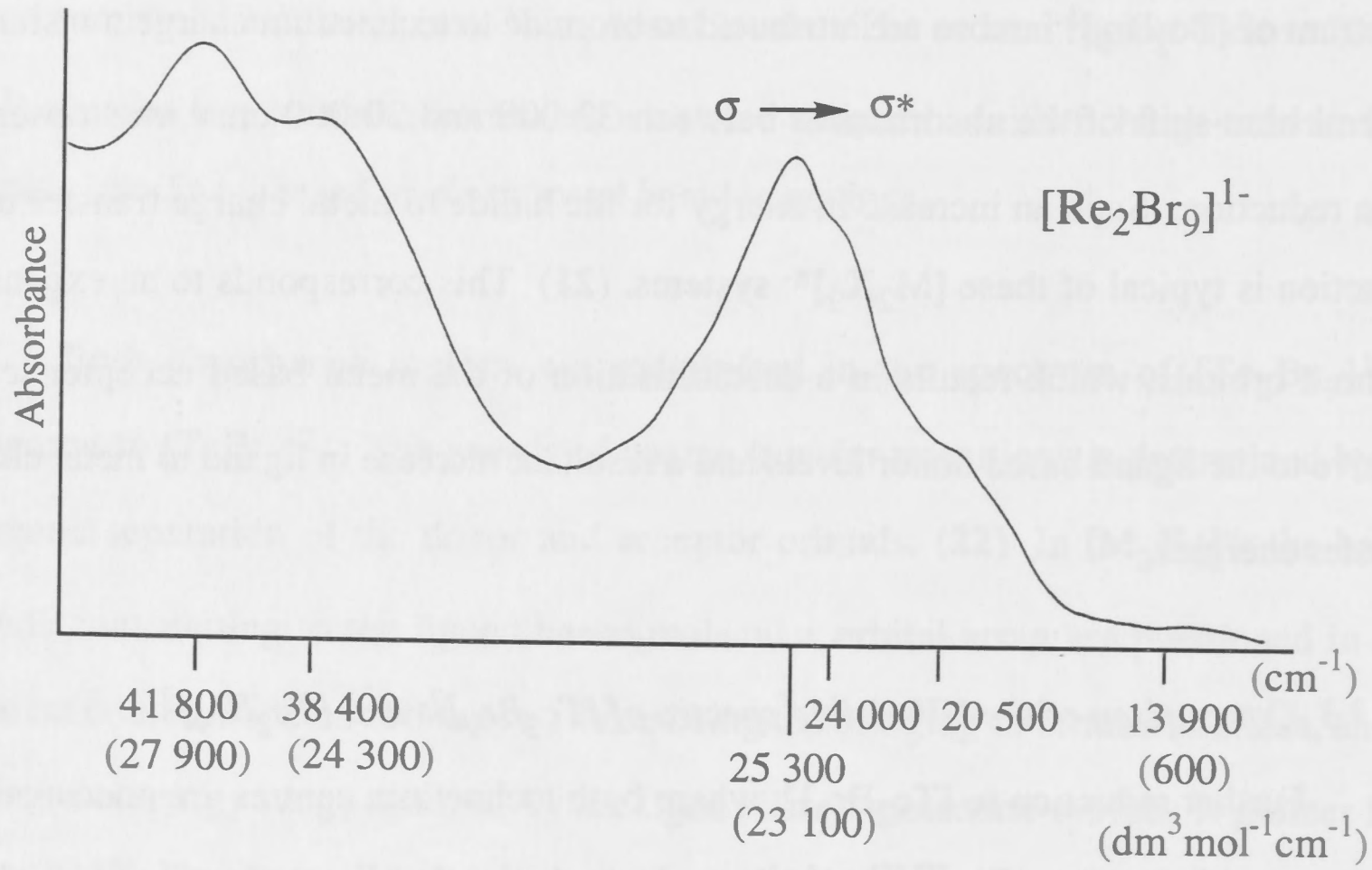

Figure 1.20 *The UV-visible absorption spectrum of (TBA)$[Re_2Br_9]$ as recorded in CH_2Cl_2 at room temperature. (**15**)*

The most important difference between the spectra of $[Re_2Br_9]^{1-}$ and $[Tc_2Br_9]^{1-}$ is the absence of a band in the spectrum of $[Tc_2Br_9]^{1-}$ which is likely to be the equivalent of the band attributed to the $\sigma \longrightarrow \sigma^*$ transition of $[Re_2Br_9]^{1-}$. This provides further evidence that the bonding in $[Tc_2Br_9]^{1-}$ is different from $[Re_2Br_9]^{1-}$.

1.1.4 Conclusions

The metal-to-metal interaction within $[Tc_2Br_9]^{1-}$ has been shown to be best described as localised with no significant Tc-Tc bond and with antiferromagnetic coupling between the electrons. This result is supported by experimental evidence drawn from magnetic moment measurements, voltammetry and spectro-electrochemistry as well

as density-functional calculations. The different nature of the bonding in $[Tc_2Br_9]^{1-}$ as compared to $[Re_2Br_9]^{1-}$ also results in different chemical properties. In particular, no inter-conversion between $[Tc_2Br_9]^{n-}$ and $[Tc_2Br_8]^{n-}$ was observed during the course of these studies, in contrast to those previously reported for the rhenium species (**16**,**17**). This inter-conversion (or lack thereof) will be further investigated in the next chapter which describes the voltammetry and spectro-electrochemistry of $[Tc_2X_8]^{n-}$.

Chapter 1.2: Physicochemical properties of ditechnetium octahalide complexes, $(TBA)_2[Tc_2X_8]$ (where X = Cl or Br)

Previous workers have found that it is possible to prepare $[Re_2X_9]^{n-}$ from $[Re_2X_8]^{n-}$ under conditions where $[Re_2X_8]^{n-}$ is in the appropriate high oxidation state (n = 1 or 0) and free halide is present. (**23**) It was of interest in this work to see if similar reactions could be performed with $[Tc_2X_8]^{n-}$ to form $[Tc_2X_9]^{n-}$. Given the current inaccessibility of $[Tc_2Cl_9]^{n-}$ and the apparent lack of a conversion from $[Tc_2Br_9]^{n-}$ to $[Tc_2Br_8]^{n-}$ (as described in chapter 1.1) this chapter is devoted to an analysis of the voltammetry and spectroscopy of $[Tc_2X_8]^{n-}$ and to ~~a comparison~~ comparisons of these results ~~to~~ with $[Re_2X_8]^{n-}$, with a view to deriving an indication of why these conversions are possible when M = Re but not for M = Tc.

This chapter will first outline some of the previously established observations on the structure and relative stability of $[Tc_2X_8]^{n-}$. The observed reactivity along with voltammetric and spectroscopic data recorded during this thesis will then be presented and compared to previous reports for this species as well as the isoelectronic $[Re_2X_8]^{n-}$. Comparisons with a series of other $[M_2X_8]^{n-}$ species, as described for $[M_2X_9]^{n-}$ (chapter 1.1) and $[MX_6]^{n-}$ (chapter 1.4), are hampered by the smaller number of $[M_2X_8]^{n-}$ species which have been isolated (see the introduction). This chapter will conclude with an analysis of our attempts to prepare $[Tc_2Cl_9]^{n-}$ within the context of the properties of $[Tc_2X_8]^{n-}$ and $[Tc_2Br_9]^{n-}$ described in this chapter and chapter 1.1, respectively.

1.2.1 X-ray crystallographic data

$[Tc_2X_8]^{n-}$ has been chemically isolated in both the $[Tc_2^{II,III}X_8]^{3-}$ (d^5d^4) and $[Tc_2^{III,III}X_8]^{2-}$ (d^4d^4) oxidation states. (**24**,**25**) Crystal structures have been published for both oxidation states of the dimer (where X = Cl), thus providing an interesting insight into the bonding in these complexes (see table 1.22).# Both anions were found to have an eclipsed configuration which is characteristic of a quadruple metal-metal bond. (**25**,**26**,**27**)

Table 1.22 Crystal structures of $Y[Tc_2Cl_8]$ and $(TBA)_2[Tc_2Cl_8]$.

Anion	Tc-Tc (Å)	av. Tc-Cl (Å)	Reference
$[Tc_2^{II,III}Cl_8]^{3-}$ (d^5d^4)	2.105(1)	2.364(2)	**27**
$[Tc_2^{III,III}Cl_8]^{2-}$ (d^4d^4)	2.147(4)	2.320(4)	**25**

Table 1.22 highlights that the Tc-Tc bond is shorter in $[Tc_2Cl_8]^{3-}$ than in the $[Tc_2Cl_8]^{2-}$ anion. This result is initially rather surprising because, as is indicated in figure 1.23, the $[Tc_2Cl_8]^{3-}$ anion has an additional electron, which has been shown by EPR (**27b**) and SCF-Xα-SW calculations (**28**) to reside in a δ^* orbital, resulting in a bond order of 3.5. In comparison, $[Tc_2Cl_8]^{2-}$ does not possess this electron in δ^*, and therefore has a higher bond order of 4. On the basis of the lower bond order, it might have been expected that $[Tc_2Cl_8]^{3-}$ would have a weaker Tc-Tc interaction and hence a longer Tc-Tc bond than $[Tc_2Cl_8]^{2-}$. This was not observed, and is therefore an indication that occupation of the δ and δ^* levels is not the dominant factor in the determination of Tc-Tc bond length in $[Tc_2X_8]^{n-}$. Rather, the shorter bond length in $[Tc_2Cl_8]^{3-}$ has been attributed to the better overlap of Tc 4d levels which is facilitated by an expansion of the 4d orbitals in the more reduced species resulting in stronger σ and π bonding which counteracts the reduction in δ bonding relative to that of $[Tc_2Cl_8]^{2-}$. (**27**,**28**)

No structures of $[Tc_2Br_8]^{n-}$ have been published to date.

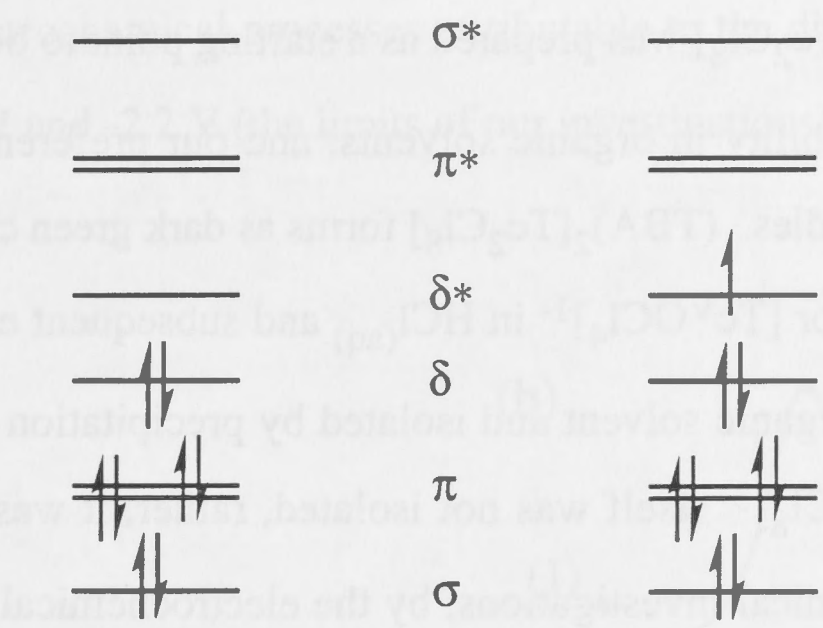

Figure 1.23 *A qualitative representation of the molecular orbitals derived from the 4d levels of the technetium centres in* $[Tc_2Cl_8]^{n-}$ *(where n = 2 and 3). The electron configuration corresponding to each oxidation state is also shown.*

1.2.2 Chemical reactivity

Another intriguing property of the two anions of $[Tc_2Cl_8]^{n-}$ (n = 2 and 3) is their relative stability in different solvents and the relative stability of the anions compared to those of $[Tc_2Br_8]^{n-}$ and $[Re_2X_8]^{n-}$.

It was observed previously (**27b**) and confirmed during the course of this study, that $[Tc_2Cl_8]^{3-}$ is the more stable oxidation state in the hydrochloric acid solutions from which these $[M_2Cl_8]^{n-}$ dimers are normally prepared. It is likely that this is the reason why $[Tc_2Cl_8]^{3-}$ was first isolated in this oxidation state. The $[Tc_2Cl_8]^{2-}$ anion was isolated some 20 years later by taking advantage of its comparatively higher stability in organic solvents. (**25**,**29**) In contrast, previous studies (**30**) have noted the relative instability of $[Tc_2Br_8]^{3-}$ in aqueous HBr and detailed its oxidation to $[TcBr_6]^{2-}$ while in solution by atmospheric oxygen. In our hands, $[Tc_2Br_8]^{2-}$ (**29**) was found to be the more stable oxidation state for the bromide species, regardless of the solvent environment.

These indications of the relative stabilities of $[Tc_2X_8]^{n-}$ species were further reflected in the electrochemical measurements which are described in the next two

sections. $(TBA)_2[Tc_2Cl_8]$ was prepared as a starting point to our investigations because of its enhanced stability in organic solvents, and our preference for such solvents for electrochemical studies. $(TBA)_2[Tc_2Cl_8]$ forms as dark green crystals upon reduction of either $[Tc^{IV}Cl_6]^{2-}$ or $[Tc^{V}OCl_4]^{1-}$ in $HCl_{(aq)}$ and subsequent exposure to air. It is then extracted into an organic solvent and isolated by precipitation (**31**) (see chapter 1.5 for full details). $[Tc_2Cl_8]^{3-}$ itself was not isolated, rather, it was prepared *in situ* during spectro-electrochemical investigations, by the electrochemical reduction of $[Tc_2Cl_8]^{2-}$. $(TBA)_2[Tc_2Br_8]$ was also prepared from $(TBA)_2[Tc_2Cl_8]$, in a halide substitution reaction involving treatment of a CH_2Cl_2 solution of the latter with bromine free $HBr_{(g)}$ (**31**) (see chapter 1.5). $[Tc_2Br_8]^{3-}$ was the only member of this quartet which could not be prepared during the course of this study. It proved too unstable in our hands to be isolated using the reported chemical methods (**31**) nor it could it be successfully electro-generated *in situ* from $[Tc_2Br_8]^{2-}$, as will discussed in section 1.2.4.

1.2.3 Voltammetry of $[Tc_2X_8]^{n-}$ (where n = 2, 3)

The voltammetry of $(TBA)_2[Tc_2X_8]$ was studied in a solution of 0.5 M $(TBA)PF_6$ in CH_2Cl_2, at -60°C. Both species showed a one-electron reduction, at -0.04 and +0.15 V for the chloride and bromide species, respectively (see figure 1.24 and table 1.25). The process was found to be reversible for $[Tc_2Cl_8]^{2-/3-}$ at temperatures below -30°C. The cyclic voltammagram for the $[Tc_2Br_8]^{2-}$ reduction shows a separation of the forward and return potentials of 0.32 V, which is unusually large.# The two signals are related however, because in scans commencing from +0.43 V but only going to -0.05 V, that is not out to the reduction process, the wave at +0.15 V was not observed in the return scan. The acV signal, on the other hand, though broadened, remains centred at +0.15 V for scans in both directions. It is therefore proposed that the observed voltammetry corresponds to a chemically reversible one electron reduction of $[Tc_2Br_8]^{2-}$ to $[Tc_2Br_8]^{3-}$, but that this process is sluggish and is controlled by charge-transfer kinetics, thus resulting in the quasi-reversible voltammetric response which was

The criteria for reversibility require a 0.059 V separation of forward and return potentials for a one electron process.

observed. No other electrochemical processes attributable to the dimeric species were observed between +2.5 V and -2.2 V (the limits of our investigations).

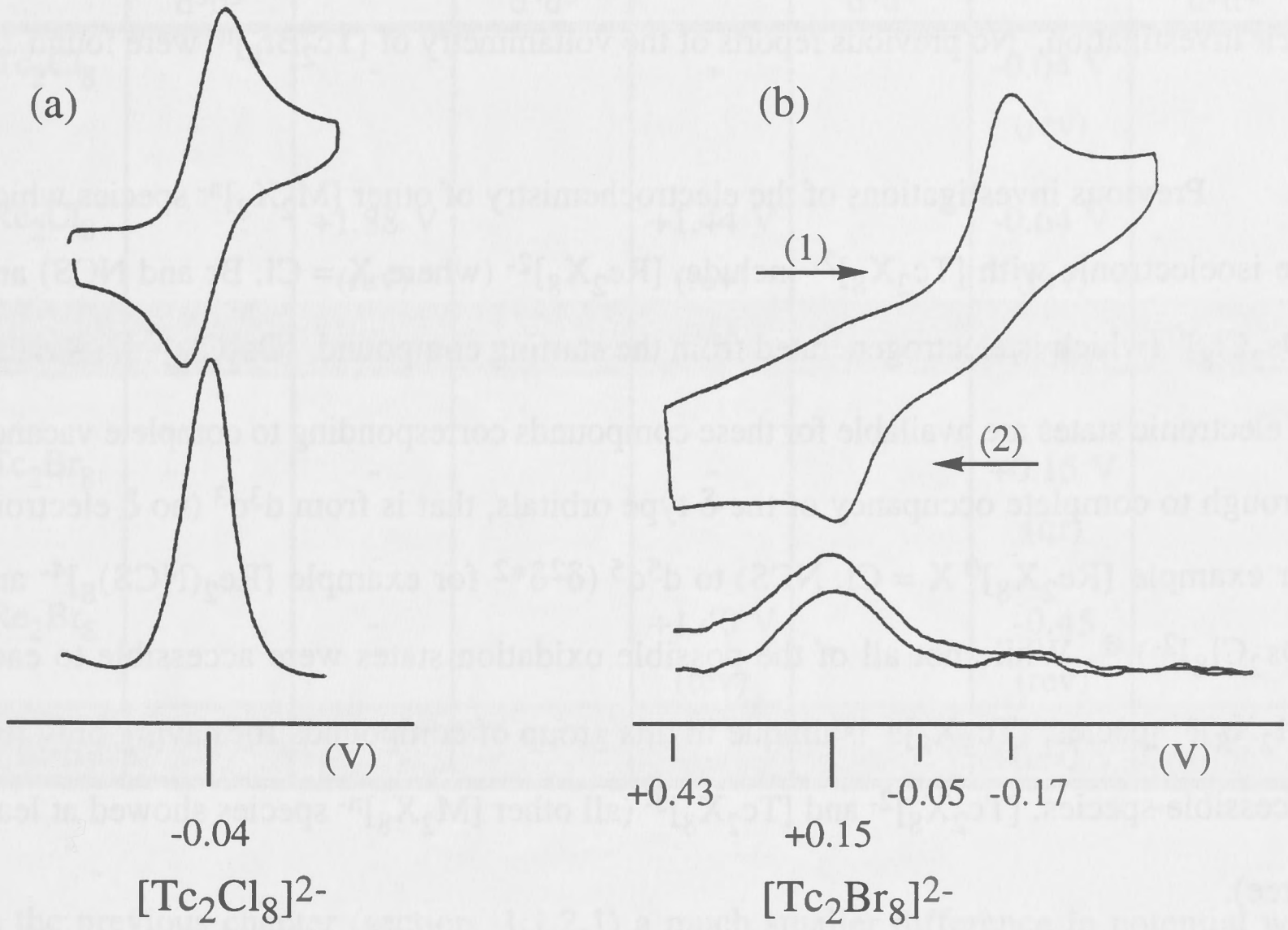

Figure 1.24 *The voltammetric reduction of (a) $[Tc_2Cl_8]^{2-}$ and (b) $[Tc_2Br_8]^{2-}$ recorded in 0.5M $TBAPF_6/CH_2Cl_2$ at 220 K.*

Table 1.25 The observed voltammetry for complexes of the type $[Tc_2X_8]^{n-}$ recorded in 0.5M $TBAPF_6/CH_2Cl_2$ at -60°C.

	$[Tc_2^{III,III}X_8]^{2-}$ (d^4d^4)	⇌	$[Tc_2^{II,III}X_8]^{3-}$ (d^5d^4)
X = Cl		-0.04 V (rev)	
X = Br		+0.15 V (qr)#	

There is one previous report of an electrochemical study commencing from $[Tc_2Cl_8]^{3-}$. (**27b**) These authors conducted their study in a mixture of 10% by volume 12 M $HCl_{(aq)}$ in absolute ethanol. This solvent choice was made necessary because

qr = quasi-reversible. The potential presented was derived from the acV signal.

$[Tc_2Cl_8]^{3-}$ is more stable in aqueous hydrochloric acid solutions than organic solvents.# An oxidation to $[Tc_2Cl_8]^{2-}$ at +0.14 V on a rotating platinum disk electrode *vs* SCE was reported.## No other processes were cited between -0.15 V and +0.90 V, the limits of their investigation. No previous reports of the voltammetry of $[Tc_2Br_8]^{n-}$ were found.

Previous investigations of the electrochemistry of other $[M_2X_8]^{n-}$ species which are isoelectronic with $[Tc_2X_8]^{2-}$ include, $[Re_2X_8]^{2-}$ (where X = Cl, Br and NCS) and $[Os_2Cl_8]^{0}$ (which is electrogenerated from the starting compound, $[Os_2Cl_8]^{2-}$). A range of electronic states are available for these compounds corresponding to complete vacancy through to complete occupancy of the δ type orbitals, that is from d^3d^3 (no δ electrons for example $[Re_2X_8]^0$ X = Cl, NCS) to d^5d^5 ($\delta^2\delta^{*2}$ for example $[Re_2(NCS)_8]^{4-}$ and $[Os_2Cl_8]^{2-}$).@ While not all of the possible oxidation states were accessible to each $[M_2X_8]^{n-}$ species, $[Tc_2X_8]^{n-}$ is unique in this group of compounds for having only two accessible species, $[Tc_2X_8]^{2-}$ and $[Tc_2X_8]^{3-}$ (all other $[M_2X_8]^{n-}$ species showed at least three).

1.2.3.1 Comparison of the voltammetry of $[Tc_2X_8]^{n-}$ and $[Re_2X_8]^{n-}$

A comparison of the voltammetry observed for $[Tc_2X_8]^{n-}$ and $[Re_2X_8]^{n-}$ is presented in table 1.26.

The table shows that the potential for the $[M_2X_8]^{2-}$ to $[M_2X_8]^{3-}$ reduction is 0.6 V more positive for M = Tc than Re. This difference (Δ Tc-Re) is similar to that observed for a comparison of reduction potentials of $[MX_6]^{n-}$ where M = Tc and Re, and Δ Tc-Re = 0.6 to 0.2 V (chapter 1.3). For the $[MX_6]^{n-}$ species this difference on changing from a second row to third row transition metal has been attributed to the relativistic destabilisation of 5d levels (**18**).

The addition of ethanol rather than the use of pure 12 M HCl was reported to be necessary for instrumental reasons. (**27b**)

correction factor to compare with values in the table would be to add +0.38 V to the SCE data.

@ Complexes in the extremes of the ranges where quadruple bonding is no longer present can be stabilised by rotation about the M-M bond axis, such that a staggered arrangement of the axial ligands X is adopted.

Table 1.26 Comparison of the voltammetry of $[Tc_2X_8]^{n-}$ and $[Re_2X_8]^{n-}$.

	$[M_2Cl_8]^0$ d^3d^3	⇌	$[M_2Cl_8]^{1-}$ d^4d^3	⇌	$[M_2Cl_8]^{2-}$ d^4d^4	⇌	$[M_2Cl_8]^{3-}$ d^5d^4
Tc_2Cl_8		-		-		-0.04 V (rev)	
Re_2Cl_8		+1.88 V (rev)		+1.44 V (rev)		-0.64 V (rev)	
Δ Tc-Re						+0.60 V	
Tc_2Br_8		-		-		+0.15 V (qr)	
Re_2Br_8		-		+1.40 V (rev)		-0.45 (rev)	
Δ Tc-Re						+0.60 V	

In the previous chapter (section 1.1.2.1) a much smaller difference in potential was noted between the reversible reductions of $[Tc_2Br_9]^{1-}$ and $[Re_2X_9]^{1-}$. This was attributed to differences in the nature of the metal-to-metal interactions in these species offsetting the factors which contribute to this difference between second and third row transition metals. Therefore, the 0.6 V difference observed here for $[M_2X_8]^{n-}$ species is consistent with $[Tc_2X_8]^{n-}$ maintaining similar metal-metal bonding properties to those which were deduced for $[Re_2X_8]^{n-}$.

As mentioned earlier, when the oxidation of $[Re_2X_8]^{2-}$ to $[Re_2X_8]^{1-}$ is performed in the presence of free halide, $[Re_2X_9]^{n-}$ is formed as the n = 1 anion at the prevailing potential. Hence it was of interest to determine what potential might be necessary to generate the equivalent $[Tc_2X_8]^{1-}$. Assuming an increase of 0.6 V to the observed potentials of $[Re_2X_8]^{n-}$ a potential of around +2 V would be predicted for the oxidation $[Tc_2X_8]^{2-}$ to $[Tc_2X_8]^{1-}$. No process was observed at this potential or upto the solvent limit (+ 2.5 V) of our investigations for either $[Tc_2Cl_8]^{2-}$ or $[Tc_2Br_8]^{1-}$.

1.2.4 The UV-visible spectra of $[Tc_2X_8]^{n-}$ (where n = 2, 3)

The UV-visible electronic absorption spectra were recorded for $[Tc_2X_8]^{2-}$ and $[Tc_2Cl_8]^{3-}$ in 0.5 M $TBABF_4/CH_2Cl_2$ at -60°C during the course of this thesis (see figure 1.27 and tables 1.28 and 1.29). The spectrum of $[Tc_2Cl_8]^{3-}$ was obtained using spectro-electrochemistry and reversibly reducing $[Tc_2Cl_8]^{2-}$ *in situ*.. No such reduction was successful for $[Tc_2Br_8]^{2-}$, as all attempts irreversibly generated a spectrum recognisable as $[TcBr_6]^{2-}$.

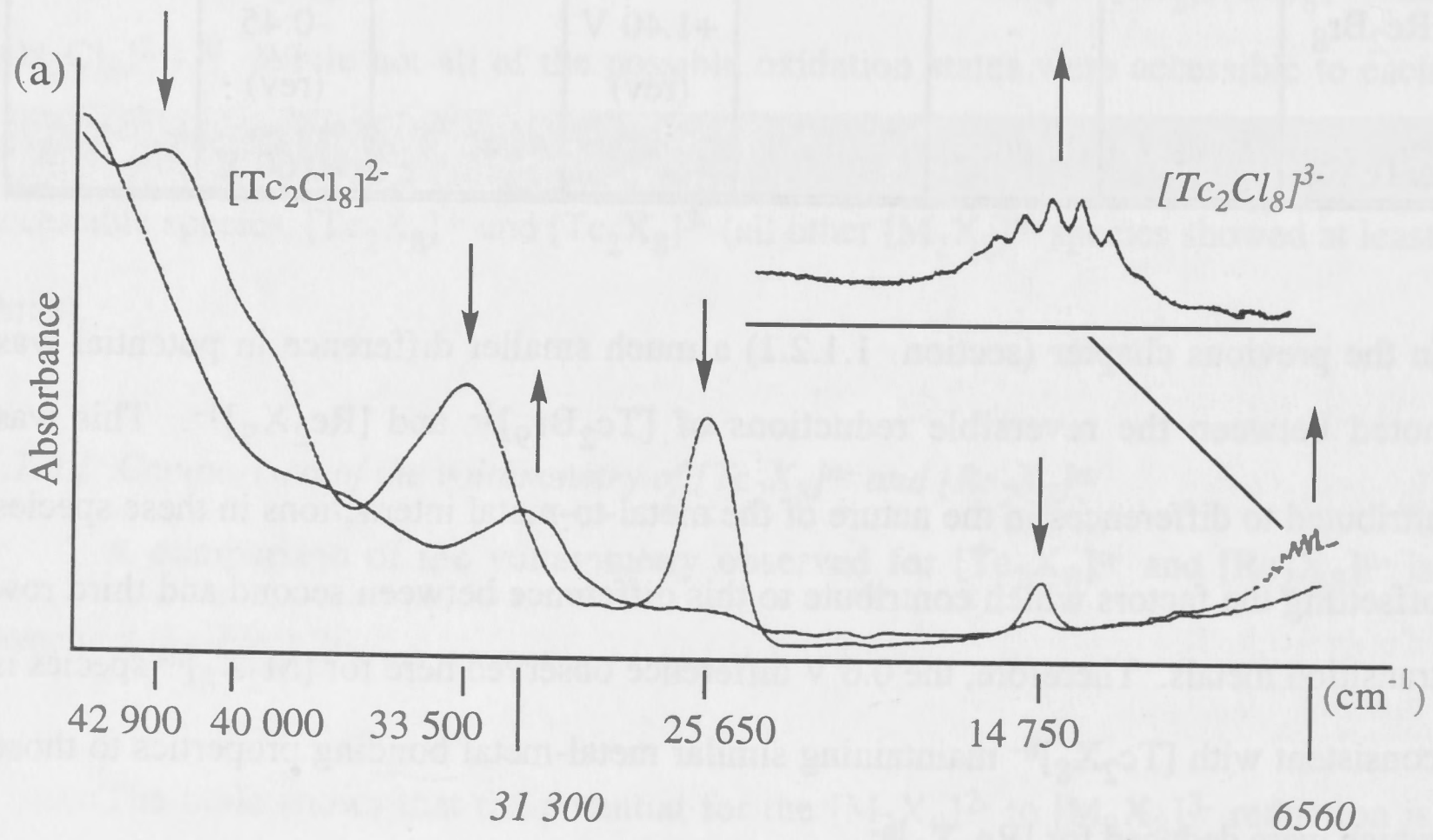

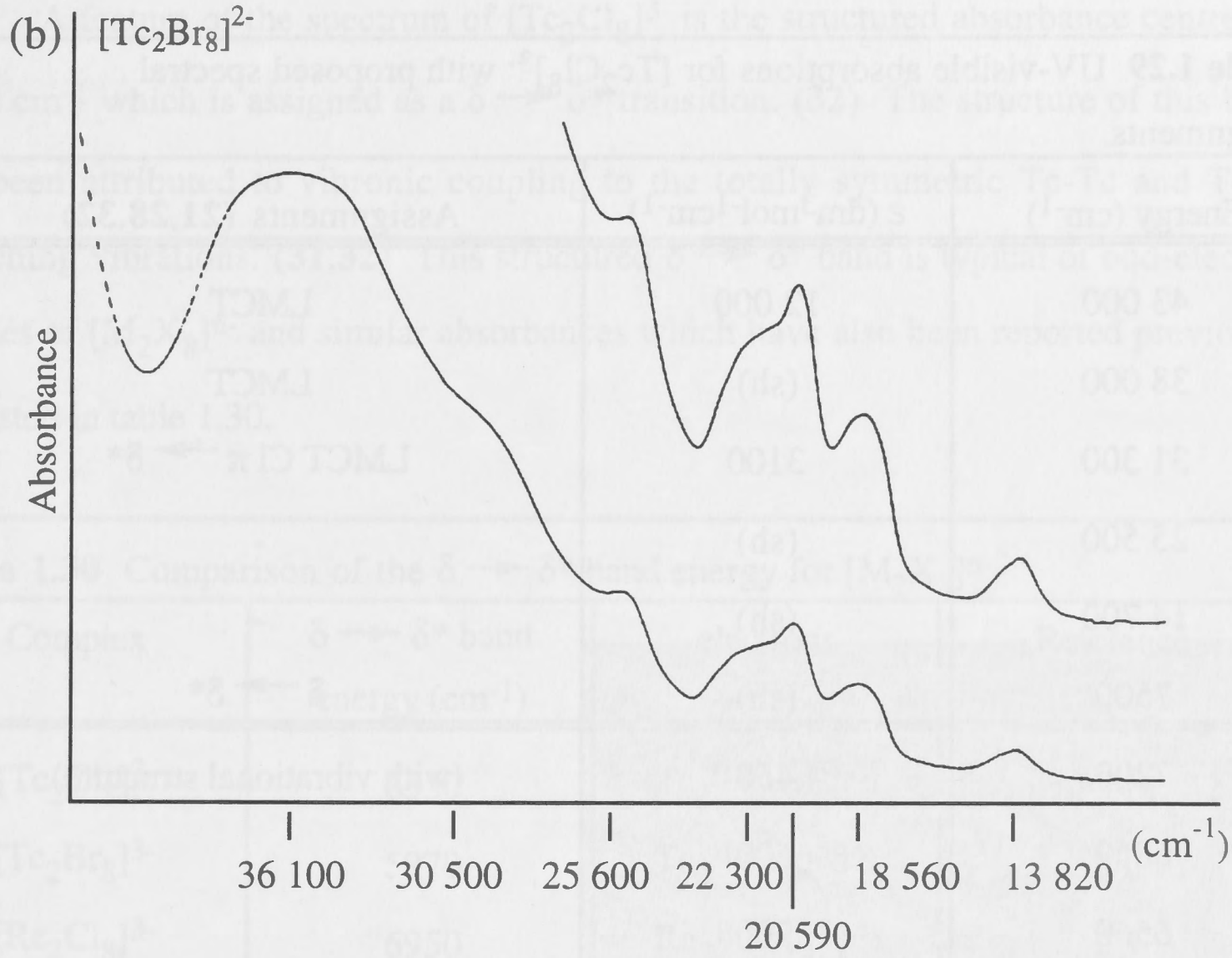

Figure 1.27 *Showing the UV-visible absorption spectra of (a) the reduction of* $[Tc_2Cl_8]^{2-}$ *(with wavenumbers in normal print) to* $[Tc_2Cl_8]^{3-}$ *(in italic print). The expansion of the structured absorption centred at 6560 cm^{-1} is at double the width along the x axis. (b)* $[Tc_2Br_8]^{2-}$ *as recorded in* CH_2Cl_2.

Table 1.28 UV-visible electronic absorption spectra of $[Tc_2X_8]^{n-}$ (X= Cl and Br) (n = 2 and 3) in CH_2Cl_2 at -60^{0}C.

$[Tc_2Cl_8]^{2-}$		Assignment	$[Tc_2Br_8]^{2-}$	
Energy (cm^{-1})	ε (dm^{3}mol^{-1}cm^{-1})		Energy (cm^{-1})	ε$^{\#}$ (dm^{3}mol^{-1}cm^{-1})
42 900	11300	LMCT	36 100	
40 000	(sh)	-	30 500	(sh)
33 500	6100	LMCT	25 600	
25 650	5300	X π → δ*	20 590	
			18 560	
14 750	990	δ → δ*	13 820	

$^{\#}$ The molar extinction coefficients were not recorded for the $[Tc_2Br_8]^{2-}$ species.

Table 1.29 UV-visible absorptions for $[Tc_2Cl_8]^{3-}$ with proposed spectral assignments.

Energy (cm^{-1})	ε ($dm^3mol^{-1}cm^{-1}$)	Assignments (**21**,**28**,**32**)
43 000	12 000	LMCT
38 000	(sh)	LMCT
31 300	3100	LMCT Cl $\pi \rightarrow \delta^*$
25 500	(sh)	-
14 700	(sh)	-
7500	(sh)	$\delta \rightarrow \delta^*$
7200	450	(with vibrational structure)
6860	600	
6560	700	
6230	700	
5920	500	
5600	(sh)	

1.2.4.1 Spectrum of $[Tc_2Cl_8]^{3-}$

The spectrum of $[Tc_2Cl_8]^{3-}$ (shown in figure 1.27a) has been previously described in detail and assigned with the aid of Xα calculations. (**28**,**32**) Those proposed assignments which correspond to bands observed here are presented in table 1.29. It is likely the extra weak absorptions at 25 500 and 14 700 cm^{-1} recorded here may actually be due to the presence of some unreduced $[Tc_2Cl_8]^{2-}$.

The absorptions above 31 000 cm^{-1} are associated with charge transfer from the $\{Cl_8\}$ array into Tc based levels. More specific assignments of these absorptions have not been given due to the presence of a number of transitions which could contribute to the bands. An exception to this is the band at 31 300 cm^{-1} which is assigned as a transition from $4e_g$ (a Cl π-type level) into δ*. (**32**)

A feature of the spectrum of $[Tc_2Cl_8]^{3-}$ is the structured absorbance centred at 6550 cm^{-1} which is assigned as a $\delta \longrightarrow \delta^*$ transition. (**32**) The structure of this band has been attributed to vibronic coupling to the totally symmetric Tc-Tc and Tc-Cl stretching vibrations. (**31**,**32**) This structured $\delta \longrightarrow \delta^*$ band is typical of odd-electron species of $[M_2X_8]^{n-}$ and similar absorbances which have also been reported previously are listed in table 1.30.

Table 1.30 Comparison of the $\delta \longrightarrow \delta^*$ band energy for $[M_2X_8]^{n-}$.

Complex	$\delta \longrightarrow \delta^*$ band energy (cm^{-1})	electrons	Reference
$[Tc_2Cl_8]^{3-}$	6550	$Tc_2^{II,III}$ (d^5d^4)	this work, **32**
$[Tc_2Br_8]^{3-}$	5970	$Tc_2^{II,III}$ (d^5d^4)	**31**
$[Re_2Cl_8]^{3-}$	6950	$Re_2^{II,III}$ (d^5d^4)	**23**
$[Re_2Br_8]^{3-}$	7200	$Re_2^{II,III}$ (d^5d^4)	**17**
$[Os_2Cl_8]^{1-}$	4600	$Os_2^{III,IV}$ (d^5d^4)	**33**
$[Re_2Cl_8]^{1-}$	4650	$Re_2^{III,IV}$ (d^4d^3)	**34**

In general the similar nature of this $\delta \longrightarrow \delta^*$ band and the charge transfer manifold in $[Tc_2X_8]^{3-}$ and $[Re_2X_8]^{3-}$ is indicative of the similar metal-metal bonding within these species.

1.2.4.2 Spectrum of $[Tc_2Cl_8]^{2-}$

This similarity in the spectra of $[M_2X_8]^{3-}$ (M = Tc and Re) was also noted in the spectra of the $[M_2X_8]^{2-}$ species. One of the most notable differences in the spectra of the oxidised species is the increase in energy and loss of structure in the $\delta \longrightarrow \delta^*$ band. The energy of this transition was observed at 14 750 cm^{-1} in $[Tc_2Cl_8]^{2-}$ and 13 820 cm^{-1} in $[Tc_2Br_8]^{2-}$. These band energies (including the ~ 900 cm^{-1} red shift for X = Br as compared to X = Cl) are consistent with those observed for $[Re_2X_8]^{2-}$ where the equivalent band is at 14 700 cm^{-1} (X = Cl) (**23**) and 14 000 cm^{-1} (X = Br) (**15**). This marked increase in energy has been attributed to contributions to the excitation

energy from increased electron correlation effects within the even electron species, rather than any significant change in the actual energy gap between the δ and δ* levels. (**21**,**35**)

The charge transfer band at 25 650 cm^{-1} which was identified as the $4e_g \longrightarrow \delta^*$ transition in the spectrum of $[Tc_2Cl_8]^{3-}$ was noted to move to higher energy in $[Tc_2Cl_8]^{2-}$ (31 300 cm^{-1}). This 5650 cm^{-1} change in energy between the same $4e_g$ and $2b_{2g}$ levels is indicative of a destabilisation of the metal based levels relative to the halide based ones, in the reduced species $[Tc_2X_8]^{3-}$. A similar 5200 cm^{-1} blue shift was observed for the equivalent band in the spectra of $[Re_2Cl_8]^{2-}$ upon reduction to $[Re_2Cl_8]^{3-}$. The equivalent bands in the spectra of $[Tc_2Br_8]^{2-}$ and $[Re_2Br_8]^{2-}$ are observed to be split by 2000 and 2600 cm^{-1} (**15**) respectively. This splitting has been attributed previously to spin-orbit coupling. (**21**)

The studies described in this section indicate that there is a similar quadruple metal-metal bond within $[Tc_2X_8]^{n-}$ and $[Re_2X_8]^{n-}$. The compounds of $[Tc_2X_8]^{n-}$ were further shown to have fewer accessible oxidation states and different relative stabilities compared to $[Re_2X_8]^{n-}$ analogues. These conclusions are in stark contrast to those presented for $[Tc_2Br_9]^{1-}$, where the metal-to-metal interaction was observed to be different compared to analogous rhenium systems and that this difference was important in comparing the properties of these compounds. In the last part of this section we will combine these observations on $[M_2X_8]^{n-}$ and $[M_2X_9]^{n-}$ species to describe attempted syntheses of $[Tc_2Cl_9]^{n-}$.

1.2.5 Attempts to synthesise $[Tc_2Cl_9]^{n-}$

$[Re_2Cl_9]^{1-}$ can be synthesised from $[Re_2Cl_8]^{2-}$ by direct chlorination in CH_2Cl_2 or CH_3CN (**24**), or alternatively by electrochemical procedures which involve the initial oxidation of $[Re_2Cl_8]^{2-}$ to $[Re_2Cl_8]^{1-}$ at +1.44 V (or further to $[Re_2Cl_8]^{0}$ at +1.88 V) in the presence of TBACl. Both oxidations have been reported to form the nonachloride which is expected to be present as $[Re_2Cl_9]^{1-}$ at the prevailing potential (**23**).

Similar reactions were attempted in this thesis as possible routes to $[Tc_2Cl_9]^{1-}$. Firstly, Cl_2 in the form of the solid chlorinating agent[#] , ~~Cl-Ph-ICl$_2$~~ p-ClC$_6$H$_4$ICl$_2$, (**36**) was added to a CH_2Cl_2 solution of $[Tc_2Cl_8]^{2-}$. This reaction was carried out on a preparative scale and on a smaller scale suitable for direct monitoring by UV-visible absorption spectroscopy. During the UV-visible monitoring the solution was cooled to -50°C and the ~~Cl-Ph-ICl$_2$~~ p-ClC$_6$H$_4$ICl$_2$ was added initially in excess (and on a separate occasion in a stoichiometric amount). The reaction mixture was then allowed to warm gradually to room temperature, with spectra being recorded at 5°C intervals. There was no reaction observed until -20°C when the chlorinating agent released Cl_2. The only product detected was $[TcCl_6]^{2-}$.

In a second set of related experiments a bulk electro-chemical cell was used to apply an oxidising potential of +1.5 V to a CH_2Cl_2 solution containing $(TBA)_2[Tc_2Cl_8]$ and TBACl.[##] As no evidence for the oxidation to $[Tc_2Cl_8]^{1-}$ under these conditions had been observed in the voltammetric studies described earlier, the potential applied was the highest possible before background current due to the presence of TBACl overloaded the cell. The colour of the reaction mixture changed from its original green to yellow. A yellow colour is characteristic of $[TcCl_6]^{2-}$ and this observation was confirmed by voltammetry and UV-visible spectroscopy.

Previous studies (**24**) of the successful $[Re_2Cl_8]^{2-}$ to $[Re_2Cl_9]^{1-}$ conversion noted the absence of $[ReCl_6]^{2-}$ from the products observed. It was suggested that the reaction proceeds by the removal of the δ electrons from $[Re_2Cl_8]^{2-}$, thus allowing rotation about the metal-metal bond, while the σ and π bonds remain, thus holding the metal-metal bond intact and promoting dimer formation over that of the monomer. (**24**) In the case of the technetium species of interest here, it may be that the potentially weaker technetium-to-technetium interaction (as compared to that between rhenium centres in $[Re_2Cl_9]^{1-}$) in the desired $[Tc_2Cl_9]^{n-}$ product (as predicted by density functional

---

[#] The chlorinating agent (**36**) was chosen over Cl_2 gas because of the ease at which the amount of Cl_2 added to the reaction can be controlled. It has been used successfully to convert $[Re_2Cl_8]^{2-}$ to $[Re_2Cl_9]^{1-}$. (**37**)

[##] It should be noted that $[Tc_2Cl_8]^{2-}$ is stable at room temperature in a CH_2Cl_2 solution containing excess (TBA)Cl for a period of hours.

calculations and deduced for the $[Tc_2Br_9]^{1-}$ species) would then be insufficient to stabilise the face-sharing dimer, such that further reaction through to the $[TcCl_6]^{2-}$ monomer proceeds in preference.

At the reducing end of the potential scale, the reduction of $[Re_2Cl_9]^{2-}$ to $[Re_2Cl_9]^{3-}$ in CH_2Cl_2 at room temperature, occurs with concurrent expulsion of one halide to give $[Re_2Cl_8]^{2-}$ (**23**). Similarly, if the reduction of $[Re_2Cl_9]^{2-}$ is conducted at low temperature (208 K) there is evidence for the presence of unstable $[Re_2Cl_9]^{4-}$ which also expels one chloride to give $[Re_2Cl_8]^{3-}$ at the prevailing potential (**23**). The equivalent experiments have been successfully repeated for the $[Re_2Br_9]^{2-}$ bromide analogues.(**17**)

The same conversions were not observed for $[Tc_2Br_9]^{n-}$ however. As described in chapter 1.1, solutions of $[Tc_2Br_9]^{3-}$ electro-generated at -60°C and allowed to warm to room temperature showed a direct conversion to $[TcBr_6]^{2-}$. It may also be the case here that the success of the conversion from $[Re_2X_9]^{n-}$ to $[Re_2X_8]^{n-}$ lies in the presence of a metal-metal bond being already present in the former (**8**) such that upon loss of one halide, rearrangement to $[Re_2X_8]^{n-}$ is favoured over monomer formation. In contrast, the absence of a metal-metal bond in $[Tc_2Br_9]^{n-}$ appears to promote monomer formation.

Another reaction attempted was the formation of the nonahalide dimer direct from $[TcCl_6]^{2-}$. This was based on the successful preparation of $[Tc_2Br_9]^{1-}$ which involved refluxing $[TcBr_6]^{2-}$ in trifluroacetic acid. (**1**) If this reaction mixture is not heated, and the cation is carefully chosen to ensure immediate precipitation upon reaction, that is, using TEA^+, then $(TEA)_2[Tc_2Br_{10}]$ is the resultant product (**38**). These $[M_2X_{10}]^{n-}$ dimers have been considered to be intermediates in the formation of $[M_2X_9]^{n-}$ (**2**). The equivalent reaction of $(TEA)_2[TcCl_6]$ in TFA did produce a likely intermediate in $[Tc_2Cl_9]^{n-}$ preparation, $(TEA)_2[Tc_2Cl_{10}]$ (yellow), upon stirring for half an hour at room temperature (**38**). However, upon heating the final product (as identified by UV-visible spectroscopy) was a red solution which appeared consistent with the formation of

polymeric, red $[TcCl_4]_n^{n-}$ (**39**). The $[M_2X_{10}]^{2-}$ dimers have been previously identified as intermediates in the formation of $[M_2X_9]^{1-}$ dimers of osmium (**2**)#.

A possible explanation for the failure of this reaction to form $[Tc_2Cl_9]^{n-}$ following the formation of $[Tc_2Cl_{10}]^{2-}$ may be that the natural bridging angle of the chloride ligands and the shorter Tc-X-Tc bond lengths, in $[Tc_2Cl_9]^{n-}$ would force the technetium metal centres to be positioned more closely together than in $[Tc_2Br_9]^{n-}$. At this point a Tc-Tc bond might form to stabilise the complex, alternatively the two Tc^{IV} metal centres could remain non-interacting but this may generate repulsive forces sufficient to drive the complex toward monomer formation. It is possible that such repulsive forces would be greater in $[Tc_2Cl_9]^{n-}$ than in the non-interacting $[Cr_2Cl_9]^{n-}$ (which does exist) due to the higher positive charge for the technetium centre M = Tc^{IV} than that of M = Cr^{III}.

It should be noted that dimers of the type $[M_2X_{10}]^{n-}$ do not possess a direct metal-metal bond, rather they are joined by two bridging halide atoms in an edge-sharing arrangement.

Chapter 1.3: Physicochemical studies on technetium hexahalide complexes, $(TBA)_2[TcX_6]$ (where X = Cl or Br)

A study of the electrochemical and UV-visible electronic absorption properties of both $[TcCl_6]^{2-}$ and $[TcBr_6]^{2-}$ was important within the context of this thesis for two reasons. Firstly, because a study of the monomeric octahedral arrangement assists with the understanding of the dimeric species. Secondly, because the attempts to prepare $[Tc_2X_9]^{n-}$ from $[Tc_2X_8]^{n-}$ by the addition of (TBA)X (X = Cl, Br) all produced $[TcX_6]^{2-}$, so it became important to be able to identify and distinguish UV-visible absorption spectroscopic and voltammetric responses due to monomeric $[TcX_6]^{2-}$ from other dimeric reaction products.

1.3.1 UV-visible electronic absorption spectra of $[TcX_6]^{2-}$

The UV-visible electronic absorption spectra of $(TBA)_2[TcCl_6]$ and $(TBA)_2[TcBr_6]$ are in good agreement with literature reports# (**40**,**41**). They were recorded here at room temperature in CH_2Cl_2 and are shown in figure 1.31 and table 1.32. The spectrum for each complex proved to be easily recognisable during other reactions which inadvertently produced $[TcX_6]^{2-}$, such as the preparation and electrochemical investigation of the dimers.

UV-Vis spectral absorbances at room temperature, literature values for $[TcCl_6]^{2-}$ in CH_2Cl_2: 41 900, 38 000, 32 175, 29 150, 25 800 cm^{-1}(**40**)
$[TcBr_6]^{2-}$ in 2.0M HBr/3.0M NaBr: 26 000, 22 500(5700) cm^{-1} ($dm^3mol^{-1}cm^{-1}$) (**41**)

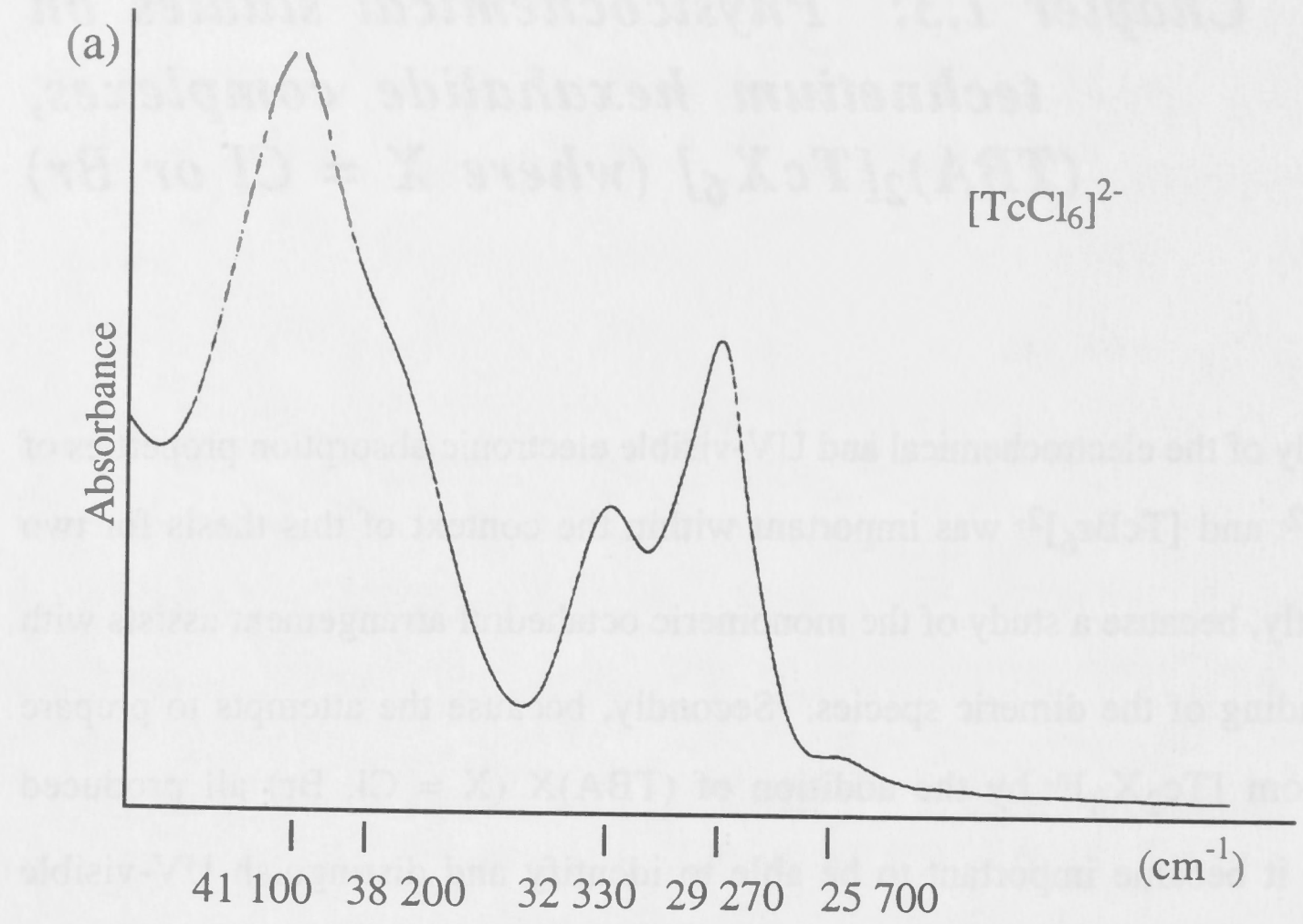

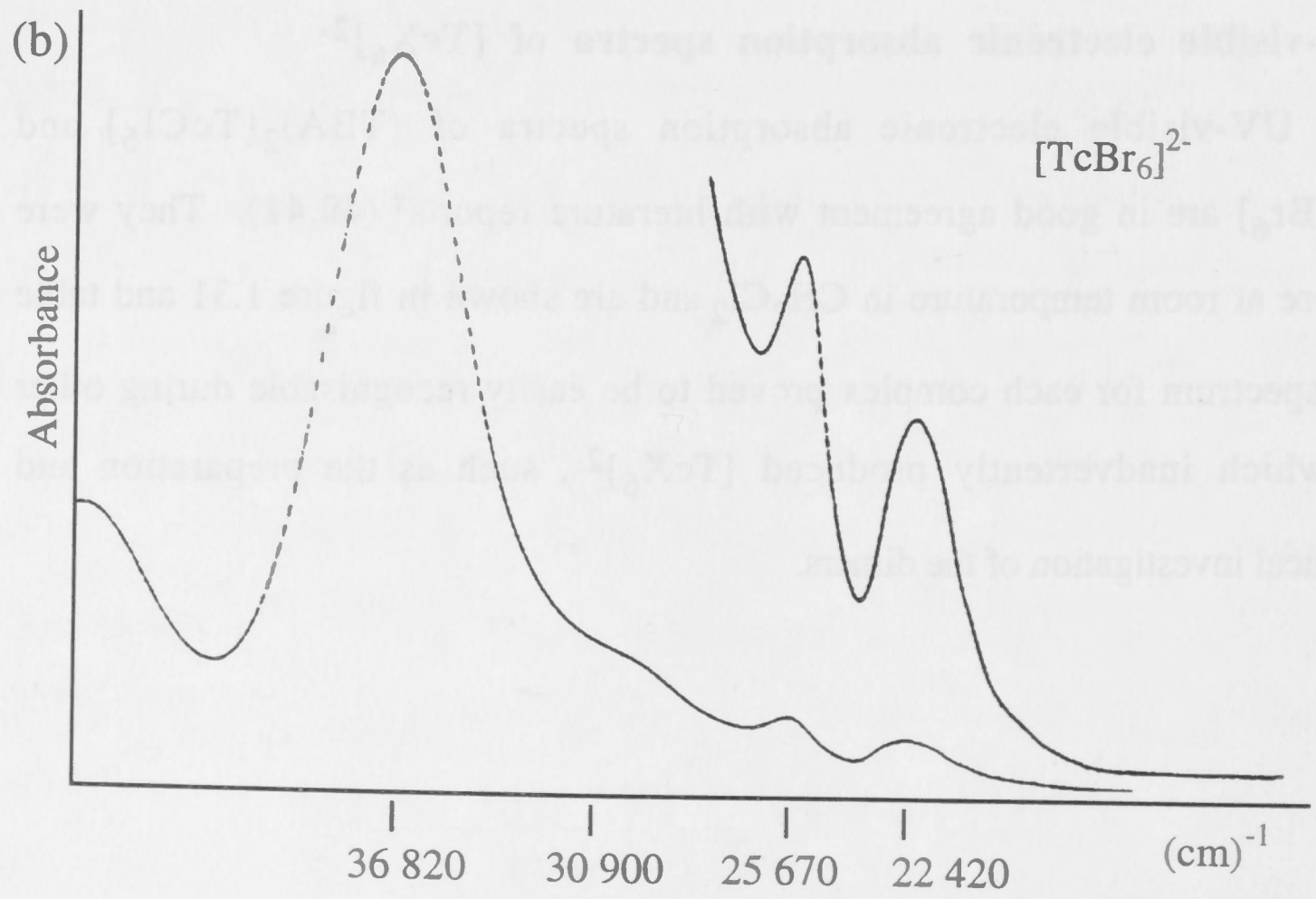

Figure 1.31 *UV-visible absorption spectra of (a) $[TcCl_6]^{2-}$ and (b) $[TcBr_6]^{2-}$ recorded in CH_2Cl_2.*

Table 1.32 UV-visible electronic absorption spectra $(TBA)_2[TcX_6]$ (X= Cl and Br) in CH_2Cl_2 at room temperature.

$[TcCl_6]^{2-}$		Assignments	$[TcBr_6]^{2-}$	
Energy (cm^{-1})	ε ($dm^3mol^{-1}cm^{-1}$)	(type of transition)	Energy (cm^{-1})	ε ($dm^3mol^{-1}cm^{-1}$)
41 100	16 000	$3t_{1u} \longrightarrow 3e_g$ (X π/σ → Tc σ*)	36 820	19 100
38 200	sh	$2t_{1u} \longrightarrow 2t_{2g}$ (X π/σ → Tc π*)	30 200	sh
32 330	6200	$1t_{2u} \longrightarrow 2t_{2g}$ (X π → Tc π*)	25 670	8300
29 270	10 200	$3t_{1u} \longrightarrow 2t_{2g}$ (X π/σ → Tc π*)	22 420	5600
25 700	sh	$1t_{1g} \longrightarrow 2t_{2g}$ (X π → Tc π*)	19 500	sh

The spectra of $[TcCl_6]^{2-}$ and $[TcBr_6]^{2-}$ are similar, in that they both possess two major absorption regions. The first is characterised by intense absorbances above 38 000 cm^{-1} in $[TcCl_6]^{2-}$ and above 30 000 cm^{-1} in $[TcBr_6]^{2-}$. The second region contains multi-component absorbances below 33 000 and 26 000 cm^{-1} for $[TcCl_6]^{2-}$ and $[TcBr_6]^{2-}$ respectively. The general red shift of 7000 to 8000 cm^{-1} upon changing X = Cl to Br for both absorbance regions is indicative of both these regions being dominated by transition processes involving the halide ligands. The extent of the red shift is associated with the difference in optical electro-negativity of chloride as compared to bromide (**22**).

The spectrum of $[TcCl_6]^{2-}$ has been previously assigned in general terms on the basis of assignments for the spectra of the isoelectronic (d^3) $[ReCl_6]^{2-}$ and $[RuCl_6]^{1-}$ species. (**42, 43**) Based on these studies both regions of the spectrum of $[TcCl_6]^{2-}$ can

be assigned as follows. The 22 000 - 35 000 cm^{-1} region is attributed to charge transfer into the metal acceptor orbital (*i.e.* Cl-based levels into Tc-based t_{2g} level). The region above 35 000 cm^{-1} is assigned as transitions into the higher lying technetium based e_g based level, or to transitions from lower energy halide orbitals into technetium t_{2g} based level. The equivalent assignments are also proposed for the corresponding regions in the spectrum of $[TcBr_6]^{2-}$.

Recent theoretical studies using density functional calculations (SCF-Xα-SW) (**21**) on a series of $[MX_6]^{n-}$ complexes lend further support to these general assignments. These studies show that the higher energy region of the spectrum is most likely to be dominated by charge transfer into the e_g technetium based levels. Transitions from lower lying halide levels into t_{2g} are most likely to be associated with the low intensity shoulder at 38 200 (Cl) and 30 200 (Br) cm^{-1}. The assignments presented in table 1.32 are derived from that study (**21**). The orbitals are described according to their orientation with respect to the Tc-X bond.

1.3.2 Voltammetry of $[TcX_6]^{2-}$

Previous reports of the electrochemistry of $[TcX_6]^{2-}$ complexes have been undertaken in acetonitrile (**44**) and acidic aqueous solution (**45**). In CH_3CN with (TBA)$[ClO_4]$ as the electrolyte at room temperature and using a rotating Pt disk and dropping mercury electrode, a large number of unassigned irreversible signals were observed, (**44**) which we suspect are possibly due to solvent coordination or contamination by oxo derivatives. In concentrated 2.0M HX/2.0M NaX at room temperature, reversible electrochemistry was observed (**45**) but the $E_{1/2}$ values obtained were a function of complex equilbria involving $[TcX_6]^{2-}$ and hydrolysed species thereof, and so are of limited value in gaining an appreciation of how $[TcX_6]^{2-}$ will behave under the conditions of main interest here.#

In water and even mildly acidic media $[TcX_6]^{2-}$ hydrolyses instantly to the insoluble $TcO_3.xH_2O$ (X = Br faster than X = Cl) and no electrochemistry of $[TcX_6]^{n-}$ can be observed under these conditions.(**45**)

There are no previous reports of the electrochemistry of $(TBA)_2[TcX_6]$ in CH_2Cl_2 / $TBAPF_6$ at reduced temperatures. These data were of vital interest within the context of this thesis because the same conditions were used when studying metal-metal bonded dimers and since it was important to be able to recognise any rogue monomeric species which may have been generated during the course of those investigations. To that end, the electrochemistry of $(TBA)_2[TcX_6]$ was recorded under the aforementioned conditions and is presented in figure 1.33 and table 1.34 below.#

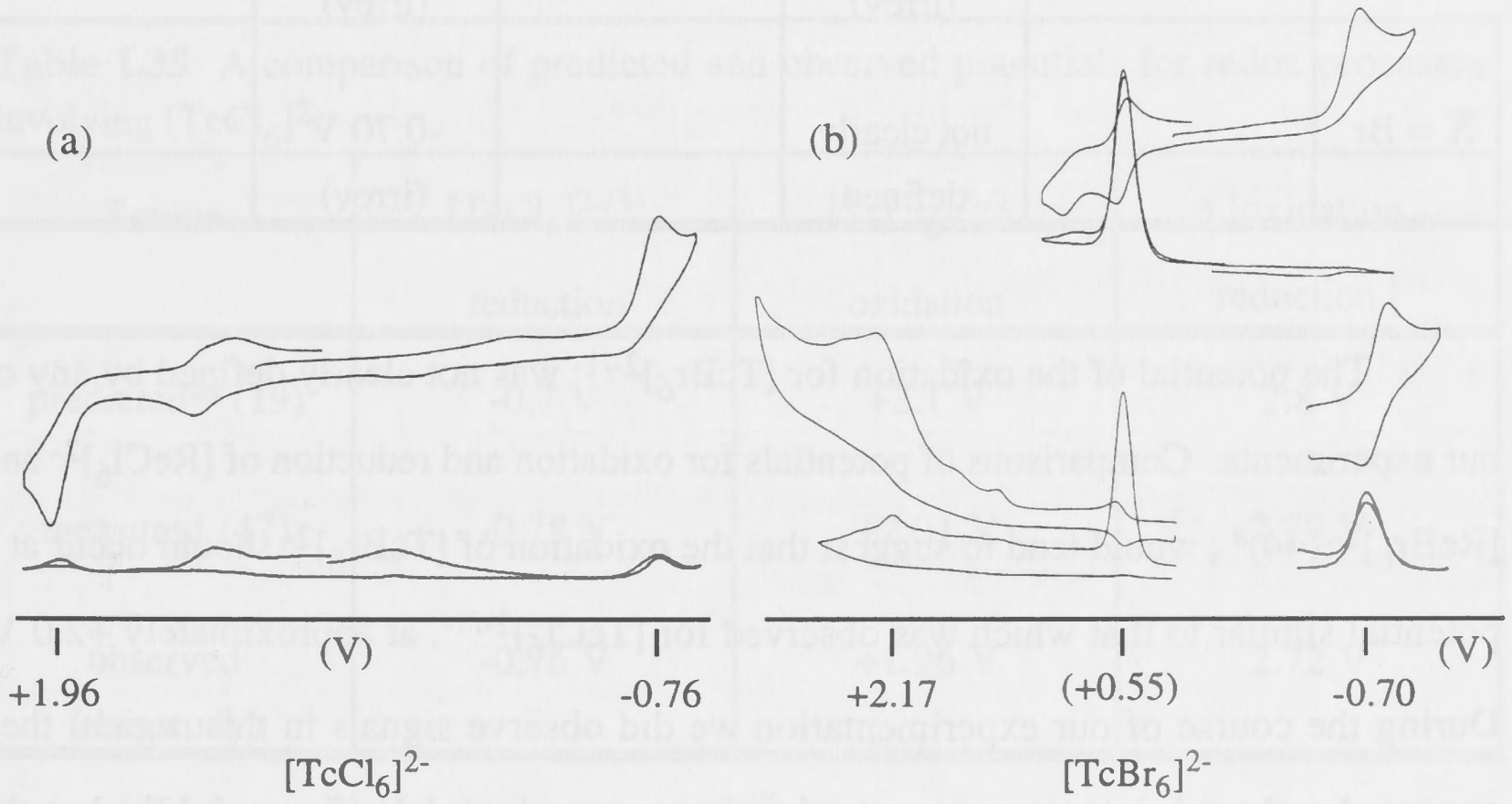

Figure 1.33 *The cyclic and alternating cyclic voltammetry of (a) $[TcCl_6]^{2-}$ in 0.5 M $TBAPF_6/CH_2Cl_2$ and (b) $[TcBr_6]^{2-}$in 0.5 M $TBAPF_6/CH_2Cl_2$ with the increased reversibility of the reduction at -0.70 V observed in the presence of a vast excess of (TBA)Br at room temperature. The measurements for $[TcBr_6]^{2-}$ also show the ferrocene oxidation at +0.55 V.*

The irreversible cyclic voltammetry was linked to the appearance of signals due to the oxidation of the free ligands $X^{1-/0}$ within the electrochemistry of both $[TcCl_6]^{2-}$ and $[TcBr_6]^{2-}$. One other feature of note is that the reduction signal appears to be more reversible in the acV than the CV mode. It is likely that this phenomen is related to the faster time domain of the acV experiment and that very fast CV experiments may also

---

Ferrocene was unreliable as an internal reference for these data because ferrocene reacts with $[TcX_6]^{1-}$ making it difficult to observe the $[TcX_6]^{2-/1-}$ oxidation. As a result these E^0 data were also referenced against (TBA)$[IrCl_6]$ which has a reduction at +0.06 V and an oxidation at +1.79 V *vs* ferrocene at +0.55 V.

show some reversibility. It is also suggestive that reduced species, $[TcX_6]^{3-}$ was stable for only a very short time, and therefore may prove difficult to prepare synthetically.

Table 1.34 Voltammetry of $[TcX_6]^{n-}$ as recorded in 0.5 M $TBABF_4/CH_2Cl_2$ at -60°C.

	$[Tc^{V}X_6]^{1-}$ d^2	←	$[Tc^{IV}X_6]^{2-}$ d^3	→	$[Tc^{III}X_6]^{3-}$ d^4
X = Cl		+1.96 V (irrev)		-0.76 V (irrev)	
X = Br		not clearly defined		-0.70 V (irrev)	

The potential of the oxidation for $[TcBr_6]^{2-/1-}$ was not clearly defined by any of our experiments. Comparisons of potentials for oxidation and reduction of $[ReCl_6]^{2-}$ and $[ReBr_6]^{2-}$ (**44**)# , would tend to suggest that the oxidation of $[TcBr_6]^{2-}$ should occur at a potential similar to that which was observed for $[TcCl_6]^{2-/1-}$, at approximately +2.0 V. During the course of our experimentation we did observe signals in this region, they appeared as broad, intense waves starting from around +1.4 V (figure 1.33b) but the nature of the signal tends to suggest that under these conditions and when bound to $[TcBr_6]^{2-}$ the bromide ligand may not be entirely innocent at this potential, that is, that bromide ligand based redox processes may be occurring.

The observed signals for the voltammetry of $[TcX_6]^{2-}$ were never found to be reversible despite the use of vacuum line procedures, a specially designed electrochemical cell (**46**), reduced temperatures and the presence of free halide. These observations are in contrast to previously reported results of reversible voltammetry for $[ReCl_6]^{n/n-1}$ couples (where n = -1, -2) analysed under the same conditions. (**16**)

While the electrochemistry of $(TBA)_2[TcBr_6]$ has not been previously reported under these conditions, the $E_{1/2}$ for both the reduction and the oxidation of $[TcCl_6]^{2-}$

The magnitude of the difference between corresponding potentials for chloride and bromide species of $[ReX_6]^{n-}$ ranges from 0 to 0.4 V. (**44**)

have been predicted (**19**) and then later, measured (**47**) by Heath and co-workers. Their predictions were based on the periodic trends observed following an extensive study of $[MX_6]^{2-/3-}$ and $[MX_6]^{2-/1-}$ redox couples along the second and third row transition elements#, and are compared to the values observed in this thesis in table 1.35 below. Despite the irreversibility of the observed cyclic voltammetric signals (figure 1.33), it is apparent that the values are of reasonable agreement for both the oxidative and reductive processes.

Table 1.35 A comparison of predicted and observed potentials for redox processes involving $[TcCl_6]^{2-}$.

Source	$[TcCl_6]^{2-/3-}$ reduction	$[TcCl_6]^{2-/1-}$ oxidation	Δ |oxidation - reduction|
predicted## (**19**)	-0.7 V	+2.1 V	2.8 V
measured (**47**)	-0.78 V	+2.01 V	2.79 V
observed (this study)	-0.76 V	+1.96 V	2.72 V

Further investigation of this extensive range of redox data reported for $[MX_6]^{n-}$ species (**19**) and including the potentials recorded here for $[TcX_6]^{n-}$ provided useful insights for the analysis of the voltammetry of $[M_2X_9]^{n-}$ species which was presented in section 1.1.2. Firstly, the differences in potential for equivalent redox processes of $[MX_6]^{n-}$ where M = a second row transition metal, as opposed to third row transition metal, were observed and are tabulated in table 1.36. This table provides an indication of the magnitude of the difference (an average of 0.6 V) which might be induced by the change of metal, all other things being equal. These differences can be attributed to relativistic effects (**18**). Other factors such as spin-orbit coupling can also be important. Spin-orbit coupling exerts its greatest influence on the d^3/d^4 couple (**19**) where it contributes to the small value for the difference between second and third row potentials

---

This study extended from Zr to Pd and Hf to Pt.

These values have been adjusted from the original report (where the oxidation of ferrocene was taken to be +0.48 V) so that both sets of data are now referenced to the oxidation of ferrocene at +0.55 V.

Table 1.36 Comparisons of second and third row reduction potentials of $[MCl_6]^{n-}$.

M =	d^0/d^1	d^1/d^2	d^2/d^3	d^3/d^4	d^4/d^5	d^5/d^6
	$M^{IV/III}$					
Zr	-2.46					
Hf	-3.0					
Δ Zr - Hf	+0.6					
	$M^{V/IV}$	$M^{IV/III}$				
Nb	+0.15	-1.25				
Ta	-0.48	-1.98				
Δ Nb - Ta	+0.63	+0.73				
	$M^{VI/V}$	$M^{V/IV}$	$M^{IV/III}$			
Mo	+2.27	+1.12	-0.21			
W	+1.66	+0.47	-1.08			
Δ Mo - W	+0.61	+0.65	+0.87			
		$M^{VI/V}$	$M^{V/IV}$	$M^{IV/III}$		
Tc			+1.96	-0.76		
Re		+2.42	+1.40	-1.05		
Δ Tc - Re		-	+0.56	+0.21		
				$M^{V/IV}$	$M^{IV/III}$	$M^{III/II}$
Ru				+1.68	+0.02	
Os				+1.35	-0.57	-1.93
Δ Ru - Os				+0.33	+0.59	-
					$M^{V/IV}$	$M^{IV/III}$
Rh					+2.50	+0.79
Ir					+1.81	+0.05
Δ Rh - Ir					+0.69	+0.74
						$M^{V/IV}$
Pd						+2.99
Pt						+2.37
Δ Pd - Pt						+0.62

for that electron configuration. These values for $[MX_6]^{n/n-1}$ can serve as a guide as to what might be expected from similar comparisons involving $[M_2X_9]^{n-}$. A direct transfer from monomer to dimer, however, may not be possible due to the added complication that changes in the nature of the metal-metal bond within $[M_2X_9]^{n-}$ are likely to have a significant impact on the result obtained when comparing electrode potentials of the second and third rows.

Secondly an analysis of the changes in potential within each complex and compared along the second (table 1.37) and third (table 1.38) rows is presented. These comparisons indicate that in general, $\Delta_{0,1,3,4}$ is of a fairly constant magnitude when the successive addition of electrons involves the same type of orbital and have the same the spin orientation. Δ_2 is noticeably larger than the other $\Delta_{0,1,3,4}$ measurements. On this occasion the two electrons are entering different environments. The first electron half fills the t_{2g} levels and the second electron is the first to undergo spin pairing as is illustrated in figure 1.39.

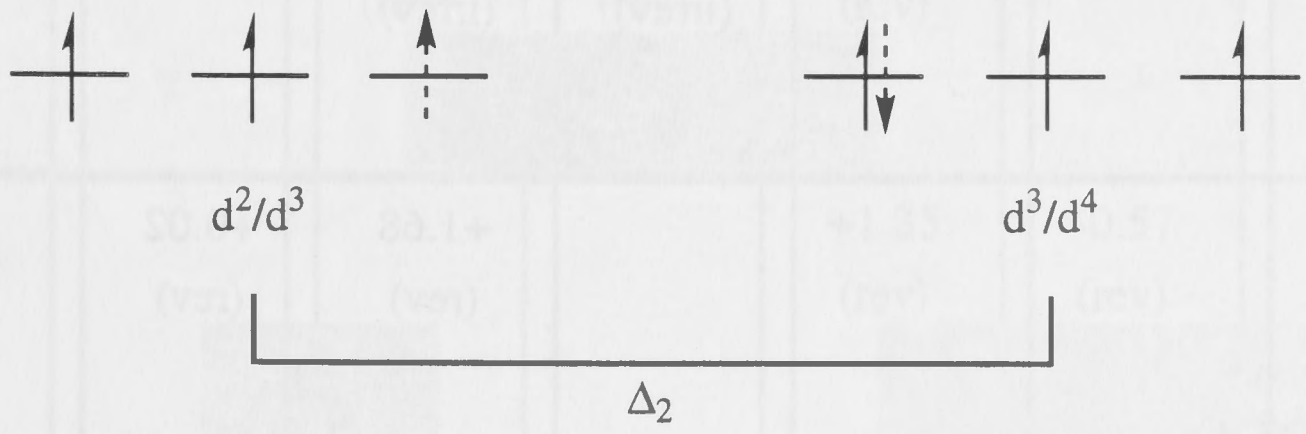

Figure 1.39 *Showing the reduction processes which contribute to Δ_2 for $[MX_6]^{n-}$ which is +2.72 V where M = Tc and +2.45 V for M = Re. The newly added electron added is shown as a dotted arrow in each case.*

Having noted that differences can be related to consecutive electrons entering different environments, we investigated the Δ values of $[M_2X_9]^{n-}$ systems and again found two Δ values with similar anomalies which might also be indicative of spin pairing for the second electron as was outlined in section 1.1.2. However, definitive assessments are difficult for $[M_2X_9]^{n-}$ because of the problems associated with defining the nature of the molecular orbital arrangement and the electron configuration arranged

therein. It is possible that cases where comparisons of the properties of $[M_2X_9]^{n-}$ complexes for corresponding second and third row species reveal different results from an equivalent comparison for the related $[MX_6]^{n-}$ species, could be due to differences in the nature of the metal-metal bond in the $[M_2X_9]^{n-}$ complexes when M = a second row transition metal as compared to M = third row metal.

Table 1.37 Comparisons of $[MCl_6]^{n-}$ reduction potentials highlighting the differences between consecutive processes, for complexes of the second row.

	d^0/d^1	d^1/d^2	d^2/d^3	d^3/d^4	d^4/d^5	d^5/d^6
Nb	+0.15 (rev)	-1.25 (rev)				
	Δ_0 +1.40					
Mo	+2.27 (rev)	+1.12 (rev)	-0.21 (rev)			
	Δ_0 +1.15	Δ_1 +1.33				
Tc			+1.96 (irrev)	-0.76 (irrev)		
			Δ_2 +2.72			
Ru				+1.68 (rev)	+0.02 (rev)	
				Δ_3 +1.66		
Rh					+2.50 (rev)	+0.79 (rev)
					Δ_4 +1.71	

Table 1.38 Comparisons of $[MCl_6]^{n-}$ reduction potentials highlighting the differences between consecutive processes, for complexes of the third row.

	d^0/d^1	d^1/d^2	d^2/d^3	d^3/d^4	d^4/d^5	d^5/d^6
Ta	-0.48 (rev)	-1.98 (rev)				
	Δ_0 +1.50					
W	+1.66 (rev)	+0.47 (rev)	-1.08 (rev)			
	Δ_0 +1.19	Δ_1 +1.55				
Re		+2.42 (rev)	+1.40 (rev)	-1.05 (rev)		
		Δ_1 +1.02	Δ_2 +2.45			
Os				+1.35 (rev)	-0.57 (rev)	-1.93 (rev)
				Δ_3 +1.66	Δ_4 +1.36	
Ir					+1.81 (rev)	+0.05 (rev)
					Δ_4 +1.76	

Chapter 1.4: Physicochemical studies of tetrahalo -oxotechnetate and -nitrido technetate complexes, (TBA)[$TcOX_4$] and (TBA)[$TcNX_4$] (where X = Cl or Br)

During the preparation of the $[TcX_6]^{2-}$ complexes just described, species of the form $[TcOX_4]^{1-}$ were regularly observed as both intermediates or impurities in the reactions. It was therefore important to record their physicochemical properties and compare them with those of $[TcX_6]^{2-}$. To that end $[TcOX_4]^{1-}$ complexes were prepared and investigated by voltammetry and UV-visible spectroscopy. $[TcNX_4]^{1-}$ complexes were also prepared and were used in comparison with their oxo counterparts, providing further insight into the chemistry of both sets of compounds.

Previous workers have achieved the chemical isolation of tetrachloro-oxotechnetate as both the $[Tc^{V}OCl_4]^{1-}$ (d^2) anion and as the neutral $[Tc^{VI}OCl_4]$ (d^1) species (**48**,**49**). The neutral species was first characterised by Guest and Lock in 1971 (**48**) and was prepared by the reaction of $Cl_{2\,(g)}$ and technetium metal at high temperature (300 - 500°C) followed by a trap-to-trap vacuum distillation. It was described as being purple in colour and very light sensitive (decomposing rapidly to brown $TcOCl_3$), though it was reported to be quite stable at room temperature, provided it was kept in the dark. (**48**)

The $(TBA)^+$ salt of $[Tc^{V}OCl_4]^{1-}$ was prepared later by the reduction of $(TBA)[Tc^{VII}O_4]$ in aqueous HCl using hypophosphorous acid, H_3PO_2, at room temperature (**49**). Subsequent modifications to the original synthetic method dispensed with the hypophosphorous acid (**24**,**50**) as its presence proved superfluous to achieving

the desired product of the reaction. Similarly H_3PO_2 was not required during the course of preparations undertaken as part of this thesis.

$(TBA)[Tc^{V}OBr_4]$ is generally prepared in an analogous manner, using HBr in place of HCl. (**29**,**51**) It is interesting to note that Deutsch *et.al.* (**51**) reported that grinding $(TBA)[TcOCl_4]$ in KBr (while making samples for infra-red studies) yields the bromo analogue via a solid state reaction.

$(TBA)^+$ and $(AsPh_4)^+$ salts of tetrahalo-nitridotechnetate(VI) (d^1), $[TcNX_4]^{1-}$, were first reported by Baldas *et.al.* in 1984 (**52**). They were prepared as air-stable compounds by refluxing $(NH_4)[TcO_4]$ and NaN_3 in concentrated HX. That these nitrido compounds are stable in concentrated HX at high temperatures is an indication of the greater stability of the Tc-N bond *vs* Tc-O bond to acid hydrolysis (as $[TcOX_4]^{1-}$ is unstable, reacting to $[TcX_6]^{2-}$ in concentrated HX at high temperatures). (**52**) The halide ligands exhibit a similar lability to that described for $[TcOX_4]^{1-}$, with the chloride ligands of $[TcNCl_4]^{1-}$ readily undergoing exchange with LiBr in acetone to give $[TcNBr_4]^{1-}$. (**53**) In contrast to $[TcOX_4]^{1-}$, there are no reports (to date) of the direct chemical synthesis of d^2 $[TcNX_4]^{2-}$ anions.

The choice of cation has some impact on the preparation of both $[TcOX_4]^{1-}$ and $[TcNX_4]^{1-}$ complexes. (**53**,**54**) The use of larger cations such as $(TBA)^+$ and $(AsPh_4)^+$ favours the precipitation of the $[TcYX_4]^{1-}$ (where Y= O, N) salts which are of interest here. However, the use of smaller cations (for example, K^+, Cs^+ and NH_4^+) results in the precipitation of $[TcYX_5]^{2-}$ salts. (**49**,**53**,**54**,**55**)

The addition of the intermediate sized cation, $(TEA)^+$ in the form of (TEA)X to the reaction of $(NH_4)[TcO_4]$ in concentrated HX with NaN_3, results in the precipitation of the six coordinate $(TEA)[TcNX_4(H_2O)]$. (**55**) Similarly, $(TEA)[TcOBr_4(H_2O)]$ can be isolated from the addition of TEABr to $(NH_4)[TcO_4]$ in concentrated HBr maintained at

-5°C. (**56**) The chloride analogue is not obtained and, (TEA)[$TcOCl_5$] is formed instead. (**56**,**57**)

The crystal structures of $[TcOX_4]^{1-}$ and $[TcNX_4]^{1-}$ have been recorded with a variety of sufficiently large cations. (**48**,**52**,**54**,**58**,**59**,**60**) In general, they show the anions to possess a square-pyramidal structure with C_{4v} symmetry.# The Tc-N bond is shorter than the Tc-O bond and the Tc-X bond lengths are longer for the nitrido complexes. The Y-Tc-X angle is greater for Y=O, resulting in the displacement of Tc out of the X_4 plane being greater for the oxo anions. (**53**) These observations are consistent with crystal structures measured for a series of complexes of $(AsPh_4)[MYCl_4]$ where M = Mo, Re, Ru and Os and Y = O or N (**58**,**53**) and are a function of the greater π donation of the nitride ligand which results in the technetium to nitride interaction being relatively stronger than the technetium to oxo one.

The following chapter will detail the UV-visible absorption solution spectroscopy and electrochemistry which were recorded during the course of this thesis for both $[TcOX_4]^{1-}$ and $[TcNX_4]^{1-}$.

1.4.1 (TBA)[$TcOX_4$]

1.4.1.1 UV-visible spectra of (TBA)[$TcOX_4$]

The UV-visible electronic absorption spectra of $[TcOCl_4]^{1-}$ and $[TcOBr_4]^{1-}$ were recorded at both room temperature and 220 K in CH_2Cl_2 and the room temperature data are presented in figure 1.40 and table 1.41. These compare well with those previously reported (under the same conditions) for each complex##.

A crystal structure of $[(Ph_3P)_2N][TcOCl_4]$ has been reported and revealed a distorted square pyramidal geometry, best described as approximate C_{2v} symmetry. (**49**) This distortion has been shown to be due to crystal packing forces. (**58**)

Previous results reported for (TBA)[$TcYX_4$] under similar conditions (CH_2Cl_2, room temperature) were: (TBA)[$TcOCl_4$] 34 100 (4450), 27 000 (sh), 21 100 (15), 17 200 (7), 11 900 (17) (**50**) and (TBA)[$TcOBr_4$] 40 300 (10 400), 28 300 (3750), 20 900 (113), 16 300 (22) (**51**) with absorbance in cm^{-1} (ε in $dm^3mol^{-1}cm^{-1}$)

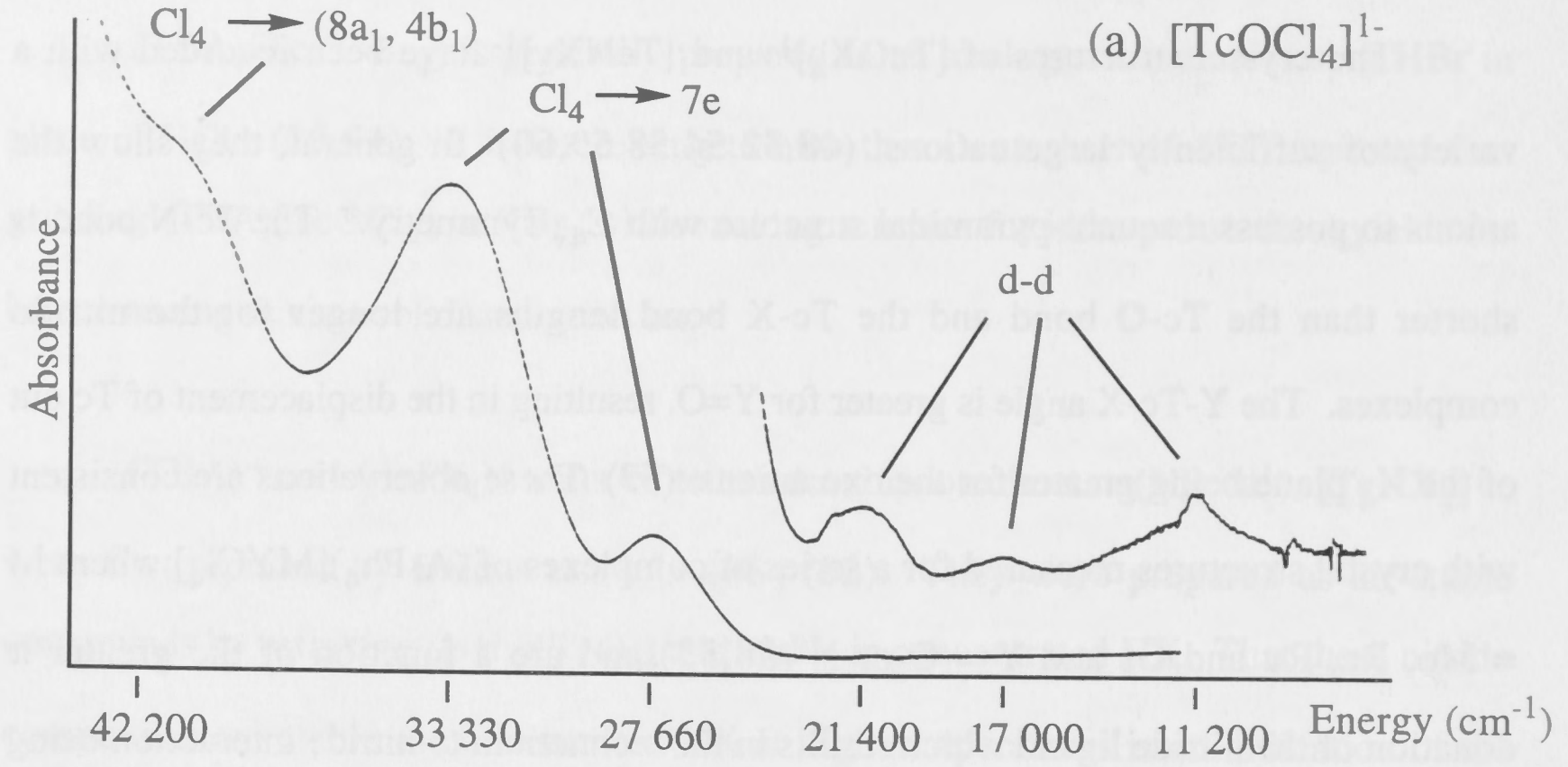

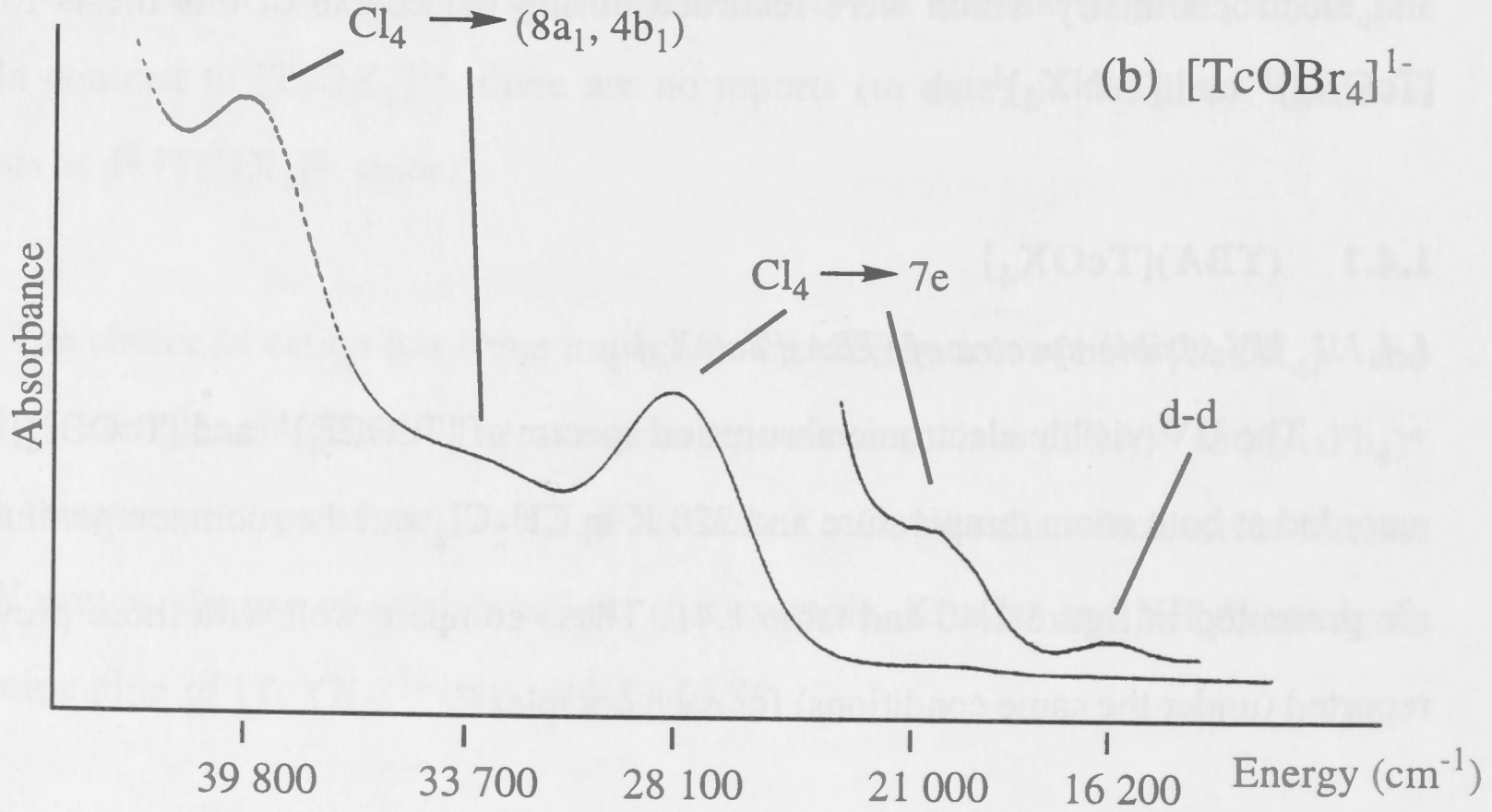

Figure 1.40 *The UV-visible electronic absorption spectra of (a) $[TcOCl_4]^{1-}$ and (b) $[TcOBr_4]^{1-}$ recorded in CH_2Cl_2 at room temperature. Spectral assignments are also indicated.*

Table 1.41 UV-visible electronic absorption spectra of $(TBA)[TcOX_4]$ (X= Cl^- and Br^-) in CH_2Cl_2 at room temperature

Energy (cm^{-1})	ε ($dm^3mol^{-1}cm^{-1}$)	Energy (cm^{-1})	ε ($dm^3mol^{-1}cm^{-1}$)
X = Cl		X = Br	
42 200	(sh)	39 800	8200
33 330	5900	33 700	(sh)
27 660	1200	28 100	4000
21 400	14	21 000	110
17 000	3	16 200	11
11 200	11		

These spectra were analysed under the C_{4v} symmetry as indicated by the crystal structures described previously. The splitting of the technetium 4d levels under this ligand field is qualitatively shown in figure 1.42. The figure indicates that the introduction of an oxo or nitrido ligand, in place of the two trans halides of an octahedral complex, results in a splitting of the t_{2g} and e_g levels.

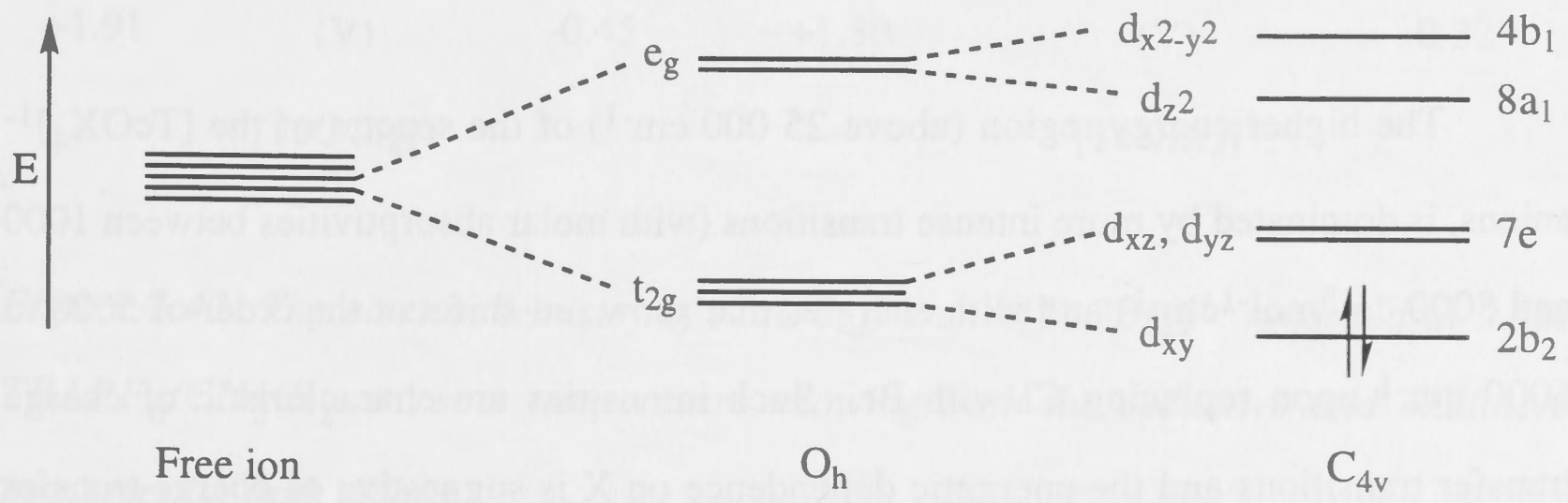

Figure 1.42 *Diagram showing the splitting of the 4d orbitals in C_{4v} symmetry. The ordering is as for $[TcOX_4]^{1-}$ and shows the d^2 occupation.*#

Previous studies employing EPR and static magnetic susceptibility measurements in conjunction with an extended Hückel analysis found these d^2 $(TBA)[TcOX_4]$

The orbital numbers are derived from the density functional calculations in chapter 2.1 and are used here to assist with the continuity of discussion between the two sections.

complexes to be diamagnetic in the temperature range of 80-300 K, indicative of a $^1A_1$ electronic groundstate, with the b_2 ($4d_{xy}$) level being fully occupied. (**54**,**61**) These results are consistent with the results of density functional calculations (**62**) which will be fully described in chapter 2.1 of this thesis. The calculations were used together with qualitative considerations to derive the spectral assignments presented in figure 1.40.

The UV-visible absorption spectra of $[TcOCl_4]^{1-}$ and $[TcOBr_4]^{1-}$ receive similar assignments and will be discussed concurrently. As can be seen from table 1.41 and figure 1.40, the spectra of both species consist of two rather distinct absorbance regions, below and above 25 000 cm^{-1}, each of these will be described in turn.

The lower energy region (below 25 000 cm^{-1}) features low intensity absorbances (with molar extinction coefficients below 120 $dm^3mol^{-1}cm^{-1}$) and with energies that show little dependence (300 - 800 cm^{-1}) on the halide, X. The most likely assignment of these absorbances are as ligand field d-d transitions. Such an assignment would be consistent with previous reports on the UV-visible spectrum of $(NH_4)_2[TcOCl_5]$ recorded in HCl which the bands at 10 700 (ε = 18), 16 700 (8) and 20 600 cm^{-1} (24) were assigned as d-d transitions (**54**).#

The higher energy region (above 25 000 cm^{-1}) of the spectra of the $[TcOX_4]^{1-}$ anions, is dominated by more intense transitions (with molar absorptivities between 1000 and 8000 $dm^3mol^{-1}cm^{-1}$) and with energies that show red shifts of the order of 5000 to 6000 cm^{-1} upon replacing Cl with Br. Such intensities are characteristic of charge transfer transitions and the energetic dependence on X is suggestive of charge transfer involving the $\{X_4\}$ ligand array, in particular.## Since the $2b_2$ ($4d_{xy}$) level is fully occupied, the absorbances are assigned as ligand to metal charge transfer from the $\{X_4\}$ manifold into 7e ($4d_{xz}$, $4d_{yz}$) the next available d level, and into the higher lying metal levels, $8a_1$ (d_{z^2}) and $4b_1$ ($d_{x^2-y^2}$). The specific levels which make up the $\{X_4\}$ manifold

---

$(NH_4)_2[TcOCl_5]$ possess a similar $^1A_1$ b_2^2 groundstate.

The density functional calculations in chapter 2.1 clearly illustrate that the oxygen based molecular orbitals are too stabilised to contribute to charge transfer of the observed energies.

and the factors which determine those which are directly involved in the observed charge transfer transitions will be described in chapter 2.1.

1.4.1.2 Voltammetry of (TBA)[$TcOX_4$]

The electrochemistry of (TBA)[$TcOX_4$] (where X = Cl and Br) was recorded in 0.5 M $TBAPF_6/CH_2Cl_2$ at both room temperature and -60°C in an evacuable electrochemical cell. The results of the room temperature measurements (where the best acV signal is observed) are illustrated in figure 1.43 and table 1.44.

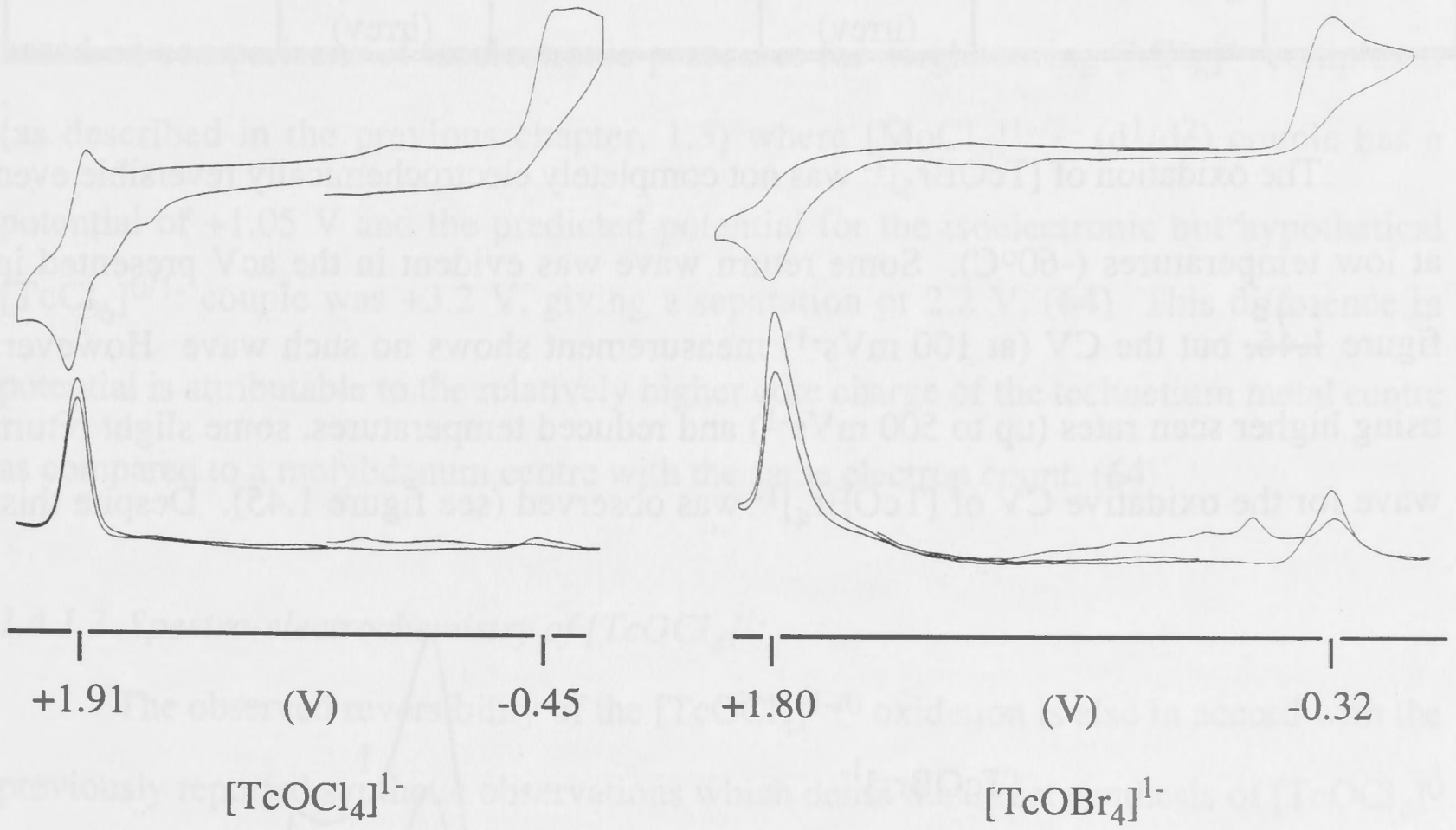

$[TcOCl_4]^{1-}$ $[TcOBr_4]^{1-}$

Figure 1.43 *The electrochemistry of $[TcOCl_4]^{1-}$ and $[TcOBr_4]^{1-}$ recorded in 0.5M $TBAPF_6/CH_2Cl_2$ at room temperature showing both the reductive and oxidative processes for both anions.*

At room temperature, the reductive process was observed to be irreversible for both complexes, while the oxidative process was reversible for X = Cl but not for X = Br. Each of the reductive processes was observed to be accompanied by the loss of halide (X) (as indicated by the emergence of daughter signals corresponding to $Cl^{1-/0}$ or $Br^{1-/0}$ in both the CV and acV measurements). The reduction remained irreversible even at low

temperatures and in the presence of excess (TBA)X. No new signals were observed, even in the presence of excess (TBA)X, which could be related to the formation of $[TcOX_5]^{n-}$ salts.

Table 1.44 Voltammetry of $[TcOX_4]^{1-}$ in 0.5M $TBAPF_6/CH_2Cl_2$ at room temperature.#

	$[Tc^{VI}OX_4]^0$ d^1	⇌	$[Tc^{V}OX_4]^{1-}$ d^2	→	$\{Tc^{IV}OX_4\}^{2-}$ d^3
X = Cl		+1.91 V (rev)		-0.45 V (irrev)	
X = Br		+1.80 V (irrev)		-0.32 V (irrev)	

The oxidation of $[TcOBr_4]^{1-}$ was not completely electrochemically reversible even at low temperatures (-60°C). Some return wave was evident in the acV presented in figure ~~1.46,~~ 1·43 but the CV (at 100 mVs^{-1}) measurement shows no such wave However, using higher scan rates (up to 500 mVs^{-1}) and reduced temperatures, some slight return wave for the oxidative CV of $[TcOBr_4]^{1-}$ was observed (see figure 1.45). Despite this,

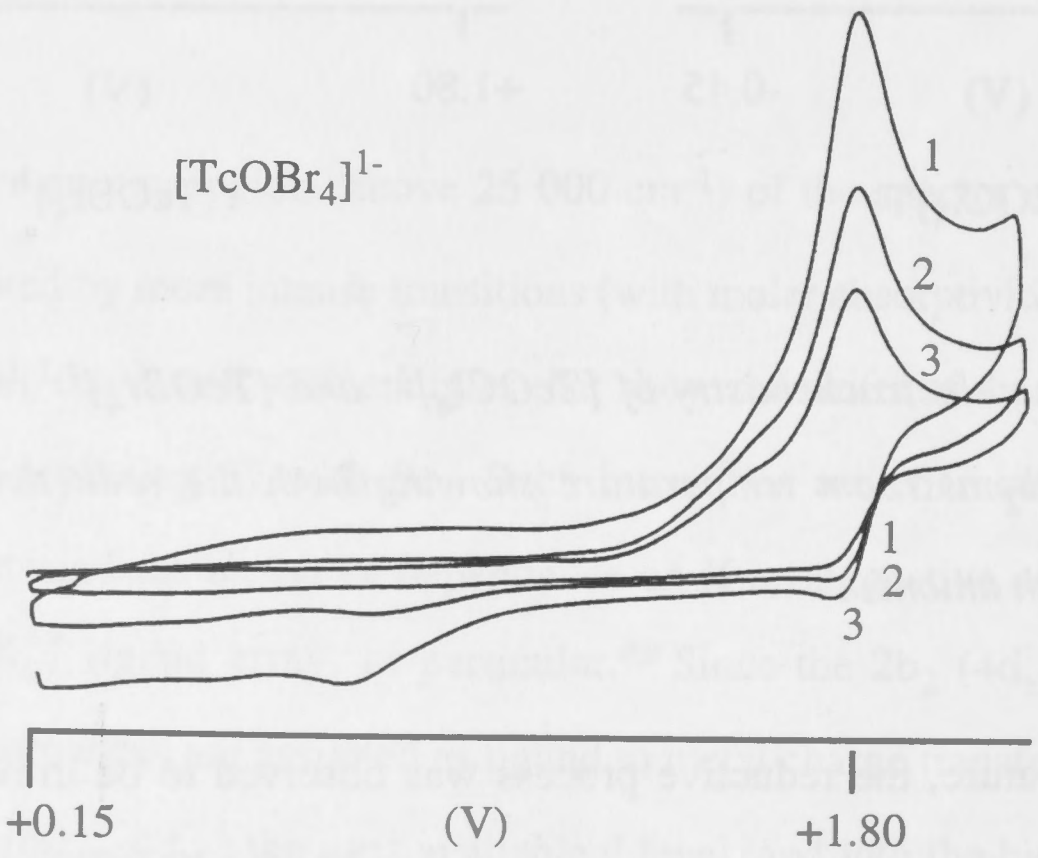

Figure 1.45 *The cyclic voltammetry of $[TcOBr_4]^{1-}$ recorded in CH_2Cl_2/0.5M $TBAPF_6$ at 220 K using different scan rates for each scan. 1 = 100, 2 = 200 and 3 = 500 mVs^{-1}.*

The numbers in the table are taken from the acV measurement.

the process was never found to be as reversible as the $[TcOCl_4]^{1-}$ to $[TcOCl_4]^0$ oxidation, under the conditions employed. It will however be assumed that the initial, transient, product formed in the oxidation was $[TcOBr_4]^0$.

The observed potentials for the oxidation and reduction of $[TcOCl_4]^{1-}$ are broadly consistent with what one would expect, based on a comparison with the previously reported voltammetry of $[MoOCl_5]^{2-}$ (recorded under similar conditions) (**63**). In this case the $[MoOCl_5]^{2-/3-}$ (d^1/d^2) couple is isoelectronic with $[TcOCl_4]^{0/1-}$. The reduction of the molybdenum system is irreversible and occurs at -0.58 V which is some 2.5 V lower than the +1.91 V observed here for technetium. This is similar to the general result based on comparisons of isoelectronic processes for neighbouring $[MX_6]^{n-}$ complexes (as described in the previous chapter, 1.3) where $[MoCl_6]^{1-/2-}$ (d^1/d^2) couple has a potential of +1.05 V and the predicted potential for the isoelectronic but hypothetical $[TcCl_6]^{0/1-}$ couple was +3.2 V, giving a separation of 2.2 V. (**64**) This difference in potential is attributable to the relatively higher core charge of the technetium metal centre as compared to a molybdenum centre with the same electron count. (**64**)

1.4.1.3 Spectro-electrochemistry of $[TcOCl_4]^{1-}$

The observed reversibility of the $[TcOCl_4]^{1-/0}$ oxidation is also in accord with the previously reported synthetic observations which detail the direct synthesis of $[TcOCl_4]^0$ as a purple, light-sensitive compound. (**29**) $[TcOCl_4]^0$ was sufficiently stable to be reversibly generated in an OTTLE cell at 220 K, and once generated remained intact (for at least 12 hours) as the solution was allowed to warm to room temperature.# The UV-visible electronic absorption spectrum for $[TcOCl_4]^0$ is detailed in figure 1.46 and table 1.47.##

Guest and Lock report samples of $[TcOCl_4]$ being stable for periods of one year when stored at room temperature and in the dark. (**29**)

An attempt to OTTLE (TBA)$[TcOBr_4]$ was made, but in the light of the observed cyclic voltammetry not showing complete reversibility, it was not surprising that as the +2 V potential was applied the spectrum of $[TcOBr_4]^{1-}$ irreversibly collapsed. The final spectrum was featureless and not recognisable as any compound in particular. There is, to the author's knowledge, no previous report of the synthesis or electro-generation of $[TcOBr_4]^0$.

In assigning the spectrum of $[TcOCl_4]^0$ it is useful to think in terms of the two absorptions regions (below and above 25 000 cm^{-1}) introduced earlier for the parent $[TcOCl_4]^{1-}$ species. The most obvious difference between the spectra of $[TcOCl_4]^{1-}$ and $[TcOCl_4]^0$ is the emergence of an intense band in the low energy region of the spectrum

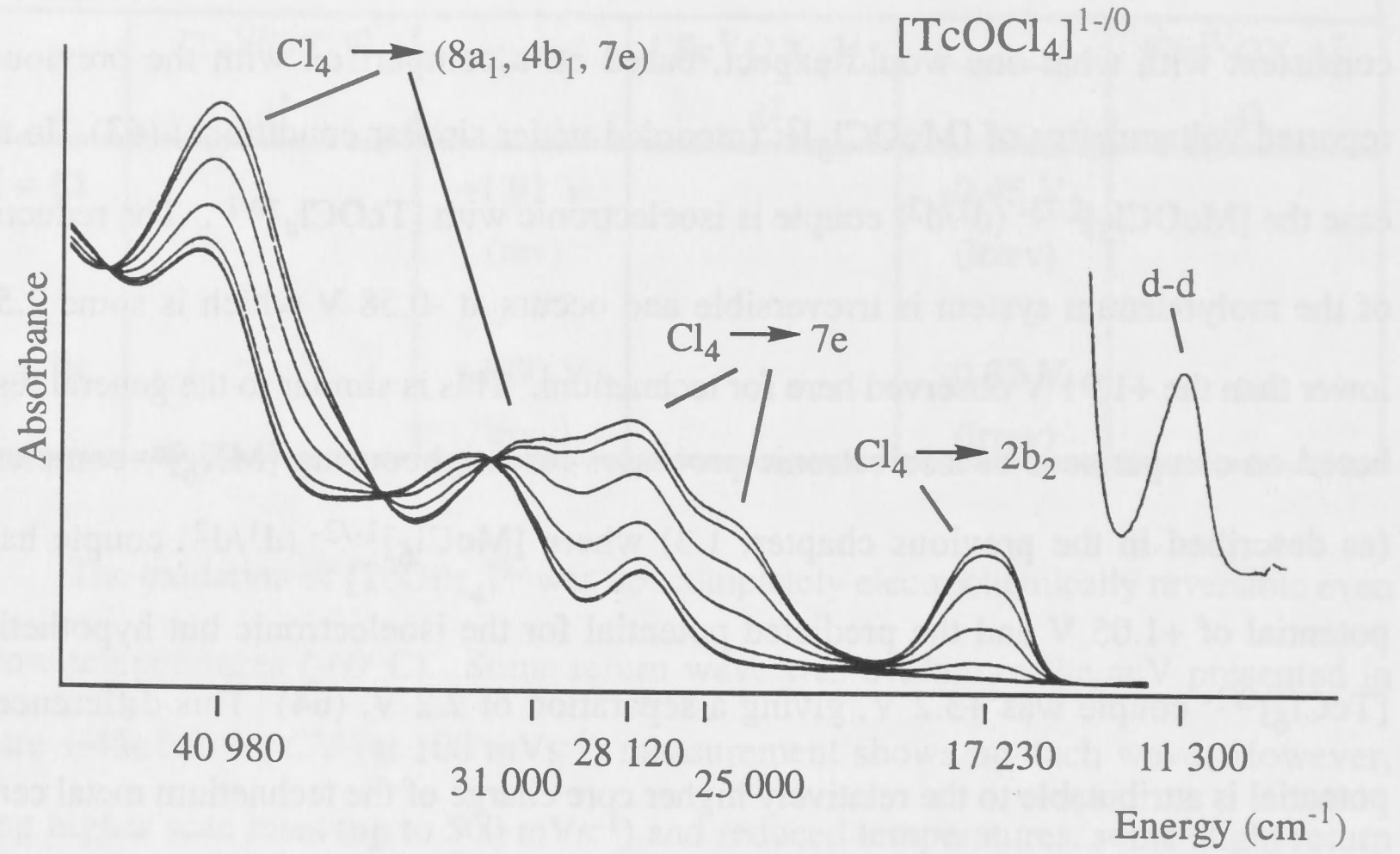

Figure 1.46 *The oxidation of $[TcOCl_4]^{1-}$ to $[TcOCl_4]^0$ in CH_2Cl_2/0.5M TBAPF$_6$ at -60^{0}C, showing also the spectral assignments for $[TcOCl_4]^0$.*

Table ~~1.49~~ 1.47 UV-visible electronic absorption spectra $[TcOCl_4]$ in CH_2Cl_2/$[TBA]PF_6$ at 220 K applied potential "+2.4 V"

Energy (cm^{-1})	ε ($dm^3mol^{-1}cm^{-1}$)
40 980	16 000
31 000	sh
28 120	7 200
25 000	sh
17 230	4 000
11 300	80

of the oxidised product (at 17 230 cm^{-1}). The intensity of this band (ε = 4000 dm^3 $mol^{-1}cm^{-1}$) is indicative of a charge transfer process. The relatively low energy of the absorption results from the metal based oxidation process which results in the removal of an electron from the previously fully occupied $2b_2$ $4d_{xy}$ level, thus making it available to accept ligand to metal charge transfer in the oxidised species. The weak band (ε = 80 $dm^3mol^{-1}cm^{-1}$) at 11 300 cm^{-1} is attributable to a d-d transition. Similar d-d transitions have also been identified in the isoelectronic $[MoOCl_5]^{2-}$ species (**53**). Three d-d bands were observed for $[TcOCl_4]^{1-}$ and only one for $[TcOCl_4]^0$, but it is possible that the other d-d bands are masked by the new charge transfer transition in the oxidised species.

The higher energy region of the spectrum (25 000 cm^{-1} and above) undergoes a less dramatic change upon oxidation to $[TcOCl_4]^0$. The same ligand to metal charge transfer transitions are observed but a general red shift of around 2000 cm^{-1} in the energy of these processes is observed. This red shift was successfully modelled by density functional calculations on $[TcOCl_4]^0$ and $[TcOCl_4]^{1-}$ which will be described in chapter 2.1). This result is consistent with stabilisation of the technetium based 4d orbitals relative to the halide based ones such as would be expected upon oxidation, by virtue of the resultant increase in the effective nuclear charge of the central Tc metal ion.

Further support for the assignments of the UV-visible absorption spectra and voltammetry of $[TcOX_4]^{1-}$ and $[TcOCl_4]^0$ ~~were~~ was obtained by comparison with the spectra of the isoelectronic and isostructural, $[TcNX_4]^{2-/1-}$.

1.4.2 (TBA)$[TcNX_4]$

The complexes of the type $[TcNX_4]^{1-}$ possess a formal triple bond between technetium and nitrogen. They therefore have the d^1 electronic configuration typical of a Tc^{VI} centre under C_{4v} symmetry, and are isoelectronic with the $[Tc^{VI}OCl_4]^0$ species just described. A reversible reduction to Tc^V (d^2) has been reported previously for both $[TcNX_4]^{1-}$ anions (**54**,**65**) and the UV-visible spectro-electrochemistry at 220 K in CH_2Cl_2 was recorded in that preliminary study but no specific details of potentials or

absorption energies have been published. The voltammetry and UV-visible spectro-electrochemisry of both nitrido complexes was repeated as part of this thesis and are detailed in this section.

1.4.2.1 Voltammetry of $[TcNX_4]^{1-}$

The voltammetry observed for both (TBA)$[TcNX_4]$ complexes was recorded in CH_2Cl_2/0.5 M $TBAPF_6$ at both room temperature and -60°C, and is presented in figure 1.48 and table 1.49 below.

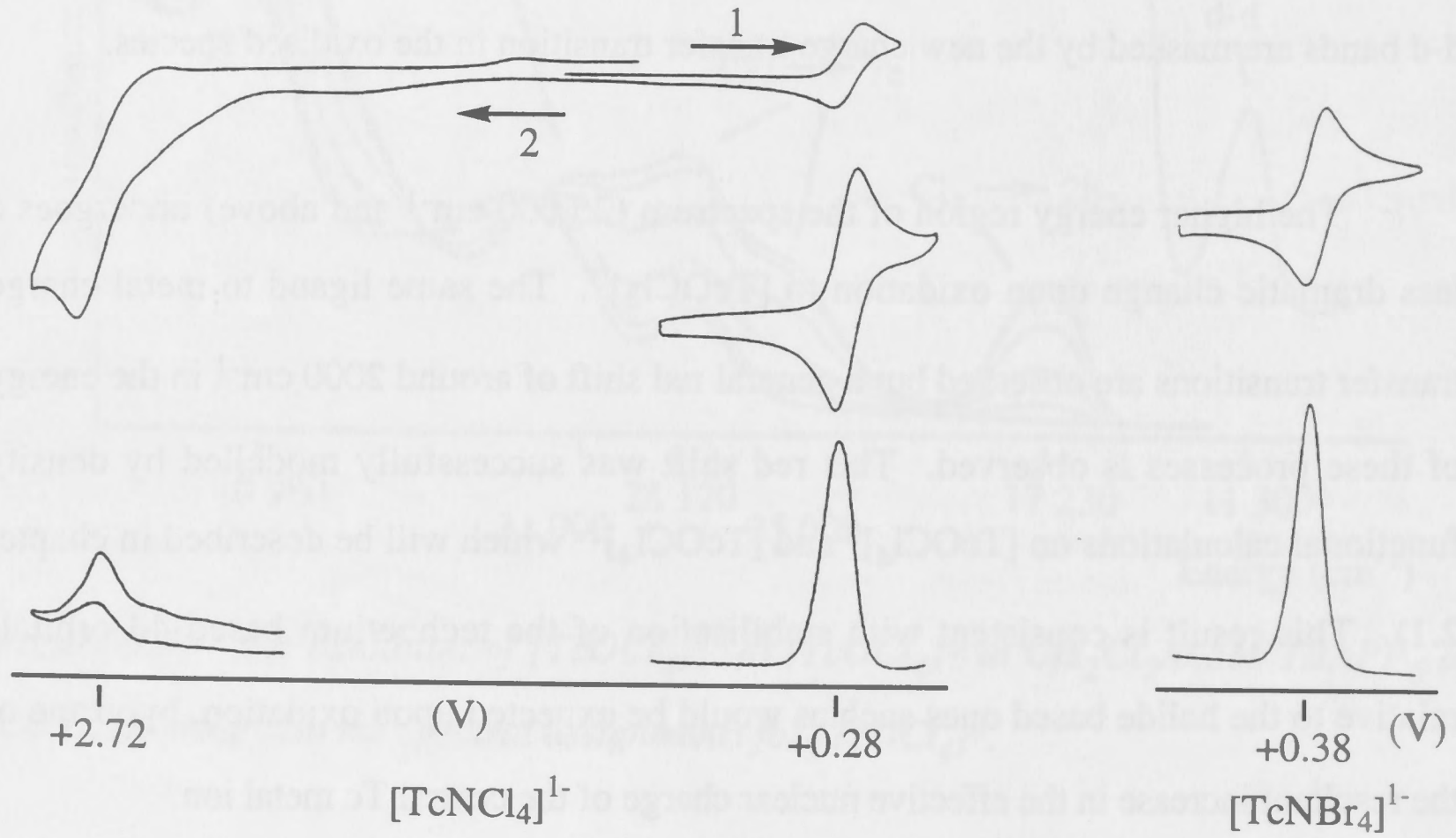

Figure 1.48 *The voltammetry of $[TcNCl_4]^{1-}$ and $[TcNBr_4]^{1-}$ recorded in* 0.5M *$TBAPF_6/CH_2Cl_2$ at room temperature showing the reductive process for both anions and the oxidation of $[TcNCl_4]^{1-}$.*

Table 1.49 Voltammetry of $[TcNX_4]^{1-}$ in 0.5M $TBAPF_6/CH_2Cl_2$ at room temperature.#

	$[Tc^{VII}NX_4]^0$ d^0	⟵	$[Tc^{VI}NX_4]^{1-}$ d^1	⇌	$[Tc^{V}NX_4]^{2-}$ d^2
X = Cl		+2.72 V (rev)		+0.28 V (rev)	
X = Br		—		+0.38 V (rev)	

The potentials in the table are taken from the acV measurement.

The reversible reduction of $[TcNX_4]^{1-}$ corresponds to the filling of the $2b_2$ ($4d_{xy}$) orbital. It is therefore not surprising that, despite the relatively mild potential required for this first reduction, no further reductive processes were observed as they would require an electron to enter the higher energy 7e (d_{xz}, d_{yz}) level. The process observed at +2.72 V in $[TcNCl_4]^{1-}$ was represented by an irreversible CV, but some return wave was observed in the acV experiment. This process was therefore ascribed to the oxidation to $[TcNCl_4]^0$ which would correspond to removal of last the technetium 4d electrons. No such process was observed for the corresponding bromide within the limits of the solvent range.

Table 1.50 shows a comparison of the potential required for the d^2/d^1 couple for $[TcNX_4]^{2-/1-}$ and $[TcOX_4]^{1-/0}$.

Table 1.50 A comparison of the potentials required for the d^2/d^1 couple for $[TcYX_4]^{n-}$.

	$[Tc^{VI}YCl_4]^{n-}$ d^1	⇌	$[Tc^{V}YCl_4]^{n-}$ d^2	$[Tc^{VI}YBr_4]^{n-}$ d^1	⇌	$[Tc^{V}YBr_4]^{n-}$ d^2
Y = N		+0.28 V (rev)			+0.38 V (rev)	
Y = O		+1.91 V (rev)			+1.80 V (irrev)	

It is immediately apparent from table 1.50 that the potential for the d^2/d^1 couple of $[TcNX_4]^{n-}$ is less positive that the corresponding one for $[TcOX_4]^{n-}$ (by 1.4 to 1.7 V) and that this oxidation is more reversible for $[TcNBr_4]^{2-}$ than $[TcOBr_4]^{1-}$, in particular. This result indicates that the nitrido ligand stabilises the higher oxidation state of technetium better than the oxo ligand. Thus it is not surprising that the nitrido complexes are prepared as the Tc^{VI} (d^1) oxidation state while oxo complexes are most commonly prepared as Tc^{V} (d^2). Replacement of N or O by two halide ligands to form $[TcX_6]^{n-}$ was shown in the previous section to render higher oxidation states even less accessible; these complexes are prepared as Tc^{IV} (d^3) $[TcX_6]^{2-}$ and no reversible oxidation processes have been observed. These observations are consistent with the findings for a similar

series of complexes, $[MCl_6]^{n-}$, $[MOCl_5]^{n-}$ and $[MNCl_4]^{n-}$ (where M = Mo, W) which showed that the stability of the higher oxidation states of the metal increased according to the ligand array, in the order $\{Cl_6\} < \{OCl_5\} < \{NCl_4\}$ (**63**). This point will be discussed further in terms of computed electronic structures of $[TcYX_4]^{n-}$ in chapter 2.1.

1.4.2.2 Spectro-electrochemistry of $[TcNX_4]^{n-}$ (where n = 1,2)

The reversible nature of the reduction facilitated a UV-visible spectro-electrochemical study of the process for both $[TcNCl_4]^{1-/2-}$ and $[TcNBr_4]^{1-/2-}$ in $CH_2Cl_2/TBAPF_6$ at 215 K. The results are presented in table 1.51 and figure 1.52.

Table 1.51 UV-visible electronic absorption spectra of $[TcNX_4]^{1-/2-}$ recorded in $CH_2Cl_2/TBAPF_6$ at 220 K.

Energy (cm^{-1})	ε ($dm^3mol^{-1}cm^{-1}$)	Energy (cm^{-1})	ε ($dm^3mol^{-1}cm^{-1}$)
$[TcNCl_4]^{1-}$ d^1		**$[TcNBr_4]^{1-}$** d^1	
43 110	9 000	37 120	5 100
33 340	1 700	33 940	5 900
24 580	6 400	30 500	sh
22 220	2 300	28 600	sh
21 570	2 300	24 380	600
20 900	sh	19 570	3 200
19 100	280	19 200	sh
		17 980	2 700
		16 320	4 800
$[TcNCl_4]^{2-}$ d^2		$[TcNBr_4]^{2-}$ d^2	
43 500	sh	40 650	10 000

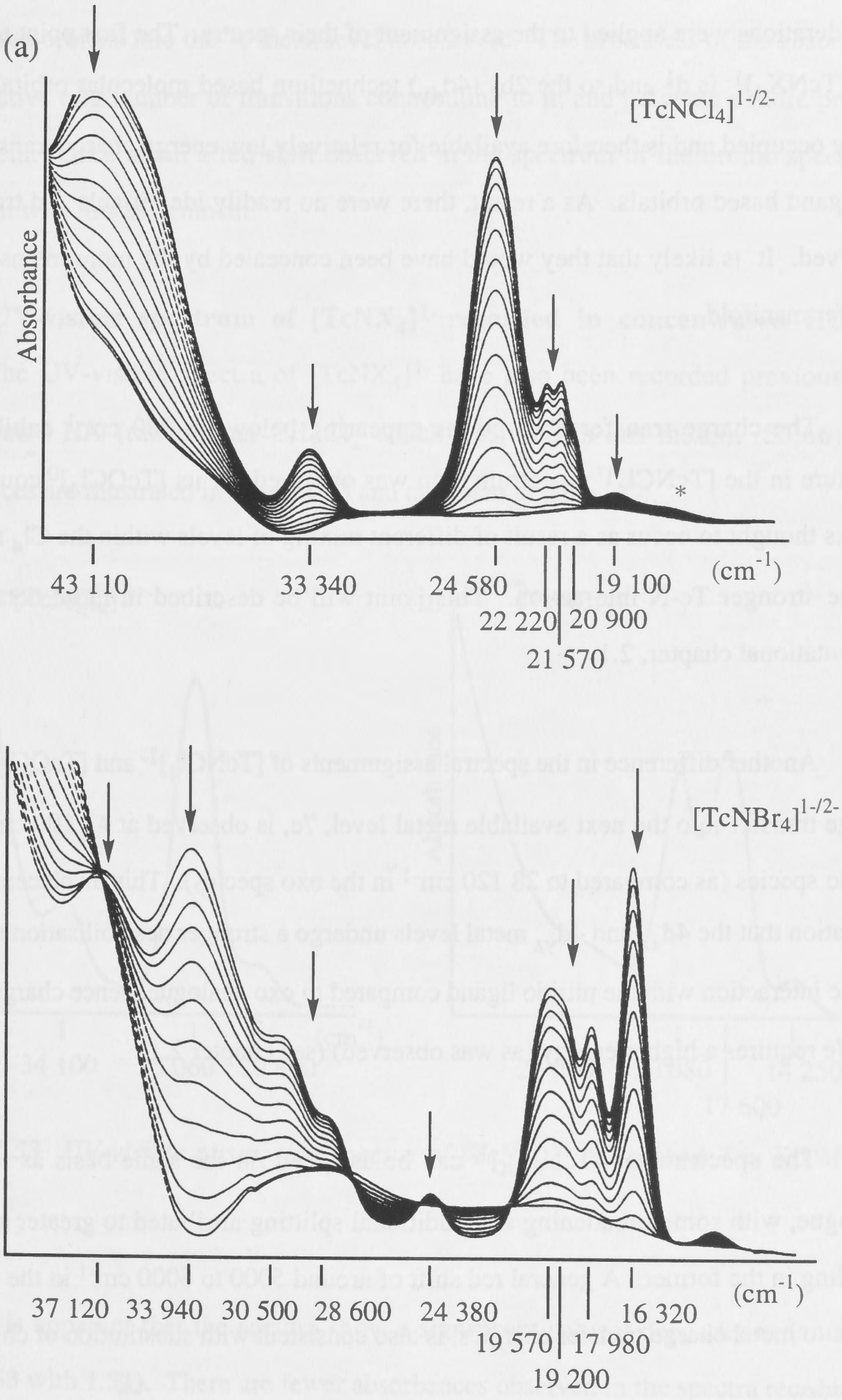

Figure 1.52 *UV-visible absorption spectra illustrating the in-situ reduction (OTTLE experiment) of $[TcNX_4]^{1-}$ to $[TcNX_4]^{2-}$ in 0.5M $TBAPF_6/CH_2Cl_2$ at 220 K, in (a) X = Cl and in (b) X = Br. Signals associated with impurities formed during the electrochemical processes are indicated by a *.*

The anions $[TcNX_4]^{1-}$ are isoelectronic with $[TcOX_4]^0$ and so similar considerations were applied to the assignment of their spectra. The first point to note is that $[TcNX_4]^{1-}$ is d^1 and so the $2b_2$ ($4d_{xy}$) technetium based molecular orbital is only singly occupied and is therefore available for relatively low energy charge transfer from the ligand based orbitals. As a result, there were no readily identifiable d-d transitions observed. It is likely that they would have been concealed by the more intense charge transfer manifold.

The charge transfer absorptions appearing below 25 000 cm^{-1} exhibit more structure in the $[TcNCl_4]^{1-}$ spectrum than was observed for its $[TcOCl_4]^0$ counterpart. This is thought to occur as a result of different mixing of levels within the Cl_4 manifold by the stronger Tc-N interaction. This point will be described in more detail in the computational chapter, 2.1.

Another difference in the spectral assignments of $[TcNCl_4]^{1-}$ and $[TcOCl_4]^0$ is that charge transfer into the next available metal level, 7e, is observed at 43 100 cm^{-1} in the nitrido species (as compared to 28 120 cm^{-1} in the oxo species). This displacement is an indication that the $4d_{xz}$ and $4d_{yz}$ metal levels undergo a stronger destabilisation through a π-type interaction with the nitrido ligand compared to oxo analogue, hence charge transfer into 7e requires a higher energy (as was observed) (see chapter 2.1).

The spectrum of $[TcNBr_4]^{1-}$ can be assigned on the same basis as its chloro analogue, with some broadening and additional splitting attributed to greater spin-orbit coupling in the former. A general red shift of around 5000 to 6000 cm^{-1} in the observed halide to metal charge transfer energies, is also consistent with substitution of chloride for bromide.

Upon reduction to $[TcNX_4]^{2-}$ the $2b_2$ ($4d_{xy}$) level becomes fully occupied and so unavailable for accepting charge transfer. As a result, the spectra of the reduced species

are featureless below 40 000 cm^{-1}.# Above this frequency, charge transfer from the $\{X_4\}$ based orbitals into the 7e metal level is observed. The broadness of the absorption is suggestive of a number of transitions contributing to it, and prevents a more precise assignment. Once again a red shift observed in the spectrum of the bromo species is consistent with this assignment.

1.4.3 UV-visible spectrum of $[TcNX_4]^{1-}$ recorded in concentrated HCl

The UV-visible spectra of $[TcNX_4]^{1-}$ have also been recorded previously in concentrated HX (rather than CH_2Cl_2 which was used in this thesis). (**53**,**66**) The absorbances are illustrated in figure 1.53 and tabulated in table 1.54.

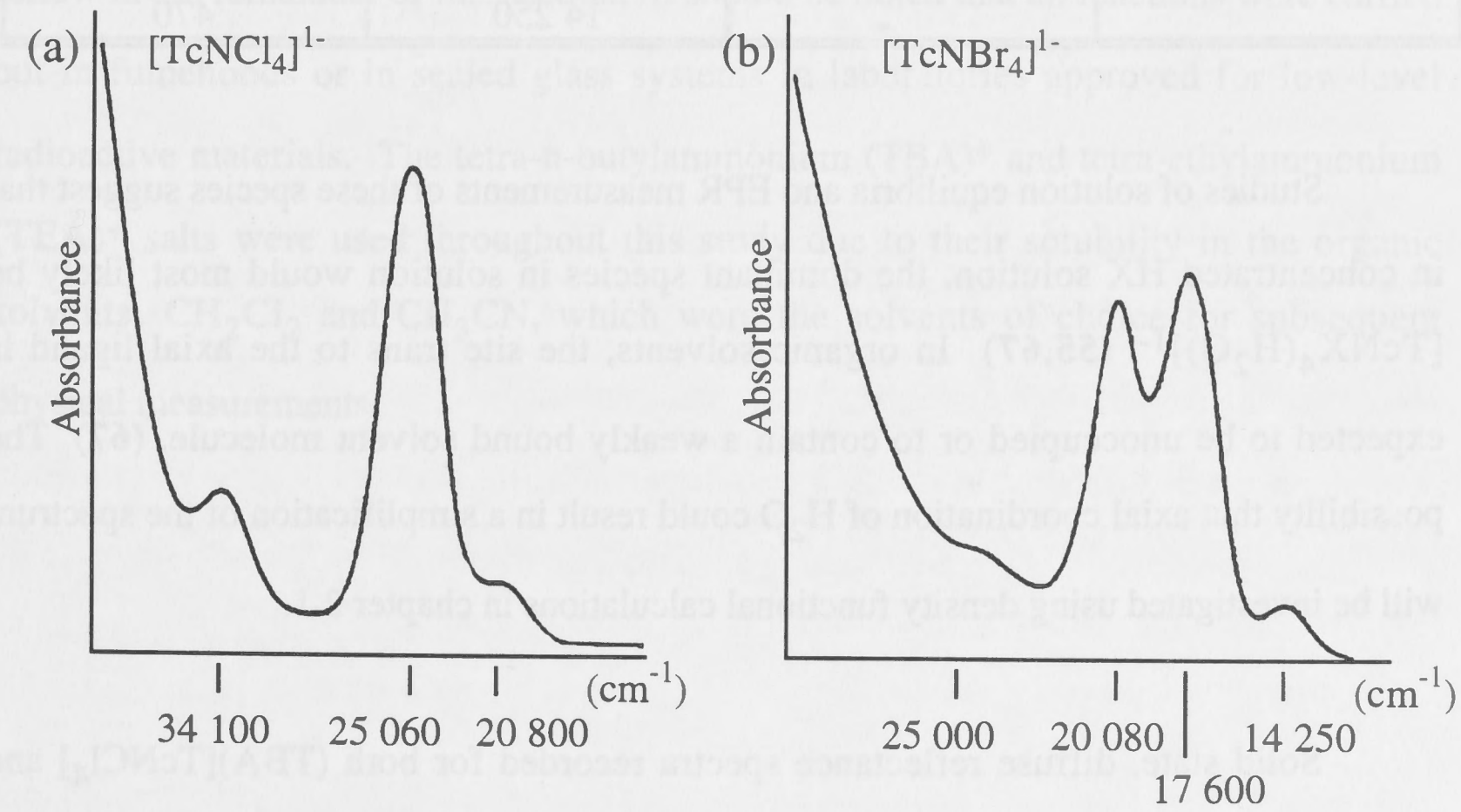

Figure 1.53 *UV-visible absorption spectra of $[TcNX_4]^{1-}$ as recorded in 7.5 M HX.* ***(52,68)***

It is apparent that the spectra show a significant solvent dependence (compare figure 1.53 with 1.52). There are fewer absorbances observed in the spectra recorded of the HX solutions than for CH_2Cl_2 or CH_3CN for that matter, which is reported to be very similar to CH_2Cl_2. (**53**,**66**) Having said that, the energies of the corresponding

---

The weak absorbances observed around 19 890 cm^{-1} in $[TcNCl_4]^{2-}$ and 28 700 and 19 000 cm^{-1} in $[TcNBr_4]^{2-}$ are attributed to impurities formed during the reduction.

absorption regions which are observed in all solvents are comparable. The spectral assignments will be discussed further in chapter 2.1.

Table 1.54 UV-visible electronic absorption spectra of $[TcNX_4]^{1-/2-}$ recorded in 7.5 M HX. (**53**,**66**)

$[TcNCl_4]^{1-}$ d^1		$[TcNBr_4]^{1-}$ d^1	
Energy (cm^{-1})	ε ($dm^3mol^{-1}cm^{-1}$)	Energy (cm^{-1})	ε ($dm^3mol^{-1}cm^{-1}$)
34 100	1540	25 000	sh (930)
25 060	4780	20 080	3030
20 800	625	17 600	3290
		14 250	470

Studies of solution equilibria and EPR measurements of these species suggest that in concentrated HX solution, the dominant species in solution would most likely be $[TcNX_4(H_2O)]^{1-}$. (**55**,**67**) In organic solvents, the site trans to the axial ligand is expected to be unoccupied or to contain a weakly bound solvent molecule. (**67**) The possibility that axial coordination of H_2O could result in a simplification of the spectrum will be investigated using density functional calculations in chapter 2.1.

Solid state, diffuse reflectance spectra recorded for both (TBA)$[TcNCl_4]$ and (TBA)$[TcNBr_4]$ (which would be expected to be five coordinate as a result of the large $(TBA)^+$ cation) (**55**) resemble the solution spectrum recorded in CH_2Cl_2 most closely. This lends further support to the notion that in CH_2Cl_2, the species in solution is authentic $[TcNX_4]^{1-}$ and not $[TcNCl_5]^{1-}$ or $[TcNCl_4(H_2O)]^{1-}$.

Chapter 1.5: Experimental

1.5.1 Synthesis

The primary source of technetium for the preparations detailed in this thesis was pertechnetate. It was obtained from Amersham International plc. as a potassium or ammonium salt and was used without any further purification. A flow chart of the technetium species prepared is presented in figure 1.55 and the details of each synthesis follow in the remainder of this section. It should be noted that all reactions were carried out in fumehoods or in sealed glass systems in laboratories approved for low-level radioactive materials. The tetra-n-butylammonium $(TBA)^+$ and tetra-ethylammonium $(TEA)^+$ salts were used throughout this study due to their solubility in the organic solvents, CH_2Cl_2 and CH_3CN, which were the solvents of choice for subsequent physical measurements.

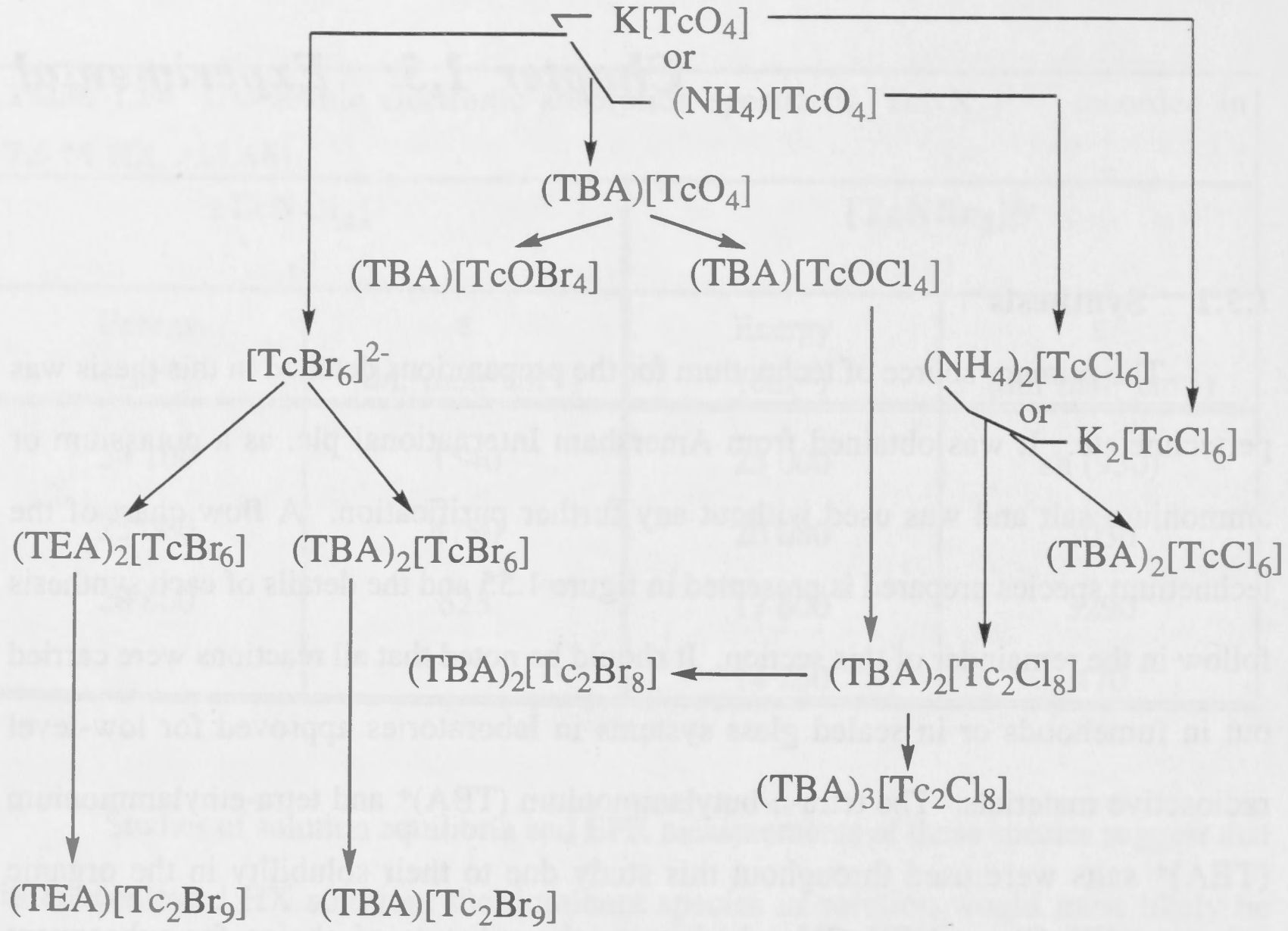

Figure 1.55 *Flowchart showing the technetium complexes which were prepared from pertechnetate during the course of this thesis.*

1.5.1.1 (TBA)[TcO_4]

(TBA)[TcO_4] was prepared in two ways: initially by dissolving K[TcO_4] in water and adding a slight excess of (TBA)Cl (dissolved in a minimal amount of water). The white precipitate of (TBA)[TcO_4] which formed was filtered and dried in vacuo. However, it was noted that K[TcO_4] more readily soluble in 0.1 M $HNO_{3\,(aq)}$ and so the second method employed that solvent and (TBA)HSO_4 also dissolved in 0.1 M HNO_3 was added. The white precipitate of (TBA)[TcO_4], obtained in quantitative yields, was filtered, washed with cold water and dried in vacuo.

1.5.1.2 (TBA)[$TcOX_4$]

(TBA)[$TcOX_4$] (where X = Cl or Br) ~~were~~ was prepared using slight variations on the methods originally described by Preetz and Peters (**29**).

1.5.1.2.1 (TBA)[$TcOCl_4$]

(TBA)[TcO_4] (400 mg) was prepared as described (in the immediately preceding section) and was collected and dried on a filter stick. To this was added concentrated aqueous HCl (7 mL). The mixture was allowed to react for 30 mins at room temperature during which $Cl_{2\,(g)}$ was formed. The HCl was then removed under vacuum through the frit. During this time the initially white solid reacted to form a grey-green precipitate.

$$(TBA)[TcO_4] + 6HCl \rightarrow (TBA)[TcOCl_4] + 3H_2O + Cl_{2\,(g)}$$

The solid was recrystallised by dissolution into CH_2Cl_2 followed by addition of *n*-hexane until precipitation of the product first commenced. The solution was then cooled to -30°C and kept at that temperature overnight. The resulting micro-crystalline solid was collected by filtration and dried in vacuo over KOH. The yield was 80% (390 mg) grey-green (TBA)[$TcOCl_4$].

1.5.1.2.2 (TBA)[$TcOBr_4$]

The preparation of (TBA)[$TcOBr_4$] required an analogous method to (TBA)[$TcOCl_4$]. (**29**) Concentrated, aqueous HBr was used in place of HCl. The HBr did not need to be particularly bromine free. After recrystallisation, the yield from 150 mg of (TBA)[TcO_4] was 75 % (190 mg) of gold coloured, micro-crystalline (TBA)[$TcOBr_4$].

1.5.1.3 $[TcX_6]^{2-}$

Two methods of preparation of $[TcCl_6]^{2-}$ were employed during the course of this thesis. The first (**39**,**68**) proved unreliable on occasions, due to contamination of

the product by $[TcOCl_4]^{1-}$, so a modification involving the use of KI (**68**) became the method of choice (both methods will be described for completeness). The preparation of $[TcBr_6]^{2-}$ (**69**) proceeded without complications.

1.5.1.3.1 $(NH_4)_2[TcCl_6]$ (method one)

The preparation of $(NH_4)_2[TcCl_6]$ involved treating $(NH_4)[TcO_4]$ in refluxing, concentrated HCl over a period of 9 hours (60 mg in 50 mL). As the HCl was added the solution became instantly yellow then this colour rapidly faded to an olive green. Continued refluxing saw the green change to a bright yellow over a period of hours. The various stages of the reaction may be represented by the scheme: (**68b**)

$$\underset{\text{white}}{(NH_4)Tc^{VII}O_4} \rightarrow \underset{\text{yellow}}{(NH_4)Tc^{VI}O_3Cl_3} \rightarrow \underset{\text{green}}{(NH_4)Tc^{V}OCl_4} \rightarrow \underset{\text{yellow}}{(NH_4)_2Tc^{IV}Cl_6}$$

The solution was concentrated on a rotary evaporator until a precipitate started to form and then it was left to stand at -30°C overnight. The solid was collected by vacuum filtration and dried overnight in a vacuum desiccator containing KOH. The yield of the first crop was 65% (75 mg) of yellow $(NH_4)_2[TcCl_6]$.

The filtrate was retained; it had a slight green tinge so further HCl was added and refluxing was continued for a further 12 hours. Further precipitation gave a final combined yield of 77% (total 90 mg).

1.5.1.3.2 $K_2[TcCl_6]$ (method two) (**68**)

A solution of $K[TcO_4]$ (100 mg) in warm concentrated HCl was prepared and an excess of KI was added (to act as a reducing agent).

$$K[TcO_4] + 3KI + 8HCl \rightarrow K_2[TcCl_6] + 4H_2O + 2KCl + 3/2I_2$$

The solution was heated and allowed to slowly concentrate to dryness (~6 hours). The brown residues which formed were redissolved in fresh concentrated HCl. This

procedure was repeated until no further iodine vapour was observed (typically three times) and yellow crystals precipitated. The crystals were isolated by filtration and were washed with a mixture of HCl/CH_3OH to remove any KCl impurities. The yield of yellow $K_2[TcCl_6]$ was 70 % (140 mg).

1.5.1.3.3 $(TBA)_2[TcCl_6]$

The cation exchange was achieved by dissolving either $(NH_4)_2[TcCl_6]$ or $K_2[TcCl_6]$ into dilute HCl and adding a slight excess of (TBA)Cl, dissolved in a minimum amount of dilute HCl, until the supernatant became colourless. The resulting yellow precipitate of $(TBA)_2[TcCl_6]$ was collected in near quantitative yields by vacuum filtration and dried in a vacuum desiccator over KOH.

1.5.1.3.4 $(NH_4)_2[TcBr_6]$ and $K_2[TcBr_6]$

Both $(NH_4)_2[TcBr_6]$ and $K_2[TcBr_6]$ were prepared by refluxing $(NH_4)TcO_4$ or $K[TcO_4]$ (165 mg) respectively in bromine free HBr for 6 hours. During which time the solution changed from colourless to red. The solution was evaporated on a rotary evaporator until precipitation commenced and then was left overnight at -30°C to crystallise. The resultant red solid was collected by vacuum filtration and then dried in a vacuum desiccator over KOH giving a 76 % yield (410 mg) .

1.5.1.3.5 $(TBA)_2[TcBr_6]$

The (organosoluble) salt was prepared by dissolving $(NH_4)_2[TcBr_6]$ or $K_2[TcBr_6]$ in dilute HBr and then adding a slight excess of (TBA)Br also dissolved in dilute HBr, until the solution was colourless (or a very pale orange). The resulting red precipitate of $(TBA)_2[TcBr_6]$ was collected in near quantitative yields by vacuum filtration and dried in a vacuum desiccator over KOH.

1.5.1.3.6 $(TEA)_2[TcBr_6]$

$(TEA)_2[TcBr_6]$ was prepared in an analogous manner to $(TBA)_2[TcBr_6]$, using (TEA)Br in place of (TBA)Br.

From the monomeric precursors described, the dimers were prepared by the following methods:

1.5.1.4 $[Tc_2X_8]^{n-}$

Two different methods, each employing a different monomeric precursor were used to prepare $(TBA)_2[Tc_2Cl_8]$. The first, reported by Cotton (**25**) uses $(NH_4)[TcCl_6]$ while the second and preferred method uses $(TBA)[TcOCl_4]$ as reported by Preetz (**31**). The synthesis of $(TBA)_2[Tc_2Br_8]$ was also based on a method reported by Preetz (**31**) and involves halide exchange of the pre-formed $(TBA)_2[Tc_2Cl_8]$ dimer. These procedures will each be described in turn.

1.5.1.4.1 $(TBA)_2[Tc_2Cl_8]$ (Cotton)

$K_2[TcCl_6]$ (254 mg) was placed in a 50 mL round bottomed flask under $N_{2\,(g)}$. 5mL concentrated HCl was added under stirring. Small pieces of freshly cut Zn metal (approx $1mm^3$) were added successively until the mixture changed colour from yellow through green to brown. The reaction was continued with stirring and further additions of zinc over a period of 2 hours until no more yellow solid was visible in the reaction mixture. At this stage the reaction mixture was filtered and evaporated in vacuo to dryness. The resulting brown oil was extracted several times with diethyl ether in 6 mL portions. On each occasion the ether was decanted from the mixture and retained (taking with it water and $ZnCl_2$). The extraction process was continued until the ether remained clear and a brown powder was left behind (3 x 6 mL). This brown solid was then dissolved in the minimum amount of HCl (8 mL) and a slight excess of (TBA)Cl (0.789 g in 30 mL), dissolved in water, was added. Upon addition of the (TBA)Cl, the technetium-based solution changed colour from brown to dark green. CH_2Cl_2 (10 mL) was added and the technetium product was extracted from the aqueous layer into this lower lying organic layer. Extractions were performed until no more coloured materials could be removed from the aqueous layer. The CH_2Cl_2 fractions were combined and the solvent was removed in vacuo. The resulting green solid was recrystallised from acetone with cooling at -30°C overnight giving a 32% yield (200 mg).

1.5.1.4.2 $(TBA)_2[Tc_2Cl_8]$ (Preetz)

$(TBA)[TcOCl_4]$ (133 mg) was dissolved in freshly distilled THF (10 mL) under an argon atmosphere. $(TBA)BH_4$ (135 mg) also dissolved in THF (5 mL) was added dropwise over a period of 5 minutes with stirring. The solution changed colour from green to brown. Ether was added until the brown product was precipitated leaving a clear supernatant layer (15 mL). The supernatant liquid was decanted and the remaining brown powder was collected and dried in vacuo, overnight. The brown powder was then redissolved in 5 mL CH_2Cl_2 and was then exposed to the air to facilitate partial oxidation. $HCl_{(g)}$ was bubbled through the solution for 20 minutes as the colour changed from dark brown to green brown. The solution was shaken in air for about 5 minutes and then returned to a Ar atmosphere;diethyl ether was added until precipitation of a dark green solid commenced. (The amount of exposure to air over these two steps is crucial and has a major impact on yields). The solution was then cooled at -30°C for 2 days. The resultant green crystals were collected by vacuum filtration and dried in vacuo giving a 39 % yield (50 mg).

1.5.1.4.3 $(TBA)_2[Tc_2Br_8]$

The halide exchange of the octachloride dimer to form the octabromide dimer was achieved by treating a solution of $(TBA)_2[Tc_2Cl_8]$ in CH_2Cl_2 with HBr gas which was produced by the dropwise addition of $HBr_{(aq)}$ to P_2O_5. The HBr gas was transported into the $[Tc_2Cl_8]^{2-}$ solution by a flow of argon gas. The initially dark green solution rapidly became dark red. The solution was evaporated to dryness under vacuum. The resulting red powder was redissolved in the minimum CH_2Cl_2 and was kept at -30°C overnight, resulting in the quantitative formation of red crystals of $(TBA)_2[Tc_2Br_8]$.

1.5.1.5 $[Tc_2Br_9]^{1-}$

$(TEA)[Tc_2Br_9]$ and $(TBA)[Tc_2Br_9]$ were prepared in a manner similar to that which was reported by Wendt and Preetz. (**1**) This preparation involves the use of trifluoroacetic acid as a halide extracting agent to prepare the nonahalide dimer from hexahalide monomers.

150 mg of red $(TBA)_2[TcBr_6]$ or $(TEA)_2[TcBr_6]$ respectively was added to trifluoroacetic acid (45 mL) in a 100 mL round bottomed flask and was heated to reflux (under nitrogen) for a period of two hours. During this time the colour changed quickly from a red suspension to brown and then more slowly to a brown-purple suspension. The product was filtered on a sintered glass funnel in air, washed with a little fresh trifluoroacetic acid and then dried under vacuum. The yield was 86% (70 mg of $(TBA)[Tc_2Br_9]$). The compound is stable as a solid in air, though some sensitivity to light was observed. Consequently it was stored under nitrogen and in the dark. The solid-state far-IR spectrum showed signals at 262, 244 and 181 cm^{-1} which correspond to those previously described at 267, 245 and 182 cm^{-1} (**6**) that were recorded under the same conditions. The purity of the sample was confirmed by comparisons of the EPR signals of samples of $(TBA)[Tc_2Br_9]$ with $(TBA)_2[TcBr_6]$ and by repeated voltammetric experiments.

1.5.1.6 Attempts to synthesise $[Tc_2Cl_9]^{1-}$

1.5.1.6.1 Method one: solid chlorinating agent

$(TBA)_2[Tc_2Cl_8]$ (22.15 mg) was dissolved CH_2Cl_2 (10 mL), under a nitrogen atmosphere at room temperature. A slight excess of *p*-$ClC_6H_4ICl_2$ (11.43 mg) was added and the green solution was stirred for 2 hours, after which time the solution was still green in colour. A further 15 mg of *p*-$ClC_6H_4ICl_2$ was added and the solution was refluxed for 1 hour. The CH_2Cl_2 was removed under vacuum, and the resultant yellow-green solid was washed with ether, redissolved in CH_2Cl_2 and the room temperature UV-visible absorption spectrum was recorded. The spectrum observed was consistent with the dominant species in solution being $[TcCl_6]^{2-}$.

$(TBA)_2[Tc_2Cl_8]$ (4.26 mg) was dissolved in CH_2Cl_2 (2 mL) and was transferred into a UV-visible cell. The solution was cooled to -40°C and a UV-visible spectrum was recorded. The solid chlorinating agent, *p*-$ClC_6H_4ICl_2$ (**36**), was added as an excess in the first instance and in a second experiment as a stoichiometric amount (2.05 mg). On both occasions the solution was allowed to gradually warm to room temperature and was monitored by UV-visible spectroscopy at 5°C intervals. The spectrum recorded at -20°C showed significant changes which corresponded to the release of Cl_2 by the chlorinating

agent and subsequent reaction of this Cl_2 with the $[Tc_2Cl_8]^{2-}$ to form $[TcCl_6]^{2-}$.

1.5.1.6.2 Method two: bulk-electrosynthesis

$(TBA)_2[Tc_2Cl_8]$ (20 mg) was added to 10 mL of electrolyte solution (0.5 M $TBABF_4/CH_2Cl_2$) in a bulk-electrosynthetic cell. The solution was cooled to -60°C and an excess of TBACl was added. Cyclic voltammetry on the green solution revealed one reversible reduction at -0.04 V ($[Tc_2Cl_8]^{2-/3-}$) accompanied by an overwhelming signal at +1.0 V corresponding to the oxidation of Cl^- to Cl_2. An oxidising potential of +1.2 V was applied to the bulk solution for a period of 4 hours during which time the green solution developed an increasingly yellow tinge. Periodic monitoring of the cyclic voltammetry of the solution during the electrolysis revealed a myriad of signals, some of which were recognisable as being due to the starting $[Tc_2Cl_8]^{2-}$ dimer, as well as free chloride, $[TcOCl_4]^{1-}$ and $[TcCl_6]^{2-}$. After 4 hours the solution was allowed to warm to room temperature. A CV was recorded and showed signals due to $[Tc_2Cl_8]^{2-}$ dimer, as well as free chloride, $[TcCl_6]^{1-}$ as well as other unidentified signals recorded at this stage indicated that $[TcCl_6]^{2-}$ was the dominant species in solution.

1.5.1.6.3 Method three: halide abstraction

$(TEA)_2[TcCl_6]$ (25 mg) was placed in a 50 mL round bottom flask under a N_2 atmosphere. CF_3COOH (12 mL) was added and the mixture was stirred to produce a suspension. Following 30 minutes of stirring at room temperature the suspension was slightly more orange-yellow in colour and the slightly-soluble product was identified as $(TEA)_2[Tc_2Cl_{10}]$. Further stirring accompanied by heating for 2 hours produced a red solution. The solution showed irreversible electrochemistry and a UV-visible spectrum which was suggestive of the formation of polymeric $[TcCl_4]_n^{n-}$ (**39**).

1.5.2 Electrochemical Techniques

1.5.2.1 Solvent and electrolytes

Voltammetric measurements, bulk electro-oxidation and spectro-electrochemical processes were all performed using CH_2Cl_2 or MeCN containing 0.5 M $(TBA)BF_4$ or $(TBA)PF_6$.

The electrolytes, $(TBA)BF_4$ and $(TBA)PF_6$ were prepared by neutralising (TBA)OH (40% in water) with HBF_4 or HPF_6, respectively, to pH = 6. The resulting white precipitate was collected by vacuum filtration and washed with large amounts of warm distilled water. It was then recrystallised twice from a 4:1 mixture of methanol/water and then dried in vacuo at 100^0C for 8 hours. At this stage the electrochemical background was checked. If contamination by chloride ions was observed then further washing with water and then recrystallisation were performed. If contamination by water was observed then further in-vacuo drying was undertaken until an acceptable background was achieved.

The solvent, dichloromethane, CH_2Cl_2, was pre-dried over KOH pellets before being distilled from P_2O_5 immediately before use. Acetonitrile was purified by refluxing and then distilling analytical grade acetonitrile from anhydrous $AlCl_3$, followed by alkaline $KMnO_4$, then $KHSO_4$ and finally, it was distilled from CaH_2 immediately before use. (**70**)

1.5.2.2 Voltammetry

Cyclic voltammetry (CV) and alternating current voltammetry (acV) measurements were conducted using a PAR 170 electrochemical system linked to a XY-recorder. One of two different electrochemical cell set-ups were used.

1.5.2.2.1 Standard electrochemical cell

The first cell employed a standard three-electrode configuration. The working electrode was a platinum bead and a platinum rod was used as a counter electrode. The reference electrode was Ag/AgCl (Metrohm) which was separated from the solution by two porous glass frits, thus forming two compartments. The internal compartment was filled with 0.05 M (TBA)Cl/0.45 M (TBA)BF_4 in CH_2Cl_2. While the external compartment was filled with the standard 0.5 M (TBA)BF_4 (or (TBA)PF_6) in CH_2Cl_2 electrolyte solution.

Ferrocene was used as a reference throughout this study and under the conditions just described it was reversibly oxidised to the ferrocinium cation at +0.55 V.

The electrochemical cell (of the first set-up) was a glass cell which was tapered to provide a volume capacity of about 5 mL of solution in the immediate vicinity of the ends of the electrodes. The electrolyte solutions were purged with either $N_{2\,(g)}$ or $Ar_{\,(g)}$ and the cell was also maintained under the same inert atmosphere.

Low temperature measurements were achieved by placing the cell in an acetone/dry-ice bath. The temperature was monitored (to within 0.2°C) during these measurements using a digital thermometer with the probe located directly in the electrochemical solution.

1.5.2.2.2 Evacuable electrochemical cell

The second set-up for voltammetry was especially designed to minimise hydrolysis, and involved the use of an evacuable electrochemical cell which has been previously described in full detail (**46**). The cell employed platinum wire for all three electrodes (that is, as working, counter and as a quasi-reference). These wires were vacuum sealed into the glass wall of the cell and were also spot welded to an external tungsten wire to make the external electrode connection more rigid. CH_2Cl_2 was vacuum distilled into the cell and solid materials could be added using break-seal techniques.

Ferrocene or $(TBA)_2[IrCl_6]$ was added to the cell at the end of each experiment to provide an internal reference for the observed potentials. $(TBA)_2[IrCl_6]$ has a reduction at +0.06 V and an oxidation at +1.79 V *vs* ferrocene at +0.55 V.

Cooling was achieved by placing an acetone/dry-ice mixture into the cooling finger, incorporated into the cells design. (**46**)

1.5.2.2.3 Scanning parameters

When using either of the electrochemical cell set-ups just described, typical scan rates were 100 mV s^{-1} for cyclic voltammetry and 10 mV s^{-1} for acV. The alternating current voltammetry measurements were recorded using feedback resistance compensation and phase-sensitive detection. The sinusoidal modulation was set at 10 mV and the frequency, ω, was 205 Hz.

1.5.2.2.4 Bulk electrolysis

The bulk electrolyses described in section 1.4 were performed using a three compartment H-cell, with a platinum-mesh, basket, working electrode. The reference electrode was the same double fritted Ag/AgCl set-up as was described earlier, section 1.5.2.2.1. The counter electrode was a platinum coil, which was separated from the bulk solution by two glass frits.

1.5.2.2.5 Criteria for reversible and irreversible voltammetry

The voltammetric measurements made using these cells were described in the previous sections, 1.2 to 1.6, as being reversible or irreversible. Unless otherwise specified these terms refer to voltammetric reversibility or irreversibility.

During the voltammetric experiment, only the small portion of the species in solution which is in the immediate vicinity of the working electrode actually undergoes the redox process. The rate of that process is controlled by the scan rate, such that a voltammetrically reversible process means charge-transfer is occurring considerably

faster than the rate of diffusion. Whether or not the process is strictly voltammetrically reversible can be determined from a set of standard criteria. (**71**) For a reversible, one-electron process these include, cyclic voltammetry with potentials independent of scan rate and the potential of the forward peak minus that of the reverse peak equals 0.059 V at room temperature and 0.042 V at 213 K. The acV shows a highly symmetric wave with a width at half height of 0.090 V (or 0.064 V at 213 K). Both CV and acV signals should look like the ferrocene to ferrocinium oxidation which is acknowledged as a voltammetrically reversible, one-electron process (**72**). This last point is important in non-aqueous media where high solution resistance can produce non-ideal responses for genuinely voltammetric reversible species (such as ferrocene). This is particularly a problem at low temperatures where resistance can be higher. (**73**)

A voltammetrically irreversible process is one where the product first formed at the electrode in the forward process is not returned to the starting species at any significant rate on the reverse scan. This irreversibility is also assessed against criteria including, when using cyclic voltammetry, the potential of the forward scan can vary with scan rate, and no significant return wave is observed. Using the acV method, normally no signal is observed.

1.5.2.3 UV-visible spectroscopy

UV-visible absorption spectra were recorded using a Perkin-Elmer λ9 double-beam UV/vis/near-IR spectrophotometer (range = 3125 - 50 000 cm^{-1}) with digital background subtraction capability.

The cell was calibrated to determine its optical path length (0.0457 cm) by recording the spectrum of a solution of a known concentration of $K_3[Fe(CN)_6]$.

1.5.2.3.1 Spectro-electrochemistry

Solutions for spectro-electrochemistry were made up as described previously for other electrochemical experiments, that is 0.5 M (TBA)BF_4 (or (TBA)PF_6) in CH_2Cl_2.

The solvent and electrolyte were also prepared in the same manner as described for the voltammetry. Prior to each experiment a UV-visible background was recorded of this electrolyte solution. Under these conditions spectra were recorded from 5000 - 45 000 cm^{-1}.

The spectra of the electro-generated species were collected *in situ*, using an optically transparent thin layer electrochemical cell (OTTLE cell). The design of this cell and the additional electrochemical set-up has been described previously (**74**). The basic design involved a platinum minigrid as a working electrode which was placed into the cell and it permitted about 70% transmission of the sample beam. A matching cell and grid set-up was placed in the reference beam of the spectrophotometer.

The top part of the sample cell was widened to also accommodate a platinum wire counter electrode and the same Ag/AgCl reference electrode described earlier. Both of these electrodes were separated from the bulk solution by salt bridges containing electrolyte solution. These two electrodes, along with the working electrode were connected to a Thompson E-series Ministat potentiostat. A platinum wire was spot welded to the top of the grid in the sample cell to facilitate this connection. This wire was sheathed by poly(tetrafluoroethylene) tubing to ensure any reaction occurred in the sample beam rather than at the top of the cell.

During a typical experiment, both the sample and reference cells, were cryostatted in gas-tight, double glazed, poly(tetrafluoroethylene) cell blocks enabling both the cell and its contents to be cooled by cold $N_{2\,(g)}$ which itself was cooled by passing through copper coils immersed in liquid nitrogen before entering the cell block. The temperature of the $N_{2\,(g)}$ was controlled by an automatic resistive heater which was driven by a Bruker variable temperature unit VT-1000. A thermocouple was positioned within the compartment, at the point of gas out flow from the cell block. A known difference between gas outflow temperature and the temperature of the solution within the cells allowed the latter to be accurately established and maintained at the desired temperature.

To prevent fogging of the cell-block windows, room temperature N_2 gas was passed between the inner and outer windows.

The electrolysis was typically carried out at a potential 200 - 300 mV beyond the relevant E^0, measured by cyclic voltammetry. The electrolysis was continued until the spectrum ceased to change and the current within the cell decayed to a minimum. After completion the potential was reset in order to regenerate the spectrum of the starting complex. The regeneration of the spectrum of the starting complex without any loss or gain of features, or any change in the intensity of same, in combination with stable isobestic points was taken as evidence for the chemical reversibility of the process. For systems such as $[Tc_2Br_9]^{1-}$ which had more than one redox process, this procedure was repeated for each step before proceeding to the subsequent process.

This reversible electrolysis in the OTTLE cell is an example of a chemically reversible process, that is, an electrogeneration procedure can be carried out to completion and can be fully reversed to recover the starting species without loss. Chemical reversibility depends on the stability of the electrode product and is independent of the kinetics of the electron transfer.

References: Part One

1. A. Wendt and W. Preetz, *Z. Anorg. Allg. Chem.*, 1993, **619**, 1669.

2. (*a*) G.A. Heath and D.G. Humphrey, *J. Chem. Soc., Chem. Commun.*, 1990, 672; (*b*) D.G. Humphrey, *Ph.D. Thesis*, The Australian National University, 1992.

3. A. Earnshaw, *Introduction to Magnetochemistry*, Academic Press, London, 1968, 70.

4. I.E. Grey and P.W. Smith, *Austr. J. Chem.*, 1971, **24**, 73.

5. I.E. Grey and P.W. Smith, *Austr. J. Chem.*, 1969, **22**, 121.

6. J.L. Hayden and R.A.D. Wentworth, *J. Am. Chem. Soc.*, 1968, **90**, 5291.

7. G.A. Heath, B.J. Kennedy and K.S. Murray, *Unpublished results.*

8. G.A. Heath, J.E. McGrady, R.G. Raptis and A.C. Willis, *Inorg. Chem.*, 1996, **35**, 6838.

9. G.A. Heath, R.G. Raptis and A.C. Willis, *Unpublished results*, (*RSC Annual Report,* 1991, 113).

10. (*a*) T. Lovell, J.E. McGrady, R. Stranger and S.A. Macgregor, *Inorg. Chem.*, 1996, **35**, 3079; (*b*) J.E. McGrady, T. Lovell and R. Stranger, *J. Chem. Phys.*, in press.

11. T. Lovell, J.E. McGrady and R. Stranger, *Personal communication*.

12. L. Noodleman and J.G. Norman Jr., *J. Chem. Phys*., 1979, **70**, 4903.

13. R. Stranger, I.E. Grey, I.C. Madsen and P.W. Smith, *J. Solid State Chem*., 1987, **69**, 162.

14. R.T. Carlin and R.A. Osteryoung, *Inorg. Chem*., 1988, **27**, 1482.

15. R.G. Raptis, *Unpublished results*.

16. G.A. Heath and R.G. Raptis, *Inorg. Chem*., 1991, **30**, 4106.

17. R.G. Raptis and G.A. Heath, *Unpublished results*, (*RSC Annual Report*, 1991, 64).

18. P. Pyykkö, *Chem. Rev*., 1988, **88**, 563.

19. G.A. Heath, K.H. Moock, D.W.A. Sharp and L.J. Yellowlees, *J. Chem. Soc., Chem. Commun*., 1985, 1503.

20. V.T. Coombe, G.A. Heath, T.A. Stephenson and D.K. Vattis., *J. Chem. Soc., Dalton Trans*., 1983, 2307.

21. (*a*) G.A. Heath and J.E. McGrady, *J. Chem. Soc., Dalton Trans*., 1994, 3759; (*b*) J.E. McGrady, *Ph.D. Thesis*, The Australian National University, 1994.

22. A.B.P. Lever, *Inorganic Electronic Spectroscopy*, Elsevier, New York, 1984, **2nd ed**., 739.

23. G.A. Heath and R.G. Raptis, *Inorg. Chem.*, 1991, **30**, 4106.

24. F. Bonati and F.A. Cotton, *Inorg. Chem.*, 1967, **6**, 1353.

25. F.A. Cotton, L. Daniels, A. Davison and C. Orvig, *Inorg. Chem.*, 1981, **20**, 3051.

26. (*a*) F.A. Cotton and W.K. Bratton, *J. Am. Chem. Soc.*, 1965, **87**, 921; (*b*) W.K. Bratton and F.A. Cotton, *Inorg. Chem.*, 1970, **9**, 789.

27. (*a*) F.A. Cotton, A. Davison, V.W. Day, M.F. Fredrich, C. Orvig and R. Swanson, *Inorg. Chem.*, 1982, **21**, 1211; (*b*) F.A. Cotton and E. Pedersen, *Inorg. Chem.*, 1975, **14**, 383.

28. F.A. Cotton and B.J. Kalbacher, *Inorg. Chem.*, 1977, **16**, 2386.

29. W. Preetz and G. Peters, *Z. Naturforsch.*, 1980, **35b**, 1355.

30. S.V. Kryuchkov and A.E. Simonov, *Bull. Acad. Sci. USSR, Div. Chem. Sci.*, 1987, **36**, 1991.

31. G. Peters, J. Skowronek and W. Preetz, *Z. Naturforsch*, 1992, **47a**, 591.

32. F.A. Cotton, P.E. Fanwick. L.D. Gage, B.J. Kalbacher and D.S. Martin, *J. Am. Chem. Soc.*, 1977, **99**, 5642.

33. S.F. Gheller, G.A. Heath and R.G. Raptis, *J. Am. Chem. Soc.*, 1992, **114**, 7924.

34. G.A. Heath and R.G. Raptis, *J. Am. Chem. Soc.*, 1993, **115**, 3768.

35. F.A. Cotton and R.A. Walton, *Multiple Bonds Between Metal Atoms*, Oxford University Press, 1993, **2nd ed.**, (*a*) Section 9.4, page 600; (*b*) Section 1.1, page 1; (*c*) Section 10.3, page 699.

36. H.J. Lucas and E.R. Kennedy, *Org. Synth.*, 1955, **3**, 482.

37. S.F. Gheller, *Personal communication.*

38. A. Wendt and W. Preetz, *Z. Anorg. Allg. Chem.*, 1994, **620**, 655.

39. A. Seidel, *Gmelin Handbook*, Tc Suppl., 1982, **1**, 91.

40. B.J. Kennedy and G.A. Heath, *Inorg. Chim. Acta.*, 1992, **195**, 101.

41. M. Kawashima, M. Kayama and T. Fujinaga, *J. Inorg. Nucl. Chem.*, 1976, **38**, 819.

42. B.J. Kennedy and G.A. Heath, *Inorg. Chim. Acta*, 1991, **187**, 149.

43. (*a*) C.K. Jørgensen and K. Schwochau, *Z. Naturforsch. A*, 1965, **20**, 65; (*b*) H.J. Schenk and K. Schwochau, *Z. Naturforsch. A*, 1973, **28**, 89.

44. H.S. Trop, A. Davison, G.H. Carey, B.V. DePamphilis, A.G. Jones and M.A. Davis, *J. Inorg. Nucl. Chem.*, 1979, **41**, 271.

45. E.W. Huber, W.R. Heineman and E. Deutsch, *Inorg. Chem.*, 1987, **26**, 3718.

46. K.H. Moock and M.H. Rock, *J. Chem. Soc., Dalton Trans.*, 1993, 2459.

47. G.A. Heath, K.H. Moock, D.W.A. Sharp and L.J. Yellowlees, *Unpublished results.*

48. A. Guest and C.J.L. Lock, *Can. J. Chem.*, 1972, **50**, 1807.

49. F.A. Cotton, A. Davison, V.W. Day, L.D. Gage and H.S. Trop, *Inorg. Chem.*, 1979, **18**, 3024.

50. A. Davison, H.S. Trop, B.V. DePamphilis and A.G. Jones, *Inorg. Synth.*, 1982, **21**, 160.

51. R.W. Thomas, A. Davison, H.S. Trop and E. Deutsch, *Inorg. Chem.*, 1980, **19**, 2840.

52. J. Baldas, J.F. Boas, J. Bonnyman and G.A. Williams, *J. Chem. Soc., Dalton Trans.*, 1984, 2395.

53. J. Baldas, *Topics in Current Chemistry*, 1996, **176**, 37.

54. J. Baldas, *Adv. Inorg. Chem.*, 1994, **41**, 1.

55. J. Baldas, S.F. Colmanet and G.A. Williams, *Inorg. Chim. Acta.*, 1991, **179**, 189.

56. D. Mantegazzi, E. Ianoz, P. Lerch and K.Tatsumi, *Inorg. Chim. Acta.*, 1990, **167**, 195.

57. R.W. Thomas, M.J. Heeg, R.C. Elder, E. Deutsch, *Inorg. Chem.*, 1985, **24**, 1472.

58. J. Baldas and S.F. Colmanet, *Austr. J. Chem.*, 1989, **42**, 1155.

59. R. Hübener and U. Abram, *Z. Anorg. Allg. Chem.*, 1992, **617**, 96.

60. J. Baldas, J. Bonnyman and G.A. Williams, *Austr. J. Chem.*, 1985, **38**, 215.

61. S.V. Kryuchkov, Yu. V. Rakitin, P.E. Kazin, A.I. Zhirov and N. Yu. Konstantinov, *Koord. Khim.*, 1990, **16**, 1230 (eng. trans. 660).

62. J. Baldas, G.A. Heath, S.A. Macgregor, K.H. Moock, S.C. Nissen and R.G. Ratpis, *J. Chem. Soc., Dalton Trans.*, manuscript in preparation.

63. K.H. Moock, S.A. Macgregor, G.A. Heath, S. Derrick and R.T. Boeré, *J. Chem. Soc., Dalton Trans.*, 1996, 2067.

64. K.H. Moock, *Ph.D. Thesis*, University of Glasgow, 1985.

65. J. Baldas, G.A. Heath, R.G. Raptis and G.A. Williams, *Unpublished results.*

66. J. Baldas, J.F. Boas, Z. Ivanov and B.D. James, *Proceedings of the 4th International Symposium on Technetium Chemistry and Nuclear Medicine*, 1994, 69.

67. J. Baldas, J.F. Boas and J. Bonnyman, *J. Chem. Soc., Dalton Trans.*, 1987, 1721.

68. (*a*) R. Colton and R.D. Peacock, *Quart. Rev.*, 1962, **16**, 299;
(*b*) D.I. Ryabchikov and A.A. Pozdnyakov, *Dokl. Akad. Nauk SSSR*, 1964, **155**, 256 (eng. trans.).

69. K. Schwochau, *Angew. Chem.*, 1964, **76**, 9.

70. M. Walter and L. Ramaley, *Anal. Chem.*, 1973, **45**, 165.

71. A.J. Bard and L.R. Faulkner, *Electrochemical Methods: Fundamentals and Applications*, John Wiley and Sons, Inc., New York, 1980.

72. (*a*) R.R. Gagné, C.A. Koval and G.C. Lisensky, *Inorg. Chem.*, 1980, **19**, 2854; (*b*) G. Gritzner and J. Kuta, *Pure Appl. Chem.*, 1982, **54**, 1527.

73. M. Kong, A.M. Bond and A.G. Wedd, *Inorg. Chem.*, 1980, **19**, 2854.

74. C.M. Duff and G.A. Heath, *Inorg. Chem.*, 1991, **30**, 2528.

PART TWO

Computers were invented by Murphy.

- Kemsley

Chapter 2.1 : Density functional calculations on tetrahalo -oxotechnetate and -nitridotechnetate complexes, $[TcYX_4]^{n-}$ (where Y = O, N; X = Cl, Br and n = 0, 1, 2)

The assignments of the UV-visible spectral data for the group of compounds, $[TcYX_4]^{n-}$ (where Y = O, N; X = Cl, Br; n = 0, 1, 2) given in chapter 1.4, were based on qualitative observations and supported by a series of density functional calculations on these species. These assignments highlighted the importance of the contribution of halide to metal charge transfer to the observed spectra, and also focussed attention on the changes in these spectra which result from a change in oxidation state of the metal and/or of changing the axial ligand, Y. The following section is devoted to a detailed account of the computational analysis that led to the proposed assignments.

2.1.1 Using calculations to assign observed UV-visible absorption spectra

In order to propose spectral assignments, the transition energies were determined using the ΔSCF method (**1**) (see chapter 2.3) for all possible transitions. The most likely spectral assignments were then selected by considering the following points relating to transition energy and intensity.

2.1.1.1 Transition energy

It has been previously shown that density functional calculations do not provide accurate absolute estimations of transition energies, especially for those involving charge transfer processes. (**2**,**3**) They have been found to under-estimate ligand to metal charge transfer by 1000 to 10 000 cm^{-1} depending on the system (**2**). Such calculations are still be of use as they generally provide satisfactory relative transition energies. They have also been found to perform better in absolute energy terms on transitions not

involving charge transfer, that is on d-d or ligand to ligand processes. Hence computed d-d and ligand to metal charge transfer transitions will be considered independently when determining spectral assignments.

2.1.1.2 Transition intensity

The ADF program employed here does not have any facility for computing oscillator strengths (and hence transition intensities) directly. However, the most intense observed transitions (with $\varepsilon > 1000$ $dm^3mol^{-1}cm^{-1}$) would be expected to be electric dipole allowed. Under C_{4v} symmetry such transitions will have transition moment operators which transform as e or a_1, equating to any transition which involves an e level as either the donor or acceptor orbital or which occurs between two orbitals of the same symmetry. Forbidden transitions, if observed at all, would be expected to have much lower intensities.

Another factor which impacts on the intensities of ligand to metal charge transfer and which has proven to be very important in determining the spectral assignments proposed in this chapter is the degree of physical overlap between the ligand donor and metal acceptor orbitals (**3**). In other words, transitions into an acceptor level which has out-of-plane π-character can be expected to have observable intensity if the donor level also has, at least some, out-of-plane π-character. For transitions involving donor or acceptor levels which are not 100% in-plane π-character, the relative intensity of that transition will show a relation to the relative amount of common character in each of the two levels. The same type of considerations apply for transitions between levels with in-plane σ- or in-plane π-character.

The major theme throughout this chapter is that the differences in the observed spectra of the $[TcOX_4]^{n-}$ (where X = Cl, n = 0, 1; X = Br, n = 1) and $[TcNX_4]^{n-}$ (where X = Cl, Br and n = 1, 2) species can be accounted for in terms of varying degrees of in-plane σ-, in-plane π-, and out-of-plane π-character within the e-type halide based donor levels in which these individual characters can mix. This extent of mixing impacts on

whether charge transfer transitions from these e-type levels into metal based acceptor levels of predominantly out-of-plane π- and in-plane σ-character will be observed at all and when observed, their relative intensity. To this end, the optimised geometry and the electronic structure for each $[TcYX_4]^{n-}$ species will be described and compared. In the second half of this chapter, transitions within the electronic structure will be determined and from these, spectral assignments proposed.

2.1.2 The calculated geometries of $[TcYX_4]^{n-}$

Density functional calculations were performed on the series of complexes $[TcYX_4]^{n-}$ (where Y = O, N; X = Cl, Br; n = 0, 1, 2). All calculations were performed under C_{4v} symmetry with the x, y, and z axes oriented as illustrated in figure 2.1.

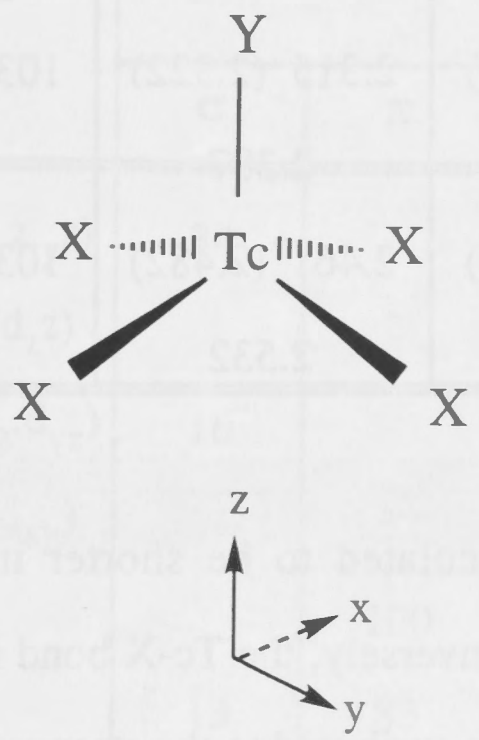

Figure 2.1 *Showing how the axes were oriented for the calculations on $[TcYX_4]^{n-}$. The z axes is oriented along the Tc-Y bond and the x and y axes are oriented along the Tc-X bonds.*

Density functional calculations have been found previously to give good results in the geometry optimisations of similar types of complexes, $[MNCl_4]^{1-}$ and $[MOCl_5]^{2-}$ (where M = Mo and W) (**4**) and $[OsNCl_4]^{1-}$ (**5**). The optimised geometries for the square pyramidal $[TcYX_4]^{n-}$ species are presented in table 2.2.

It can be seen from table 2.2 that, in general, the optimised geometries are in good agreement with the previously reported crystal structures. The agreement is particularly good for the Y-Tc-X bond angle and the Tc-X bond length. However, the optimised distance for Tc-Y is consistently over-estimated, by up to 5%. This has been previously found for the geometry optimisation of the related $[OsNCl_4]^{1-}$ complex (**5**).

Table 2.2 Geometry optimisations of $[TcYX_4]^{n-}$ compared to the available reported crystal structure data which are presented in parenthesis.

Complex#	Tc - Y (Å)	Tc - X (Å)	Y - Tc - X (degrees)	Reference
$[Tc^{V}OCl_4]^{1-}$	1.674 (1.593)	2.298 (2.309)	107.6 (106.8)	(**6**)
$[Tc^{VI}OCl_4]^{0}$	1.674	2.253	106.1	
$[Tc^{V}OBr_4]^{1-}$	1.672 (1.613)	2.445 (2.460)	107.4 (106.6)	(**7**)
$[Tc^{VI}NCl_4]^{1-}$	1.639 (1.581)	2.315 (2.322)	103.8 (103.3)	(**8**)
$[Tc^{V}NCl_4]^{2-}$	1.640	2.387	105.0	
$[Tc^{VI}NBr_4]^{1-}$	1.640 (1.596)	2.461 (2.482)	103.8 (103.0)	(**9**)
$[Tc^{V}NBr_4]^{2-}$	1.637	2.532	104.4	

The Tc-Y bond is calculated to be shorter in the nitrido complexes ~~than~~ the analogous the oxo species. Conversely, the Tc-X bond is longer in the nitrido species. These bonding trends have been attributed to the stronger technetium-nitrido interaction as compared to the interaction with oxo ligand. The calculated Tc-X bond distances were seen to lengthen upon reduction from the d^1 species to d^2 while the Tc-Y distance showed much less dependence on oxidation state. This result is consistent with crystal structures recorded in two oxidation states for the $[MoNCl_4]^{1-}$ and $[MoNCl_4]^{2-}$ species (**4**).

A detailed description of the calculated electronic structure of $[TcOCl_4]^{1-}$ (as a representative of this series of compounds) will be presented in the next section. This will be followed by an outline of the changes which occur in the electronic structure as

$[Tc^{VI}OBr_4]^{0}$ could not be generated experimentally so it was not investigated during the computational analyses.

a result of changes to the axial ligand, halide array and the oxidation state of the technetium metal centre.

2.1.3 The electronic structure of $[TcOCl_4]^{1-}$

Table 2.3 shows the calculated energy and percentage compositions of the valence molecular orbitals of $[TcOCl_4]^{1-}$. These results are also presented graphically and schematically (for selected levels) in figure 2.4.

Table 2.3 The calculated electronic structure of $[TcOCl_4]^{1-}$.

Orbital	Energy (eV)	Percentage composition						
		Tc	Cl			O		
		4d	in-plane		out-plane	$2p_x$, $2p_y$	$2p_z$	
			σ	π	π ($2p_z$)			
$4b_1$	+1.238	53 ($d_{x^2-y^2}$)	34		9			
$8a_1$	+0.950	46 (d_{z^2})			17		22	
7e	-0.212	54 (d_{xz},d_{yz})	16		2	23		
$2b_2$	-1.212	65 (d_{xy})		32				
$1a_2$	-2.397			100				
6e	-3.199		13	83				
$3b_1$	-3.333		20		80			
5e	-3.478		< 1	2	89	7		
$7a_1$	-4.492		10		75		8	
4e	-5.042		60	13		17		
$1b_2$	-5.518	30 (d_{xy})		69				
$6a_1$	-6.105	1 (d_{z^2})	76		5		6	
$2b_1$	-6.106	36 ($d_{x^2-y^2}$)	47		12			
3e	-7.009	37 (d_{xz},d_{yz})	9		3	50		
$5a_1$	-7.439	31 (d_{z^2})			4		54	

The four highest lying molecular levels, $2b_2$, 7e, $8a_1$ and $4b_1$ are predominantly metal based and represent the technetium 4d levels in the order $d_{xy} < d_{xz}, d_{yz} < d_{z^2} < d_{x^2-y^2}$ respectively. Each of these levels also contains some ligand character oriented in an antibonding fashion with respect to the metal. In $[Tc^{V}OCl_4]^{1-}$ (d^2) the d_{xy} level ($2b_2$) is fully occupied and is the highest occupied molecular orbital (it is highlighted by shading in table 2.3). An electron is removed from this level during the oxidation to $[Tc^{VI}OCl_4]^{0}$ (d^1) which was described in chapter 1.4.

The two lowest lying molecular levels in table 2.3 ($5a_1$ and 3e) are predominantly oxygen based. The orbitals of the axial oxygen are oriented in a bonding fashion with respect to the metal (see figure 2.4). In general, the oxygen based levels are lower in energy in $[TcOCl_4]^{1-}$ and therefore, are unlikely to be involved in any of the UV-visible transitions observed in the usual spectral range studied between 10 000 - 40 000 cm^{-1}.

The molecular orbitals positioned between the two extremes just described, are based on contributions from the $\{Cl_4\}$ manifold. These contributions are oriented in a number of different ways with respect to both the metal and the $\{Cl_4\}$ plane, as is shown in figure 2.4.

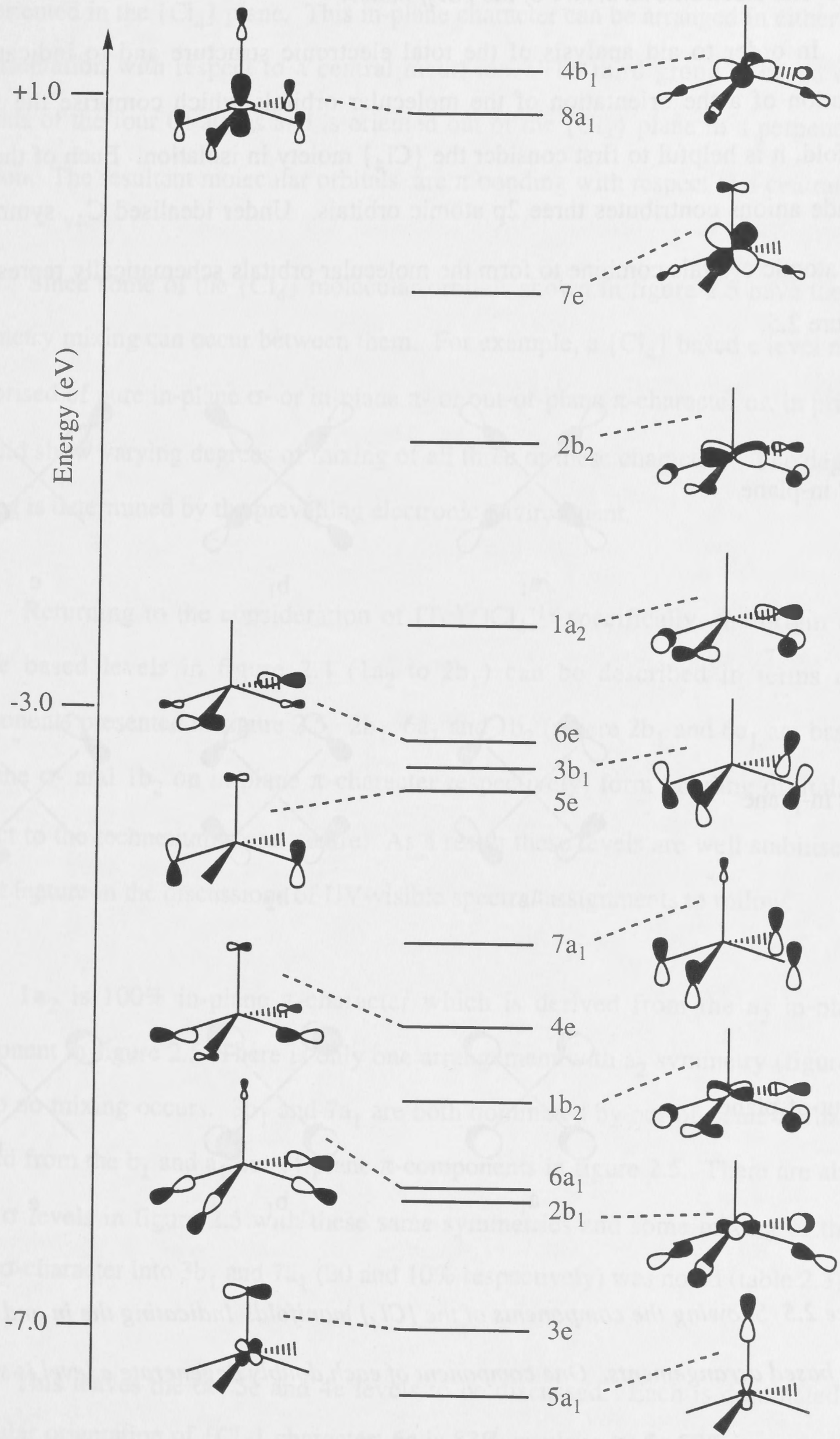

Figure 2.4 *Valence orbital molecular energy level diagram for* $[TcOCl_4]^{1-}$ *as determined by density functional calculations. Only one orientation for each doubly degenerate e pair is shown.*

2.1.3.1 *The electronic structure of the $\{Cl_4\}$ moiety*

In order to aid analysis of the total electronic structure and to indicate the derivation of the orientation of the molecular orbitals which comprise the $\{Cl_4\}$ manifold, it is helpful to first consider the $\{Cl_4\}$ moiety in isolation. Each of the four chloride anions contributes three 2p atomic orbitals. Under idealised C_{4v} symmetry, these atomic orbitals combine to form the molecular orbitals schematically represented in figure 2.5.

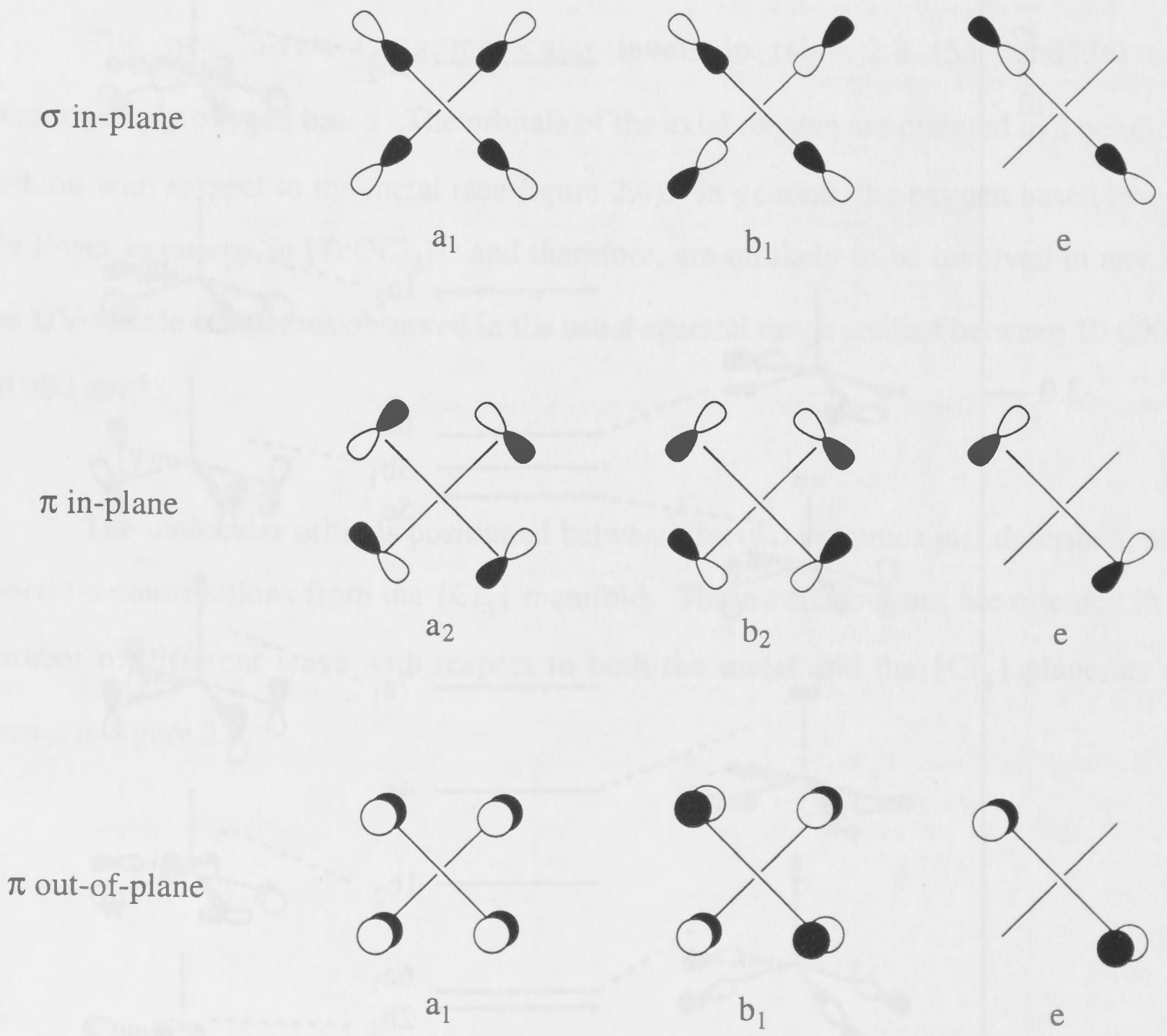

Figure 2.5 *Showing the components of the $\{Cl_4\}$ manifold. Indicating the in and out of plane based arrangements. One component of each doubly degenerate e level is shown.*

These molecular orbitals can be divided into three groups (as indicated in figure 2.5) based on their orientation with respect to the $\{Cl_4\}$ plane and a central metal ion. The first two groups are based on the $2p_x$ and $2p_y$ orbitals of the four Cl atoms and so

are oriented in the $\{Cl_4\}$ plane. This in-plane character can be arranged in either a σ or π orientation with respect to a central metal ion. The third group is based on $2p_z$ orbitals of the four Cl atoms and is oriented out of the $\{Cl_4\}$ plane in a perpendicular fashion. The resultant molecular orbitals are π bonding with respect to a central metal ion.

Since some of the $\{Cl_4\}$ molecular orbitals shown in figure 2.5 have the same symmetry mixing can occur between them. For example, a $\{Cl_4\}$ based e level may be comprised of pure in-plane σ- or in-plane π- or out-of-plane π-character or, in principle it could show varying degrees of mixing of all three of these characters. The degree of mixing is determined by the prevailing electronic environment.

Returning to the consideration of $[Tc^{V}OCl_4]^{1-}$ specifically, the origin of the halide based levels in figure 2.4 ($1a_2$ to $2b_1$) can be described in terms of the components presented in figure 2.5. $2b_1$, $6a_1$ and $1b_2$ (where $2b_1$ and $6a_1$ are based on in-plane σ- and $1b_2$ on in-plane π-character respectively) form bonding orbitals with respect to the technetium metal centre. As a result these levels are well stabilised and do not feature in the discussions of UV-visible spectral assignments to follow.

$1a_2$ is 100% in-plane π-character which is derived from the a_2 in-plane π component in figure 2.5 There is only one arrangement with a_2 symmetry (figure 2.5) and so no mixing occurs. $3b_1$ and $7a_1$ are both dominated by out-of-plane π-character derived from the b_1 and a_1 out-of-plane π-components in figure 2.5. There are also in-plane σ levels in figure 2.5 with these same symmetries and some mixing of this in-plane σ-character into $3b_1$ and $7a_1$ (20 and 10% respectively) was noted (table 2.3).

This leaves the 6e, 5e and 4e levels to be discussed. Each is dominated by a particular orientation of $\{Cl_4\}$ character; 6e is 83% in-plane π; 5e 89% out-of-plane π and 4e is 60% in-plane σ. Each of the three levels shows some mixing of $\{Cl_4\}$ character other than the one by which it is dominated but each of these contributions do not exceed 15% of the total composition of the orbital.

Analysis of the computed electronic structure of other $[TcYX_4]^{n-}$ complexes to be presented in the following sections indicated that a similar molecular orbital scheme applies for all of the species under consideration here. However some differences in the ordering and relative energetic spacings were indicated by the calculations. Differences in the compositions of some orbitals (especially the e-type levels just described) were also computed.

2.1.4 The electronic structure of $[TcOCl_4]^{1-}$ *vs* $[TcNCl_4]^{2-}$

These two species are isoelectronic (d^2). The relative energies of the molecular orbitals dominated by technetium metal based character of both species are compared in figure 2.6. The energies of these molecular orbitals are set relative to the $1a_2$ orbital, which was found to maintain 100% $\{X_4\}$ in-plane π-character in all of the calculations to be described and therefore is a good zero.

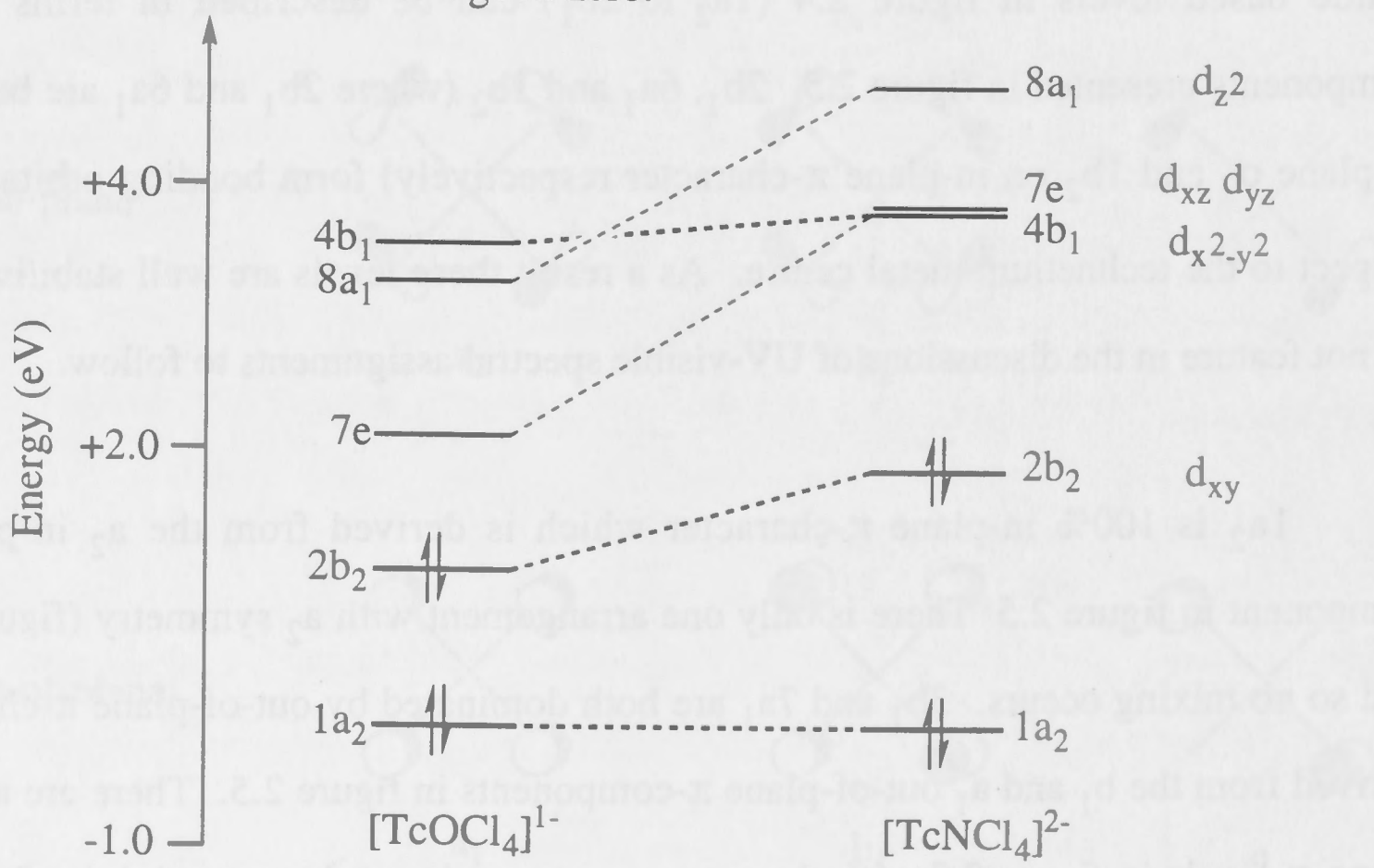

Figure 2.6 *A comparison of the energies of the metal based levels of* $[TcOCl_4]^{1-}$ *and* $[TcNCl_4]^{2-}$ *with the* $1a_2$ *non-bonding chloride level included as a zero.*

Figure 2.6 illustrates that the splitting of the metal based levels in these two species is very different. In particular, there is an increased destabilisation of the $8a_1$ and 7e orbitals in the nitrido species. These two levels involve direct anti-bonding σ and π interactions respectively with the axial ligand and so are the most likely to be

affected by this change at the axial ligand site. The relative destabilisation of both orbitals in the nitrido case is indicative of the greater σ and π donor qualities of the nitrido ligand.

Another important difference in the electronic structure of these two complexes, within the context of the spectral assignments to be presented later in this chapter, is in the degree of mixing of halide in-plane σ-, in-plane π- and out-of-plane π-character in the $\{Cl_4\}$ e levels. This is best illustrated by comparing the percentage composition of the nitrido levels listed in table 2.7 with their oxo counterparts which were detailed in table 2.3.

Table 2.7 Calculated electronic structure of $[TcNCl_4]^{2-}$.

Orbital	Energy (eV)	Percentage composition						
		Tc	Cl			N		
		4d	in-plane		out-plane	$2p_x$ $2p_y$	$2p_z$	
			σ	π	π ($2p_z$)			
$1a_2$	+2.245			100				
6e	+1.732		19	44	24	11		
$3b_1$	+1.482		15		85			
5e	+1.416		< 1	39	50	7		
$7a_1$	+0.947				69		21	
4e	+0.285		51	13	17	14		

It is clear from this comparison that there is significantly greater mixing of $\{Cl_4\}$ in-plane σ-, in-plane π- and out-of-plane π-characters in the 6e and 5e levels in particular and also to a lessor extent in the 4e level of $[TcNCl_4]^{2-}$ than in $[TcOCl_4]^{1-}$. This different degree of mixing has an impact on the appearance and assignment of UV-visible spectra, as will be discussed later in this chapter.

As found for the oxo-based levels in $[TcOX_4]^{1-}$, the equivalent nitrido-based levels in $[TcNX_4]^{2-}$ lie to low energy, some 7 eV below the lowest lying available technetium based level, $4b_1$, and so are not expected to be involved in transitions in the observed experimental region.

2.1.5 The electronic structure of $[TcOCl_4]^{1-}$ *vs* $[TcOCl_4]^{0}$ and $[TcNCl_4]^{2-}$ *vs* $[TcNCl_4]^{1-}$

In both cases, oxidation of an electron from the $2b_2$ orbital results in a stabilisation of the metal based orbitals relative to the $1a_2$ orbital (see figure 2.8). This effect is greater in the nitrido species and is most pronounced for the $2b_2$ and 7e molecular orbitals. This stabilisation facilitates a greater mixing of ligand based character into the metal based levels of the oxidised d^1 species as well as greater metal character in the stabilised chloride based orbitals ($2b_1$, $6a_1$, $1b_2$) which are in bonding combination with the metal centre. The composition of the $\{Cl_4\}$ based non-bonding orbitals remains relatively unchanged by oxidation (for example, see table 2.10).

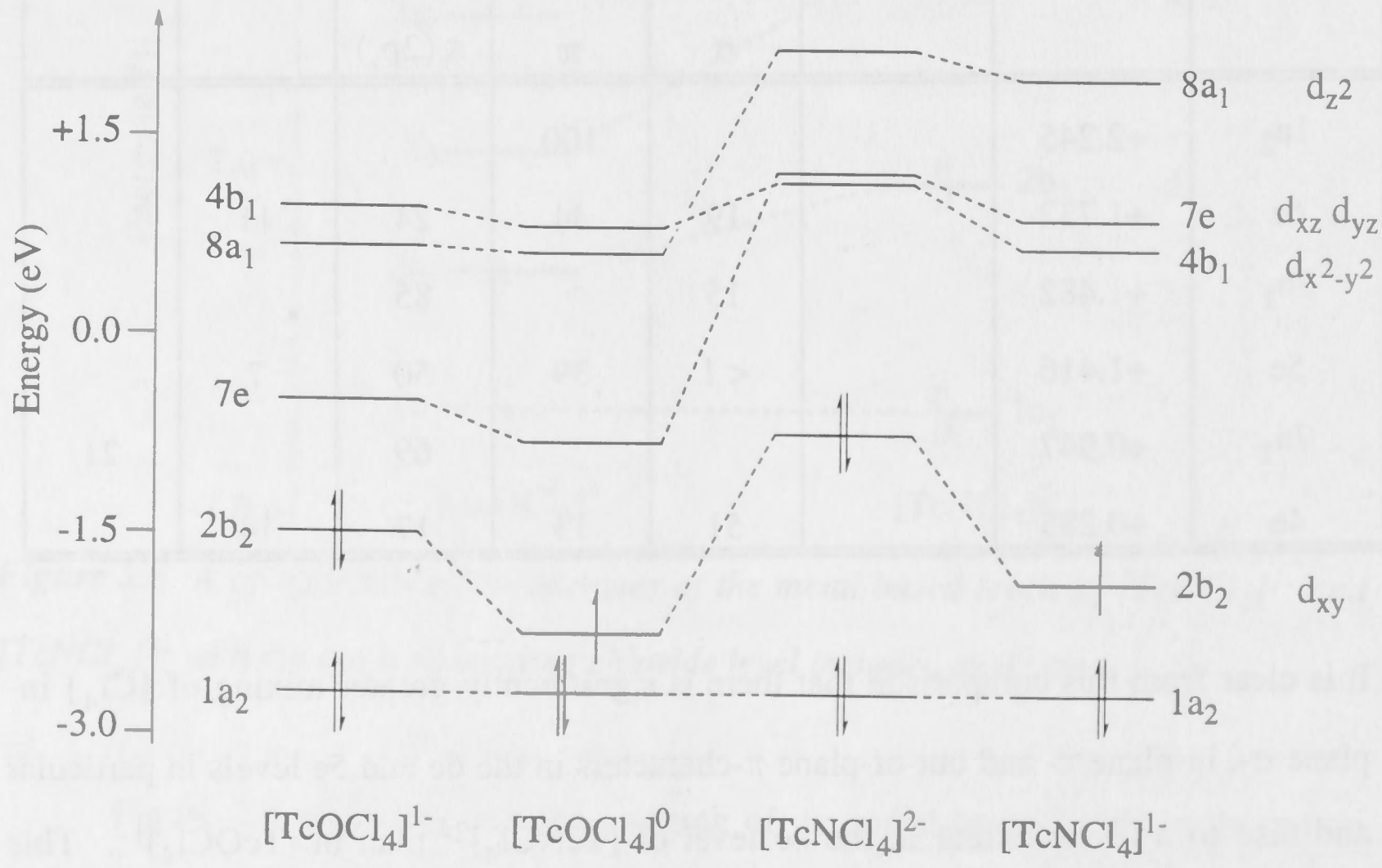

Figure 2.8 *Illustrating the energetic dependence of the metal based levels on oxidation state and the axial ligand, Y. For the d^1 species, the energies presented are derived from the β-spin component of a spin-unrestricted calculation (see section 2.3.2).*

2.1.6 The electronic structure of $[TcYCl_4]^{n-}$ *vs* $[TcYBr_4]^{n-}$

The substitution of chloride by bromide results in the relative destabilisation of the halide based orbitals, such that the $1a_2$ ($\{X_4\}$ level) to $2b_2$ (Tc based level) energy gap is reduced, as is shown in table 2.9. This destabilisation is similar for the oxo and nitrido species and is consistent with the experimental observation (presented in chapter 1.4) of a general red shift of absorptions involving charge transfer from the $\{X_4\}$ manifold into metal levels.

Table 2.9 Indicating the dependence of the energy gap between $1a_2$ and $2b_2$ on the oxidation state of the technetium metal.

Complex	Δ $2b_2$ - $1a_2$ (eV)		Δ Cl - Br (eV)
	X = Cl	X = Br	
$[Tc^{V}OX_4]^{1-}$	1.185	0.637	0.548
$[Tc^{V}NX_4]^{2-}$	1.967	1.396	0.571
$[Tc^{VI}NX_4]^{1-}$	0.827	0.293	0.534

The relative percentage compositions of the molecular orbitals of $[TcOX_4]^{1-}$ remained virtually unchanged upon substitution of chloride for bromide. However for $[TcNX_4]^{1-}$ and $[TcNX_4]^{2-}$ the relative amount of in-plane σ-, in-plane π- and out-of-plane π-character mixing in the $\{X_4\}$ based levels shows a greater dependence on the identity of X. This increased mixing is particularly apparent within the 6e and 5e levels which are dominated by in-plane π- and out-of-plane π-character respectively for the bromide species, but which show a more even mixture of each of these characters in the chloride analogues. The effect of changing X on orbital orientation is much less marked for the 4e level for each of the $[TcYX_4]^{n-}$ species; the extent to which mixing of in-plane σ-, in-plane π- and out-of-plane π-character for these three e-type levels (6e, 5e and 4e) varies is important for the following discussion and so ~~are~~ is summarised in table 2.10.

Table 2.10 Showing the degree of in-plane σ-, in-plane π- and out-of-plane π-character mixing in the complexes, $[TcYX_4]^{n-}$.

Level	Complex	Percentage composition				
	$[TcYX_4]^{n-}$	X			Y	
		in-plane		out-plane	p_x,p_y	p_z
		σ	π	π (p_z)		
6e	$[TcOCl_4]^0$	12	83	1	3	
	$[TcOCl_4]^{1-}$	13	83			
	$[TcOBr_4]^{1-}$	12	83		2	
	$[TcNCl_4]^{2-}$	19	45	24	11	
	$[TcNBr_4]^{2-}$	19	62	14	5	
	$[TcNCl_4]^{1-}$	16	39	33	12	
	$[TcNBr_4]^{1-}$	17	56	21	6	
5e	$[TcOCl_4]^0$	< 1	2	87	10	
	$[TcOCl_4]^{1-}$	< 1	2	89		
	$[TcOBr_4]^{1-}$	< 1	2	91	6	
	$[TcNCl_4]^{2-}$	< 1	39	50	7	
	$[TcNBr_4]^{2-}$	< 1	21	69	7	
	$[TcNCl_4]^{1-}$	3	44	30	5	
	$[TcNBr_4]^{1-}$	< 1	27	64	5	
4e	$[TcOCl_4]^0$	58	13	13	3	
	$[TcOCl_4]^{1-}$	60	13		17	
	$[TcOBr_4]^{1-}$	63	13		13	
	$[TcNCl_4]^{2-}$	51	13	17	14	
	$[TcNBr_4]^{2-}$	62	14	8	11	
	$[TcNCl_4]^{1-}$	57	14	11	12	
	$[TcNBr_4]^{1-}$	62	15	6	10	

2.1.7 Computed transitions *vs* the observed UV-visible spectra of $[TcOCl_4]^{1-}$

Table 2.11 shows all the computed transitions energies for ligand to metal charge transfer and d-d transitions which were calculated to be less than 45 000 cm^{-1}. The table includes an indication of the electric dipole allowedness of each transition and the orientation (that is σ or π; in-plane or out-of-plane) of the donor and acceptor orbitals of each transition (see section 2.1.2).

Table 2.11 Calculated transition energies for $[TcOCl_4]^{1-}$.

Energy (cm^{-1})	Transition	Type	Electric dipole allowed (Y/N)
9 300	$2b_2 \rightarrow 7e$	in d-d out	Y
18 600	$2b_2 \rightarrow 4b_1$	in d-d in	N
19 200	$2b_2 \rightarrow 8a_1$	in d-d out	N
22 400	$1a_2 \rightarrow 7e$	π in $\rightarrow$ out	Y
27 800	$6e \rightarrow 7e$	π/σ in $\rightarrow$ out	Y
28 500	$3b_1 \rightarrow 7e$	out $\rightarrow$ out	Y
30 900	$1a_2 \rightarrow 8a_1$	π in $\rightarrow$ out	N
31 300	$5e \rightarrow 7e$	out $\rightarrow$ out	Y
32 700	$1a_2 \rightarrow 4b_1$	π in $\rightarrow$ in	N
35 900	$6e \rightarrow 8a_1$	π/σ in $\rightarrow$ out	Y
36 500	$7a_1 \rightarrow 7e$	out $\rightarrow$ out	Y
37 200	$3b_1 \rightarrow 8a_1$	out $\rightarrow$ out	N
37 900	$6e \rightarrow 4b_1$	π/σ in $\rightarrow$ in	Y
38 900	$3b_1 \rightarrow 4b_1$	out $\rightarrow$ in	Y
39 300	$5e \rightarrow 8a_1$	out $\rightarrow$ out	Y
40 100	$4e \rightarrow 7e$	σ/π in $\rightarrow$ out	Y
41 700	$5e \rightarrow 4b_1$	out $\rightarrow$ out	Y
44 700	$7a_1 \rightarrow 8a_1$	out $\rightarrow$ out	Y
48 600	$7a_1 \rightarrow 4b_1$	out $\rightarrow$ in	N
49 700	$4e \rightarrow 8a_1$	π/σ in $\rightarrow$ out	N

The proposed assignments for the spectrum of $[TcOCl_4]^{1-}$ were selected from table 2.11 on the basis of the energy and intensity criteria where were described in section 2.11, and are presented in table 2.12 (which is an extract from table 1.41 presented in chapter 1.4).

Table 2.12 Showing proposed calculated assignments for the observed UV-visible spectrum of $[TcOCl_4]^{1-}$.#

Observed		Transition	Calculated energy
Energy (cm^{-1})	ε ($dm^3mol^{-1}cm^{-1}$)		(cm^{-1})
42 400	(sh)	$5e \longrightarrow 4b_1$	41 700
"	"	$5e \longrightarrow 8a_1$	39 300
"	"	$6e \longrightarrow 4b_1$	37 900
"	"	$7a_1 \longrightarrow 7e$	36 500
33 330	5900	$5e \longrightarrow 7e$	31 300
27 600	1200	$3b_1 \longrightarrow 7e$	28 500
21 400	14	$2b_2 \longrightarrow 8a_1$	19 200
17 000	3	$2b_2 \longrightarrow 4b_1$	18 600
11 200	11	$2b_2 \longrightarrow 7e$	9 300

The computed energies for the d-d transitions were in reasonable accord with the observed energies of the three low intensity bands at 11 200, 17 000 and 21 400 cm^{-1}. The intensities of the observed bands at 27 600 and 33 330 cm^{-1} were suggestive of charge transfer transitions. There were a number of possible assignments for these two bands based on energetic considerations alone. However the observed intensity implies electric dipole allowedness and good overlap of the donor and acceptor orbitals. Therefore, the most appropriate assignments are $3b_1 \longrightarrow 7e$ and $5e \longrightarrow 7e$ respectively, representing transitions from predominantly Cl_4 based, out-of-plane π, levels into an acceptor level dominated by Tc $4d_{xz}$, $4d_{yz}$ (out-of-plane π-character). The highest energy absorbance region is difficult to assign due to its broadness and the number of

The shaded region indicates that any combination of the calculated transitions may correspond to the observed absorptions in the region.

transitions which possess appropriate calculated transition energies that are both electric dipole allowed and involve molecular orbitals of the appropriate orientation. This absorbance region did not show a large change upon the oxidation of the $[TcOCl_4]^{1-}$ species to $[TcOCl_4]^0$ and so may be attributable to transitions into the $8a_1$ metal orbital which also showed minimal energetic dependence on oxidation state (see figure 2.8).

2.1.8 Spectral assignments of $[TcOCl_4]^{1-}$ *vs* $[TcOBr_4]^{1-}$

The spectrum of the bromide analogue can be assigned in a similar way to that of the chloride species which was just described in section 2.1.6 (see table 2.13).

Table 2.13 The proposed assignments for the observed UV-visible spectrum of $[TcOBr_4]^{1-}$.

Observed		Transition	Calculated energy
Energy (cm^{-1})	ε ($dm^3mol^{-1}cm^{-1}$)		(cm^{-1})
39 800	(sh)	$5e \rightarrow 4b_1$	35 700
33 700	(sh)	$5e \rightarrow 8a_1$	35 300
"	"	$6e \rightarrow 4b_1$	31 600
"	"	$7a_1 \rightarrow 7e$	32 600
28 100	4000	$5e \rightarrow 7e$	27 300
21 100	110	$3b_1 \rightarrow 7e$	24 200
16 200	11	$2b_2 \rightarrow 8a_1$	18 800

The main difference between the two spectra is the general red shift of the charge transfer transition energies in the bromide spectrum. This shift was most clearly observed for charge transfer into the 7e level which occurs an average of 5900 cm^{-1} lower than in the chloride analogue. The corresponding calculated energies show an average red shift of ~4200 cm^{-1}. Such a red shift is typical of charge transfer processes involving chloride and bromide based donor levels (**10**) and is consistent with the optical electro-negativities of the ligands. Computationally, this can be understood in terms of the relatively higher energy of the bromide valence orbitals, which brings them closer to the technetium based levels (see table 2.9).

2.1.9 Spectral assignments of $[TcOX_4]^{1-}$ *vs* $[TcNX_4]^{2-}$

The spectra of the isoelectronic anions $[TcOX_4]^{1-}$ and $[TcNX_4]^{2-}$ appear at first sight to be very different. Density functional calculations proved to be important in developing an understanding of this observation. The first available metal based acceptor orbital in these isoelectronic d^2 complexes is 7e. In $[TcOX_4]^{1-}$, absorptions involving charge transfer are observed between 35 000 - 25 000 cm^{-1}. However, in $[TcNX_4]^{2-}$ the 7e level is markedly destabilised relative to its position in the oxo anions (see figure 2.6) such that it is even slightly higher in energy than the $4b_1$ orbital. Charge transfer into either of those orbitals (7e or $4b_1$) will occur at high energy (~40 000 cm^{-1}) and hence no absorbances of significant intensity are observed below this energy for the nitrido species. Computed charge transfer energies start at 38 600 cm^{-1} for $[TcNCl_4]^{2-}$ ($1a_2 \longrightarrow 7e$) and at 34 100 cm^{-1} for the same lowest energy electric dipole allowed charge transfer transition in $[TcNBr_4]^{2-}$.

It is difficult to offer precise assignments for the $[TcNX_4]^{2-}$ spectra due to the broadness of the absorbance. The calculated energies for the electric dipole allowed transitions from donor orbitals based on in-plane π-character into 7e and donor orbitals based on out-of-plane π-character into $4b_1$ of appropriate energy are presented in table 2.14.

Table 2.14 The proposed spectral assignments for the broad absorbance region in the observed UV-visible spectra of the $[TcNX_4]^{2-}$ species.

Transition	Calculated Energy (cm^{-1})	
	$[TcNCl_4]^{2-}$	$[TcNBr_4]^{2-}$
$4e \longrightarrow 7e$	49 700	47 100
$5e \longrightarrow 7e$	43 700	39 400
$3b_1 \longrightarrow 7e$	43 700	39 300
$7a_1 \longrightarrow 7e$	42 700	40 600
$5e \longrightarrow 4b_1$	40 700	34 700
$6e \longrightarrow 7e$	38 600	36 100
$6e \longrightarrow 4b_1$	37 600	32 500

2.1.10 Spectral assignments of $[TcOCl_4]^{1-}$ *vs* $[TcOCl_4]^0$

The calculated transition energies for charge transfer processes of d^1 $[TcOCl_4]^0$ show a general red shift of around 2000 cm^{-1} relative to those of $[TcOCl_4]^{1-}$ (see table 2.15) which is consistent with spectroscopic observations (section 1.4.3). The calculated magnitude of the red shift is greatest for transitions involving 7e or $2b_2$ levels in accordance with trends in electronic structure which were described in section 2.1.4.

Table 2.15 A comparison of the proposed spectral assignments for the species $[TcOCl_4]^{1-}$ and $[TcOCl_4]^{2-}$.

$[TcOCl_4]^{1-}$		Assignment	$[TcOCl_4]^0$	
observed energy (cm^{-1}) (ε $dm^3mol^{-1}cm^{-1}$)	Calculated energy (cm^{-1})		Calculated energy (cm^{-1})	observed energy (cm^{-1}) (ε $dm^3mol^{-1}cm^{-1}$)
42 200 (sh)	44 700	$7a_1 \longrightarrow 8a_1$	44 300	40 980 (16 000)
"	39 300	$5e \longrightarrow 8a_1$	38 540	31 000 (sh)
"	37 900	$6e \longrightarrow 4b_1$	36 200	"
"	36 500	$7a_1 \longrightarrow 7e$	33 500	"
33 330 (5900)	31 300	$5e \longrightarrow 7e$	27 400	28 120 (7200)
27 600 (1200)	28 500	$3b_1 \longrightarrow 7e$	25 200	25 000 (sh)
–	–	$6e \longrightarrow 2b_2$	15 600	17 230 (4000)
11 200 (11)	9300	$2b_2 \longrightarrow 7e$	13 200	11 300 (80)

Upon oxidation, the $2b_2$ in-plane π, metal based orbital becomes available as a charge transfer acceptor orbital. The calculated transition energy for the $6e \longrightarrow 2b_2$ process of 15 600 cm^{-1} is consistent with the observation of a new band at 17 230 cm^{-1} in the spectrum of $[TcOCl_4]^0$. This band is also relatively intense (ε = 4000 $dm^3mol^{-1}cm^{-1}$), consistent with the proposed assignment which is both electric dipole allowed and involves donor and acceptor orbitals dominated by in-plane π character.

2.1.11 Spectral assignments of $[TcOCl_4]^0$ *vs* $[TcNCl_4]^{1-}$

The main difference in assigning these spectra arises from the relative destabilisation of the 7e orbital in $[TcNCl_4]^{1-}$ (see figure 2.6). Hence in the spectrum of $[TcNCl_4]^{1-}$ transitions into 7e are associated with the intense broad high energy absorption manifold above 35 000 cm^{-1}. Transitions into $4b_1$ and $8a_1$ may also contribute to this absorption. In contrast where transitions into 7e occur between 25 000 - 30 000 cm^{-1} in the spectrum of $[TcOCl_4]^0$.

Table 2.16 A comparison of the proposed spectral assignments for the observed UV-visible spectra of the isoelectronic species $[TcOCl_4]^0$ and$[TcNCl_4]^{1-}$.

$[TcOCl_4]^0$		Assignment	$[TcNCl_4]^{1-}$	
observed energy (cm^{-1}) (ε $dm^3mol^{-1}cm^{-1}$)	Calculated energy (cm^{-1})		Calculated energy (cm^{-1})	observed energy (cm^{-1}) (ε $dm^3mol^{-1}cm^{-1}$)
40 980 (16 000)	44 300	$7a_1 \rightarrow 8a_1$	49 500	
"	38 540	$5e \rightarrow 8a_1$	47 100	
"	36 200	$6e \rightarrow 4b_1$	35 200	43 110 (9000)
"	33 500	$7a_1 \rightarrow 7e$	39 600	"
28 120 (7200)	27 400	$5e \rightarrow 7e$	38 700	"
25 000 (sh)	25 200	$3b_1 \rightarrow 7e$	38 200	"
–	29 200	$4e \rightarrow 2b_2$	29 500	33 340 (1700)
–	18 700	$5e \rightarrow 2b_2$	20 100	24 580 (6400)
17 230 (4000)	15 600	$6e \rightarrow 2b_2$	17 300	22 220 (2300)
		$6e \rightarrow 2b_2$	17 300	21 570 (2300)
–	–	–	–	20 900 (sh)
11 300 (80)	13 200	$2b_2 \rightarrow 7e$	22 600	–
–	8800	$1a_2 \rightarrow 2b_2$	14 000	19 100 (280)

The transition from 6e into the $2b_2$ level which is dominated by in-plane π metal based character is observed in the spectra of both complexes, at 17 230 cm^{-1} in $[TcOCl_4]^0$ and centred at 21 895 cm^{-1} in $[TcNCl_4]^{1-}$. The intensity of the absorption is

almost halved in the spectrum of the nitrido species which is consistent with the 6e level having only 39% in-plane π-character in $[TcNCl_4]^{1-}$ as compared to 83% in $[TcOCl_4]^0$.

Extra absorptions were observed in the spectrum of $[TcNCl_4]^{1-}$ between those attributed to $3b_1 \longrightarrow 7e$ and $6e \longrightarrow 2b_2$. These were attributed to $4e \longrightarrow 2b_2$ and $5e \longrightarrow 2b_2$ on the basis of comparisons of calculated and observed energies. These transitions gain intensity in the spectrum of $[TcNCl_4]^{1-}$ by virtue of greater mixing of in-plane π-character into the 5e level and by the destabilisation of the 7e level such that transitions from 4e are not obscured (as is possible for $[TcOCl_4]^0$).

Assignment of the shoulder at 20 900 cm^{-1} observed in the spectrum of the nitrido species is problematic as no transition has a computed energy between 17 300 and 14 000 cm^{-1}. The $1a_2 \longrightarrow 2b_2$ transition has a calculated energy of 14 000 cm^{-1} and was assigned to the observed weak absorption at 19 100 cm^{-1} on the basis of the observed spacing of this band from the intense doublet centred at 21 895 cm^{-1} which was 2795 cm^{-1} coinciding with the calculated gap of 3300 cm^{-1} between the corresponding $1a_2 \longrightarrow 2b_2$ and $6e \longrightarrow 2b_2$ transitions. This gap of the order of 3000 cm^{-1} is similar to what has been previously observed in the related bands in the spectra of *trans*-$[RuCl_4L_2]^{n-}$ species (**1**,**2**,**3**,**4**) which will be described in chapter 2.2. The d-d transitions are calculated to higher energy in $[TcNCl_4]^{1-}$ than for $[TcOCl_4]^0$ and may be concealed amongst the charge transfer manifold. For example, it is possible that the observed shoulder at 20 900 cm^{-1} may correspond to a d-d transition.

2.1.12 Spectral assignments of $[TcNCl_4]^{1-}$ *vs* $[TcNBr_4]^{1-}$

The spectral assignments for $[TcNCl_4]^{1-}$ and $[TcNBr_4]^{1-}$ are essentially very similar. A general red shift of charge transfer transitions upon substitution of chloride for bromide has been reproduced by computed transition energies as is demonstrated in table 2.17.

Table 2.17 The proposed spectral assignments for the observed spectrum of $[TcNCl_4]^{1-}$ and $[TcNBr_4]^{1-}$.

$[TcNCl_4]^{1-}$		Assignment	$[TcNBr_4]^{1-}$	
Observed energy (cm^{-1}) (ε $dm^3mol^{-1}cm^{-1}$)	Calculated energy (cm^{-1})		Calculated energy (cm^{-1})	Observed energy (cm^{-1}) (ε $dm^3mol^{-1}cm^{-1}$)
43 110 (9000)	39 600	$7a_1 \rightarrow 7e$	37 200	37 120 (5100)
"	38 700	$5e \rightarrow 7e$	34 500	33 940 (5900)
"	38 200	$3b_1 \rightarrow 7e$	33 700	30 500 (sh)
"	35 200	$6e \rightarrow 4b_1$	29 600	"
33 340 (1700)	29 500	$4e \rightarrow 2b_2$	26 200	28 600 (sh)
–	–	–	–	24 380 (600)
24 580 (6400)	20 100	$5e \rightarrow 2b_2$	15 770	19 570 (3200)
		$5e \rightarrow 2b_2$	15 770	19 200 (sh)
		$5e \rightarrow 2b_2$	15 770	17 980 (2700)
22 220 (2300)	17 300	$6e \rightarrow 2b_2$	13 400	16 320 (4800)
21 570 (2300)	17 300	$6e \rightarrow 2b_2$		
20 900 (sh)	–	–	–	–
19 100 (280)	14 000	$1a_2 \rightarrow 2b_2$		–

The high energy region once again cannot be assigned definitively as indicated by shading in table 2.17. It is probably due to some combination of transitions similar to those derived for the chloride analogue. The spectral region between 16 000 cm^{-1} and 20 000 cm^{-1} in $[TcNBr_4]^{1-}$ is attributed to the transitions $5e \rightarrow 2b_2$ and $6e \rightarrow 2b_2$ but while the energy ordering remains the same, the relative intensity of these bands (that is the lower energy $6e \rightarrow 2b_2$ being more intense than $5e \rightarrow 2b_2$), is reversed from the equivalent bands in $[TcNCl_4]^{1-}$. This reversal of intensity is modelled by the calculations which indicated that the 5e level has more in-plane π-character than the 6e level in $[TcNCl_4]^{1-}$ but that in $[TcNBr_4]^{1-}$ the 6e level has the greater in-plane π-character. The different complexities of these bands in $[TcNBr_4]^{1-}$ as

compared with $[TcNCl_4]^{1-}$ is attributed to the larger spin-orbit coupling in the former species. The lower relative energy of the charge transfer manifold in $[TcNBr_4]^{1-}$ may be the source of the absence of any clearly defined d-d bands in that spectrum.

2.1.13 Spectral assignments for $[TcNX_4]^{1-}$ recorded in HCl

The differences in the spectra of $[TcNX_4]^{1-}$ when recorded in aqueous HX (**11**,**12**), rather than CH_2Cl_2, were described earlier, in section 1.4.3. It was also noted that the nature of the species in aqueous, acidic solution is likely to be $[TcNX_4(H_2O)]^{1-}$. A calculation on $[TcNCl_4(H_2O)]^{1-}$ was therefore performed with a view to interpreting the reported differences in the UV-visible spectra.

2.1.13.1 Geometry optimisation of $[TcNCl_4(H_2O)]^{1-}$

The geometry of $[TcNCl_4(H_2O)]^{1-}$ was optimised under C_{2v} symmetry, with the H_2O molecule in a staggered arrangement with respect to the Tc-Cl bonds. The results are compared to observed crystal structures of $[Rb(15\text{-crown-}5)_2][TcNCl_4(H_2O)]$ (**13**) and $(TEA)[TcNBr_4(H_2O)]$ (**14**) and to the observed and calculated structure of $[AsPh_4][TcNCl_4]$ and the calculated structure of isoelectronic $[TcNCl_4]^0$ (**8**) table 2.18.

Table 2.18 Geometry optimisations of $[TcYX_4(H_2O)]^{n-}$ and $[TcYX_4]^{n-}$ compared to the available reported crystal structure data which are presented in parenthesis.#

Complex	Tc - Y (Å)	Tc - X (Å)	Y - Tc - X (degrees)	Reference
$[TcNCl_4(H_2O)]^{1-}$	1.643 (1.600)	2.337 (2.320)	100.7 (94.2)	(**13**)
$[TcNCl_4]^{1-}$	1.639 (1.581)	2.315 (2.322)	103.8 (103.3)	(**8**)
$[TcNBr_4(H_2O)]^{1-}$	(1.559)	(2.514 (2))	(97.5 (4))	(**14**)
$[TcOCl_4]^0$	1.674	2.253	106.1	

The trends reported in section 2.1.1 are still followed by this latest geometry optimisation, in particular for bond lengths, in that the Tc-Y bond length was over-

The calculated Tc-O distance for the axial water ligand was 2.370 Å which was slightly shorter than the observed distance of 2.43 Å for $[TcNCl_4(H_2O)]^{1-}$ and 2.443 Å for $[TcNBr_4(H_2O)]^{1-}$.

estimated by calculation, while the Tc-X distance was close to the observed value. However, the Y-Tc-X angle was modelled surprisingly badly in light of the success with the five coordinate species (table 2.2) but importantly, the observed trend of the increase in the size of this angle in the order Y = O > N > N(H_2O) was successfully reproduced by the optimisations.

2.1.13.2 Proposed assignments for the UV-visible spectrum of $[TcNCl_4(H_2O)]^{1-}$

The difference in complexity between the spectra of $[TcOX_4]^0$ and $[TcNX_4]^{1-}$ was rationalised from calculations in terms of the varying degrees of mixing of in- and out-of-plane character within the $\{X_4\}$ e based donor levels. Table 2.19 shows an extract of table 2.10 detailing the percentage character of three e levels which contribute to the spectra of $[TcOCl_4]^0$ and $[TcNCl_4]^{1-}$ and includes the equivalent values calculated for $[TcNCl_4(H_2O)]^{1-}$. The axial water coordination in $[TcNCl_4(H_2O)]^{1-}$ causes a lowering in the symmetry from C_{4v} (of the five coordinate species) to C_{2v}, and a resultant removal of the degeneracy of the e levels to b_1 and b_2 is the result. In principle separate transitions arising from either the b_1 or b_2 level might be expected, but this was not observed in the solution spectra of interest here. In solution a rapid rotation of the (H_2O) moiety about the Tc-(H_2O) bond would be possible. Such a rotation would result in an averaging of the effects due to each distinct (H_2O) orientation (of b_1 or b_2 symmetry) which may result in the merging of absorptions due to transitions from b_1 and b_2 as was observed here. For the purposes of this discussion the orbital compositions of the b_1 and b_2 levels have been averaged to aid comparisons with the corresponding e levels of the five coordinate species.

It is interesting to note from table 2.19 that $[TcNCl_4(H_2O)]^{1-}$ was calculated to have mainly out-of-plane character in $7b_1/b_2$ and predominantly in-plane in $6b_1/b_2$. This is the opposite to what was calculated for $[TcOCl_4]^0$ where the equivalent 6e and 5e levels were virtually exclusively in-plane and out-of-plane respectively. It is also different from $[TcNCl_4]^{1-}$ where 6e and 5e both have more in-plane than out-of-plane

character, though they are extensively mixed. The extent of this mixing of in- and out-of-plane character decreases in the order $[TcNCl_4]^{1-} > [TcNCl_4(H_2O)]^{1-} > [TcOCl_4]^0$.

Table 2.19 Highlighting the different in- and out-of-plane mixing induced by coordination of a further axial water ligand.

Level	Complex	X		Axial
		in-plane#	out-plane	Y (and H_2O)
		p_x, p_y	p_z	
6e	$[TcOCl_4]^0$	95	1	3
	$[TcNCl_4]^{1-}$	55	33	12
($7b_1$, $7b_2$)	$[TcNCl_4(H_2O)]^{1-}$	25	59	15
5e	$[TcOCl_4]^0$	2	87	10
	$[TcNCl_4]^{1-}$	~~44~~ 47	30	5
($6b_1$, $6b_2$)	$[TcNCl_4(H_2O)]^{1-}$	71	21	2
4e	$[TcOCl_4]^0$	76	13	3
	$[TcNCl_4]^{1-}$	71	11	12
($5b_1$, $5b_2$)	$[TcNCl_4(H_2O)]^{1-}$	74	7	14

The proposed spectral assignments of $[TcNCl_4]^{1-}$ recorded in CH_2Cl_2 and $[TcNCl_4(H_2O)]^{1-}$ recorded in HX involve the in-plane metal acceptor orbital $4d_{xy}$, (labelled $2b_2$ or $11a_1$). Hence the transitions associated with intense absorptions would be expected to involve predominantly in-plane donor levels. The choice of donor level for each assignment is determined by the relative degree of mixing of in- and out-of-plane character in combination with its relative energy. The results are presented in table 2.20.

There is no distinguishing between in-plane σ and in-plane π character provided in table 2.19 as the lowering of symmetry due to the presence of the water molecule renders this analysis to be very difficult. This does not affect spectral assignments however, because it is clear that 6e must have less in-plane π character than for either of the two $[TcYX_4]^{1-}$ species because the total in-plane character is less in the presence of trans, axial H_2O. 4e shows little dependence on axial ligand character. The only doubt would be about the relative amount of in-plane σ and π character in 5e but the assignments using that level are based on energetic rather than intensity considerations.

The absorption observed around 33 340 cm^{-1} in $[TcNCl_4]^{1-}$ appears to show the least solvent dependence and corresponds to a similar absorption observed at 34 100 cm^{-1} in $[TcNCl_4(H_2O)]^{1-}$. This lack of solvent dependence is consistent with a transition involving a similar composition of donor and acceptor orbitals in the two species. The composition of the 4e level and its equivalent $5b_1/b_2$ were least affected by the inclusion of an axial H_2O ligand and as such the band which was assigned to the $4e \longrightarrow 2b_2$ transition in $[TcNCl_4]^{1-}$ is given the equivalent assignment of $5b_1/b_2 \longrightarrow 11a_1$ for $[TcNCl_4(H_2O)]^{1-}$.

Table 2.20 The proposed spectral assignments for the observed spectrum of $[TcNCl_4]^{1-}$ recorded in CH_2Cl_2 and $[TcNCl_4(H_2O)]^{1-}$ recorded in HCl.

$[TcNCl_4]^{1-}$		Assignment	$[TcNCl_4(H_2O)]^{1-}$	
observed energy (cm^{-1}) (ε $dm^3mol^{-1}cm^{-1}$)	Calculated energy (cm^{-1})		Calculated energy (cm^{-1})	observed energy (cm^{-1}) (ε $dm^3mol^{-1}cm^{-1}$)
33 340 (1700)	29 500	$4e \longrightarrow 2b_2$		
		$5b_1/b_2 \longrightarrow 11a_1$	29 500	34 100 (1540)
24 580 (6400)	20 100	$5e \longrightarrow 2b_2$		
		$6b_1/b_2 \longrightarrow 11a_1$	19 900	25 060 (4780)
22 220 (2300)	17 300	$6e \longrightarrow 2b_2$		
21 570 (2300)	17 300	$6e \longrightarrow 2b_2$		
		$7b_1/b_2 \longrightarrow 11a_1$	16 800	20 800 (625)
19 100 (280)	14 000	$1a_2 \longrightarrow 2b_2$	-	-

The most intense band in the spectrum of $[TcNCl_4(H_2O)]^{1-}$ at 25 060 cm^{-1} (4780 $dm^3mol^{-1}cm^{-1}$) corresponds to charge transfer from the predominantly $\{Cl_4\}$ in-plane $6b_1/b_2$ level to the Tc $4d_{xy}$ (in-plane) $11a_1$ level. This is an analogous assignment to the similarly positioned 24 580 cm^{-1} (6400 $dm^3mol^{-1}cm^{-1}$) band of the $[TcNCl_4]^{1-}$ spectrum of $5e \longrightarrow 2b_2$. In the spectrum of $[TcNCl_4]^{1-}$ there were two

distinct absorbances occurring at lower energy than this band. In the spectrum of $[TcNCl_4(H_2O)]^{1-}$ there is only one low energy band (at 20 800 cm^{-1}). This band lies at an intermediate energy to the two absorbances recorded for $[TcNCl_4]^{1-}$ and also is of an intermediate intensity. The most challenging part of this spectral assignment lies in the determination of whether the one band in $[TcNCl_4(H_2O)]^{1-}$ corresponds more closely to either of the two bands, $6e \longrightarrow 2b_2$ or $1a_2 \longrightarrow 2b_2$ of $[TcNCl_4]^{1-}$. The assignment of $7b_1/b_2 \longrightarrow 11a_1$ (equivalent to $6e \longrightarrow 2b_2$) is favoured over $4a_2 \longrightarrow 11a_1$ (equivalent to $1a_2 \longrightarrow 2b_2$) for the assignment in $[TcNCl_4(H_2O)]^{1-}$ for the following reasons. Firstly, the observed intensity of the band, 625 $dm^3mol^{-1}cm^{-1}$, is more in keeping with an electric-dipole allowed transition than that of $4a_2 \longrightarrow 11a_1$ which is electric-dipole forbidden in C_{2v} symmetry (as was the equivalent $1a_2 \longrightarrow 2b_2$ electric-dipole forbidden under C_{4v} symmetry and the intensity to the band to which it was ascribed was 280 $dm^3mol^{-1}cm^{-1}$). Secondly, the observed intensity of this band was lower than that observed for the equivalent $6e \longrightarrow 2b_2$ transition in $[TcNCl_4]^{1-}$. This is consistent with the reduction of in-plane character calculated for $7b_1/b_2$ $[TcNCl_4(H_2O)]^{1-}$ as compared to 6e in $[TcNCl_4]^{1-}$.

The spectrum of $[TcNBr_4(H_2O)]^{1-}$ is assigned in a similar manner to the chloride analogue. The high energy, solvent independent band at 25 000 cm^{-1} (sh) is assigned to the $7b_1/b_2 \longrightarrow 11a_1$ transition. The relatively intense doublet at 20 080 cm^{-1} (3030 $dm^3mol^{-1}cm^{-1}$) and 17 600 cm^{-1} (3290) is assigned to the $6b_1/b_2 \longrightarrow 11a_1$ transition and the lower energy band at 14 250 cm^{-1} (470) is assigned to the $5b_1/b_2 \longrightarrow 11a_1$ transition.

The calculation of $[TcNCl_4(H_2O)]^{1-}$ illustrates the different mixing of in- and out-of-plane character induced by axial ligand coordination and as such provides an indication of a possible explanation as to why the spectrum of $[TcNCl_4]^{1-}$ shows such a marked solvent dependence. Further spectroscopic measurements investigating $[TcNCl_4]^{1-}$ in a variety of solvents and in the solid state, together with parallel studies on an authentic sample of $[TcNCl_4(H_2O)]^{1-}$, followed by computational studies

preferably with a facility for determining oscillator strengths (which is not currently available using ADF), would be required before our suggestions as to the origin of the marked solvent dependence of the UV-visible spectra of $[TcNCl_4]^{1-}$ can be confirmed.

Chapter 2.2: Density functional calculations on trans-$[RuCl_4L_2]^{1-}$ complexes

After the analysis of the electronic structure of $[TcYX_4]^{n-}$ complexes it was of interest to extend our study to a further series of compounds containing the $\{MX_4\}$ moiety but on this occasion in combination with axially coordinated ligands recognised as being π-acceptors and π-neutral species rather than the π-donors of chapter 2.1. The series of choice was *trans*-$[Ru^{III}Cl_4L_2]^{1-}$ (d^5) (where L = MeCN, *t*-BuNC, PMe_2Ph, PEt_3 and aniline#.

2.2.1 Observed voltammetric and UV-visible data for *trans*-$[RuX_4L_2]^{1-}$ (where L = MeCN, *t*-BuNC, PMe_2Ph, PEt_3 and aniline)

UV-visible absorption and electrochemical data were available for a large series of compounds of the form *trans*-$[RuX_4L_2]^{1-}$, where L can be a variety of ligands, including nitrogen, carbon, phosphine and arsine donors (**15**,**16**,**17**,**18**,**19**). As mentioned in the introductory chapter, the redox potentials and UV-visible spectra of this series were observed to vary with L. For the purposes of this thesis a number of different complexes *trans*-$[RuCl_4L_2]^{1-}$, reflecting the range of experimental data, were selected for computational analysis. The relevant electrochemical and UV-visible electronic absorption data for these complexes are tabulated in table 2.21. The UV-visible spectra are illustrated in figure 2.22 and resemble each other. The energy of the relatively intense multi-component band found in each of the spectra (and labelled band III) is shown in bold in table 2.21 to aid comparisons. A linear relationship between the energy of band III and the potential of the corresponding $Ru^{III/II}$ reduction process has been described previously (**18**) and will be investigated toward the end of this chapter.

---

aniline = $C_6H_5NH_2$

Table 2.21 Observed potentials and UV-visible absorptions for the series *trans*-$[RuCl_4L_2]^{1-}$.

L =	$Ru^{IV/III}$ (V)#	$Ru^{III/II}$ (V)#	UV-visible for Ru^{III} band maxima (cm^{-1}) and (ε $dm^3mol^{-1}cm^{-1}$))	ref
t-BuNC	+1.52	-0.31	32 700, **23 900**, 20 600, (1500) **(5200)** (400)	**16**
MeCN	+1.44	-0.39	40 000, 32 810, 28 000, **25 200**, **24 250**, 21 150 (8100) (2100) (210) **(5400)** **(5900)** (510)	**15**
PMe_2Ph	+1.05	-0.62	**26 910**, **26 070**, 22 700, 17 960 **(5270)** **(5320)** (510) (130)	**17**
PEt_3			**27 200**, **26 440**, 23 300, 17 000 **(5000)** **(5000)** (430) (130)	**17**
aniline	+0.8	-1.0	36 800, **29 950**, **28 500**, 26 000, 21 600 (sh) **(2990)** **(2320)** (sh) (160)	**19**

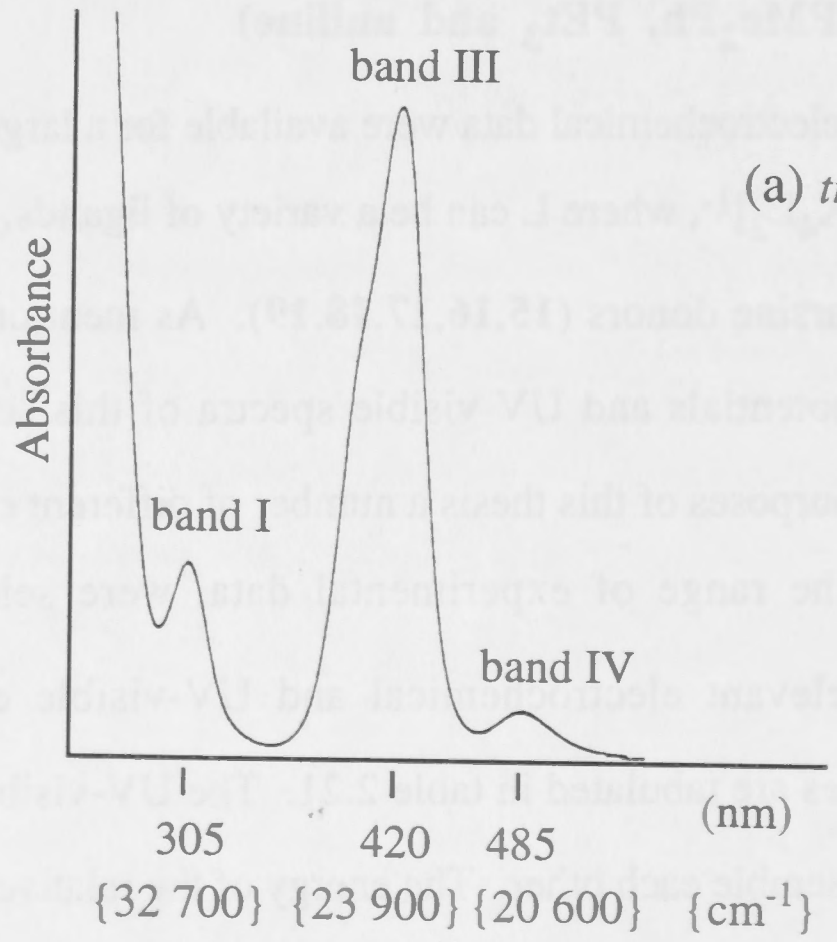

(a) *trans*-$[RuCl_4(t\text{-BuNC})_2]^{1-}$

Potentials are corrected from the publications so that the oxidation of ferrocene is at +0.55V.

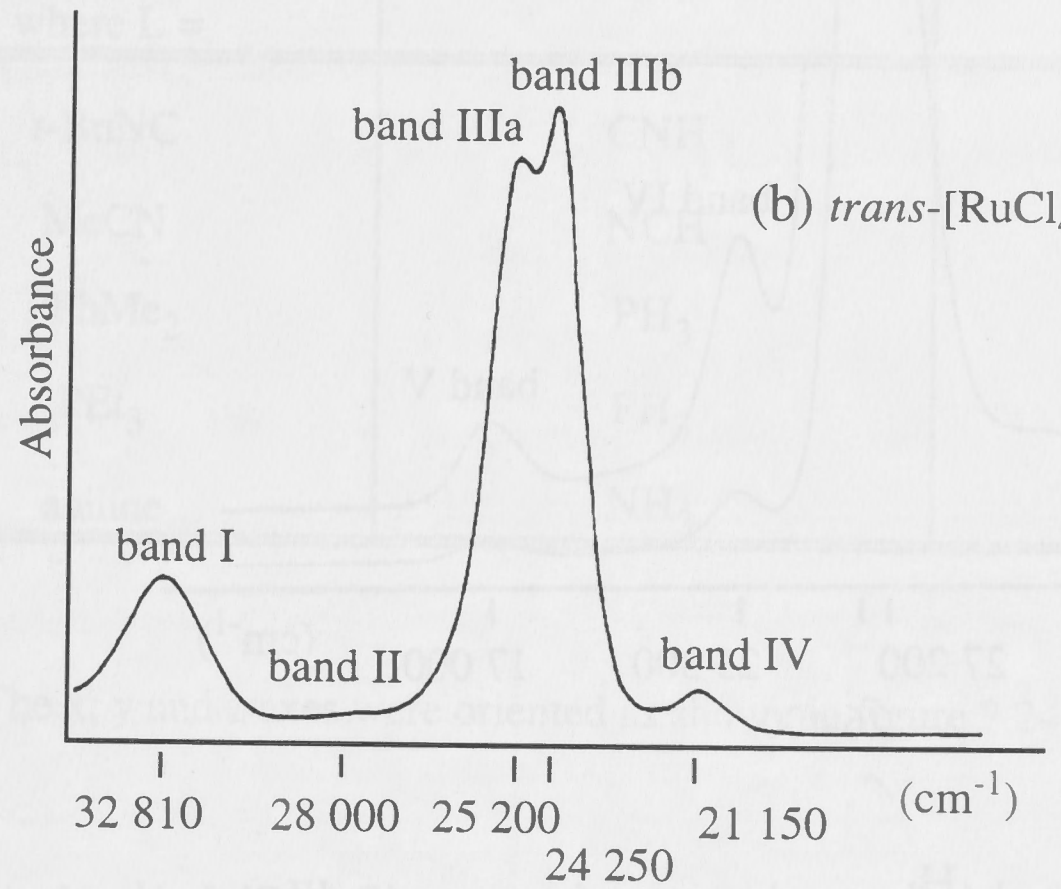
band IIIb
band IIIa
(b) trans-[RuCl4(CH3CN)2]1-
Absorbance
band I
band II
band IV
32 810
28 000
25 200
24 250
21 150
(cm-1)

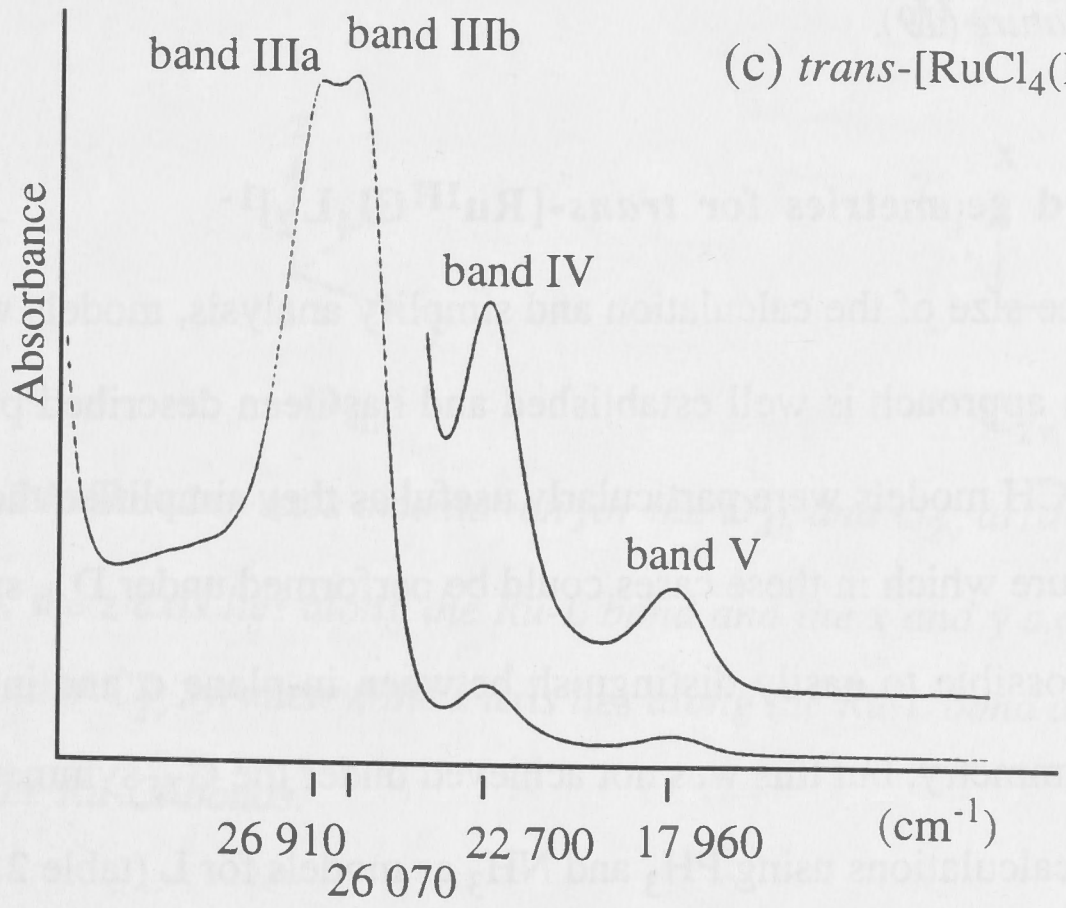
band IIIa
band IIIb
(c) trans-[RuCl4(PMe2Ph)2]1-
Absorbance
band IV
band V
26 910
26 070
22 700
17 960
(cm-1)

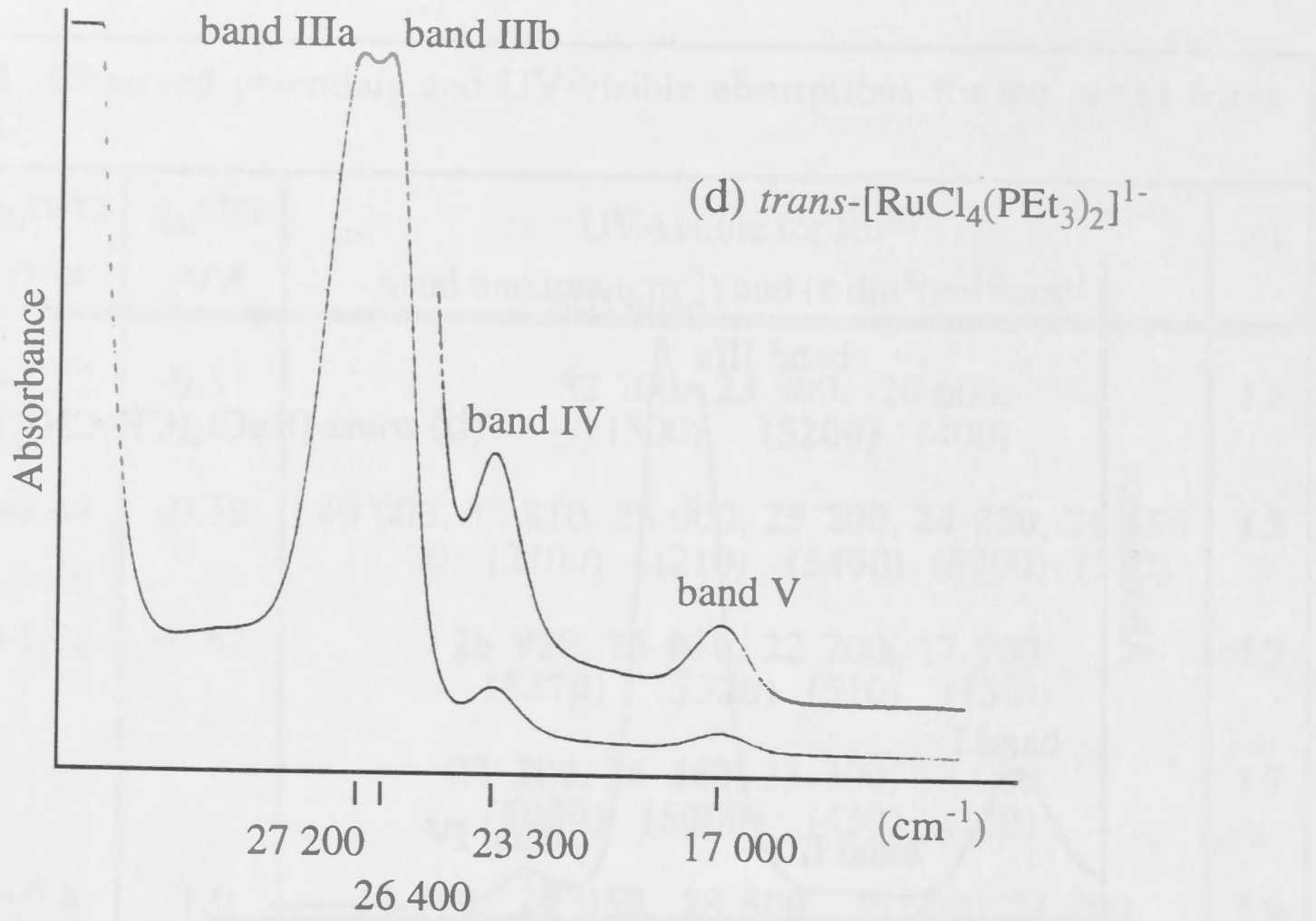

Figure 2.22 *Showing the observed spectra for trans-$[Ru^{III}Cl_4L_2]^{1-}$ where L = (a) t-BuNC (**15**), (b) MeCN (**16**), (c) PMe_2Ph and (d) PEt_3 (**17**). The spectrum (a) for L = t-BuNC was reported in nm so the wavenumber energies have been provided in brackets to assist comparison. The bands of each spectrum are labelled from I to V to assist in discussions throughout this section. A picture of the spectrum of L = aniline was not available from the literature (**19**).*

2.2.2 The optimised geometries for *trans*-$[Ru^{III}Cl_4L_2]^{1-}$

To minimise the size of the calculation and simplify analysis, models were used for ligand L. Such an approach is well established and has been described previously (**17**). The CNH and NCH models were particularly useful as they simplified the analysis of the electronic structure which in these cases could be performed under D_{4h} symmetry. In particular, it was possible to easily distinguish between in-plane σ and in-plane π-character using D_{4h} symmetry, but this was not achieved under the C_{2v} symmetry which was employed for the calculations using PH_3 and NH_3 as models for L (table 2.31). The models employed are presented along with the symmetry of each calculation in table 2.23.

Table 2.23 Models and symmetries employed during the geometry optimisations.

trans-$[RuCl_4L_2]^{1-}$ where L =	Model for L	Symmetry
t-BuNC	CNH	D_{4h}
MeCN	NCH	D_{4h}
$PPhMe_2$	PH_3	C_{2v}
PEt_3	PH_3	C_{2v}
aniline	NH_3	C_{2v}

The x, y and z axes were oriented as shown in figure 2.24.

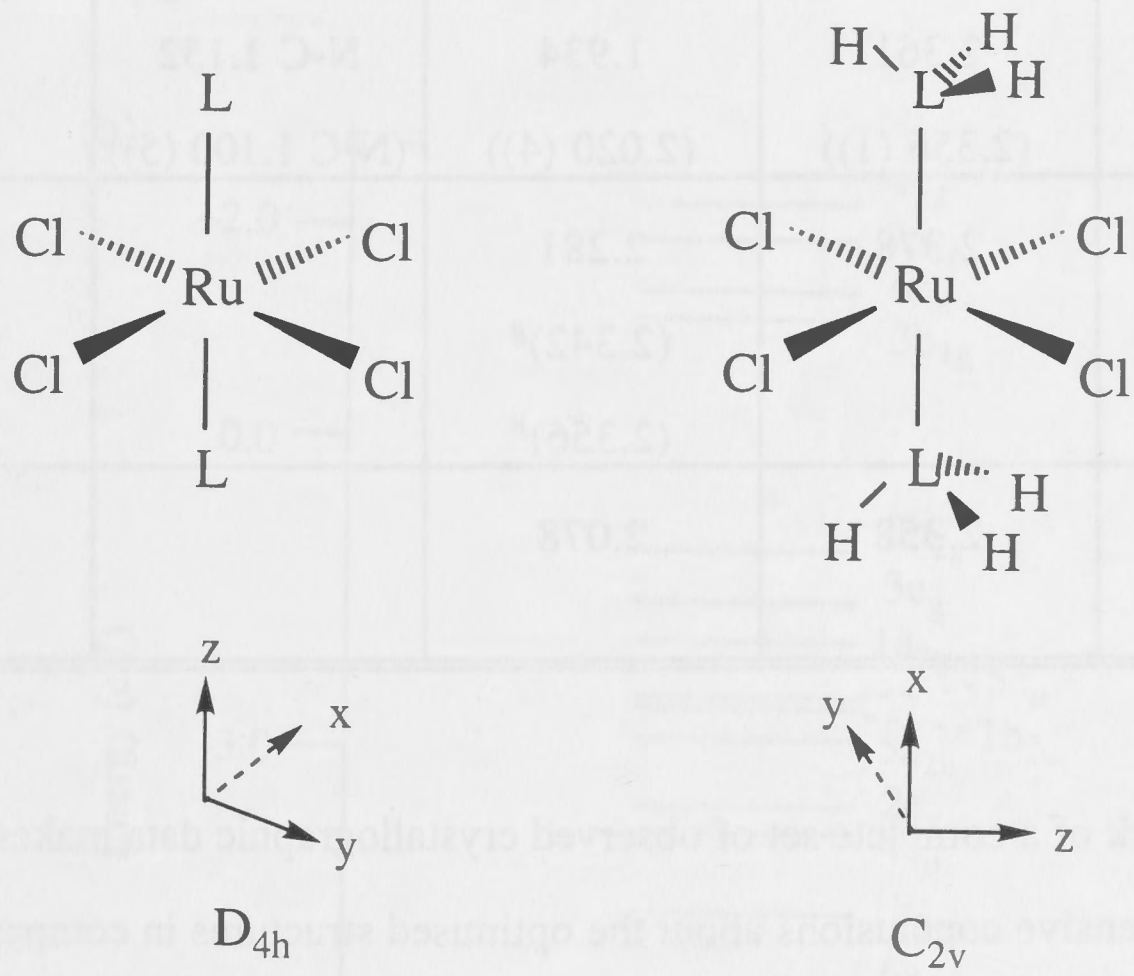

Figure 2.24 *Showing axes orientation for the D_{4h} and C_{2v} arrangements. Under D_{4h} symmetry, the z axis lies along the Ru-L bond and the x and y axes lie along the Ru-Cl bonds. Under C_{2v} symmetry, the x axis lies along the Ru-L bond and the y and z axes lie between the Ru-Cl bonds.*

The different orientation of the axes is determined by the program which defines z along the ~~principle~~ principal rotation axis. Throughout subsequent discussions comparing the effects of different ligands L, the results will be discussed in terms of the local D_{4h} symmetry

which is present about the ruthenium metal centre in each of the *trans*-$[RuCl_4L_2]^{1-}$ complexes (that is, the C_{2v} symmetry labels will be related to those from D_{4h}).

Geometry optimisations were performed on each complex in a manner similar to the $[TcYX_4]^{n-}$ computations described in chapter 2.1. The resultant calculated structural data are compared to the available observed data in table 2.25.

Table 2.25 Geometry optimisations of *trans*-$[RuCl_4L_2]^{1-}$ compared to the available reported crystal structure data which is presented in parenthesis.

Complex	Ru-Cl (Å)	Ru-L (Å)	Other (Å)	Reference
CNH (*t*-BuNC)	2.377	1.941	C-N 1.169	
NCH (MeCN)	2.361 (2.356 (1))	1.934 (2.020 (4))	N-C 1.152 (N-C 1.100 (5))	(**20**)
PH_3 (PMe_2Ph) (PEt_3)	2.378	2.281 (2.342)# (2.356)#		(**21**) (**21**)
NH_3 (aniline)	2.358	2.078		

The lack of a complete set of observed crystallographic data makes it difficult to draw comprehensive conclusions about the optimised structures in comparison with the observed structures. In general, it would appear that the optimised structures have a short Ru-L distance, which may be a function of two factors; firstly, the use of models for the trans ligands L which are, by design, less bulky than the parent L, and as a consequence more capable of closer interaction with the Ru metal centre. Secondly, the optimisation at the LDA level (used in this study, see chapter 2.3) tends to under-estimate the distance of bonds between a metal and "soft" ligands such as the Ru-L

As no crystal structure was available for the *trans*-$[RuCl_4(PR_3)_2]$ complexes under consideration here the Ru-P bond distances presented are based on a collection of bond distance averages for a number of different complexes containing Ru-P bonds trans to each other as summarised in a review of bond lengths (**21**).

bonds under investigation here (while at the same time performing well on more ionic bonds such as Ru-Cl (**22**)). No obvious trends in the Ru-Cl distance as a function of the nature of L were observed. This was in contrast to complexes of the type $[TcYX_4]^{n-}$ where a strong dependence of the Tc-X bond distance on the nature of the axial ligand Y was noted (see section 2.1.1).

2.2.2 The calculated electronic structure of *trans*-$[Ru^{III}Cl_4(NCH)_2]^{1-}$

The energies of the valence molecular orbitals of *trans*-$[Ru^{III}Cl_4(NCH)_2]^{1-}$ (d^5), as determined using spin-unrestricted density functional calculations, are presented graphically in figure 2.26 and detailed in table 2.27. Table 2.27 also includes an indication of the composition of each orbital. The singly occupied $2b_{2g}$ orbital is highlighted by shading.

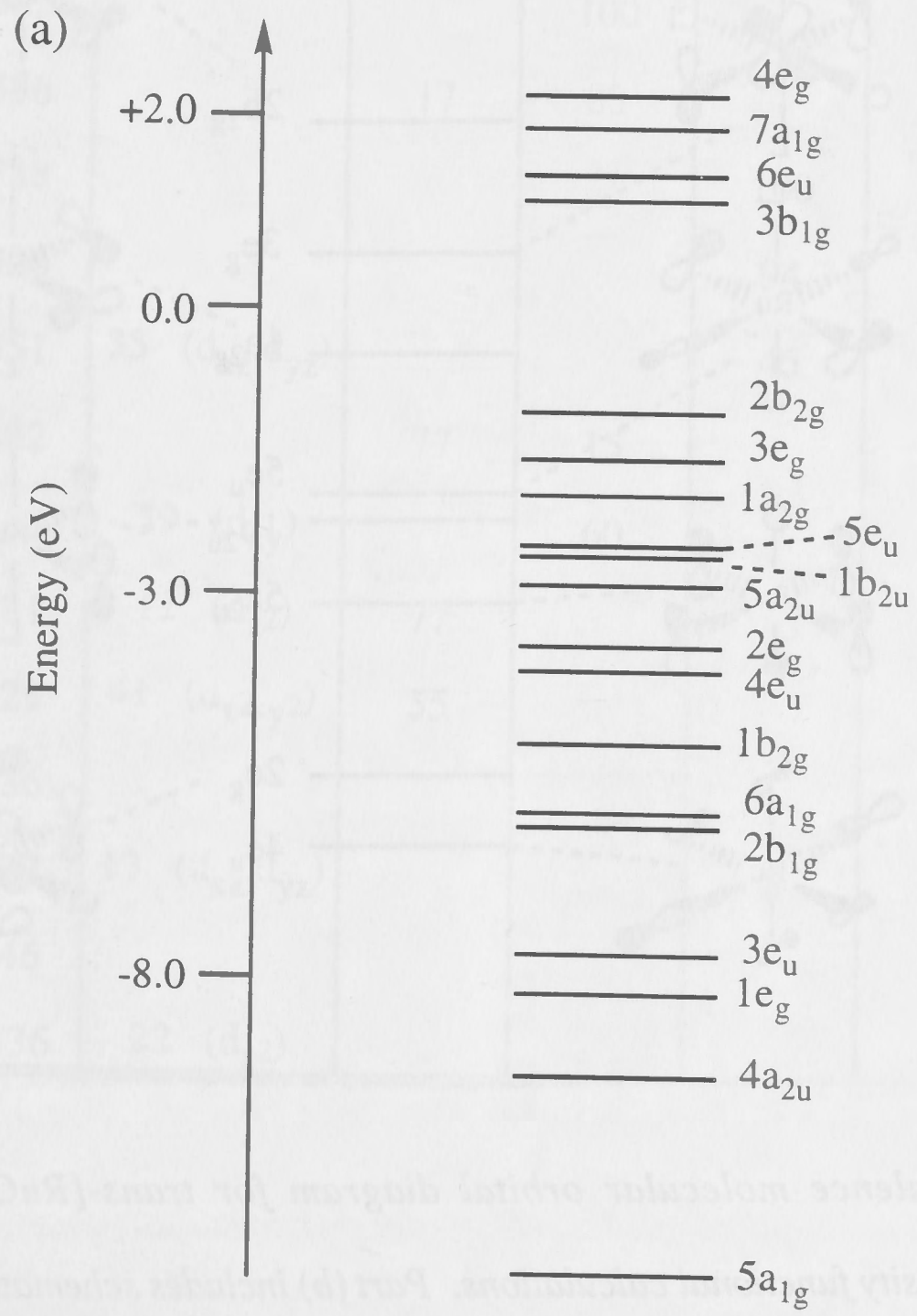

trans-$[RuCl_4(NCH)_2]^{1-}$

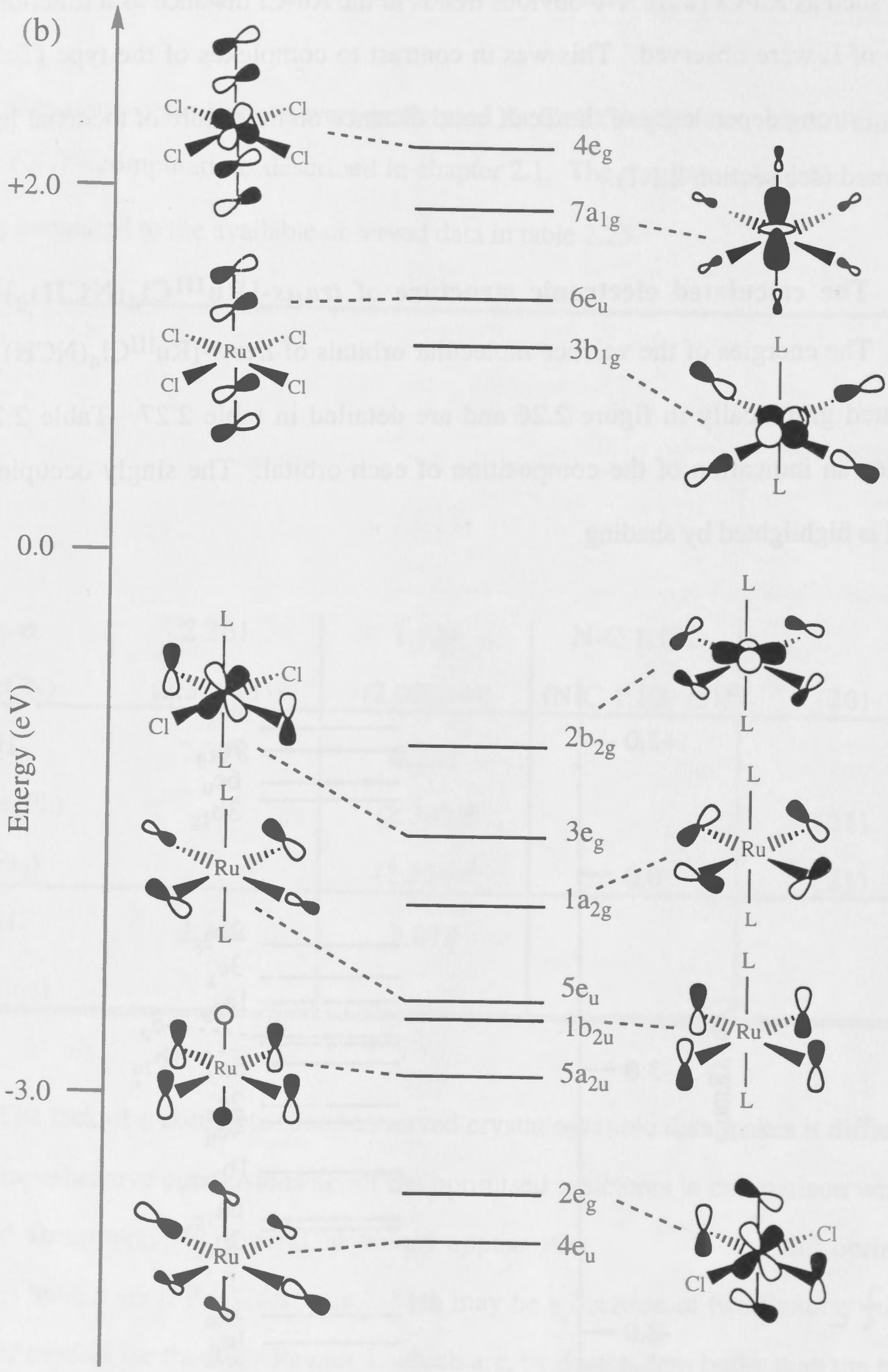

Figure 2.26 *Valence molecular orbital diagram for trans-$[RuCl_4(NCH)_2]^{1-}$ as determined by spin-unrestricted density functional calculations. The energy of the β-spin (spin-down, electron deficient) component is presented (see section 2.3.2). Part (b) includes schematic representations of the orbitals relevant to the subsequent discussion.*

Table 2.27 Calculated electronic structure for *trans*-$[Ru^{III}Cl_4(NCH)_2]^{1-}$

Orbital	Energy (eV)	Percentage Composition					
		Ru	Cl			L	
			in-plane		out-plane	2 p_x, p_y	2p_z, 3s
		4d	σ	π	π (2p_z)	π	σ
$4e_g$	+2.215	12 (d_{xz},d_{yz})				88	
$7a_{1g}$	+1.877	44 (d_{z2})	15				13
$6e_u$	+1.385					92	
$3b_{1g}$	+1.114	48 (d_{x2-y2})	46				
$2b_{2g}$	-1.060	58 (d_{xy})		39			
$3e_g$	-1.547	38 (d_{xz},d_{yz})			51	7	
$1a_{2g}$	-1.985			100			
$5e_u$	-2.556		17	83			
$1b_{2u}$	-2.588				100		
$5a_{2u}$	-2.906				94		2
$2e_g$	-3.551	35 (d_{xz},d_{yz})			45	16	
$4e_u$	-3.802		77	15		3	
$1b_{2g}$	-4.569	39 (d_{xy})		60			
$6a_{1g}$	-5.281	12 (d_{z2})	77				
$2b_{1g}$	-5.429	41 (d_{x2-y2})	55				
$3e_u$	-6.736					98	
$1e_g$	-7.157	12 (d_{xz},d_{yz})			3	87	
$4a_{2u}$	-8.046						87
$5a_{1g}$	-10.136	22 (d_{z2})					76

2.2.3.1 General description

The following discussion aims to analyse the electronic structure of *trans*-$[RuCl_4(NCH)_2]^{1-}$ in a manner similar to that which was used in chapter 2.1 for complexes of the type $[TcYX_4]^{n-}$. To that end, the analysis will be broken down into

three sections describing the contributions from the central Ru^{III} (d^5) cation, the trans NCH ligands, and finally the planar $\{Cl_4\}$ moiety.

2.2.3.2 *The ruthenium based levels*

Under D_{4h} symmetry and with axial coordination of π-acceptor ligands, the Ru 4d based levels split as indicated, qualitatively, in figure 2.28.

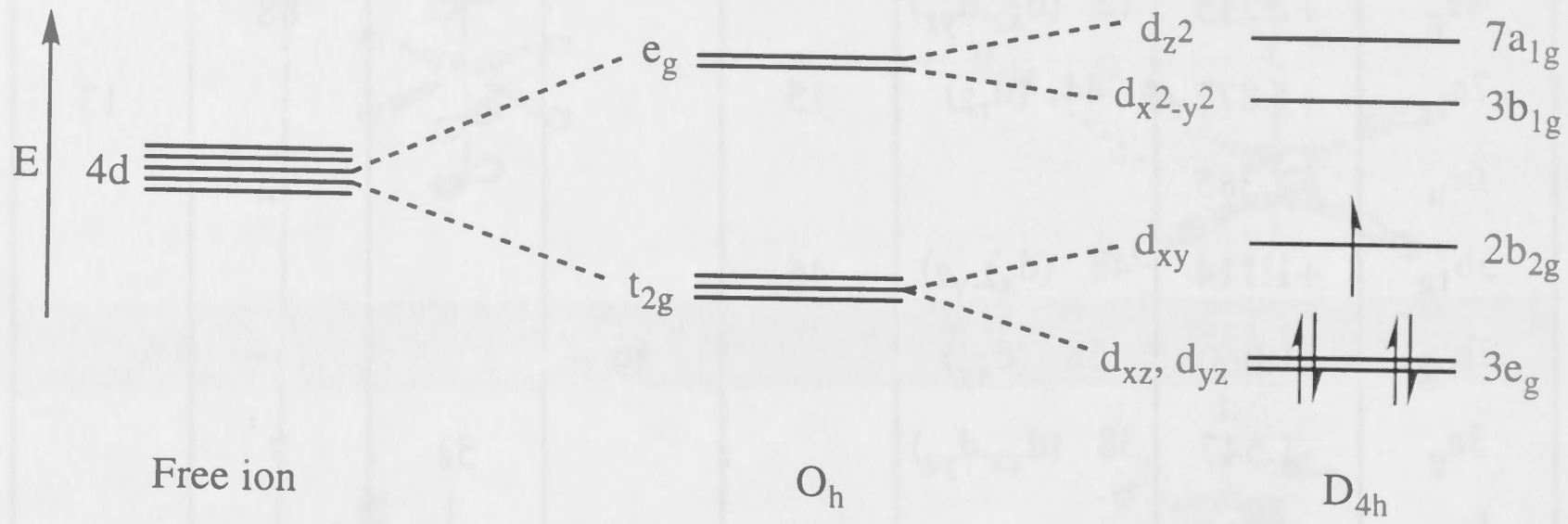

Figure 2.28 *A qualitative representation of the splitting of the 4d levels under D_{4h} symmetry and in the presence of axially coordinated π-acceptor ligands including the electronic configuration for a d^5 species.*

The axes are defined such that the z axis lies along the Ru-NCH bond (as was illustrated in figure 2.24). The $7a_{1g}$ and $3b_{1g}$ molecular orbitals are σ-antibonding with respect to the NCH and $\{Cl_4\}$ ligands respectively and hence are the most destabilised of the 4d levels. The $2b_{2g}$ level is π-antibonding to all four $\{Cl_4\}$ ligands and non-interacting with the NCH ligands. Each of the two degenerate components of the $3e_g$ level are concurrently π-antibonding with respect to only two of the $\{Cl_4\}$ ligands and π-bonding with respect to the trans NCH ligands (see figure 2.26b). Hence $3e_g$ is the most stabilised of the 4d levels.

2.2.3.3 *L = NCH based levels*

The lowest lying levels in table 2.27 ($3e_u$, $1e_g$, $4a_{2u}$ and $5a_{1g}$) are dominated by the NCH ligand. The $3e_u$ and $1e_g$ levels represent the π bonding within the NCH ligand, while $4a_{2u}$ and $5a_{1g}$ are dominated by the internal NCH σ-type bonding. The relatively stabilised energies of these orbitals are such that NCH to Ru charge transfer transitions

would be expected to be of high energy, and therefore outside the range of the observed spectra.

The $6e_u$ and $4e_g$ levels which are positioned between and immediately above the Ru based levels respectively arise from combinations of the internal π^*-type orbitals of NCH, and were potentially available as acceptor orbitals. The internal anti-bonding σ^* levels occur to higher energy (> +3.5 eV) and were not tabulated.

2.2.3.4 The $\{Cl_4\}$ based moiety

The remaining levels are based on the $\{Cl_4\}$ moiety. The basic components of an idealised $\{Cl_4\}$ manifold were outlined in chapter 2.1 (section 2.1.3.1). While they are built up from the same starting arrangement, there are some significant differences in the levels dominated by the $\{Cl_4\}$ manifold between those described for complexes of the type $[TcYCl_4]^{n-}$ in chapter 2.1 and the *trans*-$[RuCl_4(NCH)_2]^{1-}$ species under consideration here.

The first of these differences is the positioning of the metal centre relative to the $\{Cl_4\}$ moiety. Whereas for $[TcYCl_4]^{n-}$ the technetium metal centre was positioned out of the $\{Cl_4\}$ plane, here the ruthenium centre is in the same plane as the $\{Cl_4\}$ moiety. Secondly, it can be seen from table 2.26, via the compositions of $5e_u$ and $4e_u$, that there is no detectable mixing of $\{Cl_4\}$ in-plane σ-, in-plane π- or out-of-plane π-character. This is in contrast to what was observed for $[TcYCl_4]^{n-}$ (see table 2.3) and is a function of the introduction of a centre of symmetry in the *trans*-$[RuCl_4(NCH)_2]^{1-}$ species. Within the $\{Cl_4\}$ manifold there are in-plane and out-of-plane based levels with a common e-type symmetry (see figure 2.5). Under the prevailing C_{4v} symmetry in complexes of $[TcYCl_4]^{n-}$ these in- and out-of-plane $\{Cl_4\}$ orientations maintained their common e-type symmetry and mixing between them was observed in the levels of the final complex (see figure 2.4 and table 2.10). In contrast, under the prevailing D_{4h} symmetry of *trans*-$[RuCl_4(NCH)_2]^{1-}$ the in-plane $\{Cl_4\}$ e levels are of e_u symmetry while the out-of-plane e levels have e_g symmetry and so mixing of in- and out-of-plane

character does not occur in the final complex. However, mixing of in-plane σ- and in-plane π-character remains symmetry allowed.

The increased structure observed in the spectra for the $[TcNX_4]^{n-}$ species was attributed to increased mixing of in-plane σ-, in-plane π- and out-of-plane π-character in the $\{X_4\}$ manifold and so the reduced mixing calculated here appears consistent with the relatively simple UV-visible spectrum observed for *trans*-$[RuCl_4(MeCN)_2]^{1-}$ (see figure 2.22b).

Some axial ligand character can mix with the out-of-plane $\{Cl_4\}$ levels as was seen in the $5a_{2u}$, $2e_g$, $4e_u$ and $3e_g$ levels where there was mixing of σ ($5a_{2u}$ and $4e_u$) and π ($2e_g$ and $3e_g$) character. These two levels are otherwise dominated by $\{Cl_4\}$ out-of-plane π-character (see figure 2.26b).

2.2.4 Effects of changing axial ligands, L, on the electronic structure of *trans*-$[Ru^{III}Cl_4L_2]^{1-}$

2.2.4.1 The ruthenium based levels

Figure 2.29 shows the ruthenium 4d levels for each of the calculations performed. They are plotted relative to the $1a_{2g}$($8b_2$, in C_{2v}) level which is a 100% in-plane π $\{Cl_4\}$ level positioned immediately below the d levels in each calculation. The C_{2v} labels are shown for completeness, but it is clear from the diagram that as the $4a_2$ and $7b_1$ levels are virtually degenerate, the C_{2v} arrangement resembles the D_{4h} arrangement very closely and to assist comparisons subsequent discussions will use the D_{4h} labels only.

Figure 2.29 also illustrates that the destabilisation of the $2b_{2g}$ orbital (relative to the energy of the first halide based orbital, $1a_{2g}$) increases in the order CNH ~ NCH < PH_3 < NH_3. This ordering is consistent with the previously reported $Ru^{III/II}$ reduction potentials (which correspond to the introduction of a second electron into this $2b_{2g}$ level) that were listed in table 2.21.

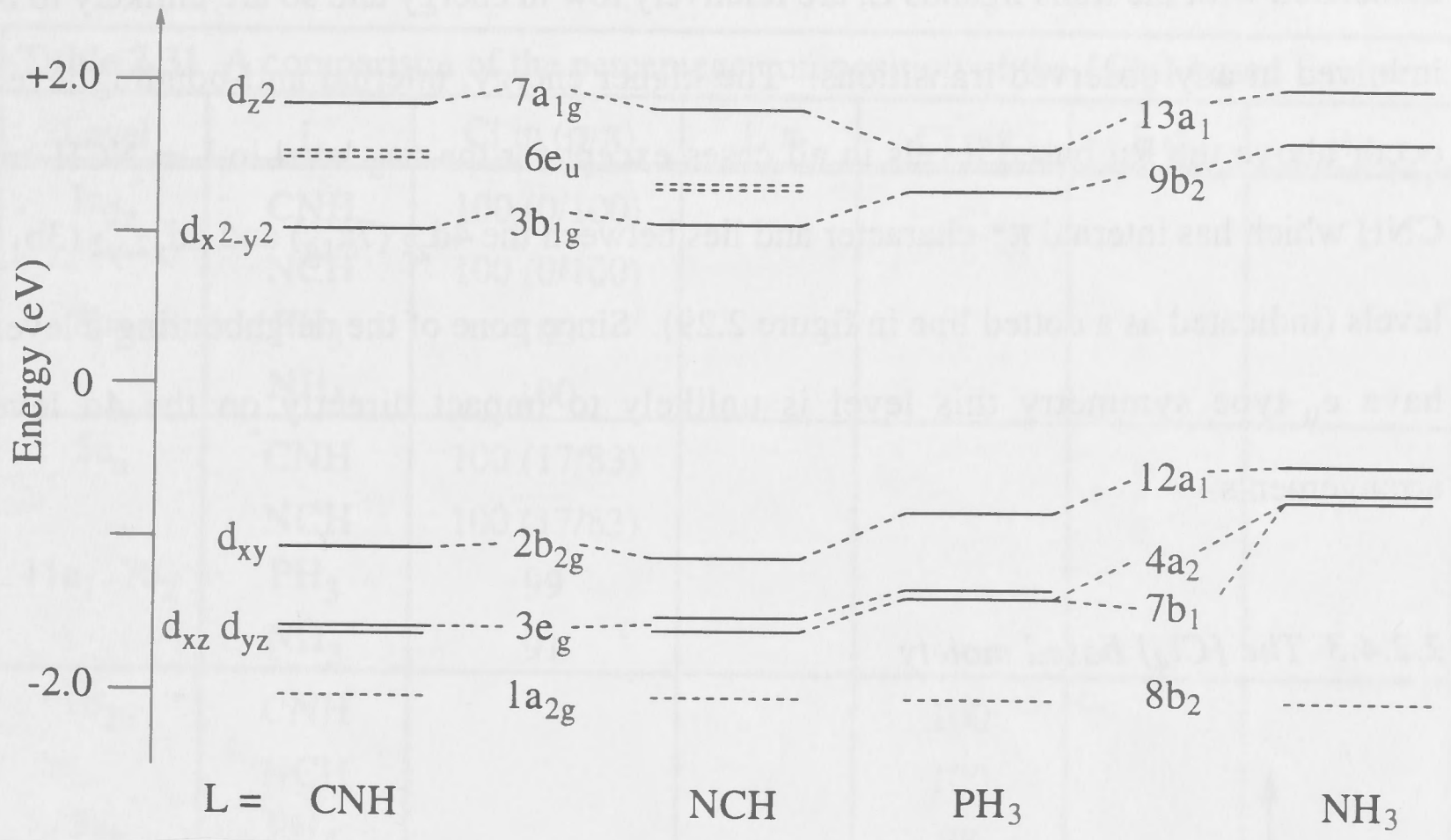

Figure 2.29 *Showing the energetic dependence of the ruthenium based levels on the axial ligands L. The ligand levels are indicated with dotted lines. In all four cases, the energies presented are derived from the β-spin component of a spin-unrestricted density functional calculation.*

The ordering of these reduction potentials is partly due to the relative π-acceptor ability of the axial ligand L, which is a factor that affects the electron density at the metal and is also important in determining the relative destabilisation of the $2b_{2g}$ level. Of the axial ligands under consideration here CNH, NCH and PH_3 are thought of as π-acceptors whereas NH_3 is not. (**10**)

Another interesting insight from figure 2.29 is how the splitting of the $4d_{xy}$ ($2b_{2g}$) and d_{xz},d_{yz} ($3e_g$) orbitals, which undergo π-type interactions with the surrounding ligand field, is affected by changes in the π-acceptor strength of the axial ligand L. For L = NCH, CNH and PH_3 (all of which might be expected to have some π-acceptor capabilities) this gap is of a similar magnitude, varying between 3900-4400 cm^{-1}. However for L = NH_3 the gap is very much smaller, measuring only 1300 cm^{-1} and this result is consistent with NH_3 generally not being thought of as a π-acceptor.

2.2.4.2 The levels associated with the trans ligands, L

In a situation which is similar to L = NCH in the other three complexes of the type *trans*-$[RuCl_4L_2]^{1-}$ (where L = CNH, PH_3 and NH_3) the bonding molecular orbitals

associated with the trans ligands L, are relatively low in energy and so are unlikely to be involved in any observed transitions. The higher energy, internal anti-bonding levels occur above the Ru based levels in all cases except for the $6e_u$ level in L = NCH and CNH which has internal π^*-character and lies between the $4d_{z2}$ ($7a_{1g}$) and $4d_{x2-y2}$ ($3b_{1g}$) levels (indicated as a dotted line in figure 2.29). Since none of the neighbouring d levels have e_u-type symmetry this level is unlikely to impact directly on the 4d level arrangements.

2.2.4.3 The {Cl_4} based moiety

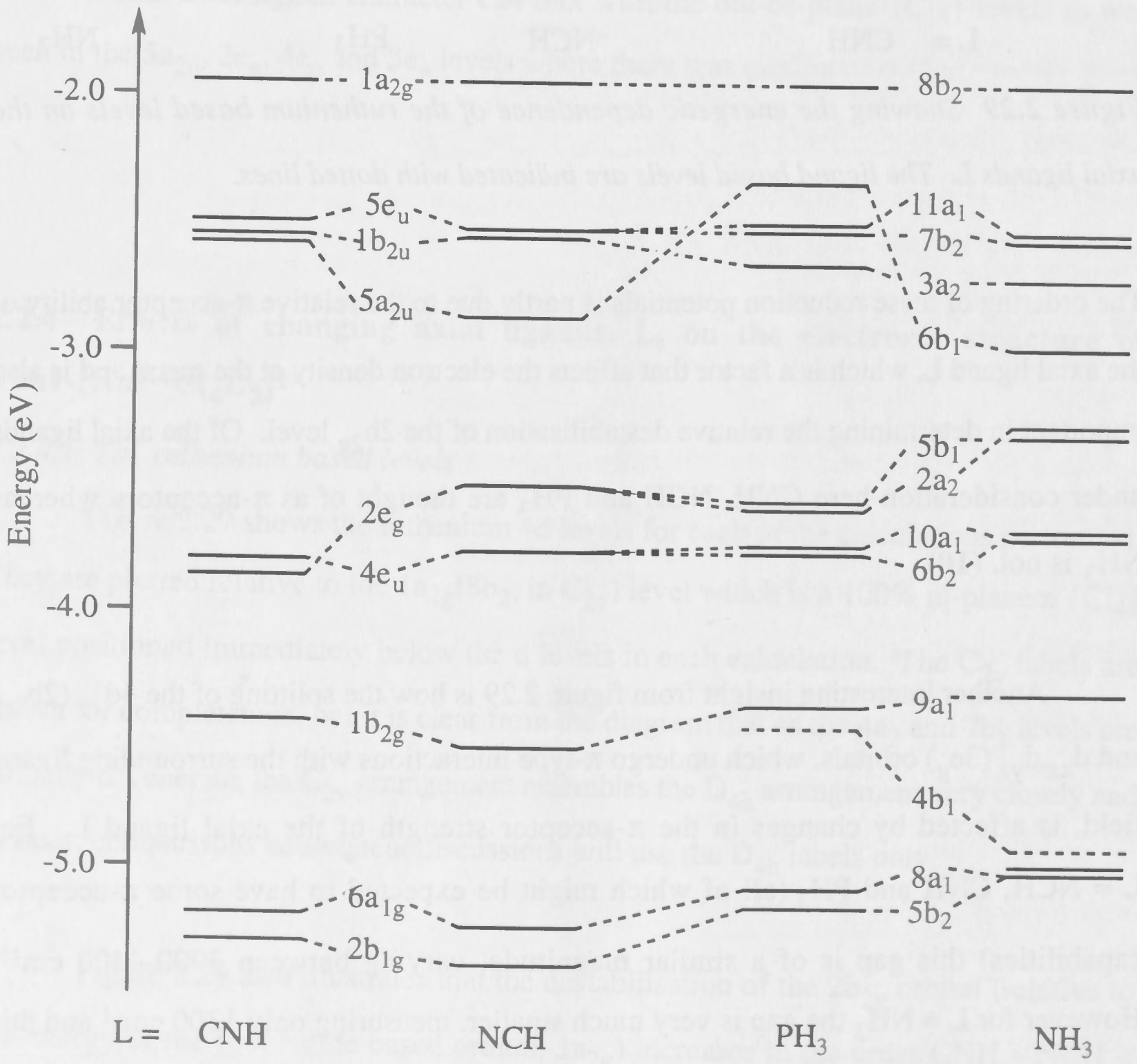

Figure 2.30 *Showing the dependence on the axial ligands L, of the energy of the occupied molecular orbitals comprising the {Cl_4} manifold (as derived from the β-spin component of a spin-unrestricted density functional calculation). The $4b_1$ levels observed for L = PH_3 and NH_3, are axial ligand based and so are indicated by dotted lines.*

Table 2.31 A comparison of the percentage composition of the $\{Cl_4\}$ based ligands.

Level	L	Cl in (σ/π)	L π	Cl out	L σ	Ru
$1a_{2g}$	CNH	100 (0/100)				
	NCH	100 (0/100)				
$8b_2$	PH_3	100				
	NH_3	100				
$5e_u$	CNH	100 (17/83)				
	NCH	100 (17/83)				
$11a_1, 7b_2$	PH_3	99				
	NH_3	91				
$1b_{2u}$	CNH			100		
	NCH			100		
$3a_2$	PH_3			98		
	NH_3			98		
$5a_{2u}$	CNH			88	12	
	NCH			94	2	
$6b_1$	PH_3			68	19	
	NH_3			83	8	
$2e_g$	CNH		16	38		42
	NCH		16	45		35
$5b_1, 2a_2$	PH_3		7	50		33
	NH_3		1	76		20
$4e_u$	CNH	92 (77/15)				
	NCH	92 (77/15)				
$10a_1, 6b_2$	PH_3	91				
	NH_3	91				
$1b_{2g}$	CNH	61 (0/61)				38
	NCH	60 (0/60)				39
$9a_1$	PH_3	65				33
	NH_3	68				22
$4b_1$	PH_3			28	46	
	NH_3				78	
$6a_{1g}$	CNH	77 (77/0)				12
	NCH	77 (77/0)				12
$8a_1$	PH_3	76				12
	NH_3	80				8
$2b_{1g}$	CNH	56 (56/0)				40
	NCH	55 (55/0)				41
$5b_2$	PH_3	58				38
	NH_3	60				36

Figure 2.30 shows the variation in relative energy of the $\{Cl_4\}$ based molecular orbitals for the four species, *trans*-$[RuCl_4L_2]^{1-}$ under consideration. As before, the energies of the levels are presented relative to the $1a_{2g}(8b_2)$ level. Generally, the $\{Cl_4\}$ based levels have similar compositions (see table 2.31) and similar orderings (see figure 2.30). The two notable exceptions to this are $5a_{2u}(6b_1)$ and $2e_g(5b_1, 2a_2)$. The $5a_{2u}$ level is relatively destabilised in the cases where L = PH_3 and CNH and table 2.31 shows that this may be associated with a lower Lσ character mixing in CNH and PH_3. While the $2e_g(5b_1, 2a_2)$ level is relatively destabilised where L = NH_3 and stabilised where L = CNH. The amount of Lπ character in the $2e_g$ level decreases from CNH ~ NCH > PH_3 > NH_3.

2.2.5 Spectral assignments for *trans*-$[RuCl_4(MeCN)_2]^{1-}$

This section contains a detailed assignment of the spectrum of *trans*-$[RuCl_4(MeCN)_2]^{1-}$ which will be used to compare with the spectra of the other *trans*-$[RuCl_4L_2]^{1-}$ species. The calculated energy for the possible charge transfer transitions (below 45 000 cm^{-1}) for *trans*-$[RuCl_4(NCH)_2]^{1-}$ are presented in table 2.32. The proposed spectral assignments as derived from table 2.32 are presented in table 2.33 and figure 2.34.

In order to be associated with an intense absorbance ($\varepsilon > 1000$ $dm^3mol^{-1}cm^{-1}$) a calculated charge transfer transition should be both electric dipole allowed and have the donor and acceptor orbitals in the same plane, with the same σ- or π-character. (**3**) (see also section 2.1.1) The first transition from table 2.32 which fulfils these criteria is the charge transfer transition $5e_u \rightarrow 2b_{2g}$ in which both levels are dominated by in-plane π-character and which has a computed energy of 14 560 cm^{-1}. This transition was therefore assigned to the lowest energy intense band observed in the spectrum which was centred at 24 725 cm^{-1} (bands IIIa and IIIb) despite the calculated energy being some 10 000 cm^{-1} below the observed energy. It is not uncommon for density functional theory to under-estimate the energy of halide-to-metal charge transfer transitions to this extent. (**2**,**3**) Previous studies on d^5 $[MX_6]^{n-}$ (M = Ru^{III}, Ir^{IV}; X = Cl, Br) monomers

found that calculated charge transfer transition energies were regularly 7500 cm^{-1} below the observed energies for the corresponding ligand-to-metal transitions (**2**). This under-estimation was attributed to an over stabilisation of the metal based orbitals relative to the ligand based ones. It did not diminish the usefulness of the calculation however, because the energy of the transitions relative to each other were consistent with observation (**2**).

Table 2.32 Calculated charge transfer energies for *trans*-$[RuCl_4(NCH)_2]^{1-}$.

Calculated energy (cm^{-1})	Transition	Type	Electric dipole allowed (Y/N)
10 270	$1a_{2g} \rightarrow 2b_{2g}$	π in $\rightarrow$ in π	N
14 560	$5e_u \rightarrow 2b_{2g}$	π/σ in $\rightarrow$ in π	Y
15 470	$1b_{2u} \rightarrow 2b_{2g}$	out $\rightarrow$ in π	N
17 770	$5a_{2u} \rightarrow 2b_{2g}$	out $\rightarrow$ in π	N
21 700	$2e_g \rightarrow 2b_{2g}$	Cl out, Lπ $\rightarrow$ in π	N
23 800	$4e_u \rightarrow 2b_{2g}$	σ/π in $\rightarrow$ in π	Y
27 220	$1a_{2g} \rightarrow 3b_{1g}$	π in $\rightarrow$ in σ	N
29 150	$1b_{2g} \rightarrow 2b_{2g}$	π in $\rightarrow$ in π	N
29 170	$3e_g \rightarrow 6e_u$	d out $\rightarrow$ L π	Y
31 470	$5e_u \rightarrow 3b_{1g}$	π/σ in $\rightarrow$ in σ	Y
32 170	$1b_{2u} \rightarrow 3b_{1g}$	out $\rightarrow$ in σ	Y
34 550	$5a_{2u} \rightarrow 3b_{1g}$	out $\rightarrow$ in σ	N
35 100	$2b_{1g} \rightarrow 2b_{2g}$	σ in $\rightarrow$ in π	N
35 210	$6a_{1g} \rightarrow 2b_{2g}$	σ in $\rightarrow$ in π	N
36 290	$1a_{2g} \rightarrow 6e_u$	π in $\rightarrow$ L π	Y
38 940	$2e_g \rightarrow 3b_{1g}$	out $\rightarrow$ in σ	N
40 530	$5e_u \rightarrow 6e_u$	π/σ in $\rightarrow$ L π	N
40 370	$1b_{2u} \rightarrow 6e_u$	out $\rightarrow$ L π	N

The assignment of band IIIa,b as the $5e_u \rightarrow 2b_{2g}$ transition is also supported by the double-component nature of this band (with maxima at 25 200 and 24 250 cm^{-1}, $\Delta = 950$

cm^{-1}) which is consistent with the involvement of an e-type level in the transition. This spectral assignment is similar to the $6e \rightarrow 2b_2$ transition described in chapter 2.1 observed in $[Tc^{VI}YX_4]^{n-}$ which also appeared as a doublet centred at around 20 000 cm^{-1} (ε 4000-2000 $dm^3mol^{-1}cm^{-1}$).

Table 2.33 Proposed spectral assignments for *trans*-$[RuCl_4(MeCN)_2]^{1-}$

Band label	Observed(cm^{-1}) (ε $dm^3mol^{-1}cm^{-1}$)	Transition	Calculated energy (cm^{-1})	Type of transition
I	32 810 (2100)	$4e_u \rightarrow 2b_{2g}$	23 800	$\{Cl_4\}$ in-σ/π → Ru $4d_{xy}$
II	28 000 (210)	$5a_{2u} \rightarrow 2b_{2g}$	17 770	$\{Cl_4\}$ out-π → Ru $4d_{xy}$
IIIa	25 200 (5400)	$5e_u \rightarrow 2b_{2g}$	14 560	$\{Cl_4\}$ in-π/σ → Ru $4d_{xy}$
IIIb	24 250 (5900)	$5e_u \rightarrow 2b_{2g}$	14 560	$\{Cl_4\}$ in-π/σ → Ru $4d_{xy}$
IV	21 250 (510)	$1a_{2g} \rightarrow 2b_{2g}$	10 270	$\{Cl_4\}$ in-π → Ru $4d_{xy}$

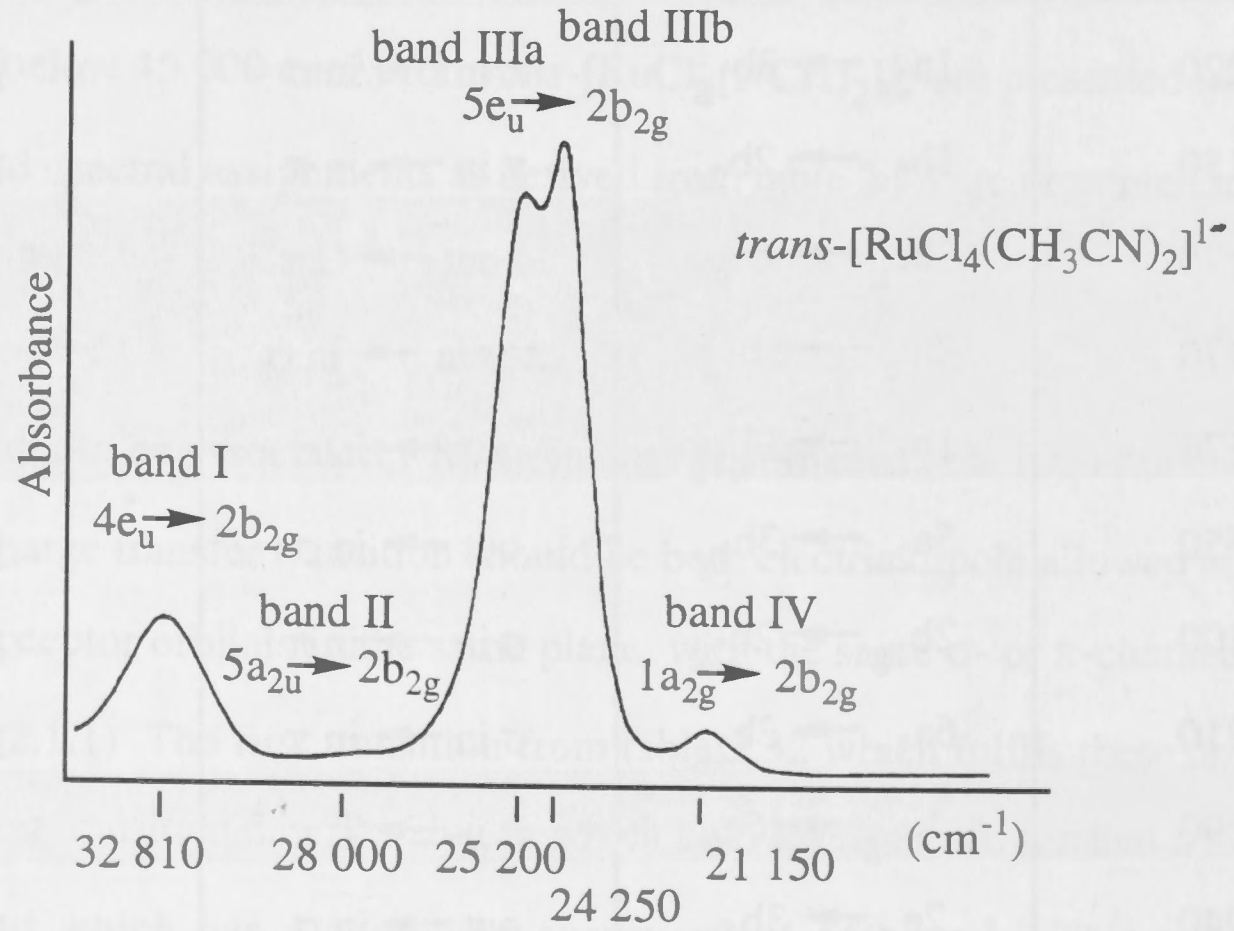

Figure 2.34 *UV-visible spectrum of trans-$[RuCl_4(MeCN)_2]^{1-}$ (**15**) showing the proposed spectral assignments determined in this thesis.*

The next transition from table 2.32 which may be associated with a relatively intense absorption is the in-plane charge transfer $4e_u \rightarrow 2b_{2g}$ transition which has a computed energy of 23 800 cm^{-1}, which is some 9240 cm^{-1} greater than the computed energy of the $5e_u \rightarrow 2b_{2g}$ transition just described. This calculated gap is similar to the gap of 8085 cm^{-1} which was observed between the two intense bands (bands IIIa,b and I) in the observed spectrum (determined by taking the average of the two maxima, IIIa and IIIb). On this basis, the second intense band, band I at 32 810 cm^{-1} (2100 $dm^3mol^{-1}cm^{-1}$) was assigned to this $4e_u \rightarrow 2b_{2g}$ transition. The relative intensity of band I (2100 $dm^3mol^{-1}cm^{-1}$) and band IIIa,b (an average of 5650 $dm^3mol^{-1}cm^{-1}$) is also modelled by the proposed assignments. Both transitions involve charge transfer into the in-plane π-based $2b_{2g}$ level. The $5e_u$ level associated band IIIa,b had 83% in-plane π-character while $4e_u$ (associated with band I) has only 15% in-plane π-character and therefore the $4e_u \rightarrow 2b_{2g}$ transition would be expected be less intense as is consistent with the proposed assignments.

The other electric dipole allowed transitions which were highlighted in table 2.32 were not expected to contribute to the observed spectrum as their calculated energies were around 30 000 cm^{-1} and above. The energies would therefore be expected to correspond to observed absorptions at, or above 40 000 cm^{-1}, on the basis that the assignments of bands I and IIIa,b had calculated energies of the order of 10 000 cm^{-1} below the observed ones.

This leaves the two low intensity absorbances, bands II and IV, to be assigned. The low intensity suggests that assignment to electric dipole forbidden processes may be appropriate. The lowest energy absorption, band IV was observed at 21 250 cm^{-1} (510 $dm^3mol^{-1}cm^{-1}$), 3475 cm^{-1} below the centre of band IIIa,b ($5e_u \rightarrow 2b_{2g}$). The only halide-to-metal charge transfer process calculated to be below band IIIa,b was the in-plane π-based $1a_{2g} \rightarrow 2b_{2g}$ transition which had a calculated energy of 10 270 cm^{-1}, some 4290 cm^{-1} lower than the calculated energy of band III which was reasonably consistent with the observed gap of 3475 cm^{-1}. This assignment is also consistent with

that proposed for the spectrum of $[TcNCl_4]^{1-}$ where the observed band gap between the equivalent intense doublet and weaker in-plane π band to lower energy was 2795 cm^{-1}, see section 2.1.11.

The assignment of band II observed at 28 100 cm^{-1} (ε 210 $dm^3mol^{-1}cm^{-1}$), approximately mid-way between the two intense absorbances band I and band IIIa,b, was somewhat more problematic. Three transitions were found to have calculated energies between those of the transitions corresponding to the two intense bands I and IIIa,b. Of these three, the electric dipole forbidden $5a_{2u} \rightarrow 2b_{2g}$ transition is favoured for the assignment of band II because its calculated energy is close to mid-way between that of the transitions corresponding to the observed bands, in accordance with the observed spectrum. The out-of-plane π orientation of $5a_{2u}$ and in-plane σ orientation of $2b_{2g}$ is also consistent with the lower intensity of band II as compared with band IV where both donor and acceptor orbitals are oriented in-plane which while both bands are electric dipole forbidden band IV has relatively more intensity.

These assignments for the spectrum of *trans*-$[RuCl_4(MeCN)_2]^{1-}$ as determined by calculation are broadly similar to those which have been published previously (**15**,**18**). Those studies relied on qualitative observations of spectra in different oxidation states, with different L and with both $\{Cl_4\}$ and $\{Br_4\}$ manifolds. All bands were assigned in the same way as was described here, except for band II, the weak absorbance at 28 000 cm^{-1}. In previous work (**15**,**18**) the assignment of $1b_{2g} \rightarrow 2b_{2g}$ for band II was made on the basis that while the transition was electric dipole forbidden, both donor and acceptor levels were in-plane π and so the transition was thought to be more likely. While the in-plane π-nature of the acceptor level is confirmed by calculation, the relative energy of the transition is not. Band II is observed at 28 000 cm^{-1}, some 4810 cm^{-1} <u>below</u> the observed energy of the relatively intense band I. However, the calculated energy for the $1b_{2g} \rightarrow 2b_{2g}$ transition is 5340 cm^{-1} <u>above</u> the calculated energy of the $4e_u \rightarrow 2b_{2g}$ transition which is assigned to band I. Hence the alternative assignment for band II of $1b_{2g} \rightarrow 2b_{2g}$ is favoured here. Given that the weak band II does not appear

in all of the *trans*-$[Ru^{III}Cl_4L_2]^{n-}$ spectra studied, its assignment is the least tested by comparisons and so should be treated with some caution.

The spectra of the other *trans*-$[Ru^{III}Cl_4L_2]^{n-}$ species under consideration displayed many of the same features as those just described for *trans*-$[Ru^{III}Cl_4(MeCN_2]^{n-}$ and they also receive similar spectral assignments to be outlined in the following sections.

2.2.6 Spectral assignments for *trans*-$[RuCl_4(t\text{-}BuNC)_2]^{1-}$

The proposed spectral assignments for *trans*-$[RuCl_4(t\text{-}BuNC)_2]^{1-}$ (see figure 2.22a) are presented in table 2.35.

Table 2.35 Proposed spectral assignments for *trans*-$[RuCl_4(t\text{-}BuNC)_2]^{n-}$

Band label	Observed (cm^{-1})	Transition	Calculated energy (cm^{-1})	Type of transition
I	32 700	$4e_u \rightarrow 2b_{2g}$	24 390	$\{Cl_4\}$ in-$\sigma/\pi \rightarrow$ Ru $4d_{xy}$
III	23 900	$5e_u \rightarrow 2b_{2g}$	14 760	$\{Cl_4\}$ in-$\pi/\sigma \rightarrow$ Ru $4d_{xy}$
IV	20 600	$1a_{2g} \rightarrow 2b_{2g}$	10 590	$\{Cl_4\}$ in-$\pi \rightarrow$ Ru $4d_{xy}$

The two things to note are that the first intense band (labelled band III) at 23 900 cm^{-1} is assigned as $5e_u \rightarrow 2b_{2g}$. The doublet structure is not as clearly resolved as it was in *trans*-$[RuCl_4(MeCN)_2]^{1-}$ but, rather, a shoulder to high energy is observed. Secondly, no low intensity band, equivalent to band II for L = MeCN, was observed between the intense $5e_u \rightarrow 2b_{2g}$ and $4e_u \rightarrow 2b_{2g}$ transitions, band III and band I respectively, in the spectrum of *trans*-$[RuCl_4(t\text{-}BuNC)_2]^{1-}$. The observed energy gap between the intense bands I and III in *trans*-$[RuCl_4(t\text{-}BuNC)_2]^{1-}$ was 8800 cm^{-1} as compared to 9200 cm^{-1} for *trans*-$[RuCl_4(MeCN)_2]^{1-}$. This apparent absence of a distinct band II in the spectrum of *trans*-$[RuCl_4(MeCN)_2]^{1-}$ could be accounted for by the calculations. It was found that the two transitions which had calculated energies between the assignments of the two intense bands were $1b_{2u} \rightarrow 2b_{2g}$ (15 690 cm^{-1}) and

$5a_{2u} \rightarrow 2b_{2g}$ (15 240 cm^{-1}). Both of these transitions had calculated energies within 925 cm^{-1} of the calculated energy of the $5e_u \rightarrow 2b_{2g}$ transition (14 760 cm^{-1}) which was assigned to band III. Hence the $1b_{2u} \rightarrow 2b_{2g}$ and/or the $5a_{2u} \rightarrow 2b_{2g}$ transitions which may be expected to contribute to a potential band II may well be obscured by the more intense electric dipole allowed transition of band III. The latter was assigned as band II in the spectrum of *trans*-$[RuCl_4(MeCN)_2]^{1-}$.

The low-intensity band IV was observed 3300 cm^{-1} below band III. This was a similar gap to the 3475 cm^{-1} gap observed between band IIIa,b and band IV in *trans*-$[Ru^{III}Cl_4(MeCN_2]^{n-}$ and the corresponding assignments are proposed. The calculated gap of 4770 cm^{-1} between the $5e_u \rightarrow 2b_{2g}$ assignment for band III and $1a_{2g} \rightarrow 2b_{2g}$, the proposed assignment for band IV, is consistent with observation.

2.2.7 Spectral assignments for *trans*-$[RuCl_4(PMe_2Ph)_2]^{1-}$, *trans*-$[RuCl_4(PEt_3)_2]^{1-}$ and *trans*-$[RuCl_4(aniline)_2]^{1-}$

The UV-visible spectra of *trans*-$[RuCl_4(PMe_2Ph)_2]^{1-}$, *trans*-$[RuCl_4(PEt_3)_2]^{1-}$ and *trans*-$[RuCl_4(aniline)_2]^{1-}$ show only one intense ($\varepsilon > 2000$ $dm^3mol^{-1}cm^{-1}$) absorbance below 35 000 cm^{-1} (labelled band IIIa,b). This absorbance appeared as a doublet and was attributed to the same $5e_u \rightarrow 2b_{2g}$ transition employed for band III throughout this chapter. The higher energy band I (assigned as $4e_u \rightarrow 2b_{2g}$ in the spectra where L = MeCN and *t*-BuNC) was not observed, possibly being obscured by transitions internal to the axial ligands#. The proposed assignments for the observed spectra are presented in tables 2.36 and 2.37.

In contrast to the spectra discussed previously, there were <u>two</u> low energy, low intensity absorbances (band IV and band V) observed in these UV-visible spectra of *trans*-$[RuCl_4(PPhMe_2)_2]^{1-}$, *trans*-$[RuCl_4(PEt_3)_2]^{1-}$ and *trans*-$[RuCl_4(aniline)_2]^{1-}$, whereas for *trans*-$[RuCl_4(t\text{-}BuNC)_2]^{1-}$ and *trans*-$[RuCl_4(MeCN)_2]^{1-}$ there was only <u>one</u> absorbance identified (see tables 2.33 and 2.35). The higher of these two bands, band

The possibility of internal axial ligand charge transfer was not represented for by the calculations due to the simplified models chosen for L.

IV, was observed at 22 700 (L = PMe_2Ph), 23 300 (L = PEt_3) and 26 000 cm^{-1} (L = aniline) which is red shifted from the centre of the band IIIa,b doublet by 2790, 3520 and 3225 cm^{-1} respectively. As before, the equivalent assignment for band IV of $1a_{2g} \rightarrow 2b_{2g}$ is favoured here (see tables 2.36 and 2.37). This assignment is also consistent with previous reports of the spectral assignments, which were based on qualitative observations (**17,19**).

Table 2.36 Proposed spectral assignments for *trans*-$[RuCl_4(PMe_2Ph)_2]^{1-}$ and *trans*-$[RuCl_4(PEt_3)_2]^{1-}$.

Band Label	*trans*-$[RuCl_4L_2]^{1-}$ L = PMe_2Ph (cm^{-1})	*trans*-$[RuCl_4L_2]^{1-}$ L = PEt_3 (cm^{-1})	Transition	Calculated energy (cm^{-1})	Type
IIIa	26 910	27 200	$5e_u \rightarrow 2b_{2g}$	17 200#	$\{Cl_4\}$ in-$\pi/\sigma \rightarrow$ Ru $4d_{xy}$
IIIb	26 070	26 440	$5e_u \rightarrow 2b_{2g}$	17 190#	$\{Cl_4\}$ in-$\pi/\sigma \rightarrow$ Ru $4d_{xy}$
IV	22 700	23 300	$1a_{2g} \rightarrow 2b_{2g}$	12 950	$\{Cl_4\}$ in-$\pi \rightarrow$ Ru $4d_{xy}$
V	17 960	17 000	$2b_{2g} \rightarrow 7a_{1g}$	(24 450)##	$d_{xy} \rightarrow d_{z^2}$

Table 2.37 Proposed spectral assignments for *trans*-$[RuCl_4(aniline)_2]^{1-}$.

Band label	Observed energy (cm^{-1}) (ε $dm^3mol^{-1}cm^{-1}$)	Transition	Calculated energy (cm^{-1})	Type
IIIa	29 950 (2990)	$5e_u \rightarrow 2b_{2g}$	21 510	$\{Cl_4\}$ in-$\pi/\sigma \rightarrow$ Ru $4d_{xy}$
IIIb	28 500 (2320)	$5e_u \rightarrow 2b_{2g}$	20 420	$\{Cl_4\}$ in-$\pi/\sigma \rightarrow$ Ru $4d_{xy}$
IV	26 000 (sh)	$1a_{2g} \rightarrow 2b_{2g}$	16 210	$\{Cl_4\}$ in-$\pi \rightarrow$ Ru $4d_{xy}$
V	21 600 (160)	$2b_{2g} \rightarrow 7a_{1g}$	(19 950)##	$d_{xy} \rightarrow d_{z^2}$

There are two calculated energies for this transition as a result of the lower C_{2v} symmetry which was used in the calculation.

Calculated transition energies for the d-d transitions should not be compared to those for charge transfer due to the different errors which are associated with their determination.

The assignment of the lower energy, low intensity band V, which was not observed in the spectra of *trans*-$[RuCl_4(MeCN)_2]^{1-}$ or *trans*-$[RuCl_4(t\text{-}BuNC)_2]^{1-}$ is non-trivial. The calculations reported here, give corresponding assignments for band IIIa,b and band IV in the spectra of all three species L = PMe_2Ph, PEt_3 and aniline. Band V has alternatively been previously assigned as phosphine to ruthenium charge transfer where L = PMe_2Ph and PEt_3 (**23**,**17**), and as a d-d transition where L = aniline (**4**).

The calculations performed here support the previously proposed d-d assignment (**4**) within the spectrum of *trans*-$[RuCl_4(aniline)_2]^{1-}$. The electronic structure presented in figure 2.30 showed that there were no $\{Cl_4\}$ or NH_3 based levels available for charge transfer which would have a lower energy than the $1a_{2g} \rightarrow 2b_{2g}$ transition which was attributed to band IV. The calculated gap between the ruthenium 4d levels was presented in figure 2.29 is smallest for L = NH_3, as a result, d-d transitions would be expected to be to lower energy and so less likely to be obscured by charge transfer transitions. The specific $2b_{2g}(d_{xy}) \rightarrow 7a_{1g}(d_{z2})$ transition is favoured here, over the $2b_{2g}(d_{xy}) \rightarrow 3b_{1g}(d_{x2-y2})$ transition due to the energetic dependence of band V on the nature of the axial ligand L, which is most effectively reproduced by the $2b_{2g}(d_{xy}) \rightarrow 7a_{1g}(d_{z2})$ assignment.

This leaves the assignment of band V where L = PMe_2Ph and PEt_3. Experimentally, the energy of this band showed the most dependence on the phosphine present. (**3**,**17**) This band V is observed at 17 960 cm^{-1} in the spectrum of L = PMe_2Ph but is red shifted by 960 cm^{-1} in the spectrum of L = PEt_3. The Ru-P distance is expected to be around 0.014 Å longer than for the former species (see table 2.25). (**21**)

It was on the basis of this phosphine dependence that previous workers using qualitative observations assigned band V to phosphine to ruthenium charge transfer (**17**). Previous studies on the isoelectronic, d^5 system, *trans*-$[IrCl_4(PR_3)_2]$ also attributed a low energy band (positioned below the equivalent band IV) to phosphine to metal charge transfer (**23**). However, the computed electronic structure for *trans*-$[RuCl_4(PH_3)_2]$

presented here (table 2.31) showed no evidence of phosphine dominated levels at a suitable energy for charge transfer into the metal levels. In particular, there was unlikely to be any kind of ligand-to-metal charge transfer with an energy below that of $1a_{2g} \rightarrow 2b_{2g}$ (the assignment attributed to band IV). Therefore the proposed assignment for band V, based on these calculations, is as to d-d transitions (in a manner similar to L = aniline).

Calculations using L = PH_3 were performed in order to model the effect of variation in the Ru-P distance from the optimised distance of 2.2813 Å (to mimic the effect of increasing the bulkiness of the phosphine ligands) (table 2.38)

Table 2.38 Calculated relative energetic dependance of levels on Ru-P distance.

Ru-P distance (Å)	Energetic gap between levels (cm^{-1})		
	$2b_{2g}$ ($12a_1$) and $7a_{1g}$ ($13a_1$) $d_{xy} \rightarrow d_{z2}$	$2b_{2g}$ ($12a_1$) and $3b_{1g}$ ($9b_2$) $d_{xy} \rightarrow d_{x2-y2}$	$5a_{2u}$ ($6b_1$) and $2b_{2g}$ ($12a_1$) $\{Cl_4\}/P \rightarrow d_{xy}$
2.2813	25 580	19 360	15 870
2.3200	24 440	19 340	16 260
2.3490	23 590	19 330	16 540

The energetic gap between $5a_{2u}$ (the first ligand based level with any significant phosphine character) and $2b_{2g}$ was calculated to increase, in contrast to observed trends, further suggesting that band V is unlikely to be due to phosphine to ruthenium charge transfer.

The observed decrease in energy of band V with increasing Ru-P distance was best modelled by the calculated gap between the $2b_{2g}$ and $7a_{1g}$ d-d levels which was also was seen to decrease as the Ru-P bond length was increased. Once again the $2b_{2g}$ and $3b_{1g}$ gap did not show any significant dependence on the Ru-P distance in accordance with the orientation of the levels within the plane of the $\{Cl_4\}$ moiety rather than toward

the axial ligands. Hence the d-d assignment for band V which seems to be most consistent with observation is as $2b_{2g} \rightarrow 7a_{1g}$.

It would be unwise to use these calculations on *trans*-$[RuCl_4(PR_3)_2]^{1-}$ to reinterpret the spectra of the isoelectronic *trans*-$[IrCl_4(PR_3)_2]$ species that ~~was~~ were mentioned earlier (**23**). The 7000 cm^{-1} difference in the energy of band III indicates that the energy of the metal levels relative to the halide ones is substantially different. Further quantitative evidence would be necessary to accurately assess the impact of a different metal centre on the appropriate assignment for band V in *trans*-$[IrCl_4(PR_3)_2]^{n-}$.

2.2.8 Conclusion

Assignments have been proposed for the UV-visible electronic absorption spectra of a series of complexes, *trans*-$[Ru^{III}Cl_4L_2]^{1-}$ (where L = MeCN, *t*-BuNC, PMe_2Ph, PEt_3 and aniline). The spectra are dominated by charge transfer from the $\{Cl_4\}$ manifold to the ruthenium metal centre and all contain at least a sub-set of the bands listed in table 2.39 along with their assignments in terms of local D_{4h} symmetry about the metal centre.

Table 2.39 Assignments of the bands of the spectra for the series *trans*-$[Ru^{III}Cl_4L_2]^{1-}$.

Band	Transition
I	$4e_u \rightarrow 2b_{2g}$
II	$5a_{2u} \rightarrow 2b_{2g}$
III	$5e_u \rightarrow 2b_{2g}$
IV	$1a_{2g} \rightarrow 2b_{2g}$
V	$2b_{2g} \rightarrow 7a_{1g}$

In general, band III was prominent in all of the spectra observed and its energy was seen to vary with the axial ligand, moving to higher energy as the π-acceptor ability of L decreased. Similarly the E^0 potential for the one electron reduction of *trans*-$[Ru^{III}Cl_4L_2]^{1-}$ also showed a dependence on the axial ligands, L. A plot of both the observed and calculated energy of band III vs the E^0 reduction potential is presented in figure 2.40. The plot reveals a linear relationship between both observed and calculated the energy of band III and the E^0 potential for the $Ru^{III/II}$ reduction.

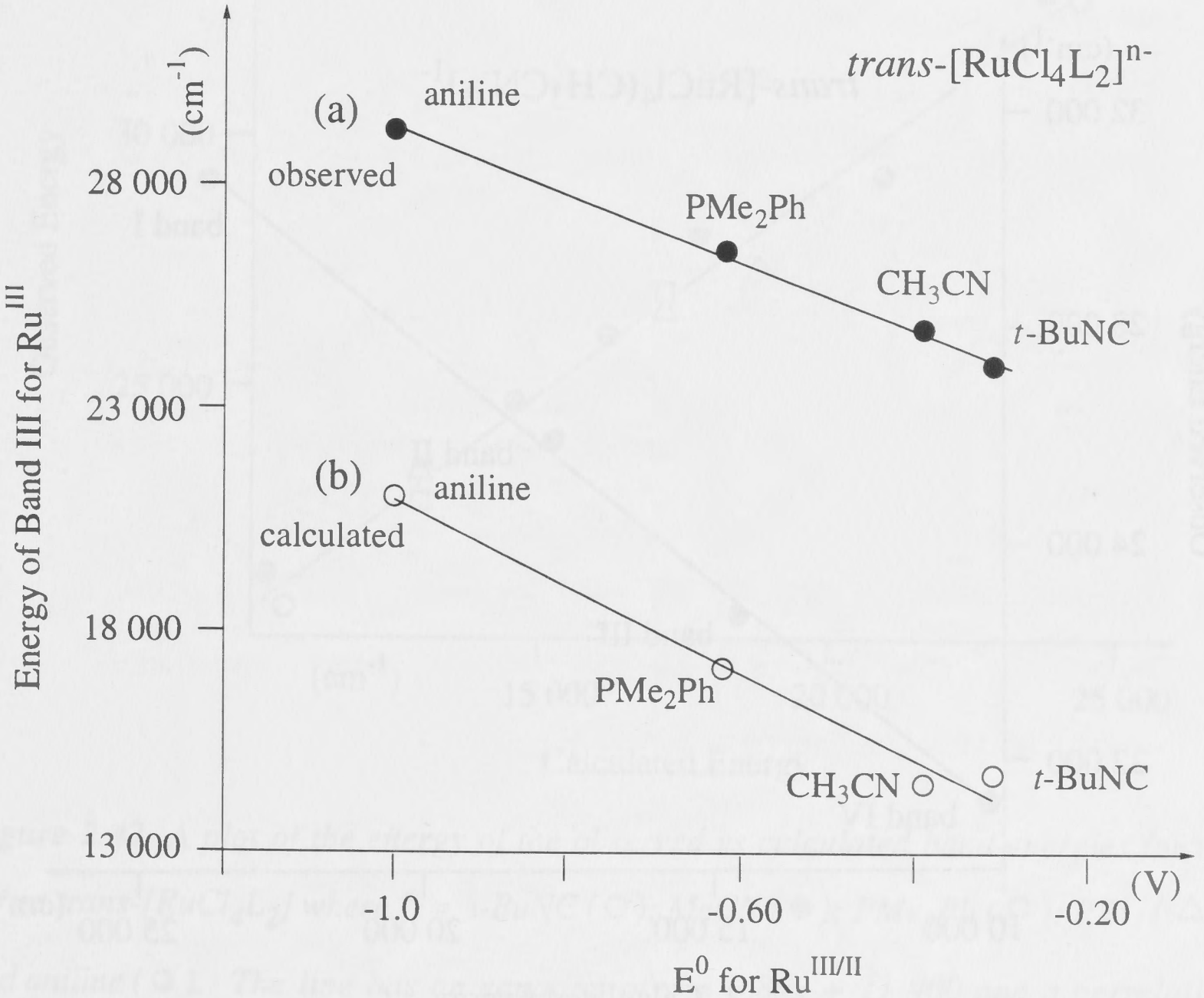

Figure 2.40 *A plot of (a) the observed energy and (b) the calculated energy of band III in the spectrum of trans-$[Ru^{III}Cl_4L_2]$ (where L is the ligand indicated beside each point on the graph) vs E^0 for the reduction from Ru^{III} to Ru^{II} for each complex. Where band III appeared as a doublet (band IIIa,b) the average energy of the two maxima is plotted. The gradient and (correlation coefficients) of each line are as follows: (a) observed data; gradient = -7600 $cm^{-1}V^{-1}$ (r^2 = 0.99) and (b) calculated data; gradient = -9600 $cm^{-1}V^{-1}$ (r^2 = 0.98).*

The assignments of the spectra of *trans*-$[RuCl_4L_2]^{1-}$ were based on intensity and energetic considerations. While the calculated transition energies differ considerably from the observed ones, they do show the correct relative energies. Figure 2.41 shows a plot of observed *vs* calculated transitions energies for all four bands of the spectrum of *trans*-$[RuCl_4(MeCN)_2]^{1-}$ (where L=NCH was used as the computational model). The linearity of the plot (r = 0.99) indicates that the calculated energy differences between transitions mirror the observed.

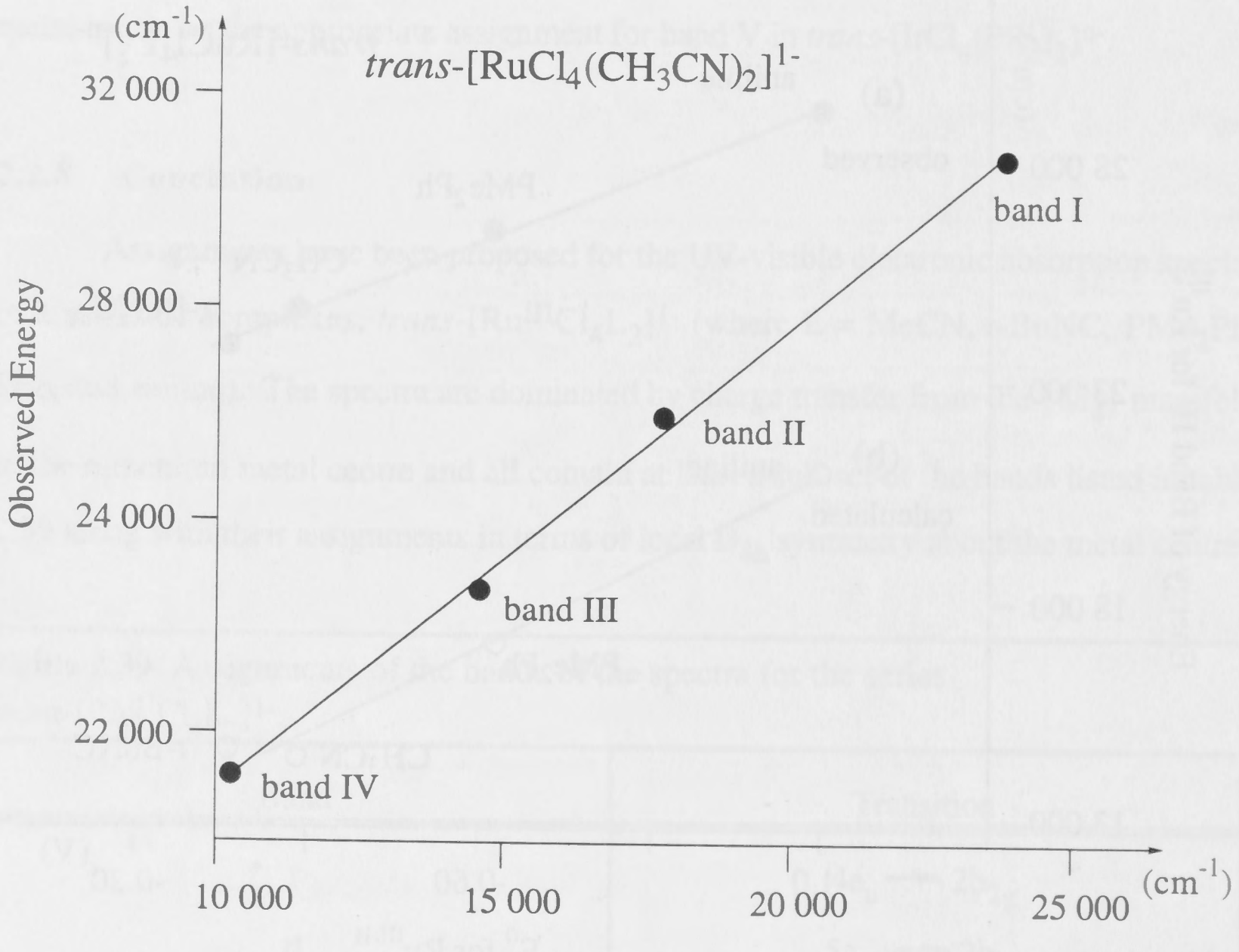

Figure 2.41 *A plot of observed vs calculated band energies for the spectrum of trans-*$[RuCl_4(MeCN)_2]^{1-}$. *The average of the observed maxima of band IIIa,b is plotted. The line has an equation of* $y = 0.86x + 12\ 400$ *and a correlation coefficient of* $r^2 = 0.99$. *This linear relationship indicates that the calculation is successfully reproducing the relative spacing of the absorbances.*

A plot for all five systems, of the observed energy of the transition corresponding to bands III and IV and bands I and II (where available) *vs* the calculated band energies shows that the same relative error was occurring over the five calculations for all the charge transfer bands from I to IV.

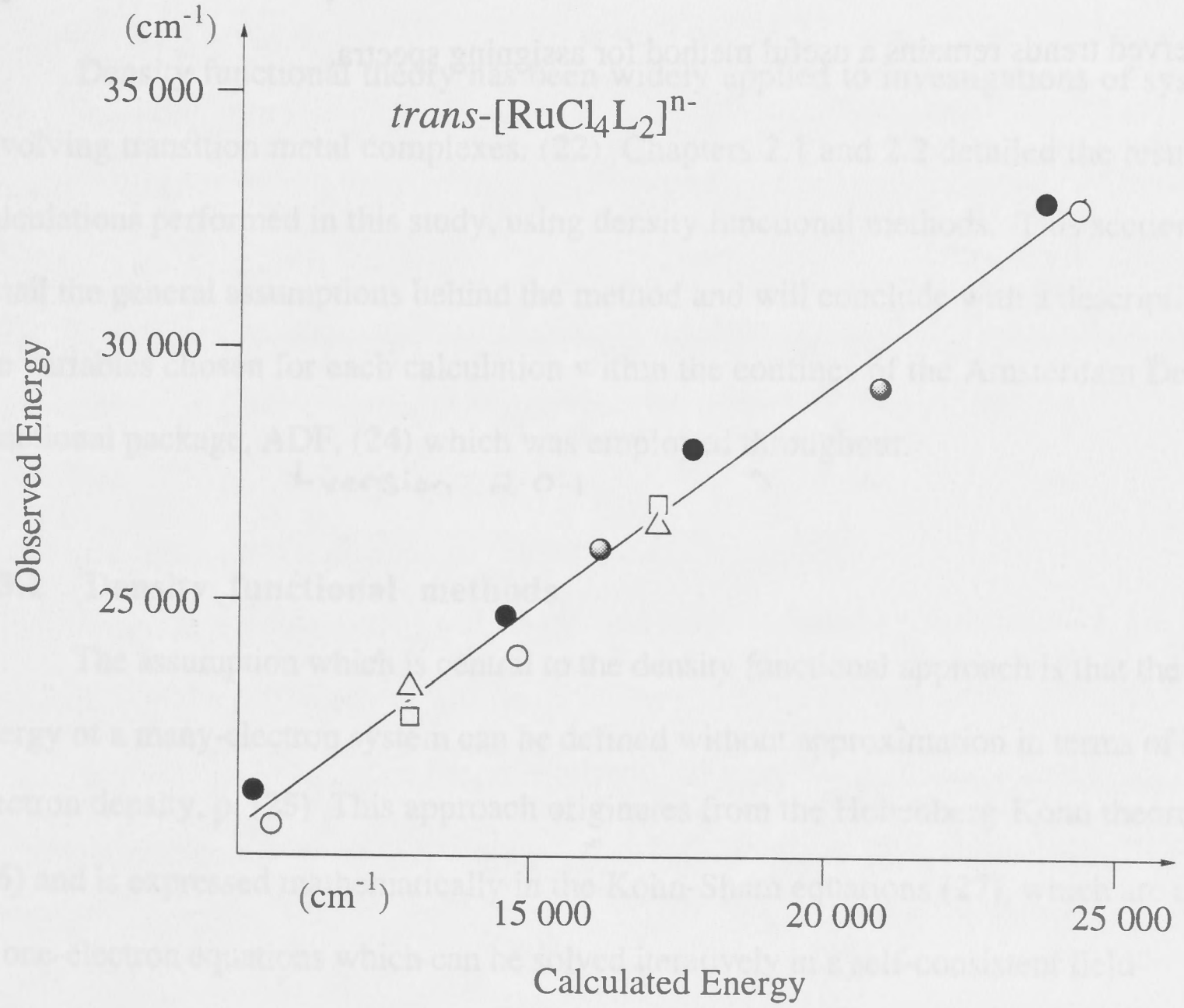

Figure 2.42 *A plot of the energy of the observed vs calculated band energies for the series trans-[$RuCl_4L_2$] where L = t-BuNC (○); MeCN (●); PMe_2Ph (□); PEt_3 (△); and aniline (◘). The line has an equation of y = 0.86x + 11 900 and a correlation coefficient of r^2 = 0.98.*

Figure 2.42 indicates that there is a reasonably constant relationship between calculated and observed charge transfer transition energies for the *trans*-$[RuCl_4L_2]^{1-}$ system. Further investigation reveals that this specific relationship applies only to this system and it is not generally applicable to other species. A similar plot to that presented in figure 2.42 has been previously reported for $[MX_6]^{n-}$ systems (**2**). On that occasion the average error for the calculated charge transfer transition energies was an under-estimation of the order of 7500 cm^{-1}. While the errors associated with calculated *vs*

observed for the $[TcYX_4]^{n-}$ system discussed in chapter 2.1 range from under-estimation by upto 5000 cm^{-1} to over-estimation by upto 3000 cm^{-1}. These three different systems reveal that there is no obvious correction factor which can be applied across the board to bring density functional calculated charge transfer transition energies in line with observation. Calculations of series of closely related compounds and modelling of observed trends remains a useful method for assigning spectra.

Chapter 2.3: Computational Method

Density functional theory has been widely applied to investigations of systems involving transition metal complexes. (**22**) Chapters 2.1 and 2.2 detailed the results of calculations performed in this study, using density functional methods. This section will detail the general assumptions behind the method and will conclude with a description of the variables chosen for each calculation within the confines of the Amsterdam Density functional package, ADF, (**24**) which was employed throughout.

Lversion 2.0.1

2.3.1 Density functional methods

The assumption which is central to the density functional approach is that the total energy of a many-electron system can be defined without approximation in terms of its electron density, ρ. (**25**) This approach originates from the Hohenberg-Kohn theorem (**26**) and is expressed mathematically in the Kohn-Sham equations (**27**), which are a set of one-electron equations which can be solved iteratively in a self-consistent field scheme:

$$\varepsilon_i \phi_i(r_1) = \hat{H}_{KS} \phi_i(r_1)$$

$$\text{where} \quad \hat{H}_{KS} = \left[-\frac{1}{2}\nabla^2 + \sum_A \frac{Z_A}{|R_A - r_1|} + \int \frac{\rho(r_2)}{|r_1 - r_2|} dr_2 + V_{XC} \right]$$

(i) (ii) (iii) (iv)

equation (1)

The total energy of the system is defined in terms of the four terms of the Kohn-Sham operator, $\hat{H}_{KS}$. (i) the kinetic energy of a system of N non-interacting electrons, of the same density as the actual system,

(ii) classical nuclei-electron coulomb interactions,

(iii) classical electron-electron coulomb interactions, and

(iv) a combination of non-classical electron-electron interactions, including exchange, correlation and a small kinetic energy component.(**27**)

The final term (iv), the exchange-correlation potential, V_{XC} is defined as the functional derivative of the energy of the exchange-correlation potential, E_{XC}, with respect to the electron density, ρ. (**27**)

$$V_{XC}(\rho) = \frac{\partial E_{XC}(\rho)}{\partial \rho} \qquad \textit{equation (2)}$$

Density functional theory, of the kind employed here, is unique in its approach, in that, in principle it describes all of the non-classical electron-electron interaction terms implicitly, using the V_{XC} term. As a result, it has been particularly effective in dealing with transition metal systems where electron-electron interactions provide a significant contribution to the total energy of the system. Other methods are not as well suited. Hartree-Fock methods for example, define both the classical columbic interactions and the non-classical exchange term exactly but ignore correlation effects. Results demonstrate that Hartree-Fock methods can be satisfactory for main group elements, but are not so useful for species containing transition metals where electron-electron correlation is important. Post-Hartree-Fock, *ab initio* methods can, in principle, be applied to transition metal systems but for these systems the computations are large and as such are inconvenient, particularly when attempting to analyse series of complexes, such as has been done in this thesis.

If the exact functional dependence of the non-classical exchange correlation energy, E_{XC}, with respect to electron density was known, the solution to a set of Kohn-Sham equations would lead to the exact result. Unfortunately while such a relation can be established for the other three terms of $\hat{H}_{KS}$, it cannot be derived exactly for E_{XC} and approximations are necessary. This point represents the major obstacle in the application of calculations based on density-functional theory. (**25**) In order to facilitate these approximations, E_{XC} is thought of in terms of its exchange (E_X) and correlation (E_C) parts, such that,

$$E_{XC} = E_X + E_C \qquad \textit{equation (3)}$$

The simplest approach is to use the local density approximation, LDA, (**28**) which firstly involves expressing E_{XC} as a functional similar to that developed by Slater,

which is itself based on the analytically known expression for the exchange interaction in a homogenous electron gas. (**29**)

$$E_X^{LDA} = -\frac{9}{4}\alpha_{ex}\left[\frac{3}{4}\pi\right]^{\frac{1}{3}}\sum_{\gamma}\int\left[\rho_1^{\gamma}(r_1)\right]^{\frac{4}{3}}dr_1$$

$$\alpha_{ex} = \frac{2}{3} \qquad \textit{equation (4)}$$

There is however, no corresponding functional for the correlation part of the electron-electron interaction and so that part must be solved numerically. Accurate calculations of the correlation energy of a homogenous electron gas (**30**) used by Vosko, Wilk and Nusair (**31**) have led to an expression for the correlation energy per particle $\varepsilon_c\left[\rho_1^{\alpha},\rho_1^{\beta}\right]$ with spin densities ρ_1^{α} and ρ_1^{β}. This ε_c, multiplied by the density of electrons over the space, gives the correlation energy of the electronic system E_c.

$$E_c = \int\rho_1(r_1)\varepsilon_c\left[\rho_1^{\alpha}(r_1)\rho_1^{\beta}(r_1)\right]dr_1 \qquad \textit{equation (5)}$$

Calculations performed at the LDA level alone often significantly over-estimate binding energy. (**32**) As mentioned earlier, the local density approximation is derived from expressions describing exchange and correlation of a homogeneous electron gas. In a homogeneous electron gas, it is assumed that the charge variation around each electron is the same over all space. (**33**) In such a system, a description of the local density will therefore be sufficient to describe the whole system. However, in reality, systems tend to be inhomogeneous; that is, the charge around each electron varies very slowly and is spherically symmetric out to a defined radius. In order to account for this inhomogenity of $\rho(r)$ in an atom or molecule, non-local corrections can be applied to both the exchange and correlation functionals. In this way, V_{XC} from equation (1) is then expressed both in terms of location $V((\rho)r)$ and as a function of the gradient of the charge density $V(\rho(r), \nabla\rho(r))$ which accounts for the inhomogenity , (**25**) such that

$$\tilde{E}_{XC} = E_X^{LDA} + E_X^{NL} + E_C^{LDA} + E_C^{NL} \qquad \textit{equation (6)}$$

The two non-local corrections used during the course of this study are those suggested by Becke, which is a non-local exchange correction which includes a

correction for the measure of inhomogeneity of the electron density in finite systems (**34**), and that suggested by Perdew, which is a non-local correlation correction (**35**).

This combination of corrections has been shown previously to result in better results for the optimisation of metal to ligand bond lengths than can be achieved by using LDA alone. E_C^{NL} tends to shorten metal-ligand bond lengths while E_X^{NL} tends to lengthen them. A combination of these non-local corrections gives the most accurate results (**32**). Throughout this thesis, geometry optimisations were performed using LDA and the Becke and Perdew non-local corrections were used as a post-optimisation treatment. This method is less computationally expensive than including the non-local corrections from the beginning, while still producing geometries satisfactory for this study.

Having discussed the approximations and corrections involved in describing an approximation, $\tilde{E}_{XC}$, for the exact exchange-correlation energy, E_{XC}, from which one can derive V_{XC}, it is now possible to set out to solve equation (1). There exists a set of solutions ($\phi_i(r_1)$; i = 1, N) from which the electron density and then the total energy can be obtained. (**22**)

In practice, it is customary to expand $\phi_i(r_1)$ in terms of a known basis set of functions, $\{\chi_k(r_1)$; k = 1, M$\}$.(**22**)

$$\phi_i(r_1) = \sum_{k=1}^{k=M} C_{ik}\chi_k(r_1) \qquad \textit{equation (7)}$$

In this way the problem of solving equation (1) is transformed into the more simple task of finding a set of eigenvectors $\{C_{ik}$; i = 1, N and k = 1, M$\}$ and corresponding eigenfunctions from a secular equation. (**22**)

2.3.2 ADF parameters

The calculations were performed using the Amsterdam Density Functional (ADF) package, Version 2.0.1, developed by Baerends and co-workers (**24**) and included the numerical integration scheme of te Velde and co-workers (**36**). Spin-polarised, unrestricted calculations were performed on all open-shell species. For all unrestricted calculations the unpaired electron was placed in the α-spin (spin-up) molecular orbitals. The energies of corresponding levels vary slightly between α and β spins, especially in the region of the singly occupied molecular orbital, hence discussions throughout chapters 2.1 and 2.2 consistently refer to the β-spin molecular orbital energies. Despite the energetic variations, the percentage composition of each molecular orbital is identical in both α and β spin orientations. The local density approximation (LDA) (**28**) was employed using the parameterisation of Vosko, Wilk and Nusair. (**31**) Geometry optimisation was performed at the LDA level using the method developed by Ziegler and Versluis (**37**) and incorporated the quasi-relativistic correction of Ziegler and co-workers. (**38**) The energies of the LDA optimised species were recalculated to include the non-local gradient corrections of Becke (**34**) and Perdew (**35**). Triple-ζ STO basis sets were employed for Tc and Ru and double-ζ STO basis sets extended with a polarisation function were used for all other atoms. (**39**) An auxiliary set of s, p, d, f and g STO basis functions centred on all nuclei was used in order to fit the molecular density and describe accurately the coulomb and exchange potentials in each SCF cycle. (**40**) Core electrons (up to and including 3d for Tc, Ru and Br; 2p for P, Cl and 1s for C, N and O) were treated using the frozen core approximation.

Transition energies were calculated by the ΔSCF method which involved calculating both the ground-state and designated excited-state of the transition. The difference between the final energies of the ground-state and the excited-state was used as the calculated transition energy. (**1**) The optimised ground-state geometries were employed throughout primarily because they represent the true minimum and groundstate of the calculated potential energy surface and also to facilitate comparisons between transition energies associated with species for which there is crystal structure data available and those for which there is none to date. These same optimised geometries were also maintained for both the

ground-state and excited-state of each transition in accordance with the assumption that an electronic transition (of the kind of interest throughout this thesis) would occur on a time scale faster than geometrical changes. (**41**) For open-shell species analysed using spin-unrestricted calculations, the ΔSCF method was consistently applied to the β-spin molecular orbitals, except in cases where the transition of interest specifically involved the unpaired electron, where the α-spin molecular orbitals were employed exclusively for that particular transition.

References: Part Two

1. T. Ziegler and A. Rauk, *Theoret. Chim. Acta*, 1977, **46**, 1.

2. (*a*) G.A. Heath and J.E. McGrady, *J. Chem. Soc., Dalton Trans.*, 1994, 3759;
(*b*) J.E. McGrady, *Ph.D. Thesis*, The Australian National University, 1994.

3. E. Solomon, *Comments on Inorg. Chem.*, 1983, **3**, 225.

4. K.H. Moock, S.A. Macgregor, G.A. Heath, S. Derrick and R.T. Boeré, *J. Chem. Soc., Dalton Trans.*, 1996, 2067.

5. P.D. Lyne and D.M.P. Mingos, *J. Chem. Soc., Dalton Trans.*, 1995, 1635.

6. J. Baldas and S.F. Colmanet, *Austr. J. Chem.*, 1989, **42**, 1155.

7. R. Hübener and U. Abram, *Z. Anorg. Allg. Chem.*, 1992, **617**, 96.

8. J.Baldas, J.F. Boas, J. Bonnyman and G.A. Williams, *J. Chem. Soc., Dalton Trans.*, 1984, 2395.

9. J.Baldas, J. Bonnyman and G.A. Williams, *Austr. J. Chem.*, 1985, **38**, 215.

10. A.B.P. Lever, *Inorganic Electronic Spectroscopy*, Elsevier, New York, 1984, 2nd ed., 739.

11. J. Baldas, *Topics in Current Chem.*, 1996, **176**, 37.

12. J. Baldas, J.F. Boas, Z. Ivanov and B.D. James, *Proceedings of the 4th International Symposium on Technetium Chemistry and Nuclear Medicine*, 1994, 69.

13. J. Baldas, *Adv. Inorg. Chem.*, 1994, **41**, 1.

14. J. Baldas, S.F. Colmanet and G.A. Williams, *Inorg. Chim. Acta*, 1991, **179**, 189.

15. C.M. Duff and G.A. Heath, *J. Chem. Soc., Dalton Trans.*, 1991, 2401.

16. C.M. Duff and R.A. Schmid, *Inorg. Chem.*, 1991, **30**, 2938.

17. (*a*) B.D. Yeomans, *Ph.D. Thesis*, The Australian National University, 1995; (*b*) B.D. Yeomans and G.A. Heath, *Unpublished results*.

18. D. Menglet, *Ph.D. Thesis*, The Australian National University, 1996.

19. (*a*) G.A. Heath, *Personal communication*; (*b*) D.L Key, L.F. Larkworthy and J.E. Salmon, *J. Chem. Soc. (A)*, 1971, 2583.

20. S.F. Gheller, G.A. Heath and D.C.R. Hockless, *Acta Cryst.*, 1995, **C51**, 1805.

21. A.G. Orpen, L. Brammer, F.H. Allen, O. Kennard, D.G. Watson and R. Taylor, *J. Chem. Soc., Dalton Trans.*, 1989, S1.

22. T. Ziegler, *Chem. Rev.*, 1991, **91**, 651.

23. M.D. Rowe, A.J. McCaffery, R. Gale and D.N. Copsey, *Inorg. Chem.*, 1972, **11**, 3090.

24. (*a*) E.J. Baerends, D.E. Ellis and P. Ros, *Chem. Phys.*, 1973, **2**, 41; (*b*) E.J. Barends, J.G. Snijders, C.A. de Lange and G. Jonkers, *Local Density Appoximations in Quantum Chemistry and Solid State Physics*, Plenum, New York, 1984. (c) ADF version 2·0·1, released Dec 11 1995.

25. R.H. Hertwig and W. Koch, *J. Comput. Chem.*, 1995, **16**, 576.

26. P. Hohenberg and W. Kohn, *Phys. Rev. A,* 1964, **136**, 864.

27. W. Kohn and L.J. Sham, *Phys. Rev. A,* 1965, **140**, 1133.

28. (*a*) O. Gunnarsson, B.I. Lundqvist and J.W. Wilkins, *Phys. Rev. B,* 1974, **10**, 1319; (*b*) O. Gunnarsson and B.I. Lundqvist, *Phys. Rev. B,* 1976, **13**, 4274; (*c*) O. Gunnarsson, M. Jonson and B.I. Lundqvist, *Phys. Rev. B,* 1979, **20**, 43136.

29. J.C. Slater, *Phys. Rev.*, 1951, **81**, 285.

30. D.M. Ceperly and B.J. Alder, *Phys. Rev. Lett.*, 1980, **45**, 566.

31. S.J. Vosko, L. Wilk and M. Nusair, *Can. J. Phys.*, 1980, **58**, 1200.

32. L. Fan and T. Zeigler, *J. Chem. Phys.*, 1991, **95**, 7401.

33. M.A. Whitehead, *Self-Consistent Field, Theory and Applications*, eds. R. Carbó and M. Klobukowski, Elsevier, New York, 1990, 605.

34. A.D. Becke, *J. Chem. Phys.*, 1986, **84**, 4524.

35. J.P. Perdew, *Phys. Rev. B,* 1986, **33**, 8822, (and erratum, 1986, **34**, 7406).

36. G. te Velde and E.J. Barends, *J. Comp. Phys.*, 1992, **99**, 84.

37. L. Versluis and T. Ziegler, *J. Chem. Phys.*, 1988, **88**, 322.

38. (*a*) T. Ziegler, V. Tschinke, E.J. Baerends, J. G. Snijders and W. Ravenek, *J. Chem. Phys.*, 1989, **93**, 3050; (*b*) R. van Leeuwen, E. van Lenthe, J.G. Snijders and E.J. Baerends, *J. Chem. Phys.*, 1994, **101**, 1272.

39. (*a*) G.J. Snijders, E.J. Barends and P. Vernooijs, *Data Nucl. Data Tables*, 1982, **26**, 483; (*b*) P. Vernooijs, G.J. Snijders and E.J. Barends, *Slater-Type Basis Functions for the Whole Periodic System*, Internal Report, Free University of Amsterdam, 1981.

40. J. Krijn and E.J. Baerends, *Fit Functions in the HFS-method*, Internal Report, Free University of Amsterdam, 1984.

41. (*a*) J. Franck, *Trans. Farad. Soc.*, 1925, **21**, 536; (*b*) E.U. Condon, *Phys. Rev.*, 1928, **32**, 858.